86th ARFTG Microwave Measurement Conference

Microwave Measurements with Applications to Bioengineering and Biomedicine

December 3rd-4th 2015
Georgia Tech Hotel and Conference Center
Atlanta, Georgia

IEEE Catalog Number: CFP15ARG-USB
ISBN: 978-1-4673-9246-4

Copyright and Reprint Permission: Abstracting is permitted with credit to the source. Libraries are permitted to photocopy beyond the limit of U.S. copyright law for private use of patrons those articles in this volume that carry a code at the bottom of the first page, provided the per-copy fee indicated in the code is paid through Copyright Clearance Center, 222 Rosewood Drive, Danvers, MA 01923. For reprint or republication permission, email to IEEE Copyrights Manager at pubs-permissions@ieee.org. All rights reserved. Copyright ©2015 by IEEE.

86th ARFTG Conference Organizers

General Co-Chair	**Mohamed Sayed**
General Co-Chair and Technical Program Chair	**Joe Gering**

86th ARFTG Technical Program Committee

Peter Aaen, *University of Surrey*

Dave Blackham, *Keysight Technologies*

James Booth, *NIST*

Roland Clarke, *University of Leeds*

Gayle Collins, *Intel Corp.*

Joe Gering, *Qorvo, Inc.*

Chad Gillease, *Keysight Technologies*

Leonard Hayden, *Qorvo, Inc.*

Karel Hoffmann, *Czech Technical University*

Masahiro Horibe, *NMIJ*

Bill Hunt, *Georgia Institute of Technology*

Jim Hwang, *Lehigh University*

Mauro Marchetti, *Maury Microwave*

Jon Martens, *Anritsu Corporation*

Rusty Myers, *Maury Microwave*

Basim Noori, *Apple Inc.*

J. Apolinar Reynoso-Hernandez, *CICESE*

Nick Ridler, *NPL*

Patrick Roblin, *The Ohio State University*

Andrej Rumianstev, *Brandenburg University*

Mohamed Sayed, *MMS*

Dominique Schreurs, *KU Leuven*

Kubilay Sertel, *The Ohio State University*

Jörgen Stenarson, *Chalmers University of Technology*

Paul Tasker, *Cardiff University*

Frans Verbeyst, *National Instruments*

Mitch Wallis, *NIST*

Ken Wong, *Keysight Technologies*

John Wood, *Maxim Integrated Products*

The 2015 ARFTG Executive Committee (ExCom)

President and Publicity	**Mohamed Sayed**, MMS
Vice President and Strategic Planning	**Jon Martens,** Anritsu
Secretary and Nominations	**Dominique Schreurs**, K.U.Leuven
Treasurer and Standards	**Ronald Ginley**, NIST
Nonlinear Network Analyzers and Publicity	**Jean-Pierre Teyssier**, Keysight Technologies
Electronic Communications	**Mitch Wallis**, NIST
Education and Workshops	**Patrick Roblin**, The Ohio State University
Publications	**David Blackham**, Keysight Technologies
Sponsorship & Exhibits	**Joe Gering**, Qorvo, Inc.
Technical Coordination and Planning	**John Wood,** Maxim Integrated Products
Membership and Standards	**Ken Wong**, Keysight Technologies
Publicity & Sponsorship	**Gayle Collins**, Intel Corp.
Technical Coordination and Planning	**Nick Ridler**, NPL
Electronic Publicity	**Peter Aaen**, University of Surrey
MTT-S Liaison and Awards	**Leonard Hayden**, Qorvo Inc.

Ex-Officio

Executive Secretary	**John Cable**

Session A: RF/Microwave Applications to Bioengineering/Biomedicine

Chair: James Booth, NIST

Microwaves in Biomedical Science — A Path Forward (INVITED)

W. D. Hunt, Georgia Institute of Technology, Atlanta, United States

Sensor-on-CMOS Dielectric Characterization Using Temperature Modulation

J. Chien, A. M. Niknejad, University of California, Berkeley, Berkeley, United States

Broadband Single-Cell Detection with a Coplanar Series Gap

X. Ma, X. Du, C. Multari, Y. Ning, C. Palego, X. Luo, V. Gholizadeh, X. Cheng, J. C. Hwang, Lehigh University, Bethlehem, United States

Optimized Matching of an Implantable Medical Device Antenna in Different Tissue Medium Using Load Pull Measurements

P. Li, L. Zhang, F. Liu, J. Amely-Velez, St. Jude Medical, Sylmar, United States

Session B: Characterization of Flexible Substrates

Chair: Mitch Wallis, NIST

Microwave Characterization of Ink-Jet Printed CPW on PET Substrates

A. Sahu[1], V. Devabhaktuni[1], A. Lewandowski[2], P. Barmuta[2], T. M. Walllis[3], M. Shkunov[4], P. H. Aaen[4], [1]University of Toledo, Toledo, United States, [2]Warsaw University of Technology, Nowowiejska, Poland, [3]NIST, Boulder, United States, [4]University of Surrey, Guildford, United Kingdom

Measurement Methods for the Permittivity of Thin Sheet Dielectric Materials

J. Kim, J. Kang, J. Park, T. Kang, Korea Research Institute of Standards and Science, Daejeon, Republic of Korea

Session C: Nonlinear Measurements, Modeling, and Linearization

Chair: Dominique Schreurs, KU Leuven

Frequency-scalable nonlinear behavioral transistor model from single frequency X-parameters based on time-reversal transformation properties (INVITED)

D. E. Root[1], R. M. Biernacki[1], M. Marcu[1], M. Koh[3], P. J. Tasker[2], [1]Keysight Technologies, Santa Rosa, United States, [2]Cardiff University, Cardiff, United Kingdom, [3]M/A-COM Technology Solutions, Belfast, United Kingdom

Automatic Feed-Forward Cancellation of Modulated Harmonic

H. Yu1, V. Ratnasamy[1], P. Roblin[1], M. Rawat[2], C. Xie[3], [1]The Ohio State University, Columbus, United States, [2]Indian Institute of Technology, Roorkee, India, [3]Rockwell Collins, Cedar Rapids, United States

Enhanced PHD Model Extraction by Improving Harmonic Response Superposition During Extraction

D. T. Bespalko, S. Boumaiza, Emerging Radio Systems Group, Waterloo, Canada

Session D: Novel Measurement Techniques and Applications

Chair: Leonard Hayden, Qorvo

Towards Faster, Swept, Time-Coherent Transient Network Analyzer Measurements

J. Martens, E. Vayner, J. Tu, Anritsu, Morgan Hill, United States

Hurdles to On-Wafer Harmonic Measurements

K. J. Muhonen, Qorvo, Greensboro, United States

A compact measurement set-up for envelope-tracking RF PAs with calibrated sensing of baseband V/I at the supply terminal

J. Couvidat[1,2], G. Gibiino[1,3], G. Pailloncy[4], M. Vanden Bossche[4], A. Ghiotto[2], D. Schreurs[1], [1]KU Leuven, Leuven, Belgium, [2]University of Bordeaux, Talence, France, [3]University of Bologna, Bologna, Italy, [4]National Instruments, Zaventem, Belgium

Session E: Millimeter-wave and Terahertz Measurements and Calibration

Chair: Dave Blackham, Keysight

Continuing Challenge of Improving Measurement Accuracy in Terahertz Vector Network Analyzers - The Taming of "Terahertz Vector Network Analyzers" (INVITED)

M. Horibe, National Institute of Advanced Industrial Science and Technology (AIST) - National Metrology Institute of Japan (NMIJ), Tsukuba, Japan

Performance assessment of VNA calibration schemes for millimeter-wave and submillimeter-wave frequencies, using the 33 GHz-50 GHz band

K. Drazil, A. Pavlis, M. Hudlicka, Czech Metrology Institute, Prague, Czech Republic

An IQ-Steering Technique for Amplitude and Phase Control of mm-Wave Signals

A. Visweswaran[1,2], C. de Martino[1], E. Sirignano[1], M. Spirito[1], [1]Delft University of Technology, Delft, Netherlands, [2]IMEC, Leuven, Belgium

Session F: Calibration and Verification

Chair: Jon Martens, Anritsu

The Impact of Knowing the Impedance of the Lines Used in the TRL Calibration on the Load-Pull Characterization of Power Transistors

M. A. Pulido-Gaytan[1], J. A. Reynoso-Hernandez[1], M. d. Maya-Sanchez[1], J. R. Loo-Yau[2], [1]Cicese, Ensenada, Mexico, [2]Cinvestav, Zapopan, Mexico

Improved RSOL Planar Calibration via EM Modelling and Reduced Spread Resistive Layers

M. Spirito[1], L. Galatro[1], G. Lorito[2], T. Zoumpoulidis[2], F. Mubarak[3,1], [1]Delft University of Technology, Delft, Netherlands, [2]Iszgro Diodes BV, Delft, Netherlands, [3]Van Swinden Laboratorium , Delft, Netherlands

Calibration/Verification Standards for Measurement of Extremely High Impedance

M. Haase, K. Hoffmann, Czech technical university in Prague, Prague, Czech Republic

Evaluation and Modeling of Measurement Resolution of A Vector Network Analyzer for Extreme Impedance Measurements

F. Mubarak[1,2], R. Romano[2], M. Spirito[2], [1]Van Swinden Laboratorium (VSL), Delft, Netherlands, [2]Delft University of Technology, Delft, Netherlands

Interactive Forum

Chair: Ken Wong, Keysight Technologies

Uncertainty Analysis in Coplanar Waveguide with Unscented Transformation

A. A. Savin[1], V. G. Guba[2], O. N. Bykova[2], [1]Tomsk State University of Control Systems and Radioelectronics, Tomsk, Russian Federation, [2]NPK TAIR, a subsidiary of Copper Mountain Technologies, Tomsk, Russian Federation

Comparison Analysis of VNA Residual Errors Estimation Algorithms with Time Domain Separation

A. A. Savin[1], V. G. Guba[2], O. N. Bykova[2], [1]Tomsk State University of Control Systems and Radioelectronics, Tomsk, Russian Federation, [2]NPK TAIR, a subsidiary of Copper Mountain Technologies, Tomsk, Russian Federation

Impedance Standard Substrate Fabricated by Screen Printing Technology

M. Horibe, R. Sakamaki, AIST, Tsukuba, Japan

Joint Self-Heating and RF Large Signal Characterization

F. J. Martinez-Rodriguez[1,2], P. Roblin[1], J. I. Martinez-Lopez[2], [1]The Ohio State University, Columbus, United States, [2]Universidad Nacional Autónoma de México, Coyoacan, Mexico

Sensor-on-CMOS Dielectric Characterization Using Temperature Modulation

Jun-Chau Chien and Ali M. Niknejad

Department of Electrical Engineering and Computer Science, University of California, Berkeley, CA

Abstract — In this paper, on-chip temperature modulation is applied in a CMOS-based dielectric sensor for the determination of sample temperature coefficients in a microfluidic setting. System uncertainties are taken into account by a multi-step calibration with the use of on-chip metal-based switched-capacitors. Using de-ionized water as reference, the temperature coefficients of saline and methanol-water mixture are extracted at 17.5 GHz with temperature spanning from 32 ~ 37 °C.

Index Terms — dielectric relaxation, permittivity, temperature modulation, CMOS, injection-locked oscillators, microfluidics.

I. Introduction

Dielectric characterization of aqueous solutions at microwave frequencies shows great potential for rapid chemical and biological sensing [1-3]. As dielectric relaxation exhibits dispersion spanning over a broad frequency range, wideband measurements are inevitable, mandating a versatile instrumentation, i.e. the network analyzer, with frequency sweeping capability. On the other hand, it is desirable to lower both the system complexity and the form factor in practical applications including food monitoring and point-of-care diagnostics. Consequently, there exists a direct trade-off between the precision of material classification and the instrument size. A good example is the issue of classification ambiguity if measurements are carried out only at a spot frequency, as shown in Fig. 1(a). To avoid such coincidence problem (two material-under-test (MUT) exhibits same permittivity at one particular frequency), the number of sampling frequencies must be larger than two.

As the thermal energy of the molecular system plays a crucial role in the dielectric relaxation for polar solutions, we are motivated to explore the feasibility of utilizing the temperature dependency of polarization to facilitate the material classification. The idea is to quantify the temperature coefficient of the material permittivity to expand signal dimensions, as depicted in Fig. 1(b).

Recently, our group has demonstrated a highly sensitive capacitor sensor implemented in CMOS technology for glucose and protein sensing [4-5]. With the combination of microfluidics, such heterogeneous integration offers an excellent platform for rapid chemical and biological sensing. Previously, the measurements are all performed with regulated chip temperature. In this work, the same sensor chip is utilized to study the effect of temperature modulation on dielectric characterization. As sensing is performed directly on the CMOS chip, calibration is essential and is discussed with the aid of system model.

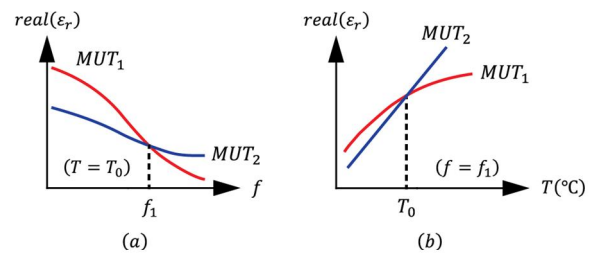

Fig. 1. (a) Coincidence problem in material characterization at spot frequency. (b) Dielectric classification utilizing temperature dependency.

II. Sensor Architecture

Fig. 2 shows the sensor architecture for microwave dielectric characterization [6]. Two oscillators (ILO_1 and ILO_2), embedded with coplanar electrode capacitive sensors, are injection-locked to the quadrature outputs of an on-chip signal source (QVCO). As the frequencies of both ILOs remain locked, the modulation of the sensing capacitors is transduced into phase shift at the outputs, which can be detected with a mixer-based phase detector. Benefiting from the nature of interferometry, such an architecture offers substantial phase noise rejection against the signal source, thereby improving the sensitivity to sub-aF resolution, ultimately limited by the residual frequency noise of each sensing ILO [7]. The phase difference presented to the mixer can be derived as [6]:

$$\Delta\theta = \theta_1 - \theta_2 = 2 \cdot Q_1 \cdot \left(\frac{I_{osc}}{I_{inj}}\right)_1 \cdot \frac{\Delta\omega_1}{\omega_{osc1}} - 2 \cdot Q_2 \cdot \left(\frac{I_{osc}}{I_{inj}}\right)_2 \cdot \frac{\Delta\omega_2}{\omega_{osc2}}, \quad (1)$$

where $Q_{1\text{-}2}$, $(I_{osc}/I_{inj})_{1\text{-}2}$, and $\omega_{osc1\text{-}2}$ represent the tank-Q, the inverse of the injection strength, and the oscillation frequencies, respectively. It is worth mentioning that two ILOs are necessary in order to match both ILO paths for optimum noise rejection.

To relax the dynamic range requirement, feedback is applied around the sensor by compensating the sample-induced capacitance change with an on-chip varactor [5]. In such a feedback-around-sensor architecture, the dielectric signal can be read out directly from the V_{ctrl} of the loop filter. The measurement can be referred as the frequency shift of the

978-1-4673-9247-1/15/$31.00 ©2015 IEEE

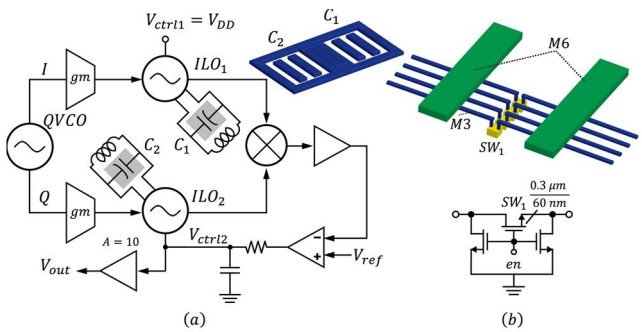

Fig. 2. (a) Sensor block diagram. (b) On-chip switched-capacitor.

sensing oscillator if the gain (K_{VCO}, MHz/V) and the center frequency (f_{osc}) are measured before closing the loop:

$$\frac{\Delta\omega}{\omega_0} = \Delta V_{ctrl} \cdot \frac{K_{VCO}}{f_{osc}}. \tag{2}$$

To perform fluidic experiments, a microfluidic chip is fabricated in PDMS with two U-shaped fluidic channels (width = 50 µm, height = 100 µm), each covering one sensing electrode. To interface with the CMOS die, the PDMS is first bonded onto a glass holder and placed manually onto a PCB under a microscope.

Temperature modulation is performed through on-chip heating and off-chip water-cooling with a dedicated fluidic channel running across the chip surface (Fig. 3). By controlling the flow rate in the cooling channel, the chip temperature can be modulated through the change in the convective heat transfer coefficient, thereby eliminate the need for a temperature chamber. In this work, gravitational flow is used instead of a mechanical pump to avoid any pulsatile flow. The flow rate is controlled by either elevating the outlet of the cooling channel or by lowering the position of the water reservoir. Chip temperature is measured using an on-chip diode sensor (Fig. 3). Though the absolute V_{BE} is sensitive to both the biasing current and the process spread, the temperature coefficient maintains relatively constant at -2 mV/ºC according to the circuit simulation based on the model provided by the foundry. The power delivered to the loaded sample (estimated volume ~ 200 pL) by the oscillator sensor is less than 0.8 mW (0.7-V amplitude across a 300-Ω load) and hence microwave heating has negligible impact on the actual chip temperature.

III. Calibration Procedure

A multi-step calibration is necessary in the proposed sensor-on-CMOS dielectric characterization using temperature modulation. To understand the procedure, an equation is derived to model the sensor output as a function of temperature according to eq. (1):

$$V_{out}(\Delta T) = K_1 \cdot C_{sense,1}(\Delta T) - K_2 \cdot C_{sense,2}(\Delta T) + V_0(\Delta T), \tag{3}$$

where

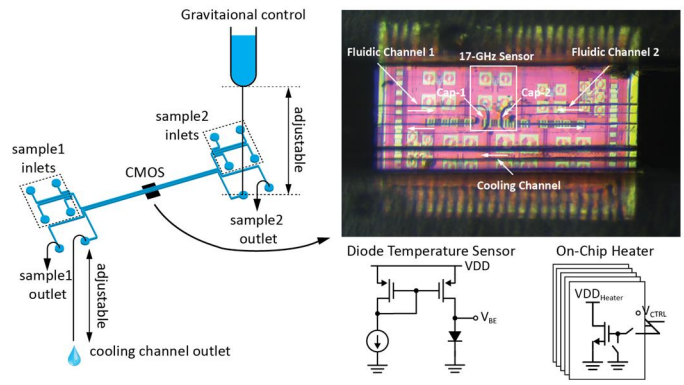

Fig. 3. Microfluidic setup, water-cooling control, die photo, and on-chip temperature sensor/heaters.

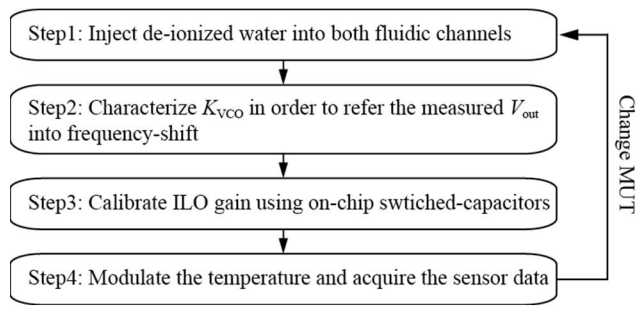

Fig. 4. Calibration procedure.

$$K_i = f\left(Q_i, \omega_{osc,i}, \left(\frac{I_{osc}}{I_{inj}}\right)_i\right), \qquad i = 1 \text{ or } 2. \tag{4}$$

Here K_i models the transducer gain of each sensing oscillator and its value is dependent on the polarization and the dielectric loss of the material as well as the injection strength. $V_0(\Delta T)$ captures the temperature dependency of the on-chip circuitry, and is quantified by measuring the unloaded sensor, i.e. the air. Note that the sensing capacitors are not only related to both the permittivity of the MUT but also the effective sensing area, which is determined by the coverage of the electrode by the fluidic channel. To capture such an effect, the sensing capacitors are expressed with a scaled factor, A_i:

$$C_{sense,i}(\Delta T) = A_i \cdot \varepsilon_{r,i}(\Delta T), \qquad i = 1 \text{ or } 2. \tag{5}$$

In (5), $\varepsilon_{r,i}$ represents the real part of the material permittivity. The uncertainty of the sensing area is due to the variation of fluidic channel geometry and the misalignment between the fluidic channels and the sensing electrodes. With (5), (3) can be expressed in the form of temperature coefficient:

$$\frac{\partial V_{out}}{\partial T} - \frac{\partial V_0}{\partial T} = K_1 A_1 \chi_1 - K_2 A_2 \chi_2. \tag{6}$$

Here χ_1 and χ_2 are the temperature coefficients (%/ºC) of the material permittivity. According to (6), the sensor output is nulled out with temperature modulation if A_1 matches perfectly with A_2. Such a property is highly desirable in sensor design as the temperature drift is completely rejected. On the contrary, we take advantage of such mismatch for temperature dependency study in this work.

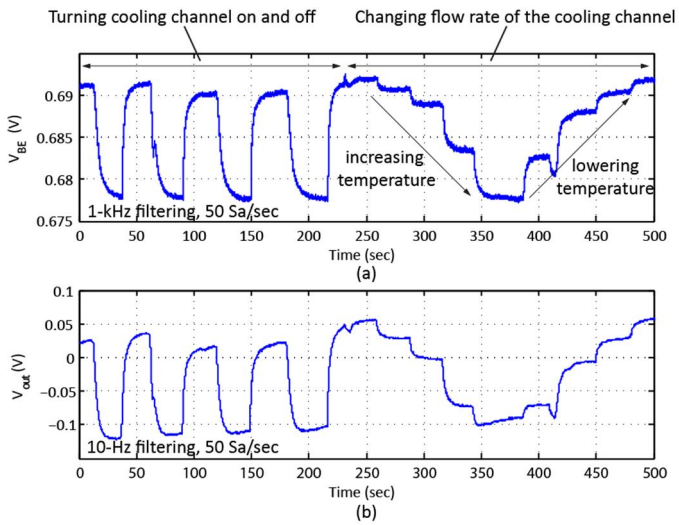

Fig. 5. Measured time-domain waveforms: (a) V_{BE} and (b) V_{out}.

Fig. 4 details the calibration procedure. First, the K_{VCO} is characterized for each material. Next, K_i are quantified using on-chip switched-capacitors embedded within each ILO (Fig. 2(b)). Such switched-capacitors are implemented using metal interconnection and serves as temperature-insensitive on-chip references. K_i is then calibrated to some fixed value for each material by adjusting the injection strength using an on-chip current DAC. Afterward, de-ionized water, which serves as reference material for the quantification of the effective sensing area, is injected into both channels. Temperature modulation is then applied and the sensor output is monitored. Finally, the entire procedure is repeated for the unknown material (MUT) and its temperature coefficient is calculated.

IV. Measurements

Fig. 5 shows the measured time-domain waveforms when temperature modulation is applied. Correlation between diode V_{BE} and the sensor output is clearly observed. Such a demonstration is performed at 17-GHz sensing channel while the two electrodes are both immersed with identical saline solutions (used for contact lens cleansing). The thermal time constant is approximately 10 sec and is different for temperature rising and falling. This is because the temperature modulation is achieved by changing the thermal convection, not the ambient temperature. The sensor output has a filtering bandwidth of 10 Hz.

By sampling the measured waveforms after the temperature reaches steady state, frequency-shift versus temperature change are plotted. Fig. 6 shows the results from measuring (1) air, (2) de-ionized water, (3) saline, and (4) methanol-water mixture prepared by mixing 10 mL of methanol and 40 mL of water solutions (16.5 w/w%). In Fig. 6, several conclusions can be made. First, the measured frequency shift due to sensor electronics alone exhibits linear and positive temperature dependency. On the other hand, the measured frequency shift

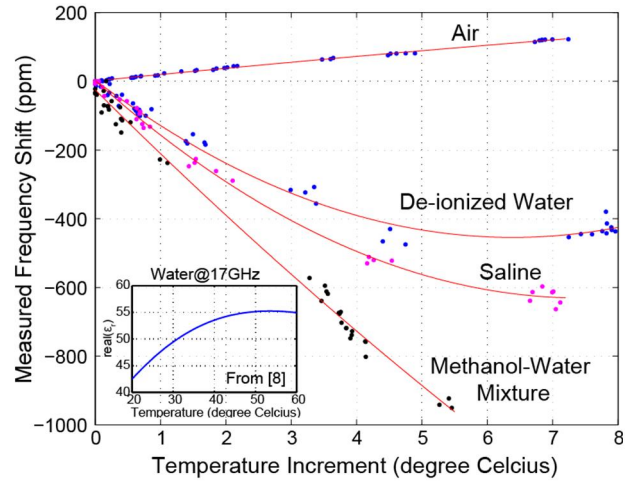

$$\Delta f(ppm) = a\Delta T^2 + b\Delta T + c$$

Sample	a	b	c
Air	-0.257	18.855	1.083
DI-Water	112.14	-143.29	3.254
Saline	3.418	189.27	24.666
Methanol Mixture	11.413	170.01	2.151

Fig. 6. Measured frequency shift vs. temperature change when both C_1 and C_2 are loaded with the same medium.

when both C_1 and C_2 are immersed in pure water exhibits not only 2nd-order but also negative temperature dependency. Such a result matches the trend of the previous investigations by [8] and [9] where the interpolated function of the Debye relaxation model versus temperature is plotted in the inset of Fig. 6. Next, saline also exhibits 2nd-order temperature dependency but exhibiting substantial difference compared to water, justifying that the salinity of solution can indeed change the temperature coefficient of the medium. Finally, it is found that the inclusion of methanol increases the temperature coefficient significantly. However, 2nd-order dependency for such a mixture cannot be observed due to limited temperature modulation range (~ 5 ºC). This is because these experiments are carried out with the medium also in their flowing states, thereby reducing the efficacy of the cooling. Keeping the mixture flowing is necessary as it is found that the property of the methanol mixture changes over time when not in flow, even if the temperature is locked through temperature regulation. This could possibly due to methanol vaporizing faster at an elevated chip temperature above 32 ºC. In addition to methanol, both isopropyl alcohol and ethanol exhibits similar property change if the measurement is performed at zero flow rate. Note that such an issue has not been addressed in other sensor-on-CMOS literatures [10-12]. All the measured curves are fitted with 2nd-order polynomials and the extracted temperature coefficients are tabulated in Fig. 6. After correcting for the temperature effect due to CMOS electronics, the temperature coefficients of saline and methanol-water are extracted as 1.189 and 1.314 %/ºC at 32 ºC, respectively, when reference to that of pure water (1.017

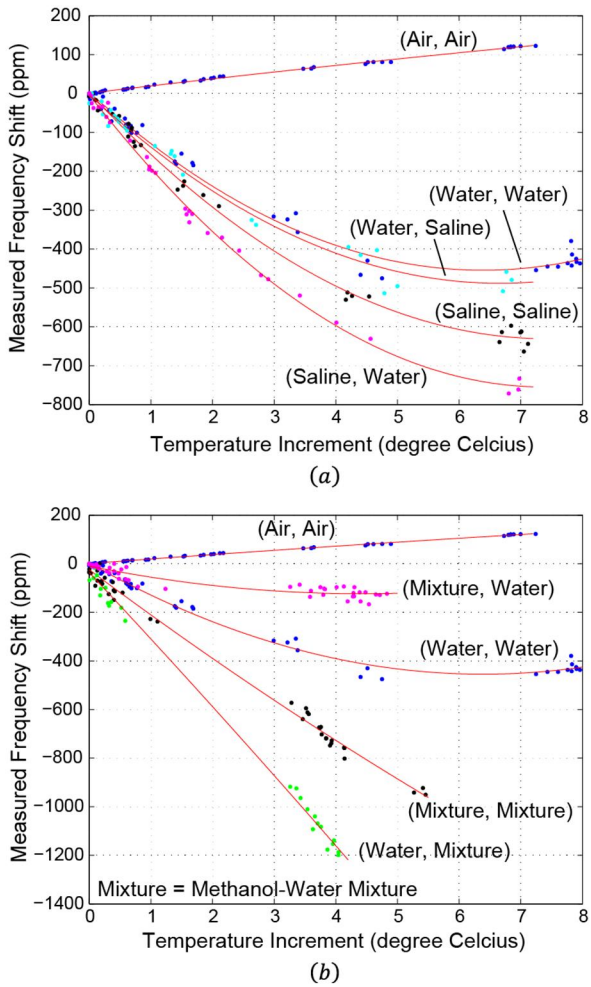

Fig. 7. Measure frequency shift vs. temperature change when C_1 and C_2 are loaded with different medium.

%/ºC) . The exact measurement frequency is between 17.4 ~ 17.5 GHz.

With two sensing capacitors, additional measurements can be performed for any combination of two mediums by alternating them between the two fluidic channels. The results are plotted in Fig. 7. With these additional measurements, the effective sensing area (A_i in eq. (6)) for each sensing capacitor can be extracted separately.

V. Conclusion

In this work, temperature modulation is proposed to expand the signal dimensions and hence the accuracy of the material classification using microwave dielectric spectroscopy. A calibration procedure is presented for sensor-on-CMOS temperature characterization. Measurements from pure water exhibit non-linear temperature coefficients at 17.5 GHz, matching the trend with previous work. The concept of temperature modulation is supported by measured differences in temperature coefficients between water, saline, and methanol-water mixture.

References

[1] M. Hofmann, et. al., "Microwave-based noninvasive concentration measurements for biomedical applications," *IEEE Trans. Microw. Theory Tech.*, vol. 61, no. 5, pp. 2195 – 2204, May 2013.

[2] G. A. Ferrier, et. al., "A microwave interferometric system for simultaneous actuation and detection of single biological cells," *Lab on a Chip*, vol. 9, no. 23, pp. 3406 – 3412, Oct. 2009.

[3] K. Grenier, et. al., "Recent advances in microwave-based dielectric spectroscopy at the cellular level for cancer investigations," *IEEE Trans. Microw. Theory Tech.*, vol. 61, no. 5, pp. 2023 – 2030, May 2013.

[4] J.-C. Chien, et. al., "A Microwave Reconfigurable Dielectric-based Glucose Sensor with 20 mg/dL Sensitivity at Sub-nL Sensing Volume in CMOS," in *IEEE MTT-S Int. Microw. Symp.*, May. 2015, pp. 1 – 4.

[5] J.-C. Chien, et. al., "A Near-Field Modulation Chopping Stabilized Injection-Locked Oscillator Sensor for Protein Conformation Detection at Microwave Frequency," *in Proc. Symp. VLSI Circuits Dig. Tech. Papers*, Jun. 2015, pp. 332 – 333.

[6] J.-C. Chien, et. al., "A 6.5/11/17.5/30-GHz high throughput interferometer-based reactance sensors using injection-locked oscillators and ping-pong nested chopping," *in Proc. Symp. VLSI Circuits Dig. Tech. Papers*, Jun. 2014, pp. 107 – 108.

[7] J.-C. Chien, *Advanced High-Frequency Measurement Techniques for Electrical and Biological Applications*, Ph.D. Dissertation, UC Berkeley, Spring 2015.

[8] T. Meissner, et. al., "The complex dielectric constant of pure and sea water from microwave satellite observations," *IEEE Trans. Geoscience and Remote Sensing*, vol. 42, no. 9, pp. 1836 – 1849, Sep. 2004.

[9] W. J. Ellison, "Permittivity of pure water, at standard atmospheric pressure, over the frequency range 0 – 25 THz and the temperature range 0 – 100 ºC," *J. Phys. Chem. Ref. Data*, vol. 36, no. 1, pp. 1 – 18, 2007.

[10] M. M. Bajestan, et. al., "A 0.62 - 10 GHz complex dielectric spectroscopy system in 0.18-um CMOS," *IEEE Trans. Microw. Theory Tech.*, vol. 62, no. 12, pp. 3522 – 3537, Dec. 2014.

[11] O. Elhadidy, et. al., "A wide-band fully-integrated CMOS ring-oscillator PLL-based complex dielectric spectroscopy system," *IEEE Trans. Circuits Syst. I, Reg. Papers*, vol. 62, no. 8, pp. 1940 – 1949, Aug. 2015.

[12] S. Guha, et. al., "Label free sensing of creatinine using a 6 GHz CMOS near-field dielectric immunosensor," *Analyst*, 140, pp. 3019 – 3027, 2015.

Broadband Single-Cell Detection with a Coplanar Series Gap

X. Ma, X. Du, C. R. Multari, Y. Ning, C. Palego, X. Luo, V. Gholizadeh, X. Cheng, and J. C. M. Hwang

Lehigh University, Bethlehem PA 18015, USA

***Abstract* — Using a coplanar waveguide with a series gap in conjunction with dielectrophoresis trapping, consecutive *S*-parameter measurements between 0.5 and 20 GHz were quickly performed with and without a Jurkat cell trapped to compensate for a relatively noisy and drifting background. This allowed the small cytoplasm capacitance, on the order of 10 fF, to be reliably extracted. The extracted cytoplasm capacitance is within a factor of 2 of the previously reported value by using a shunt trap but is believed to be more accurate. The present technique can complement previously developed microwave and RF techniques in characterizing the capacitances and resistances of plasma and membrane for complete characterization of the electrical properties of a simple cell.**

***Index Terms* — Biological cells, biosensors, microwave measurements, sensitivity.**

I. Introduction

For detection of biological cells, electrical detection can be faster, more compact, and less destructive than traditional chemical or optical detection [1]. However, although broadband electrical detection with single-cell sensitivity has been demonstrated [2], [3], it remains challenging mainly due to low signal-to-noise ratio. This paper differs from [2] by using electrical instead of mechanical trapping to allow quick release of a trapped cell and comparison with the background signal. This paper differs from [3] by using a series instead of shunt trap to boost the sensitivity to a single cell, especially to its cytoplasm capacitance. These differences led to statistically meaningful signals for distinguishing a single live Jurkat cell from a dead one as described in the following.

II. Test Setup and Protocol

Fig. 1(a) shows that the present test setup is based on a homemade microwave probe station on top of an inverted fluorescent microscope similar to that of [3]. The device under test (DUT) comprises a gold coplanar waveguide (CPW) intersected at a right angle by a poly-dimethyl-siloxane (PDMS) microfluidic channel. Fig. 1(b) shows that, different from [3], the center electrode of the CPW is tapered to a 10 μm × 10 μm series gap for single-cell dielectrophoresis (DEP) trapping as shown in greater detail in Fig. 1(c). Similar to [3], the CPW is patterned in 2-μm-thick gold on top of 635-μm-thick quartz. The CPW is 1-cm long with the widths of center electrode, electrode spacing, and ground electrodes being 40 μm, 10 μm and 100 μm, respectively. The PDMS cover is 5-mm wide and 4-mm high. The microfluidic channel molded into the underside of PDMS is 150-μm wide and 50-μm high.

The DUT was tested from 0.5 to 20 GHz by using an Agilent Technologies 5230A precision network analyzer and a pair of Cascade Microtech ACP40 GSG probes. DEP signal at 10 MHz and 4.4 V peak-to-peak generated by an Agilent 8116A function generator was coupled to the microwave signal through an Agilent 11612A bias network. Although the series gap in the center electrode and the shunt gap between the center and ground electrodes were both 10-μm wide, the electric field gradient in the series gap was significantly enhanced by the taper. As simulated by using Ansys HFSS, the maximum filed gradient in the series and shunt gaps were approximately 1.3×10^{12} V/m^2 and 0.4×10^{12} V/m^2, respectively. Thus, a cell could be preferentially trapped and released in the series gap by turning the DEP signal on and off. This allowed consecutive *S*-parameter measurements to be made quickly with and without a cell and the difference recorded as shown in the following section.

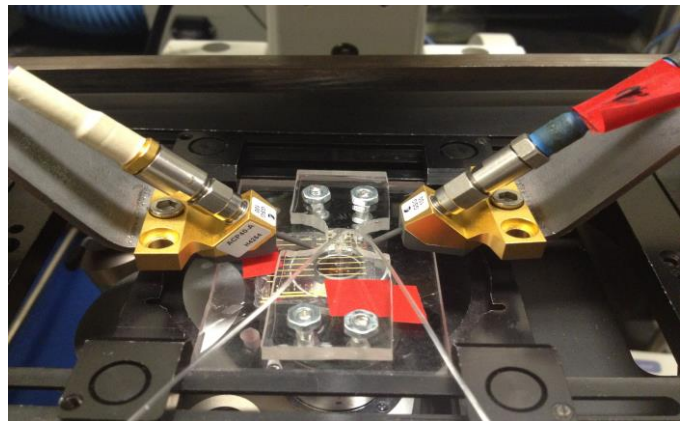

(a)

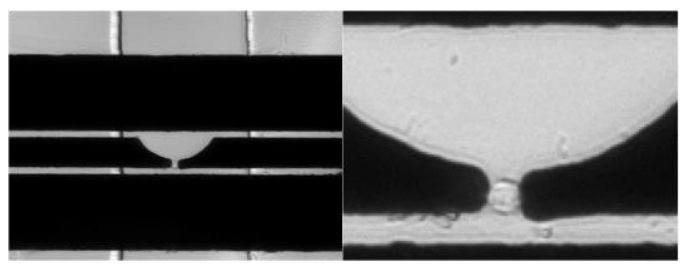

(b) (c)

Fig. 1. (a) DUT on top of an inverted microcope. (b) Details of DUT with a coplanar series gap. Vertical lines beside the gap delineate a transparent microfluidic channel. (c) Greater details of the gap with a Jurkat T-lymphocytes human cell trapped.

For proof of concept, Jurkat T-lymphocytes human cells were used due to their large diameter (~10 μm), non-adherent nature, and simple structure. Live cells were prepared

978-1-4673-9247-1/15/$31.00 ©2015 IEEE

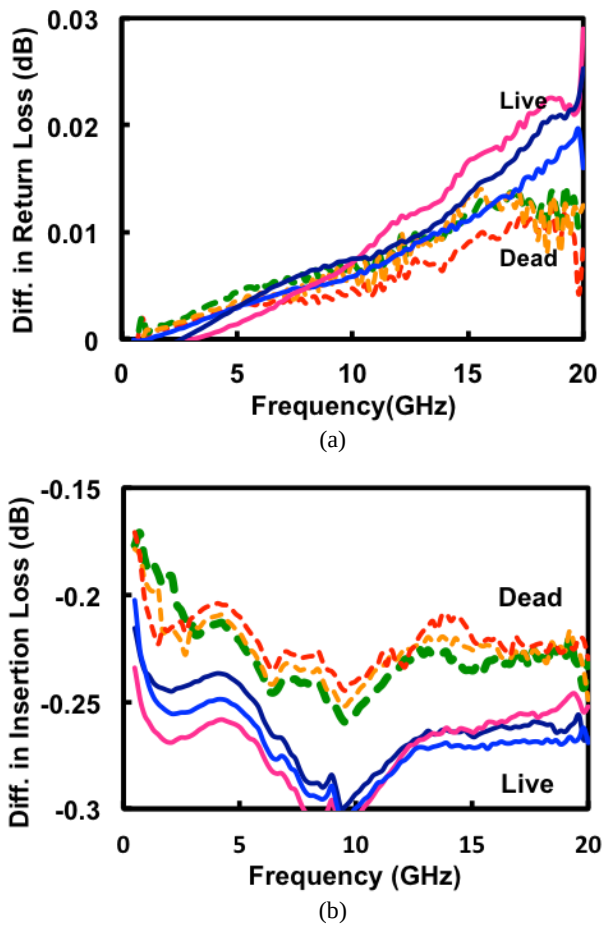

Fig. 2. Measured differences in (a) return loss $|S_{11}|$ and (b) insertion loss $|S_{21}|$ of a Jurkat cell with measurements repeated six times on three live cells (solid curves) and three dead cells (dashed curves).

according to the same protocol as in [3] and re-suspended in a 8.5% sucrose solution at a concentration of 3×10^6 cells/ml. Dead cells were similarly prepared except an extra heating step of 120 °C for 6 min. Suspensions of live or dead cells were injected into the microfluidic channel at a rate of 0.1 µl/min using a FUSION 400 syringe pump.

III. Results and Discussion

Fig. 2 compares the measured differences in return loss $|S_{11}|$ and insertion loss $|S_{21}|$, respectively, of a Jurkat cell. To illustrate the repeatability of the measurement, the measurement was repeated six times on three live cells and three dead cells. It can be seen that, although the differences in return and insertion losses are as small as 0.01 dB, they are nevertheless significant between live and dead cells especially in the insertion loss. While the difference in the return loss appears to increase linearly with increasing frequency, the relatively flat difference in the insertion loss suggests that the detection can be much easier and faster by sampling only a few fixed frequencies instead of sweeping through all frequencies. This is opposite to that of [3] in which cells were trapped in shunt configuration, so that the difference in the return loss is greater than the difference in the insertion loss.

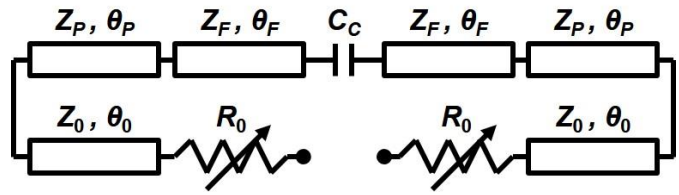

Fig. 3. Equivalent circuit of a capacitor C_C coupling three sets of transmission lines under sucrose (Z_F, θ_F), PDMS (Z_P, θ_P) and air (Z_0, θ_0) respectively with losses lumped into two frequency-dependent resistors R_0.

TABLE I
Equivalent-Circuit Parameter Values

Subcircuit	Parameter	Symbol	Jurkat Cell		Sucr-ose
			Live	Dead	
Gap	Coupling Capacitance	C_C (fF)	14.8	14.9	15.3
CPW under Fluid	Char. Impedance	Z_F (Ω)	20		
	Length @ 1 GHz	θ_F (°)	0.37		
CPW under PDMS	Char. Impedance	Z_P (Ω)	31		
	Length @ 1 GHz	θ_P (°)	4.9		
CPW under Air	Char. Impedance	Z_0 (Ω)	62		
	Length @ 1 GHz	θ_0 (°)	5.6		
Loss	Freq.-dep. Resistor	R_0 (Ω)	$0.71\times 10^{-9} f$		

For the present series trap configuration, the measured difference in the insertion loss is mainly due to the difference in capacitive (as opposed to resistive) coupling across the series gap. Fig. 3 shows an equivalent circuit of a coupling capacitance C_C connected in series with three sets of transmission lines under sucrose, PDMS and air with characteristic impedances Z_F, Z_P, Z_0 and electrical length θ_F, θ_P and θ_0, respectively. The transmission line losses are lumped into two frequency-dependent resistors, whose linear dispersion was verified by using Ansys HFSS. Using the equivalent circuit with parameter values listed in Table I, coupling capacitances of 14.8 pF, 14.9 pF and 15.3 pF for a live cell, a dead cell and without any cell, were found to best fit the measured data as shown in Fig. 4(a) where the average of data from three different cells are plotted. Better fit at the low-frequency end can be obtained by adding a resistance in parallel to the coupling capacitance as in [4], but the overall difference is not significant.

To further validate the equivalent-circuit model, Fig. 4(b) compares the measured and simulated insertion and return losses with the microfluidic channel empty or filled with the sucrose solution. For the empty channel, C_C = 1.8 pF, Z_F = 62 Ω, and θ_F = 0.13° at 1 GHz, while all other parameters were the same as that listed in Table I. Note that unlike Fig. 4(a), the much larger scale of Fig. 4(b) does not allow the difference with and without a cell to be shown.

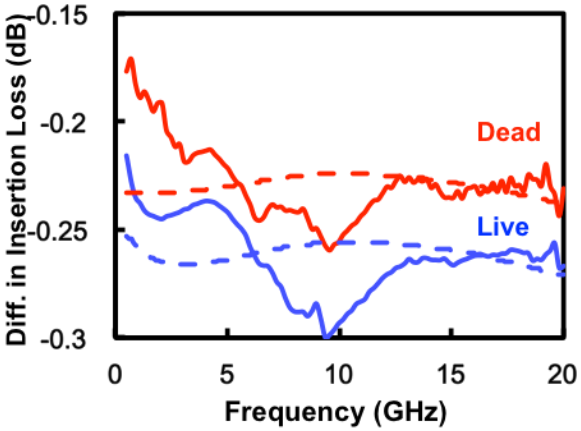

(a)

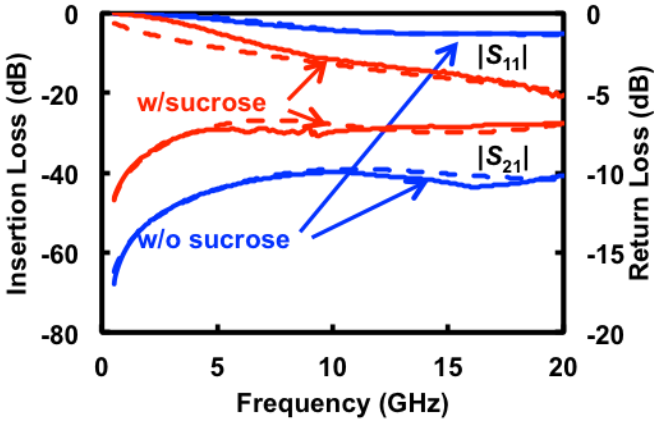

(b)

Fig. 4. Measured (solid curves) vs. simulated (dashed curves) (a) difference in insertion loss for a live or dead Jurkat cell, and (b) insertion and return losses with the microfluidic channel empty or filled with sucrose soltion.

For the present frequency range of 0.5−20 GHz, the membrane capacitance is largely bypassed so that coupling capacitance with a cell trapped can be attributed mainly to the cytoplasm capacitance [4]. The presently extracted cytoplasm capacitance is approximately half of the previously reported value of 29 fF [4]. However, as the present series trap is more sensitive to cytoplasm capacitance whereas the previous shunt trap is more sensitive to cytoplasm resistance, it is believed that the present cytoplasm capacitance value is more accurate than the previously reported value. In any case, giving the difficulty in measuring capacitances on the order of 10 fF, it is interesting to observe that the two different methods agree within a factor of 2. Additionally, using the shunt trap, the difference in cytoplasm capacitances of live and dead cells are indistinguishable, whereas the present series trap appears to be capable of detecting subtle differences in cytoplasm capacitance on the order of 0.1 fF. The fact that $C_{C,\,LIVE} < C_{C,\,DEAD} < C_{C,\,SUCROSE}$ is consistent with the lower permittivity of cytoplasm (~67) compare to that of the 8.5% sucrose solution (~82) [5]. As a cell dies, its membrane becomes more permeable to sucrose so that the cytoplasm permittivity approaches that of sucrose.

IV. Conclusion

The dielectric property of a cell is dominated by that of its membrane at radio frequencies, but that of its plasma at microwave frequencies [6]. The present microwave technique with a series trap was found useful for extracting the cytoplasm capacitance, which could complement the previous developed microwave technique with a shunt trap [4] for extracting the cytoplasm resistance, and the previously developed RF technique [7] for extracting the membrane resistance and capacitance. Together they could help completely characterize the electrical properties of a cell at the most basic level.

Acknowledgement

The project depicted is sponsored in part by the U.S. Department of Defense, Defense Threat Reduction Agency under Contract No. HDTRA1-12-1-0007 and Army Research Office under Contract No. W911NF-14-1-0665.

References

[1] K. Grenier, D. Dubuc, T. Chen, F. Artis, T. Chretiennot, M. Poupot, and J.-J. Fournie, “Recent advances in microwave-based dielectric spectroscopy at the cellular level for cancer investigations,” in *IEEE Trans. Microw. Theory Techn.*, vol. 61, no. 5, pp. 2023–2030, May 2013.

[2] W. Chen, D. Dubuc, and K. Grenier, “Microwave dielectric spectroscopy of a single biological cell with improved sensitivity up to 40 GHz,” in *IEEE MTT-S Int. Microw. Symp. Dig.*, Phoenix, Arizona, May 2015, pp. 1–3.

[3] Y. Ning, X. Ma, C. R. Multari, X. Luo, V. Gholizadeh, C. Palego, X. Cheng, and J. C. M. Hwang, “Improved broadband electrical detection of individual biological cells,” in *IEEE MTT-S Int. Microw. Symp. Dig.*, Phoenix, Arizona, May 2015, pp. 1–3.

[4] Y. Ning, C. Multari, X. Luo, C. Palego, X. Cheng, J. C. M. Hwang, A. Denzi, C. Merla, F. Apollonio, and M. Liberti, “Broadband electrical detection of individual biological cells,” in *IEEE Trans. Microw. Theory Techn.*, vol. 62, no. 9, pp. 1905–1911, Sep. 2014.

[5] A. Denzi, C. Merla, C. Palego, A. Paffi, Y. Ning, C. R. Multari, X. Cheng, F. Apollonio, J. C. M. Hwang, and M. Liberti, “Assessment of cytoplasm conductivity by nanosecond pulsed electric fields,” *IEEE Trans. Biomed. Eng.*, vol. 62, no. 6, pp. 1595−1603, Jun. 2015.

[6] K. R. Foster and H. P. Schwan, “Dielectric properties of tissues and biological materials: A critical review,” in *Rev. Biomed. Eng.*, vol. 17, pp. 25–104, 1989.

[7] C. Palego, C. Merla, Y. Ning, C. R. Multari, X. Cheng, D. G. Molinero, G. Ding, X. Luo, and J. C. M. Hwang, “Broadband microchamber for electrical detection of live and dead biological cells,” in *IEEE MTT-S Int. Microwave Symp. Dig.*, Seattle, WA, Jun. 2013, pp. 1−3.

Optimized Matching of an Implantable Medical Device Antenna in Different Tissue Medium Using Load Pull Measurements

Perry Li, Lequan Zhang, Franklin Liu, Jorge Amely-Velez

St. Jude Medical, Sylmar, California, 91342, USA

***Abstract* — RF communication with implantable medical devices (IMD) such as a pacemaker experience unique challenges due to the operating conditions within a human body. This includes added body losses caused by the different tissue compositions where material properties range from ε_r=58 (muscle) to ε_r=5.58 (fat). In order to achieve maximum throughput for a 402MHz RF signal, it is important to have minimum mismatch losses between the RF front end of a device and the embedded antenna. This paper presents a method to optimize the matching with various tissues using load pull analysis with a prototype implantable medical device as an example. By using automated impedance tuners, an optimum impedance point was found, improving the mismatch loss by as much as 3dB compared to a design with no consideration given to tissue variation.**

***Index Terms* — Biomedical telemetry, implantable biomedical device, load pull, impedance measurement, impedance matching, implantable antenna.**

I. Introduction

Wireless communications have been enormously beneficial for implantable medical devices in the way of improved patient care. Implantable devices with RF communications, in particular, offer a number of advantages over their predecessors which communicated over an inductive link [1]. During an operation, they allow for the device to be implanted while the basestation resides outside the sterile field of the patient. This removes the need for an inductive wand which would need to be sterilized and placed close to the implant. Thus, patient safety is improved while at the same time reducing the complexity of the surgical procedure for the physician. During follow up clinic visits, RF communications allow for less invasive examinations. The inductive wand which would normally be placed in direct contact with the patient is replaced with the RF basestation which can be placed at a distance where it is out of the notice of the patient. One of the most important benefits of RF communication is in the area of remote care. Setting up a remote basestation at a patient's home enables nightly device checks without patient involvement. One such remote care system is the Merlin@Home system [2] from St. Jude Medical. Using this system, certain parameters such as device diagnostics, programming, and patient activity can be monitored from the physician's office while being transparent to the patient.

Many wireless implantable medical devices operate at the Medical Implant Communications System (MICS) frequency band of 402-405MHz. Implantable antennas at this frequency are electrically small and therefore usually do not have a 50 ohm characteristic impedance. As the antenna impedance deviates from 50 ohms, it is strongly influenced by the surrounding tissue that the device is implanted in. The surrounding tissue can detune the antenna's resonance frequency causing the antenna to drift from its natural impedance [3]. This is true even for an implantable device with an antenna embedded in insulating material [4] so that the antenna is not in direct contact with the tissue. A device such as a pacemaker may operate in different tissue compositions depending upon location and depth of the implant. Fig. 1 shows some typical implant locations beneath various tissue layers.

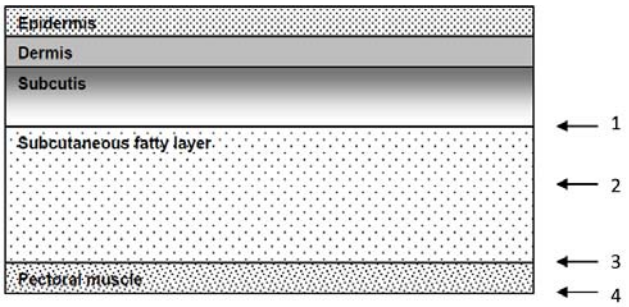

Fig. 1. Typical tissue layers in which an implantable cardiac device operates with common implant pocket locations pointed out.

The deeper implants reside in the muscle layer or at the muscle/ fat interface while the shallower implants reside just below the skin or in the fat layer. Table 1 shows the dielectric properties of some common tissue types [5]. Since dielectric constants (ε_r) can vary greatly from tissue to tissue, the corresponding antenna impedances within the different tissue layers will also experience large variation.

TABLE I

DIELECTRIC PARAMETERS OF DIFFERENT BODY TISSUE AT 402MHZ

Tissue	ε_r	σ (S/m)
Fat	5.58	0.04
Skin	47	0.69
Muscle	58	0.8
Blood	64	1.35

978-1-4673-9247-1/15/$31.00 ©2015 IEEE

The choice of implant pocket location and depth is based upon physician preference and cannot be controlled; therefore, it is advantageous to design a matching network that can minimize the losses regardless of where the implant is located [6], [7]. Since many implantable devices already have severe power limitations, additional mismatch losses which degrade overall RF performance must be avoided. One way to accomplish this is to use an automated load pull system [8] to simulate the antenna impedance embedded in different tissue and then find the optimum match to the implant's RF front end. To demonstrate this, a prototype implantable cardioverter defibrillator (ICD) is tested. The ICD uses a loop antenna embedded into the header and a MicroSemi ZL70102 RF transceiver [9]. The loop antenna was designed to operate in the 402-405MHz range with a simulated characteristic impedance of 47+j106 ohms in a ½ muscle-equivalent phantom (ε_r=30, σ =0.55).

II. In vivo antenna impedance measurements

While simulations with tissue phantoms or human body models serve as an essential first step towards establishing the antenna characteristics [10], in vivo testing is necessary to either verify the simulated characteristics or adjust them to fit realistic conditions.

In order to determine realistic implanted antenna impedances, an in vivo measurement needs to be performed using antenna prototypes in an ICD device [7], [11]. The antenna was embedded within an insulating epoxy (ε_r=3, δ=0.033) header which is common for ICD's and pacemakers as the headers also house the lead connectors. A semi-rigid cable was used to connect the antenna through the device housing to a Keysight E5071C vector network analyzer where impedance at 402MHz was measured. A picture of the prototype is shown in Fig. 2.

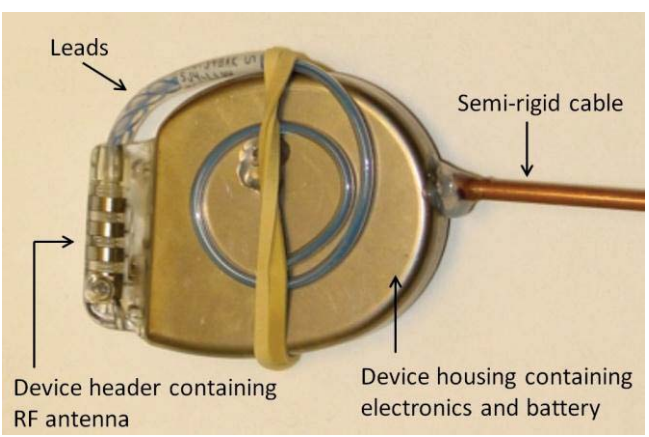

Fig. 2. Prototype implantable cardioverter defibrillator (ICD) device with embedded antenna used for in vivo study.

The prototypes were implanted at the locations indicated in Fig. 1. Each device was measured in all four tissue pockets and the S11 data was recorded. For this testing, 18 prototype devices were used during two different in vivo studies to generate 36 impedance points per tissue pocket. Results of the impedance measurements are shown in Fig. 3 with each pocket shown in a different color. Pocket 1 lies in the subcutis layer directly beneath the skin, between skin and fat. Pocket 2 lies completely in the fat later. Pocket 3 lies just above the muscle at the boundary between fat and muscle. Pocket 4 is the deepest implant, being completely within muscle tissue.

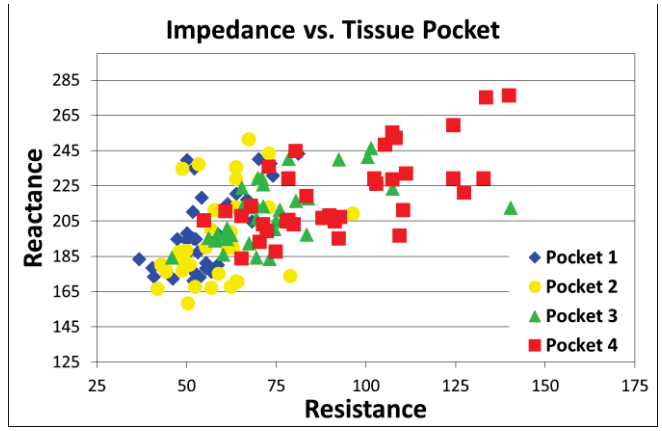

Fig. 3. Results of in-vivo studies with ICD devices.

The data shows that the empirically measured impedances had higher reactance when compared to the simulated antenna impedance. This is to be expected as the simulations were run in a uniform phantom material with a single dielectric constant. In reality, an implant pocket can be composed of more than one tissue type including fluid or blood which can easily account for the reactance shift. The results also show an impedance variation depending upon the type of tissue that the antenna was in contact with. The devices implanted along or inside the muscle layer displayed significantly higher resistance and reactance than the devices implanted in the fat layer or directly beneath the skin. Based on the measured data, the antenna resistance can vary from 36 to 140 while the reactance can range anywhere from 158 to 276. Since the RF transceiver was designed to be matched to a single impedance, any amount of variation from varying tissue pockets can create significant mismatch. In order to properly optimize the matching network thereby decreasing mismatch loss, a load pull analysis can be run using the constellation of realistic antenna impedances from tissue measurements.

III. Load pull measurements

For the preliminary design of the matching network, lumped components were selected based on Agilent ADS simulations of the RF layout using the published transceiver impedance and a simulated antenna impedance of 47+j106 ohms. A load pull measurement was run using the test setup shown in Fig. 4. In this setup, the ICD device was used as the signal source and

DUT. The header of the device including the embedded antenna were removed and replaced with an interface board to connect the device's internal RF front end to external test instrumentation. This allows the load pull system to determine the real input impedance of the front end which includes the Microsemi ZL70102 transceiver, the PCB as well as any flexes and connectors used to route the RF signal to the antenna. In this occasion, a Maury automated impedance tuner was connected to the DUT to simulate the impedance of the antenna implanted in different tissues. A power measurement at the output of the tuner can then be made to determine the output power at each impedance point measured from the in vivo study. The DUT was programmed to output a 402MHz CW signal. To measure the signal coming out of the tuner, a Keysight power meter was used. The Maury Automated Tuner System software [12] performed the load pull procedure including the de-embedding of the interface board.

Fig. 4. Diagram of the load pull test setup. Shown are the implantable device (with interface board in place of header/antenna) serving as both signal source and DUT, a Keysight E3631A DC Power Supply, a Maury MT981A Automated Tuner, a Keysight E4419B Power Meter with Power Sensor, and the Maury Automated Tuner System Software v.5.0.

The tuner can generate a wide range of impedance points by mechanically moving a reflective probe along a slabline. The probe moving along the slabline changes the phase while the probe moving towards the slabline affects the magnitude. For this test, the tuner was programmed to move to every point in the constellation of tissue impedances. Since the initial DUT impedance match usually does not fall within that constellation on the first design run, other programmed impedance points were also selected with 0.2Γ uniform spacing within the same quadrant of the Smith Chart. All the programmed impedances (displayed as crosses) along with the results are shown in Fig. 5. The square at the center of the contour circles represents the impedance that generated the highest output power and therefore, the current impedance match of the DUT. The circles are Pout contours at steps of 0.5dB.

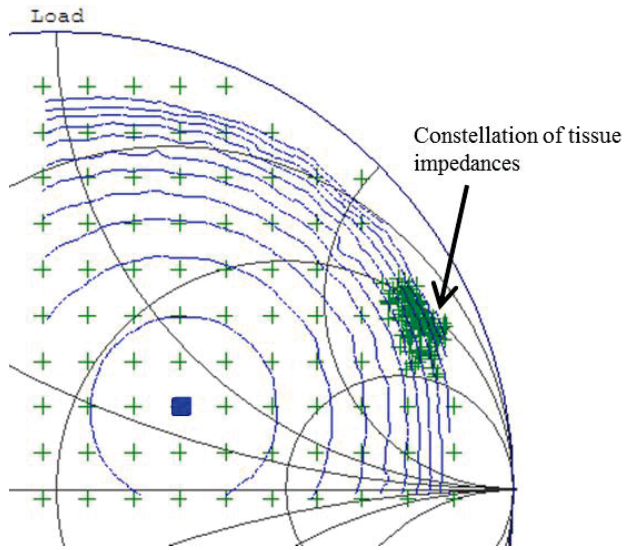

Fig. 5. Initial load pull where RF front end is not matched to real impedances.

A few observations can be made from this first load pull measurement. Although the target matching impedance for this prototype was 47+j106 ohms, the actual DUT impedance turned out to be 80+j32 ohms. There are a number of reasons for this discrepancy. There can be inaccuracies in the published RF transceiver input impedance, components such as flexes or connector pins may not be accounted for in the simulations, and there may be other parasitics in the layout that were not included in the simulation. A second observation is that as the contours get closer to the targeted tissue impedances, the spacing between the contours decreases. This means for a relatively small change in impedance or implant tissue, there is a corresponding large change in loss, making it important to match the DUT to a point in the constellation that minimizes the loss at the outer impedances.

Knowing the DUT's impedance match from Fig. 5, a change to the matching network can be made to shift the DUT's match closer to the tissue impedances. A 2nd load pull measurement was made yielding a better match between the DUT and the tissue. Although some of the tissue impedances showed low mismatch (<0.5dB), the farthest impedances showed large loss (>5dB). It was clear from this data that a further optimization step could be taken to get minimum mismatch loss across all tissue impedances. Even though the DUT could be matched to any of the tissue impedance points, the Pout contour circles showed that the difference between the two farthest impedance points is potentially 6dB. Thus, careful consideration must be given to minimize the loss even at the worst case impedances at the edge of the constellation. Since the load pull software is programmed to measure all the tissue impedances and then generates the contours based on this data, the optimum match occurs when the farthest impedance points are able to be covered by the smallest possible contour circle. With this in mind, a final optimization

was made to the matching network and a 3rd load pull measurement was made. The results are shown in Fig. 6. The final DUT match location (blue) and contour circles are shown along with the DUT match after the 2nd load pull run (red).

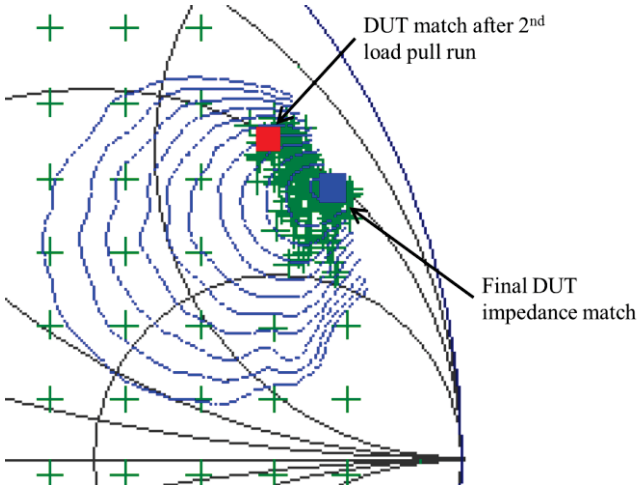

Fig. 6. Final results of 3rd load pull run. The final DUT matched impedance is shown as a square. The DUT match after the 2nd run is also shown as a circle.

The results show that the DUT impedance match is now at a more preferred location of 51+j220 ohms. From Fig.6, the minimum contour size was found to be the 3dB circle which leads to a maximum mismatch loss of 3dB or less at all the tissue variances. For this ICD device, the matching network has now been optimized. Using this process, we are able to ensure minimal mismatch loss across different tissue types found in implant pockets.

IV. Conclusion

For an implantable medical device where there are inherent challenges to achieving good wireless communication, it is critical to eliminate extra losses created by tissue mismatches. A method to optimize impedance matching between an implantable antenna and the RF front end using load pull testing has been presented. Using an implantable cardioverter defibrillator as an example, we show that the load pull analysis can help accurately match the impedance of the RF front end to empirically measured antenna impedances. Furthermore, using the Pout contours as a guide, the match can be fine-tuned to give the lowest possible mismatch loss across the entire range of tissues that the embedded antenna may encounter. This approach is very valuable in scenarios where the tissue composition of the implant pocket can vary.

Acknowledgement

The authors would like to thank Rusty Myers, Eric Kueckels, and Steve Dudkiewicz of Maury Microwave for their contributions and support for this paper.

References

[1] A. J. Johansson, "Performance of a Radio Link Between a Base Station and a Medical Implant Utilising the MICS Standard," *26th Annual Int. Conf. of IEEE EMBS,* San Francisco, U.S.A., 2004.

[2] St. Jude Medical, "Merlin@Home Transmitter", January 2015. [Online]. http://sjm.com/professional/products/crm/connectivity-remote-care/remote-care/merlin-home-transmitter

[3] N. Vidal, S. Curto, J. M. Lopez-Villegas, J. Sieiro, and F. M. Ramos, "Detuning Effects on Implantable Antenna at Various Human Positions," *6th European Conf. on Antennas and Propagation,* Prague, Czech Republic, 2012.

[4] T. Dissanayake, K. P. Esselle, and M. R. Yuce, "Dielectric Loaded Impedance Matching for Wideband Implanted Antennas," *IEEE Trans. Microwave Theory & Tech.,* vol. 57, no. 10, pp. 2480-2487, October 2009.

[5] FCC "Body Tissue Dielectric Parameters Tool". [Online]. https://transition.fcc.gov/oet/rfsafety/dielectric.html

[6] F. C. W. Po, E. de Foucauld, P. Vincent, F. Hameau, D. Morche, C. Delavaud, R. Dal. Molin, P. Pons, R. Pierquin, and E. Kerhervé, "A Fast and Accurate Automatic Matching Network Designed for Ultra Low Power Medical Applications," *IEEE Int. Symp. Circuits Systems,* Taipei, Taiwan, 2009.

[7] E. Chow, M. M. Morris, and P. P. Irazoqui, "Implantable RF Medical Devices," *IEEE Microwave Magazine,* vol. 14, no. 4, pp. 64-73, June 2013.

[8] G. Simpson, "Impedance Tuning 101: A Beginner's Guide To All Things Load Pull," *Microwaves and RF Magazine.,* December 2014. [Online]. http://mwrf.com/test-measurement/impedance-tuning-101

[9] Microsemi Corporation, "ZL70102 datasheet", May 2012. [Online]. http://www.microsemi.com/document-portal/doc_view/125431-zl70102-full-datasheet

[10] J. Kim and Y. Rahmat-Samii, "Implanted Antennas Inside a Human Body; Simulations, Designs, and Characterizations," *IEEE Trans. Microwave Theory & Tech.,* vol. 52, no. 8, pp. 1934-1943, August 2004.

[11] P. K. Abbassi, A. M. M. A. Allam, and R. M. Abdelkader, "Design and Implementation of Implanted Antenna Inside a Human Body," *IEEE Conf. on Antenna Measurements and Applications,* Antibes Juan-les-Pins, France, 2014.

[12] Maury Microwave Corporation, "Automated Tuner System software v5", May 2012. [Online]. https://www.maurymw.com/pdf/datasheets/4T-020A.pdf

Microwave Characterization of Ink-Jet Printed CPW on PET Substrates

A. Sahu*,V. Devabhaktuni*,A. Lewandowski†, P. Barmuta†, T. M. Wallis‡, M. Shkunov§, and P. H. Aaen§
*Department of Electrical Engineering and Computer Science,The University of Toledo,Toledo,Ohio,USA
† Institute of Electronic Systems, Warsaw University of Technology, Warsaw, Poland
‡National Institute of Standards and Technology Boulder, Colorado, USA
§Department of Electronic Engineering, Advanced Technology Institute, University of Surrey, UK
Email: Abhishek.Sahu@utoledo.edu

***Abstract*— This paper describes microwave characterization of coplanar waveguide (CPW) lines formed by ink-jet printed technology on flexible polyethylene terephthalate (PET) substrates. The reel-to-reel printing process uses inkjet printing as a precursor for 2μm copper plating, which allows significantly lowered resistances as compared to traditional inks. A multiline TRL calibration technique has been used to characterize the propagation constant and reflection coefficient of the CPW lines. With the aid of four sets of measurements at two identical labs, it is shown that the fabricated samples have contact repeatability, permitting redundant multiline calibrations**

***Index Terms*— Ink-jet printed CPW, flexible substrates, multiline calibration**

I. INTRODUCTION

Fabrication of microwave devices by use of ink-jet printing technology is an emerging and rapidly growing field. Ink-jet printed microwave circuits using flexible substrates present a number of significant advantages, including mechanical flexibility and the capability to conform to non-planar geometries. This approach presents an additive manufacturing approach for mass production that is cost-effective, low loss, and has rapid printing times. Recent research has led to the development of various components such as radio frequency identification (RFID) tags [1], antennas [2], [3], and coplanar waveguides (CPW) [4] by use of ink-jet printing on flexible substrates, for example Kapton [5].

Polyethylene terephthalate (PET) is another widely used flexible substrate that is being explored for microwave circuit design. K. Hettak et al. reported CPW on flexible PET with an attenuation of 0.6 dB / mm at 40 GHz [6]. Menicanin et al. have reported inkjet printed CPW meander inductors based on PET substrate [7], [8]. In order to fully realize the promise of flexible, ink-jet-printed RF and microwave applications, there is a need for robust metrology to characterize circuits fabricated by use of such techniques. Furthermore, and perhaps just as important, reliable measurements are needed to characterize the material components, such as substrates and inks. Very recently, several attempts have been made to measure the electrical properties of inkjet printed CPW meander sprial inductors [8] and graphene patterns on PET based substrate [9]. However, the development of metrology to characterize the ink properties on PET-based substrates is still in the early stages of development. Hence, in this paper, we perform calibrated microwave measurements of ink-jet-printed CPW lines on a PET substrate as a first step toward developing a broadly-applicable test platform for evaluation of flexible, ink-jet-printed microwave circuits as well as their constituent materials. The multiline TRL calibration is well-established and provides a well-understood foundation for this test platform. Additionally, TRL enables the extraction of transmission line properties via the calibration [10]. Section II describes the fabrication process of the CPW lines along with their dimensions. Measurement details and discussion of the results are presented in Sections III and IV, respectively.

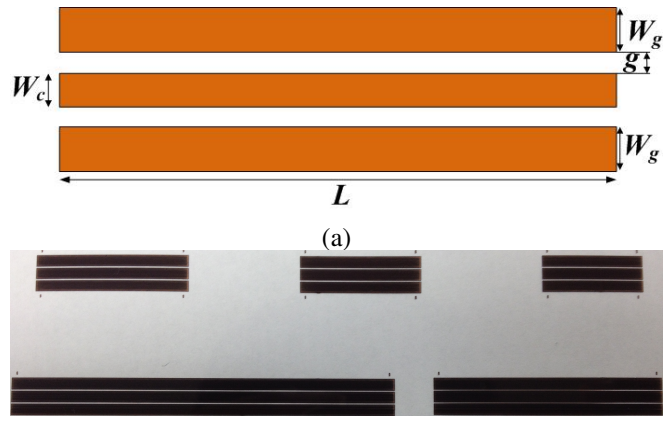

Fig. 1. (a) CPW dimensions (b) Photograph of fabricated CPW lines.

II. FABRICATION OF CPW LINES

A. Fabrication

The fabrication process was carried out using a commercial process with Inkjetflex [11]. The process uses ink-jet printing as a precursor on which copper is electroplated. This overcomes the low resistance issues that commonly occur with traditional and nano-particle inks used in ink-jet processes. In this work, the copper is plated to be approximately 2 μm thick. The process uses reel-to-reel printing in which a circuit of almost any length can be fabricated. We used a clear PET substrate for our work due to its much lower cost compared to other flexible circuits such as polymide and Kapton, good chemical resistance to acids and solvents and ability to withstand higher operating temperature than other thermoplastics. The fabrication was performed at 360 dots per inch in a single printing pass.

978-1-4673-9247-1/15/$31.00 ©2015 IEEE

The prototyping for the circuit was performed using a sheet resistance of 30 mΩ/mm^2.

B. Line Geometry

Figure 1(a) depicts a sketch of a CPW line with (W_c) 1.983 mm, gap width (g) 0.13 mm, ground conductor width (W_g) 1.983 mm, substrate thickness 125 μm and copper thickness 2 μm. The line lengths were determined based on the approach [12]. To enable a multiline TRL calibration, six CPW lines have been fabricated with lengths 14.97, 18.42, 23.57, 35.78, 61.60, and 97.93 mm. Additionally, a CPW Short circuit has been fabricated for use as a reflect standard in the mulitline TRL calibration.

Finally, a mismatch (or Beatty) CPW device has been fabricated on the same substrate as the standards for use as a verification device. A photograph of fabricated 50Ω ink-jet printed CPW lines appears in Fig. 1(b).

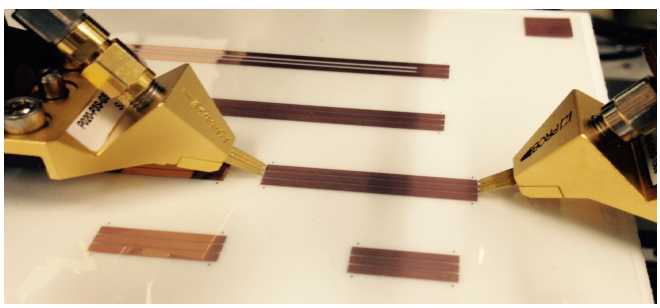

Fig. 3. Measurement set up for CPW lines.

III. Measurement and Parameter Extraction

The CPW lines have been measured using a commercial on-wafer probe station, a vector network analyzer (VNA), and ground-signal-ground contact probes (1.0 mm pitch). During measurements, the PET substrate has been supported by a 0.5 cm-thick porous, dielectric. The power level of VNA has been set to -17.0 dBm. The raw complex scattering parameters have been measured for each device from 10 MHz to 20 GHz. We adopted a multiline Thru-Reflect-Line calibration [6] technique to characterize the propagation constant and reflect reflection coefficient of the CPW lines. In order to test the repeatability of the results, all standards have been measured before and after the measurement of the verification DUT, thus yielding two sets of calibration coefficients. Additionally, four sets of measurements have been carried out at two separate laboratories on nominally identical sets of devices from the same ink-jet-printed batch in order to further confirm repeatability of the results. Figure 3 depicts a photograph of a measurement set-up. Similar measurement setups have been used at both the Institute of Electronics Systems, Warsaw, Poland and the National Institute of Standards and Technology (NIST), Boulder.

IV. Results

We utilized a calibration-DUT measurement-calibration approach to examine the repeatability of the CPW lines. In order to simplify the procedure, we adopted a first-tier

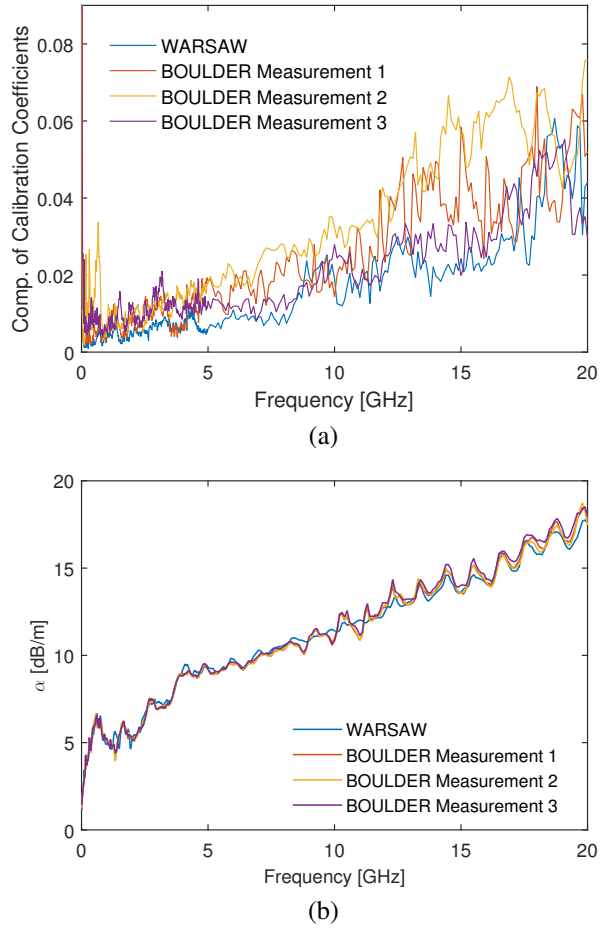

Fig. 4. (a) Comparison of attenuation constant from four sets of measurements (b)Difference of calibration coefficients from pre-calibration and post calibration of all standards from 4 sets of measurements.

calibration that included the VNA switch terms. After the pre-calibration is complete, the mismatch CPW devices have been measured. To verify the repeatability of the fabricated prototypes, we performed four sets of measurements; each with a pre and post calibration. Figure 2 depicts the comparison of DUT S-parameters from the measurements. It can be seen that the four sets of measurements agree quite well with each other, confirming the repeatability of the measurements. However, as can be observed, there is a small difference in the phase of S_{11} which might be due to inconsistent probe positioning during the measurement or can be attributed to the damage of link after repeated contacts from the probe. The calibration comparison technique [13], [14] has been used to evaluate repeatability of results. This technique evaluates the worst-case deviations of the measured S-parameters of passive devices for an examined calibration with respect to a benchmark calibration. Deviations are treated as $|S_{ij} - S_{ij'}|$ for ij $\in$ 11, 12, 21, 22, where $S_{ij'}$ is the S-parameter measured by the first (or pre) calibration to be tested, and S_{ij} is the S-parameter measured by the second (or post) calibration. At each frequency, the deviation is calculated for all four

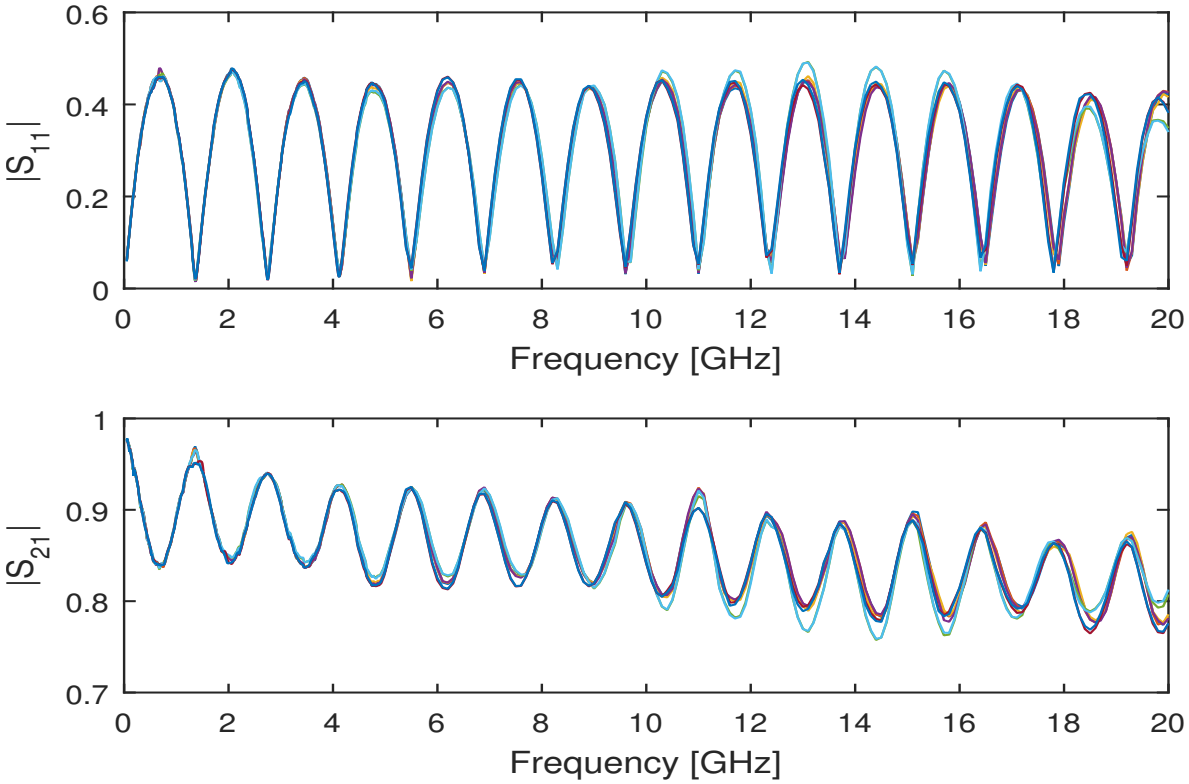

(a)

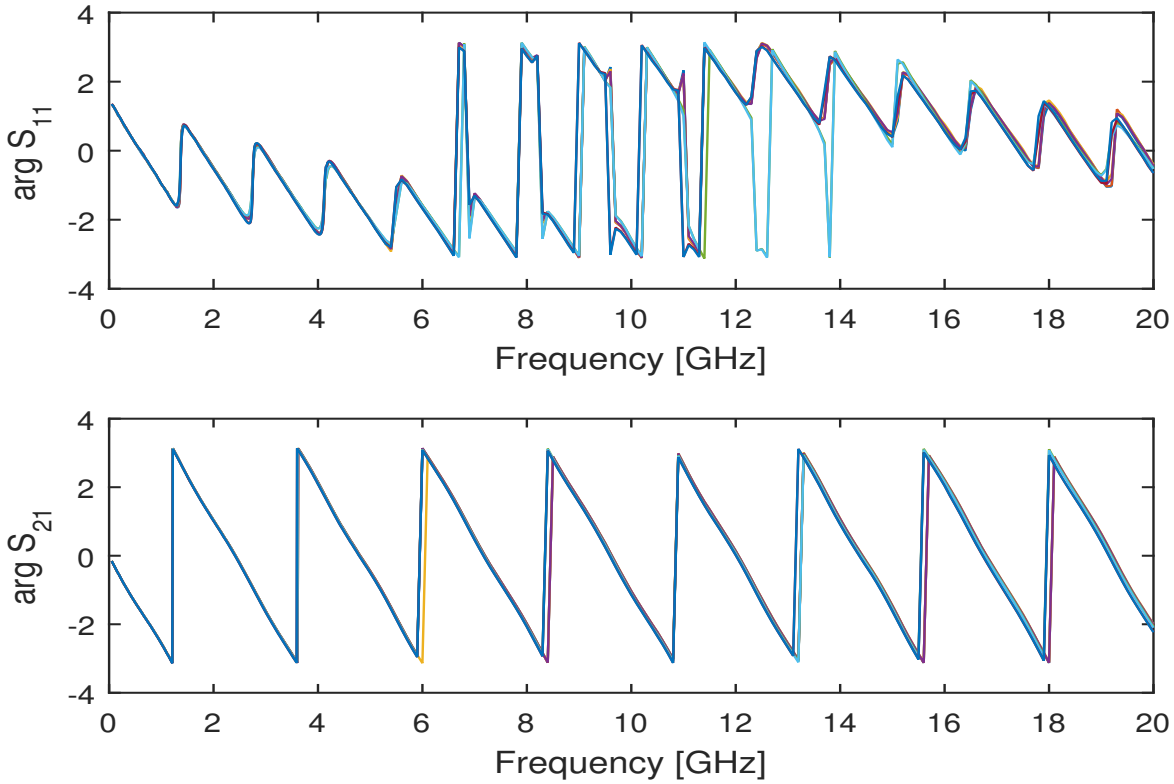

(b)

Fig. 2. Comparison of DUT S-Parameters (a)Magnitude of S-Parameters (b)Phase of S-Parameters. (note that each figure represents four sets of measurements from two separate, nominally identical sets of devices at two different laboratories at **BOULDER** and **WARSAW**.)

S-parameters and the largest deviation is determined, as shown in Fig. 4(a). The worst-case difference is quite small, indicating high repeatability of calibration results. Finally, we were able to extract the propagation constant from the multiline TRL which will be further used to extract the other material properties such as characteristic impedance, line capacitance and load resistance in our future work. Fig. 4(b) shows plot for the attenuation constant from four measurements. As expected, it can be seen that loss increases with frequency.

V. CONCLUSIONS

This paper presents characterization of CPW lines on flexible PET substrate. Using a multiline calibration technique, we were able to extract the propagation constant for the ink-jet printed CPW devices, which may be used to extract the complete set of material properties of the devices in the future. The demonstrated calibration comparison indicated high repeatability of the calibrated measurements. Additionally, a nominally identical set of devices was measured multiple times in a separate lab, demonstrating repeatability of both the DUT measurements and the fabrication process. Results indicated a high level of agreement between the calibrated S parameters of a mismatch verification device. Together, these results demonstrate a viable test platform for characterization of ink-jet printed microwave circuits as well as the constituent materials.

ACKNOWLEDGMENT

Arkadiusz Lewandowski was supported by the Polish National Science Center in the framework of the project no. 2011/03/D/ST7/01731.

REFERENCES

[1] M. A. Ziai and J. C. Batchelor, "Temporary on-skin passive UHF RFID transfer tag," *IEEE Trans. Antennas Propag.*, vol. 59, no. 10, pp. 35653571, Oct. 2011.

[2] G.A. Casula, G. Montisci and G. Mazzarella, "A Wideband PET InkjetPrinted Antenna for UHF RFID," *IEEE Antennas Wireless Propag. Lett.*, vol. 12, pp. 1400-1403, 2013.

[3] T. Peter, Y.Y. Sun, T.I. Yuk, H.F. AbuTarboush, R. Nilavalan and S.W.Cheung, "Miniature transparent UWB antenna with tunable notch for green wireless applications," *Antenna Technology (iWAT)*, 2011 International Workshop on, pp. 259-262.

[4] K. Hettak, T. Ross, R. James, A. Momciu and J. Wight, "Flexible Polyethylene Terephthalate-based inkjet printed CPW-fed monopole antenna for 60 GHz ISM applications," *Microwave Conference (EuMC), 2013 European*, pp. 1447-1450.

[5] S. Swaisaenyakorn, P. R. Young and M. Shkunov,"Characterization of inl-jet printed CPW on Kapton substrates at 60 GHz" *Loughborough Antennas and Propagation Conference (LAPC), 2014, UK*, pp. 676-678.

[6] K. Hettak et al, "Flexible Polyethylene TerephthalateBased Inkjet Printed CPW-Fed Monopole Antenna for 60 GHz ISM Applications," *Proc. of of the 43rd EuMW*, 6-8 Oct. 2013, pp: 476-479.

[7] A. B. Menicanin, L. D. Zivanov, M. S. Damnjanovic and A. M. Maric, "Low-cost CPW meander inductors utilizing ink-jet printing on flexible substrate for high-frequency applications," *IEEE Trans. Electron Devices*, vol. 60, no. 2, pp. 827-832, Jan. 2013.

[8] A. Manicanin, L. Zivanov, C. Zlebic, M. Kisic, N. Blaz and M. damnzanovic, "Fully inkjet printed CPW meander inductors on PET flexible substrate," *in 38th Int. Spring Seminar on Elect. Tech.*, Eger, May 6-10 2015, pp. 43-46.

[9] C. Zlebic et al., "Electrical properties of inkjet printed graphene patterns on PET based substrate," *in 38th Int. Spring Seminar on Elect. Tech.*, Eger, May 6-10 2015, pp. 414-417.

[10] R.B. Marks, "A multiline method of network analyzer calibration," *IEEE Trans. Microwave Theory Tech.*, vol.39, no. 7, pp. 1205-1215, July 1991.

[11] http://inkjetflex.com/site/rapid-prototyping/.

[12] A. Lewandowski, W. Wiatr, L.J. Opalski, R. Biedrzycki, "Accuracy and bandwidth optimization of the over-determined offset-short reflectometer calibration" *IEEE Trans. Microw. Theory Tech.*, vol. 63, no. 3, pp. 1076-1089, March 2015.

[13] D. F. Williams and R. B. Marks, "Comparison of on-wafer calibrations," *in 38th ARFTG Cong. Dig.*, San Diego, CA, Mar. 1992, pp. 68-81.

[14] D. F. Williams, P. Corson, J. Sharma, H. Krishnaswamy, W. Tei, Z. George, D. Ricketts, P. Watson, E. Pacquay and S. P. Voinigescu, "Calibration-Kit design for millimeter-wave silicon integrated circuits" *IEEE Trans. Microw. Theory Tech.*, vol. 61, no. 7, pp. 2685-2694, July 2013.

Measurement Methods for the Permittivity of Thin Sheet Dielectric Materials

Jeong-Hwan Kim, Jin-Seob Kang, Jeong-Il Park, and Tae-Weon Kang

Center for Electromagnetic Wave

Korea Research Institute of Standards and Science (KRISS)

267 Gajeong-ro, Yuseong-gu, Daejeon 34113, Korea

Tel:+82-42-868-5170/E-mail:kimjh@kriss.re.kr

Abstract — This paper presents a new method for the determination of the complex permittivity of thin sheet dielectric materials that are flexible and elastic. Instead of the traditional method to install a doughnut shape sample in the transverse plane used in transmission line methods, most widely used methods for broadband permittivity measurements, a thin sheet sample is installed onto the outer conductor of the coaxial transmission line. The proposed method has much large sensitivity compared to the traditional one and is a broadband technique useful for thin sheet materials. Measurement results and comparison with other approaches agree very well, particularly at high frequency range.

Index Terms — Dielectric materials, complex permittivity, reflection and transmission characteristics, transmission line methods, NRW method.

I. Introduction

Measurements of material properties in RF and microwave frequency regions have been getting more important, especially in the research fields, such as material science, microwave circuit design, absorber development, biological research, etc., as the frequency of the applications goes up to sub-millimeter wave range and the areas of the applications are being wider. Dielectric measurement is important because it can provide the electrical or magnetic characteristics of the materials, which proved useful in many research and development fields. The most widely used techniques in the microwave region are: cavity resonators, free space, open-ended coaxial probe, and transmission-line [1]–[4]. Among these techniques transmission-line techniques are the simplest methods for electromagnetic characterization in wideband frequencies for the growing number of wideband applications of various RF and microwave materials.

For the transmission/reflection method (TR), the measuring holder is made up of a section of coaxial line or rectangular wave guide filled with the sample to be characterized. One of the traditional ways to insert the sheet dielectric samples into the holder is to install the doughnut type samples in the transverse plane of the transmission line. For the thin, flexible sheet, it is very hard to maintain the sample in the transverse plane, right angle to the holder axis, and sometimes supporters usually made of Styrofoam are used to keep the sample in the transverse plane. In that case there arise gaps between the sample and the supporters, causing measurement uncertainties. Very often, for the thin sheet samples, there are air gaps at the inner and outer conductors. The gaps are major sources of the measurement uncertainties, particularly the gap at the inner conductor. So methods to compensate the effect of the gaps have been developed and used [5].

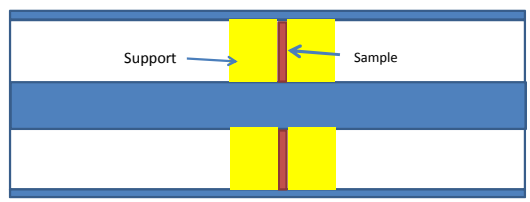

Fig. 1. A traditional way to install the sample in the coaxial transmission line.

II. Formulation

When the thickness, t, of the sheet is around 100 um, the interaction of the material with the electric field, in 7-mm coaxial line supporting TEM mode, is as follows.

$$E_{trad} = \ln\left(\frac{7}{3.04}\right) t \tag{1}$$

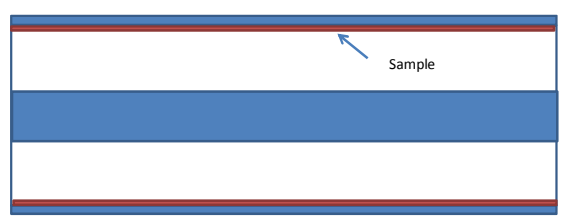

Fig. 2. The proposed installation method of the sample in the coaxial transmission line.

978-1-4673-9247-1/15/$31.00 ©2015 IEEE

As can be seen it is very small and it is very hard to measure the material characteristics accurately, particularly when thickness becomes very thin. To overcome these problems a new way to insert the sample in the coaxial line is proposed as in Fig. 2

The interaction of the sample with the electric field, assuming the sample loaded transmission line supports TEM or Quasi-TEM (TM_{00}) mode, can be expressed as (2).

$$E_{prop} = \ln\left(\frac{7}{7-2\,t}\right) L \tag{2}$$

In (2) L is the length of the sample in the longitudinal direction. When L is close to 100 mm, available when using 100 mm coaxial air line as the holder, the ratio of the two interactions is around 34, which means we have much higher sensitivity to measure the material characteristics.

As can be seen in Fig. 2, if the air region and the sample region are switched, the sample region becomes the air gap in the outer conductor and we can apply the air gap correction formula [5] to get the permittivity of the sample, assuming the transmission line supports TEM mode as mentioned above

$$\frac{\ln\left(\frac{b}{a}\right)}{\epsilon_m} = \frac{\ln\left(\frac{b}{b-t}\right)}{\epsilon_s} + \frac{\ln\left(\frac{b-t}{a}\right)}{\epsilon_{air}} \tag{3}$$

In (3), a is the radius of the inner conductor and b the radius of the outer conductor, $\epsilon_m, \epsilon_s, \epsilon_{air}$ are the complex relative permittivity of the measurement, the sample, and the air, respectively. As can be expected there might be a gap between the sample and the outer conductor, but a small gap there does give very small effect to the measurement results, particularly for the low permittivity materials.

To check the validity of the assumption the propagation constant in the air region is calculated and the electric field distribution of the TM00 mode is shown in Fig. 3 with ϵ_s=4 at 10 GHz. The thickness of the sample is 0.11 mm. As can be seen the field distribution resembles the 1/ρ behavior in the sample and air regions.

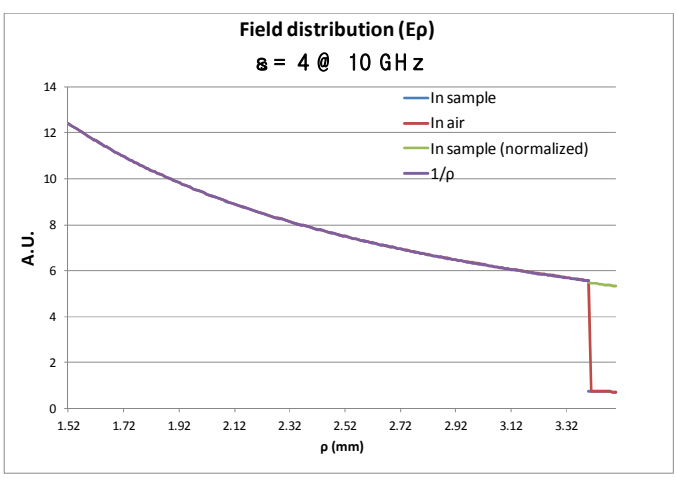

Fig. 3. Field distribution of TM_{00} mode in the sample and air regions.

The exact propagation constant in the sample loaded section of the coaxial transmission line can be calculated using the characteristic equation for the propagation constant, derived by applying the boundary condition between the regions. For the preliminary calculation an approximate formula is derived assuming the thickness of the sample is very small using the small argument approximation and the multiplication theorem for the Bessel functions as follows.

$$h^2 \approx \frac{\left(\frac{1}{\epsilon_s}-1\right)k_0^2\left(\frac{t}{b}\right)}{\ln\left(\frac{b}{a}\right)+\left(\frac{1}{\epsilon_s}-1\right)\frac{t}{b}\left(1+k_0^2\frac{b^2}{2}\ln\left(\frac{b}{a}\right)+k_0^2\left(\frac{a^2}{4}-\frac{b^2}{4}\right)\right)} \tag{4}$$

In (4) h is the propagation constant in ρ direction in the air region and $\gamma_{TM00}^2 = k_0^2 - h^2$, and k_0 is the propagation constant in free space. The calculated propagation constant using (4) agrees very well with the calculated one for TEM mode when the sample changes the capacitance of the empty transmission line.

III. Experiments

As a preliminary measurement we measured the permittivity of a paper, being used in printers and copy machines, using the proposed method. We used a 100 mm 7-mm air line as the holder and the length of the sample sheet is 95.2 mm, and the thickness 0.11 mm. In Fig. 4, the magnitude and phase of the transmission coefficients $S_{21,sample}/S_{21,holder}$ are shown and we can see the large phase change due to the sample.

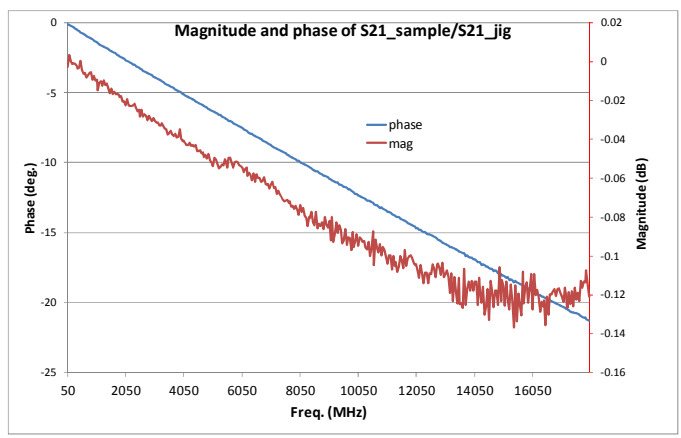

Fig. 4. The magnitude and phase of the ratio of the transmission coefficients with sample and without sample.

In Fig. 5, the measured permittivity results of the paper sample sheet are shown from 50 MHz to 18 GHz. As we used $\varepsilon_r = \varepsilon_{r,Re} + j\varepsilon_{r,Im}$ convention, the imaginary parts are negative. The legend 'Gap corr' represents the results obtained by applying the gap correction formula in (3) to the measured permittivity using The Nicolson–Ross–Weir (NRW)

procedure [6], [7]. The measured raw data were fitted to a model developed in NIST [8] to get the measured permittivity. The legend 'Phase fit' represents the results obtained by adjusting the real part of the permittivity of the sample and thus the propagation constant, using (4), and correspondingly fitting the calculated phase shift to the measured phase change shown in Fig. 4. As we just used the phase information, only real parts are obtained and agree well with the results from other methods, particularly at high frequency range as expected. The legend 'Ch. Eq.' represents the results obtained by adjusting the complex permittivity of the sample and thus the complex propagation constant obtained by solving the characteristic equation and correspondingly fitting the calculated phase shift and attenuation to the measured phase change and attenuation shown in Fig. 4.

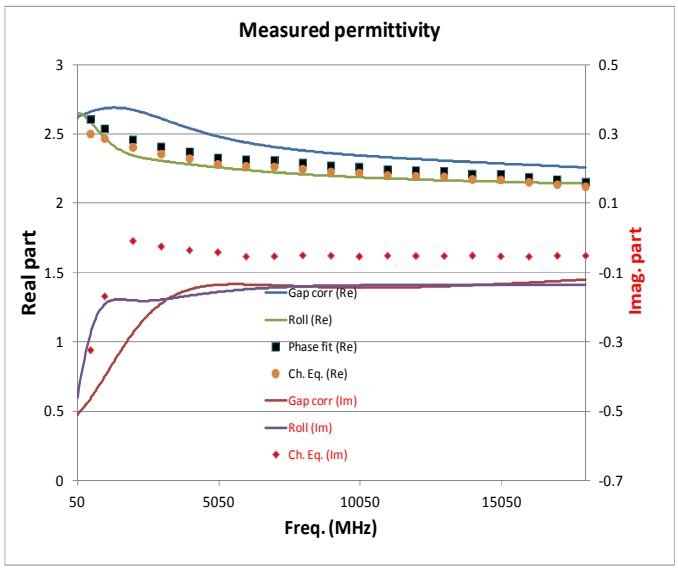

Fig. 5. The measurement results of the permittivity of the paper sheet.

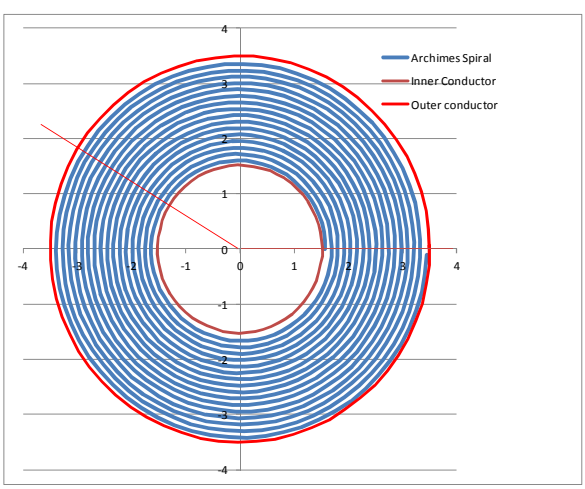

Fig. 6. Archimedean spiral to model the roll made by the paper sheet.

And the legend 'Roll' represents the results obtained by making the paper sheet sample into a roll and installing it by the traditional way and using the NRW procedure for the measured scattering parameters. The width is 10.365 mm and the length of the sheet used to make the roll is 268.1 mm, and the thickness is 0.11 mm. The volume ratio of the sample is calculated to be 0.9443 using the measured dimensions and the data of the 3 mm 7-mm air line used as the holder for the roll.

Fig. 6 shows the roll shape modeled by an Archimedean spiral, and the multi-layer model, 17 layers of the paper of 0.11 mm thickness and having a constant air gap between layers, shown in Fig. 7 was used to get the volume ratio taking into consideration of the electric field distribution of TEM mode, i.e. 1/ρ dependence.

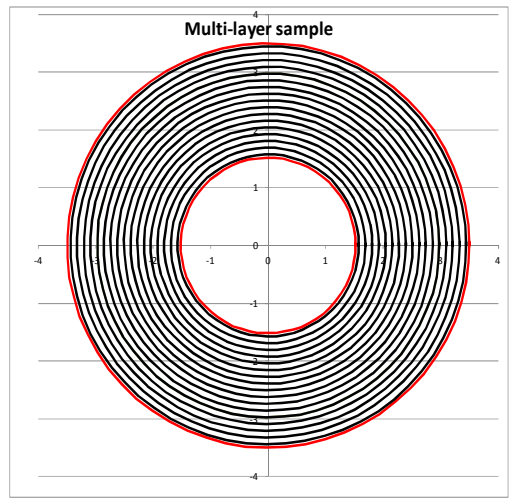

Fig. 7. Multi-layer model used for the roll.

As a validation of the proposed methods, comparisons of the results of the proposed methods with the capacitance method, usually used in the low frequency range, and the resonator method at several discrete high frequencies have been carried out. The measurement results of the complex relative permittivity of the paper sheet are shown in Fig. 8 and Table 1, respectively obtained using a commercial material analyzer (HP 4291A RF IMPEDANCE/MATERIAL ANALYZER with HP 16453A DIELECTRIC MATERIAL TEST FIXTURE) and four split post dielectric resonators with commercial software.

In Fig. 8, the measurement results for the Teflon plate of 0.750 mm thickness used as the load in the fixture compensation are also shown as a reference. As can be seen by the results noted by legends of 'LP' and 'HP', the permittivity varies as the pressure adjustment of the fixture electrode. And we observed some variations in the measurement results using the resonator technique as the condition of the sample surface's contact to the resonator surface as well.

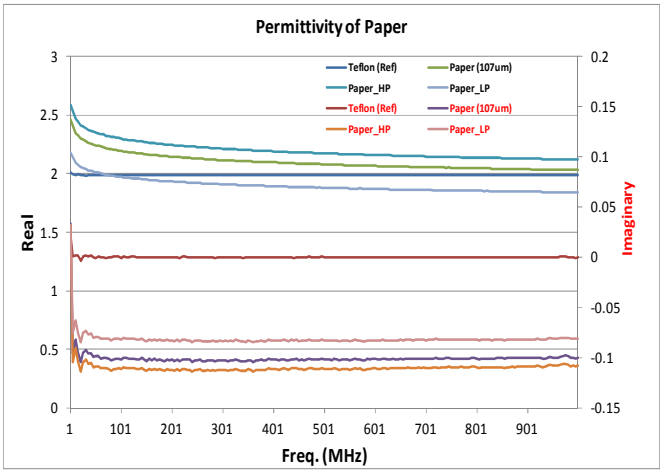

Fig. 8. Measurement results using a commercial material analyzer.

Table 1 Measurement results using split post dielectric resonators

Freq. (GHz)	Relative permittivity εr - jεi	
	εr	εi
1.891	2.800	0.393
3.094	2.772	0.397
9.925	2.495	0.232
15.570	2.406	0.167

As Fig. 5, Fig. 8, and Table 1 show, the measurement results agree well with each other. However the proposed methods give some differences in the low frequency range as expected and the results from the resonators show higher values in both the real and imaginary parts than others.

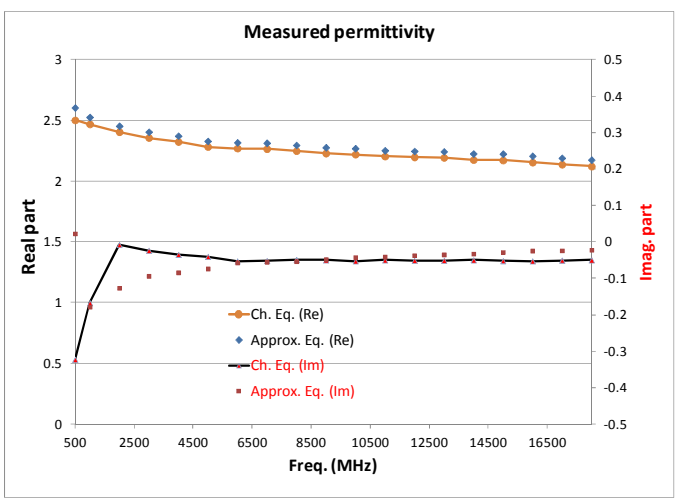

Fig. 9. Comparison of the results obtained using the approximate equation and the characteristic equation.

In Fig. 9 the measurement results using the approximate equation (4) and the characteristic equation for the propagation constant of the two-layer dielectric, composed of the air and sample, in the coaxial fixture as shown in Fig. 2 are presented. The results agree very well except the imaginary part in the low frequency range. So the results from the approximate equation can be used as initial values for the solution of the characteristic equation. The measured loss of the empty coaxial fixture was modeled as the skin effect loss, proportional to $\sqrt{F_{GHz}}$, and the complex propagation constant, k_0, of the empty fixture was used for (4) and the characteristic equation.

For more accurate measurements, tools for cutting and installing the samples will be improved. And the complex propagation constant could be measured by using two samples of different lengths.

IV. Conclusion

Very broadband methods, using the coaxial transmission and reflection technique, for measuring the complex permittivity of thin flexible sheets are proposed. They are validated by comparisons to the results using other techniques, capacitance method and resonator method. They are expected to be useful particularly in the high frequency range.

The preparation of the sample for the methods is very easy, just rectangular strips, no hole-cutting, no deposition of the electrical contacts, etc.

For more accurate measurements, accurate root finding routine for the characteristic equation and more accurate reference data of the air are to be provided.

References

[1] M. N. Afsar, J. R. Birch, and R. N. Clarke, "The measurement of the properties of materials," *Proc. IEEE*, vol. 74, pp. 183–199, Jan. 1986.

[2] R. J. Cook, "Microwave cavity methods," in *High Frequency Dielectric Measurement*, J. Chamberlain and G. W. Chantry, Eds. Guildford, U.K.: IPC Science and Technology, 1973, pp 12–17.

[3] M. A. Stuchly and S. S. Stuchly, "Coaxial line reflection method for measuring dielectric properties of biological substances at radio and microwave frequencies—A review," *IEEE Trans. Instrum. Meas.*, vol. 29, pp 176–183, Sept. 1980.

[4] D. K. Godgaonkar, V. V. Varadan, and V. K. Varadan, "Free-space measurement of complex permittivity and complex permeability of magnetic materials at microwave frequencies," *IEEE Trans. Microwave Theory Tech.*, vol. 39, pp. 387–394, Apr. 1990.

[5] Baker-Jarvis, J.R., M.D. Janezic, J.H. Grosvenor Jr., and R.G. Geyer. Transmission/Reflection and Short-Circuit Line Methods for Measuring Permittivity and Permeability (Tech. Note 1355-R). Nat. Inst. Stands. Tech., Dec 1993.

[6] A. M. Nicolson and G. Ross, "Measurement of intrinsic properties of materials by time domain techniques," *IEEE Trans. Instrum. Meas.*, vol. 19, pp. 377–382, Nov. 1970.

[7] W. B. Weir, “Automatic measurement of complex dielectric constant and permeability at microwave frequencies,” *Proc. IEEE*, vol. 62, pp 33–36, Jan. 1974.
[8] J. Baker-Jarvis, E. J. Vanzura, and W. A. Kissick, “Improved technique for determining complex permittivity with the Transmission/Reflection method,” *IEEE Trans. Microwave Theory Tech.*, vol. 38, pp. 1096–1103, Aug. 1990.

Frequency-scalable nonlinear behavioral transistor model from single frequency X-parameters based on time-reversal transformation properties (INVITED)

David E. Root[1], Radoslaw M. Biernacki[1], Mihai Marcu[1], Minghao Koh[2], and Paul J. Tasker[3]

[1]Keysight Technologies, Inc. Santa Rosa, CA, 95403, (707) 577-4091
[2] M/A-COM Technology Solutions Ltd., Belfast, UK
[3]Cardiff University, Wales, UK

***Abstract* — This paper presents a powerful new method that generates a frequency-scalable nonlinear simulation model from single-frequency large-signal transistor X-parameter data. The method is based on a novel orthogonal identification (direct extraction) of current source and charge source contributions to the spectrally rich port currents under large-signal conditions. Explicit decomposition formulae, applied entirely in the frequency domain, are derived in terms of sensitivity functions at pairs of large-signal operating points related to one-another by time-reversal transformation. The method is applied and validated with respect to data from a measurement-based model of a pHEMT transistor. It is demonstrated that the scalable model can predict the nonlinear performance of the transistor over several orders of magnitude in frequency, all from X-parameters at a single fundamental frequency.**

***Index Terms* — device modeling, behavioral modeling, X-parameters, nonlinear vector network analyzers, large-signal microwave measurements, transistor modeling, time-reversal, frequency scaling, direct extraction.**

I. Introduction

Within the last decade, native frequency-domain nonlinear behavioral models, based on large-signal measurements, have become more and more capable as commercial large-signal microwave instruments (e.g., nonlinear vector network analyzers - NVNA) have become more widely available. Models such as X-parameters[1] [1, 2] and the Cardiff model [3] provide an accurate measurement-based nonlinear behavioral model of the DUT, enabling nonlinear circuit and system design from knowledge only of the behavior of the constituent nonlinear functional blocks. These approaches have been used to characterize and model transistors, power amplifiers, microwave MMICs, mixers [2], and even design oscillators [4].

A frequently-cited limitation of such behavioral approaches, however, is that the model must be used under the same conditions as the measurements used to construct (extract) it. This means one can only simulate a design using the behavioral transistor model within the range of frequencies at which data exists. Interpolation between measured data can be used, but this requires a great deal of independent measurements over the frequency range of interest, sampled densely enough for accurate results for any possible application. This process can be quite time-consuming and can generate gigabytes of data. For some designs, the application frequency, and therefore the frequency at which the model is required to operate, is greater than what is possible to measure on the available instruments. In general, the inability of the models to extrapolate, or preferably *predict* performance beyond the accessible measurements, has limited their perceived benefits and slowed their adoption.

Recently [5], however, it was demonstrated that X-parameter transistor models could be enhanced to provide performance *predictions* for devices of substantially different sizes from the DUT used to extract the model. This was accomplished by deriving rigorous geometrical scaling rules to transform X-parameters from measurements of a device of one size into those corresponding to devices of a continuous range of geometrical dimensions.

This paper extends the notion of scalability of X-parameter models to the frequency dimension. This means X-parameters measured by exciting a transistor with large signal periodic stimuli at a single fundamental frequency can be used to *predict* the broad-band nonlinear performance of the transistor over a very wide, continuous range of frequencies, often by a factor of 100 or more, and well beyond the limitation of the measurement hardware.

Combining geometrical scalability with the present frequency-scalable methodology reported here, provides powerful predictive design capabilities similar to those of "compact" time-domain transistor models, but with the accuracy of the underlying fully calibrated NVNA large-signal X-parameter measurements.

The present work extends the initial work of [6] both fundamentally and practically. It can be considered a rigorous large-signal generalization of the seminal "direct extraction" work of the mid-1980s where the

[1] "X-parameters" is a trademark of Keysight Technologies, Inc.

978-1-4673-9247-1/15/$31.00 ©2015 IEEE

methodologies to construct broad-band small-signal models from single-frequency CW S-parameter data were first developed [7,8]. The present work overcomes limitations of previous attempts to separate nonlinear currents and charges from single-fundamental-frequency large-signal stimuli, and reduces exactly to the standard results in the small-signal limit.

II Previous Work

(a) Small-Signal case

At a fixed DC operating point, FET transistor small-signal S-parameter measurements can be de-embedded through parasitic elements and then converted to intrinsic admittance representation (Y-parameters) [7-9]. Over the wide range of frequencies from the inverse thermal and trap emission time constants (typically in the kilohertz range), up to a large fraction of the cutoff frequency (typically many tens of GHz or more), the measured intrinsic admittance matrix decomposes (approximately) into a sum of a real conductance matrix with frequency independent elements, and an imaginary part with elements depending linearly on frequency. That is, the contributions from the resistive and reactive device can be separated, at nearly any CW frequency in this range, by taking the real and imaginary parts, respectively, of the measured, de-embedded, intrinsic Y-parameters. The accuracy of the resulting broad-band model simulation performance is then fully determined by these linear circuit element values and their arrangement in the equivalent circuit topology. Data at one frequency predicts performance over a wide range of frequencies.

(b) Large-Signal case

Unfortunately, the contributions to the complex port current spectra produced by a nonlinear component of two or more ports, under large-signal excitations, cannot generally be separated by taking real and imaginary parts. The problem of separating contributions from two-port FET current and charges sources directly from large-signal measurements was first examined in [10]. With an intrinsic device model assumed to be a parallel combination of current and charge sources, the authors showed separating the I and Q contributions required *engineering multiple trajectories* (a minimum of three) going through each specified point in Vgs-Vds space. The authors were able to prescribe excitations at multiple frequencies, designed in simulation, to approximately achieve the multiple trajectories. This is a cumbersome and non-automatable procedure, and did not provide a general solution.

An elegant and general solution to the direct large-signal extraction for the special case of a one-port nonlinear device (e.g. diode) was given in [11]. This made use of the even and odd symmetry of the Fourier transform of a single function of voltage (the current source) and the time-derivative of a second function of voltage (the charge source), respectively. This method does not apply directly to two or more ports as required for transistors, however.

The work of [12] extended the approach of [11] to two ports by constraining the output impedance into which the device was presented. In this case, the v_1 and v_2 voltage excitations were forced to be always 180 degrees out of phase. The waveforms then have the requisite even-odd symmetry to apply the technique of [11]. Harmonic load control was still necessary to constrain the waveforms.

III New Approach

This work proposes a new, direct path from single-frequency transistor X-parameters to a frequency-scalable nonlinear simulation model valid over a wide frequency range. Fundamental, new relationships are derived that decompose "admittance-space X-parameters", denoted here by "XY-parameters", into independent contributions from capacitances and current sources at a single fundamental frequency. Unique identification is established by simple algebraic relationships combining XY-parameters from forward and time-reversed periodically varying large-signal operating points (LSOPs). The resulting frequency-independent terms can be recombined with explicit, distinct frequency-dependent scaling rules to predict the DUT performance at (nearly) any frequency of practical interest. A simplified diagram illustrating the flow is shown in Fig. 1.

(a) Time-Reversal

We derive the formalism by considering, at first, an *intrinsic FET* assumed to be represented by the standard parallel combinations of lumped nonlinear voltage-controlled current sources (VCCS) and voltage-controlled charge sources (or nonlinear capacitances). This is the

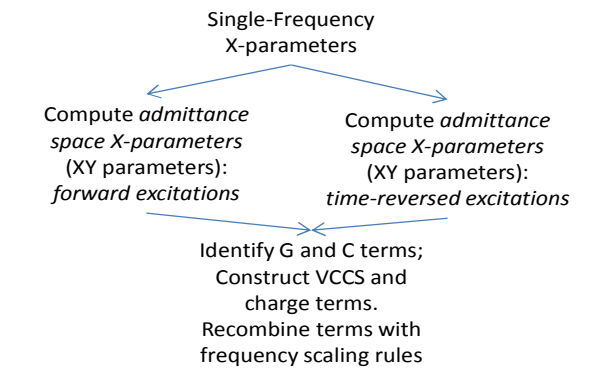

Fig. 1: Simplified scalable model relationship

familiar quasi-static approximation that is valid up to frequencies approaching the cutoff frequency of the transistor. It should be noted, however, that the scalable model formalism presented here applies, to a useful extent, even to devices where additional dynamical variables (e.g., junction temperature and trap states) generally contribute to the transistor performance. In particular, the methodology and scalable behavioral model developed in this work are valid for frequencies between the inverse thermal and trap emission time constants and a large fraction of the transistor cutoff frequency. This is validated in Section IV.

The quasi-static equations for the port intrinsic currents are given by (1).

(1)

$$I_p(t) = I_p^{VCCS}\left(\mathrm{v}_1(t), \mathrm{v}_2(t)\right) + \frac{d}{dt} Q_p\left(\mathrm{v}_1(t), \mathrm{v}_2(t)\right)$$

Here I_p^{VCCS} and Q_p are the presently unknown nonlinear static functions of the controlling voltages at each port, p, (p = 1, 2, or gate, drain).

A key observation is that the contributions to the port currents from the current source and charge source in (1) transform differently from one another *under time-reversal.* Time reversal in this context means a replacement $t \to -t$ in the arguments of all functions and operators in (1). This induces a transformation of all voltage excitations according to (2).

(2) $v_q(t) \to v_q^{tr}(t) = v_q(-t)$

But because of the additional presence of the time-derivative operator applied to the charge function in (1), the *form* of the equation changes according to the following transformation property under time-reversal, where the superscript *"(tr)"* means time-reversed signal.

(3)

$$I_p^{tr}(t) = I_p(-t)$$

$$= I_p^{VCCS}\left(\mathrm{v}_1^{tr}(t), \mathrm{v}_2^{tr}(t)\right) - \frac{d}{dt} Q_p\left(\mathrm{v}_1^{tr}(t), \mathrm{v}_2^{tr}(t)\right)$$

That is, under time-reversal, the contribution from the charge enters with an opposite sign compared to the forward direction (compare to equation (1)).

(b) Admittance-space X-parameters

We now consider the case where the large-signal equations (1) are linearized around a particular periodically time-varying excitation at each port, taking voltages (currents) as the independent (dependent) variables, respectively. The port current spectra, and the first order response to additional small sinusoidal voltage excitations at each port, can be written according to (4). The formalism is completely equivalent to that of X-parameters [2], but now in I-V space.

(4)

$$I_{p,k} = XY_{p,k}^{(F)} P^k + \sum_{p',k'} \left[XY_{p,k;\mathrm{p',k'}}^{(S)} \Delta V_{p',k'} P^{k-k'} + XY_{p,k;\mathrm{p',k'}}^{(\mathrm{T})} \Delta V_{p'k'}^{*} P^{k+k'} \right]$$

The following relationships can be derived between the Fourier coefficients of the partial derivatives of the model constitutive relations, I_p^{VCCS} and Q_p, and the computed $XY^{(S)}$ terms extracted from the forward LSOP and the corresponding $XY^{(S\text{-}tr)}$ terms from the same system but in *the time-reversed condition*. Key results are shown in (5), where "*" indicates complex conjugation:

(5)

$$XY_{p,k;q,k'}^{(S)} = G_{p,\mathrm{q;k-k'}} + jk\omega_0 C_{p,\mathrm{q;k-k'}}$$

$$XY_{p,k;q,k'}^{(S-tr)} = G_{p,\mathrm{q;k-k'}}^{*} + jk\omega_0 C_{p,\mathrm{q;k-k'}}^{*}$$

In (5), $G_{p,q;k}$ and $C_{p,q;k}$ are the complex-valued Fourier coefficients of the partial derivatives of the terminal current source and charge source constitutive relations (1), respectively, at the periodically time-varying LSOP of the DUT in the forward state, given by (6).

(6)

$$\sum_{k=-N}^{N} G_{p,q;k} e^{jk\omega_0 t} = g_{p,q}(t) = \frac{\partial}{\partial v_q} I_p^{VCCS}\Big|_{LSOP}$$

$$\sum_{k=-N}^{N} C_{p,q;k} e^{jk\omega_0 t} = C_{p,q}(t) = \frac{\partial}{\partial v_q} Q_p\Big|_{LSOP}$$

At any one frequency, ω_0, it is impossible to separate C and G terms from forward (or reverse) $XY^{(S)}$ terms (with the same indices) alone, but the relationship of these terms at corresponding forward and time-reversed LSOPs enables their identification. These relations are given in (7).

(7)

$$G_{p,\mathrm{q;k-k'}} = \frac{1}{2}\left(XY_{p,k;\mathrm{q;k'}}^{(S)} + XY_{p,k;\mathrm{q;k'}}^{(S-tr)*} \right)$$

$$C_{p,\mathrm{q;k-k'}} = \frac{XY_{p,k;\mathrm{q;k'}}^{(S)} - XY_{p,k;\mathrm{q;k'}}^{(S-tr)*}}{2jk\omega_0}$$

The results (7) show that each required spectral coefficient of the derivatives of the constitutive relations depends only on the forward and time-reversed $XY^{(S)}$ coefficients with *distinct differences, k-k',* of their two harmonic indices *k* and *k'*. This means a large number of independently computed $XY^{(S)}$ terms, when combined in (7), should produce *the same values* for *G* and *C* terms. This is a testable *prediction* that is validated in Section IV.

We note that in the small-signal limit, we have

$$(8)\quad XY^{(S)}_{p,k;p',k'} \text{ and } XY^{(S-tr)}_{p,k;p',k'} \rightarrow Y_{p,p'}(k\omega_0)\delta_{k,k'}$$

In (8) *Y* is the standard complex-valued frequency-dependent small-signal admittance matrix defined at the DC operating point reached in the limit of small applied RF signal. The limiting expressions (8), when used in (7) reduce, therefore, to the well-established results [7,8], that the real and imaginary parts of the small-signal admittance separate conductances from capacitances at (nearly) any frequency.

We can now subtract the contribution of the charge (capacitance) contributions at the measurement frequency, ω_0 , from the total port current, to obtain a frequency independent expression for the contribution to the port current spectra from the VCCS. This is shown in (9). That is, the RHS of (9), evaluated at the reference frequency, provides the port spectra from the VCCS at the (intrinsic) terminals at *all* frequencies. Here $P = e^{j\phi(V_{1,1})}$.

(9)

$$I^{VCCS}_{p,k} = I_{p,k}\left(\omega_0\right)P^{-k} - \sum_{p',k'=-N}^{N} C_{p,p';k-k'}jk'\omega_0 V_{p',k'}P^{-k'}$$

The first term on the RHS of (4) can then be written in a *frequency-scalable form* given by (10).

$$(10)\; XY^{(F)}_{p,k} = I^{VCCS}_{p,k} + j\omega \sum_{p',k'=-N}^{N} C_{p,p';k-k'}k'V_{p',k'}P^{-k'}$$

Finally, the frequency scalable model equations can then be written by substituting (10), (9), and (5) (but this time at the simulation frequency, ω), and a similar expression for $XY^{(T)}$, into (4). That is, the frequency-scaling rules for the $XY^{(S)}$ (and $XY^{(T)}$ parameters, not shown) are given by (5) but at the simulation frequency, ω .

IV. Experimental Validation and Results

(A) Procedure

A 2x50 µm GaAs pHEMT was characterized using the Keysight NVNA – based active-source injection system reported in [13,14]. The primary purpose of the experimental and numerical work is to systematically validate the new formalism for predicting performance at new frequencies from data at a single frequency. Since the theory developed in Section III applies to the intrinsic device, we choose a procedure for validation of intrinsic scaling first, and then expand the validation to the full transistor by adding the effects of a parasitic network.

To facilitate the validation at the intrinsic device level, we choose to convert the raw transistor measured waveform data into a measurement-based dynamic nonlinear (DynaFET) simulation model [13,14]. DynaFET has a specific parasitic topology that can be removed to access the intrinsic device directly. The DynaFET model incorporates multiple sources of intrinsic device frequency dependence and memory effects, including dynamic self-heating and trapping phenomena. It was extensively validated for broad-band linear and large-signal behavior, and is valid for this device from DC to 50 GHz. The DynaFET model, therefore, is an accurate and convenient surrogate for the raw data. Single-frequency X-parameters, first at the intrinsic level, and then for the full device, are computed using the W2305 X-parameter generator in ADS.

(B) Validation at the Intrinsic Model Level

The single-frequency intrinsic X-parameters are brought into the simulator to be processed and converted into the $I_{p,k}$ and $C_{p,p';k}$ parameters of the new scalable model. In the first step, the X-parameter model is stimulated with simultaneous voltage-source excitations at input and output ports, at different magnitudes and relative phases, at the single fundamental frequency of 1 GHz. Each of these large signal conditions establishes a forward-time LSOP for the intrinsic device. For each case, the simulation is repeated for the same set of voltage waveforms but with *all phases conjugate* to those of the forward excitations. This is the method to achieve an *exact periodically varyin*g *time-reversed LSOP* corresponding to each of the forward conditions. From each pair of corresponding forward and time-reversed LSOPs, the XY parameters are computed by SSM analysis. Next, the *G* and *C* terms are computed according to (7).

The first quantitative test of the theory of Section III is the validation of the claimed (practical) equality of $C_{p,p';k}$ values computed from (7) , across all independent $XY^{(S)}_{p,k';p',k''}$ and $XY^{(S-tr)}_{p,k';p',k''}$ terms for which $k = k' - k''$. Results are shown for selected C values in Table 1.

TABLE 1: $C_{P,P',K}$ VALUE CONSISTENCY FROM DIFFERENT COMBINATIONS OF $XY^{(S)}$ and $XY^{(S-tr)}$ TERMS

Terms	Order of magnitude	Largest deviation	
		absolute [fF]	relative
Dominant $C_{1,1;k}$	100 fF	0.243	0.22%
Other $C_{1,1;k}$	0.1fF (max)	0.245	88%
Dominant $C_{1,2;k}$	10 fF	0.017	0.24%
Other $C_{1,2;k}$	0.1 fF (max)	0.017	28%
Dominant $C_{2,1;k}$	50 fF	0.437	0.83%
Other $C_{2,1;k}$	0.05 fF (max)	0.162	73%
Dominant $C_{2,2;k}$	20 fF	0.018	0.08%
Other $C_{2,2;k}$	0.5 fF (max)	0.055	24%

Relative deviations of less than 1% are obtained for all significant (dominant) C values. Larger relative deviations occur only for C values that are orders of magnitude smaller than the dominant terms.

The $C_{p,p',k}$ terms are stored in a new model datafile, along with the computed $I_{p,k}$ values at the single reference frequency of 1 GHz. The scaling equations (9) and (10) are applied to create the scaled intrinsic model.

Figure 2 shows a three-way comparison among the new scalable intrinsic model, the single-frequency X-parameter model from which the scalable model was generated, and the intrinsic DynaFET model that gave rise to the X-parameters, at the reference frequency of 1 GHz. The agreement is nearly perfect, as expected, at this frequency.

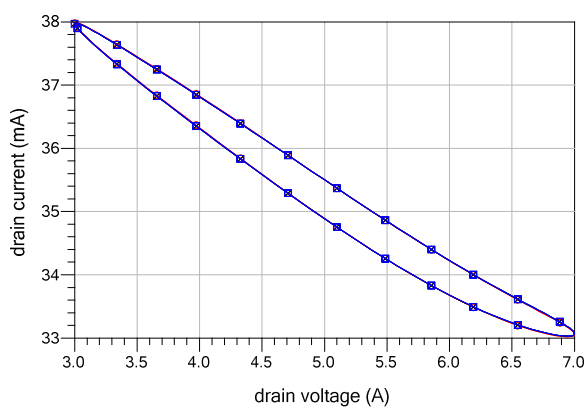

Fig. 2: Comparison of baseline DynaFET model (red), single-frequency X-parameter model (black), and new scalable intrinsic model (blue) at the reference frequency of 1 GHz.

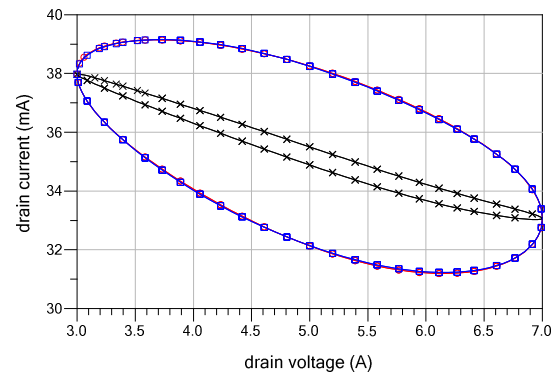

Fig. 3: Comparison of scalable intrinsic model *prediction* (blue), independently simulated DynaFET model (red), and the single-frequency X-parameter model (black), at 10 GHz.

Next, the scalable intrinsic behavioral model *predictions* are validated at a frequency of 10 GHz – an order of magnitude faster than the X-parameter data used as the basis of its creation. Results are shown in Fig. 3. The agreement between the new scaled behavioral model (blue) and the independent simulation of the DynaFET intrinsic model (red) is also superb. The inability of the 1 GHz X-parameter model (black) to predict the 10 GHz performance is shown to highlight its limited predictive capability. In Figures 4 and 5, the validation of the new scalable intrinsic model is extended up to the very high frequency of 50 GHz, and down to the relatively low frequency of 100 MHz, respectively, with similar degrees of validity. At very low frequencies, the scaled behavioral model performance degrades. This is seen in Fig. 6 for the case of 50 kHz. This is because the thermal and trapping dynamics of the FET, as represented by the detailed DynaFET compact model, are becoming "active" (causing looping of the red trace). The behavioral model cannot

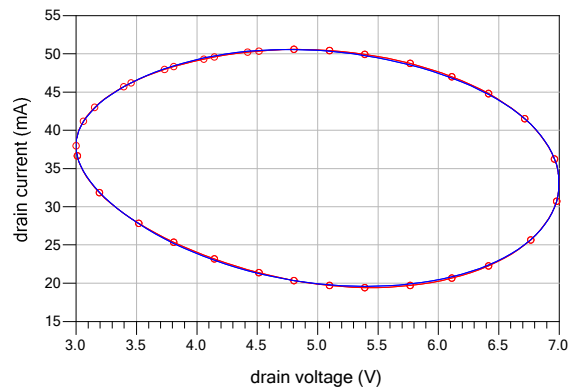

Fig. 4: Comparison of scalable intrinsic model *prediction* (blue) and independently simulated DynaFET (red), at 50 GHz.

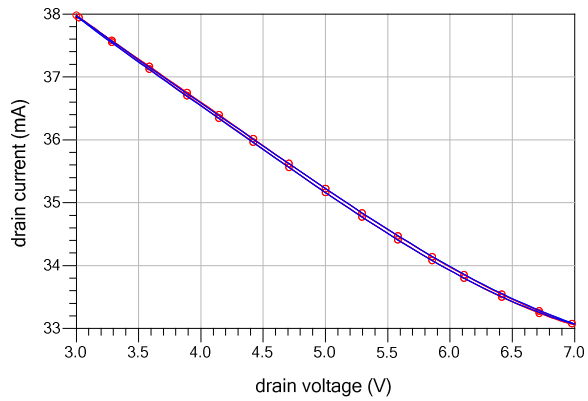

Fig. 5: New scalable intrinsic model *prediction* (blue) and independently simulated DynaFET (red) at 100 MHz.

account for the time-variation of these variables as modulated by the very low-frequency excitations. This proves the scaling theory from single-frequency X-parameters, and also indicates where it breaks down.

(C) Dealing with parasitic elements

The intrinsic validation presented in (B) used the fact that the LSOPs at the reference and the desired frequencies were easily specified to be precisely the same. Frequency-dependendent losses and phase rotations through the parasitic network make a direct comparison of LSOPs at the different frequencies more difficult than the intrinsic case. As a first step, the following procedure is adopted. Shells of negative parasitic elements in an "inverted" parasitic network [5] are applied to the full (extrinsic) DynaFET model. A similar process to *(B)* is applied to generate a scalable intrinsic model, but now over a dense set of excitations sampling the entire set of possible operating conditions. The parasitic network, in

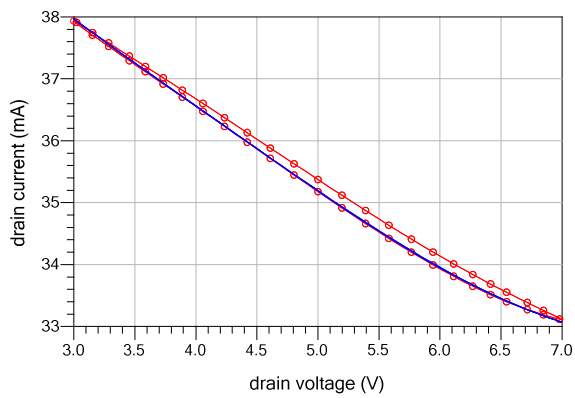

Fig. 6: Comparison of scaled intrinsic model *prediction* (blue) vs DynaFET (red) at 50 kHz. At very low frequencies, where the junction temperature and trap states are being modulated by the electrical signal, the scaled model shows a degraded accuracy.

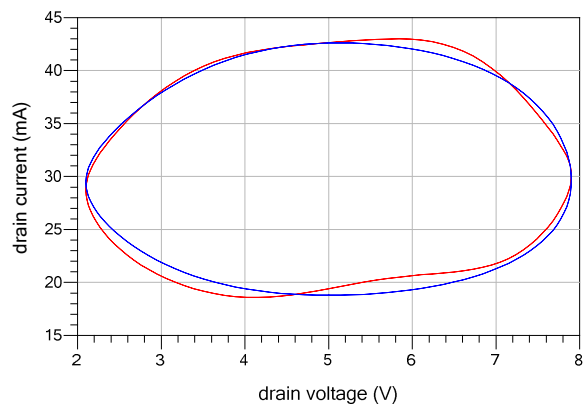

Fig. 7 Comparison of new complete scalable model *prediction* (blue) vs DynaFET (red) at 30 GHz

this case taken from DynaFET but otherwise easily obtained from independent transistor S-parameter measurements using conventional methods [9], is added back around the resulting scalable intrinsic model to create the complete behavioral model.

Now the predictions of the complete model can be simulated and compared to the DynaFET performance as reference. Typical results are presented in Figs. 7 and 8, showing predictions for scaling to higher and lower frequencies, respectively. The predictions of the complete new scalable behavioral model, based on only 1 GHz X-parameter data, show good agreement with the baseline measurement-based DynaFET model performance over a frequency range of several orders of magnitude.

The accuracy of the full model scaling is not quite as excellent as that of the intrinsic model scaling. This is attributed to interpolation errors between the corresponding intrinsic LSOPs at the reference and scaled frequencies. We expect improvements by denser sampling during the XY-parameter generation process and/or by adding model sensitivity terms with their own frequency scaling rules based on (5). This work is in progress.

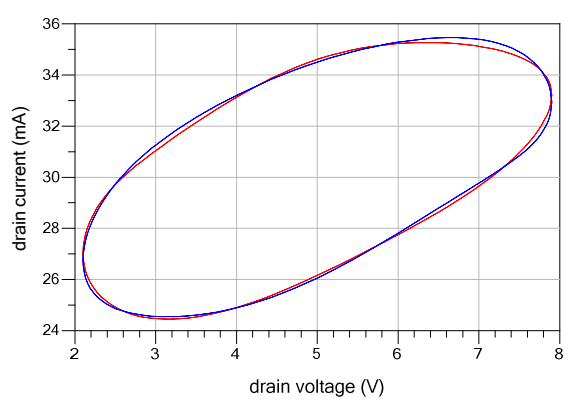

Fig. 8 Comparison of new complete scalable model *prediction* (blue) vs DynaFET (red) at 100 kHz.

V. CONCLUSION

A new theory and method of creating a frequency-scalable behavioral model from X-parameter data at a single fundamental frequency has been presented and verified using a measurement-based model of a GaAs pHEMT device. The method is based on the time-reversal transformation properties of the intrinsic large-signal equations, and the resulting relationships between the linearized XY-parameters (admittance space X-parameters) and the partial derivatives of the current and charge constitutive relations of the device. The method and resulting new scalable transistor behavioral model provide accurate *predictions* of large-signal transistor performance over a very wide and continuous range of frequencies, despite the fact that the model was constructed from data at *only one applied fundamental frequency*. It is a rigorous large-signal generalization of direct extraction methods for frequency-scalable linear models from single-frequency S-parameters, to which the new formalism reduces in the small-signal limit. The prototype new scalable behavioral model and model generator were implemented in Keysight ADS.

The X-parameter data used in this work were computed from a measurement-based (DynaFET) model to prove the theory, validate each step of the new methodology, and evaluate the new scalable model. In practice, we fully expect the same degree of *predictable frequency scalability* to be achieved starting directly from *measured* single-frequency transistor X-parameters. This validation work is now in progress.

ACKNOWLEDGMENT

The first author acknowledges a useful early discussion on this topic with Dr. Jan Verspecht. Dr. Masaya Iwamoto provided helpful feedback on the manuscript.

REFERENCES

[1] J. Verspecht and D. E. Root, “Poly-Harmonic Distortion Modeling,” in *IEEE Microwave Theory and Techniques Microwave Magazine*, June 2006.

[2] D. Root, J. Verspecht, J. Horn, M. Marcu, *X-Parameters: Characterization, Modeling, and Design of Nonlinear RF and Microwave Components*, Cambridge University Press, 2013.

[3] Woodington, S. Williams, T.; Qi, H.; Williams, D.; Pattison, L.; Patterson, A.; Lees, J.; Benedikt, J.; Tasker, P.J., “A novel measurement based method enabling rapid extraction of a RF Waveform Look-Up table based behavioral model,” *IEEE MTT-S International Microwave Symposium Digest,* 2008, pp. 1453 – 1456.

[4] Pelaez-Perez, A.M.; Woodington, S.; Fernandez-Barciela, M.; Tasker, P.J.; Alonso, J.I., "Large-Signal Oscillator Design Procedure Utilizing Analytical X-Parameters Closed-Form Expressions," in *IEEE Transactions on Microwave Theory and Techniques*, vol. 60, no. 10, pp. 3126-3136, Oct. 2012.

[5] Root, D. E.; Marcu, M.; Horn, J.; Xu, J.; Biernacki, R. M.; Iwamoto, M., ”Scaling of X-parameters for device modeling,” *IEEE MTT-S International Microwave Symposium Digest (MTT),* June 2012,

[6] M. Koh, J. J. Bell, D. Williams, A. Patterson, J. Lees, D. E. Root, P. J. Tasker, “Frequency Scalable Large Signal Transistor Behavioral Model based on Admittance Domain Formulation,” *International Microwave Symposium Digest*, Tampa, FL. June 2014,

[7] Hughes, B.; Tasker, P.J., "Bias dependence of the MODFET intrinsic model elements values at microwave frequencies," in, *IEEE Transactions on Electron Devices*, vol. 36, no. 10, pp. 2267-2273, Oct. 1989,

[8] Dambrine, G.; Cappy, Alain; Heliodore, F.; Playez, E., "A new method for determining the FET small-signal equivalent circuit," *IEEE Transactions on Microwave Theory and Techniques*, vol. 36, no. 7, pp. 1151-1159, Jul. 1988,

[9] M. Rudolph, C. Fager, D. E. Root , editors*, Nonlinear Model Parameter Extraction Techniques*, Cambridge University Press, 2012.

[10] D. Schreurs, J. Verspecht, B. Nauwelaers, A. Van de Capelle, and M. Van Rossum, “Direct extraction of the non-linear model for two-port devices from vectorial non-linear network analyser measurements,” in *Proc. 27th European Microwave Conference*, Jerusalem (Israel), pp. 921-926, September 1997.

[11] T.M. Martín-Guerrero, C. Camacho-Peñalosa, “Frequency domain-based extraction method of one-port device’s non-linear state functions from large-signal measurements,” in *Proc. 13th Gallium Arsenide Application Symposium*, Paris (France), pp. 449-452, October 2005.

[12] T.M. Martín-Guerrero , J.D. Baños-Polglase, C. Camacho-Peñalosa, M. Fernández-Barciela, D.G. Morgan, P.J. Tasker, “Frequency domain-based approach for nonlinear quasi-static FET model extraction from large-signal waveform measurements,” *Proceedings of the 1st European Microwave Integrated Circuits Conference*, Manchester, UK, September, 2006, pp 441- 444.

[13] J. Xu, S. Halder, F. Kharabi, J. McMacken, J. Gering, and D. E. Root, “Global Dynamic FET Model for GaN Transistors: DynaFET Model validation and comparison to locally tuned models,” *83rd IEEE ARFTG Conf.*, Tampa, FL., June 2014.

[14] J. Xu, R. Jones, S. A. Harris, T. Nielsen, and D. E. Root, “Dynamic FET Model – DynaFET - for GaN Transistors from NVNA Active Source Injection Measurements,” *International Microwave Symposium Digest*, Tampa, FL., June 2014.

Automatic Feed-Forward Cancellation of Modulated Harmonic

Hai Yu[1], Varun Ratnasamy[1], Patrick Roblin[1], Meenakshi Rawat[2], and Chenggang Xie[3]

[1]The Ohio State University, [2]Indian Institute of Technology, Roorkee, India, [3]Rockwell Collins

Abstract — This paper presents an algorithm for the simultaneous linearization and cancellation of modulated harmonics of broadband power amplifiers (PA). The algorithm relies on a joint system identification of the nonlinearity, memory effects and group delay of both the main and harmonic cancellation channels using a recently reported cubic spline basis. The filter-less cancellation of the modulated harmonics uses both the method of predistortion and feedforward while the synchronized PA linearization relies solely on digital predistortion. Experimental verification with a broadband PA yields a reduction of 31 dB of the third harmonic to 59 dBc below the main channel. Simultaneously the linearization provides -40 dB NMSE and 49.5 and 50 dBc ACPR at the fundamental frequency.

Index Terms — Harmonic cancellation, PA linearization, digital predistortion, cubic spline, concurrent multiband PA.

I. Introduction

Growing demand for higher data rate pushes the development of ultra-wideband and multiband systems. When the separation between two bands becomes large, harmonics of the lower band signal start to interfere with the higher band's signal. In order to suppress the interfering harmonic in concurrent multi-band transmission system, the solution of using bulky and lossy switchable filter banks is common practice. However, digitally-controlled feed-forward harmonic cancellation is emerging as an alternative solution because of the frequency programing flexibility this filter-less solution brings to multi-band transmission system.

Active harmonic cancellation uses an upper band channel to send a cancelling signal which is in opposite-phase (180 phase shift) to the modulated RF harmonics generated by the broadband nonlinear power amplifier (PA) from the lower band signal. The system requires thus the careful characterization of the modulated harmonics [1]. Further, due to the upper band channel's group delay, nonlinearity and dispersion, a frequency-selective correction for the gain, phase shift and time delay must be applied to the cancelling signal so that it exactly cancels the harmonics at the coupler placed after the PA. In a previous report [1] this three-fold adaptation of the cancelling signal was performed manually. In this work, a joint PA distortion modelling and compensation algorithm is developed to ensure that the cancellation is automatic.

The remainder of this paper is organized as follows. Section II explains the principle of the digitally supported feed-forward harmonic cancellation. Section III describes the measurement test bed that is used as a proof of concept for demonstrating the filter-less cancellation of the modulated third harmonic signal generated by a wide band PA. Section IV presents the results obtained to validate the theory.

II. Automatic Cancellation Algorithm

A. Feed-forward harmonic cancellation

Figure 1 shows the feedforward harmonic cancellation scheme. In the phase of concept-proving, the upper band channel is only used to send a cancelling signal to sum it up with the signal in the lower band channel after the PA. The output of the PA contains the amplified fundamental signal and different orders of harmonics caused by the PA's nonlinearity. As indicated in Section I, the cancelling signal is 180 degree out of phase from one of the *p*-th order harmonic which is meant to be cancelled. Therefore, the *p*-th harmonic should be cancelled at the combiner after the PA when it is summed up with its 180 degree out-of-phase version. The negative version of the *p*-th harmonic is generated digitally based on the behavioral model of the PA to predict the real harmonic. To achieve effective cancelling result, two key features are required: (1) the accurate harmonic modelling and (2) the accurate modelling and compensation for the channel's distortion and delays in the cancelling signal by upper channel.

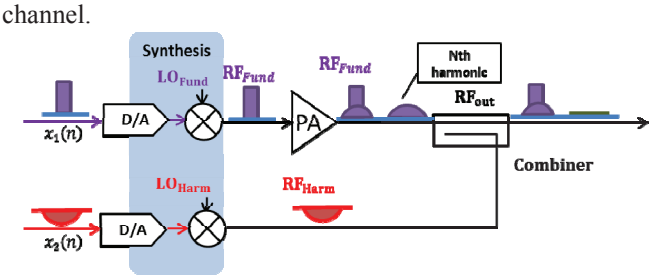

Fig. 1. Digital feed forward harmonic cancellation scheme.

The first key point can be guaranteed by using effective modelling tools such as memory polynomial in case of a moderately nonlinear PA [1]. On the other hand, fast and accurate modelling and compensation for the cancelling channel's distortion remains a hurdle in the way of harmonic cancellation's application in practical time-variant transmission system. Given the distortions and delay of the upper band channel, the cancelling signal needs to be pre-distorted to compensate for those distortions to exactly cancel the modulated harmonic at the PA output. Therefore, accurate model of the distortions and delay is also required to achieve proper compensation. Previous digitally supported feed-forward harmonic cancellation scheme [1] adopted a manual

978-1-4673-9247-1/15/$31.00 ©2015 IEEE

adjustment of the cancelling signal's amplitude, phase and time delay based on a trial-and-error method. This work presents a faster and more accurate modelling and predistortion algorithm to enable the automatic feedforward cancellation of the p-th harmonic of PA.

B. System Identification

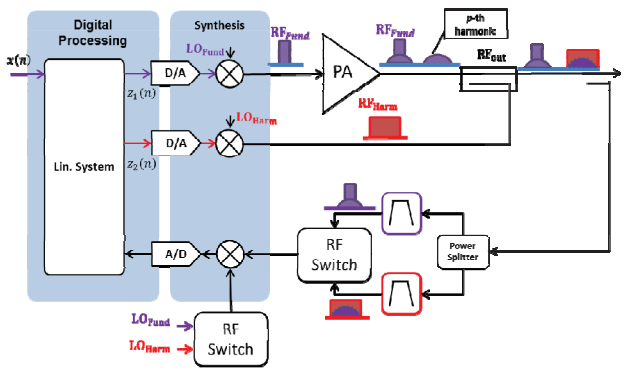

Fig. 2. System identification scheme.

To conduct the system identification, i.e., to obtain the needed modelling parameters of the two channels, two sets of signal x_1 and x_2 are transmitted simultaneously through the two channels. As shown in Fig. 2, the purple signal RF_{fund} sent through the PA channel is for PA channel identification and the red signal RF_{harm} sent through the cancelling channel at the frequency band of the p-th harmonic is used for the cancelling channel identification. A generalized behavioral model is used to represent the multi-harmonic output of the PA channel main channel, as follows:

$$y_{1,p} = \sum_{m=0}^{M-1} G_{1,p,m}\left[\,|x_1(n-m)|^2\,\right]\cdot x_1^p(n-m) \quad @p\omega. \qquad (1)$$

In (1), $y_{1,p}$ is the output of the system at the fundamental or p-th harmonic. $x_1(n-m)$ is the input of the corresponding band with memory delay term m. M is the memory depth. Memory delay terms are included in the model to account for the frequency dependence of the PA nonlinearities in wideband communication system [2]. $G_{1,p,m}(|x_1(n\text{-}m)|^2)$ are the gain functions of each delay channel, which are a function of the envelope squares of the signal in the corresponding channel. These gain functions can be implemented in different forms such as memory polynomials and splines, to represent the higher order nonlinearity caused by the PA. This model thus takes into account both the PA's p-th modulated harmonics for cancellation purpose as well as its in-band intermodulation terms for in-band linearization purpose. Although the feed-forward cancelling channel is not typically driven in strong saturation, a similar model can also be used as will be discussed next.

There are two requirements for the identification signal x_2 in the cancelling channel (RF_{harm} in Fig. 2). First, it has to be uncorrelated to the identification signal x_1 used for the PA channel. Since the identification signal in the cancelling channel occupies the same frequency band as the p-th harmonic to be cancelled, the two signals will overlap after the coupler combining them. Being uncorrelated enables us to separate them in the digital domain to identify the corresponding gain functions of the two channels. Second, because the channel's distortion extends over a p-th time the bandwidth and exhibits an amplitude varying within a certain dynamic range, the identification signal should have a bandwidth that covers the entire frequency band that the p-th harmonic to be cancelled occupies and exhibits peaks with larger amplitude than the p-th harmonic of the PA.

At the p-th harmonic frequency, the received signal is as follows:

$$\begin{aligned} y_2(n) &= y_{2,1}(n) + y_{1,p}(n) \quad @\ p\omega \text{ with} \\ y_{2,1} &= \sum_{m=0}^{M-1} G_{2,1,m}\left[\,|x_2(n-m)|^2\,\right]\cdot x_2(n-m) \\ y_{1,p} &= \sum_{m=0}^{M-1} G_{1,p,m}\left[\,|x_1(n-m)|^2\,\right]\cdot x_1^p(n-m) \end{aligned} \qquad (2)$$

The component $y_{1,p}$ is the modelled PA p-th harmonic introduced in (1) and the component $y_{2,1}$ is the modelled version of the output of the cancelling channel. $G_{1,p,m}(|x_1(n\text{-}m)|^2)$ is the gain function on which the modelling of p-th harmonic is based and $G_{2,1,m}(|x_2(n\text{-}m)|^2)$ is the gain function that models the distortions and delay of the cancelling channel. Utilizing the least-square method, the gain functions in (2) can be readily extracted. For accurate representation, we use cubic-spline [2] with 4 bases to represent the gain functions of the two channels. The fidelity of the model can be verified by comparing the modelled signal y_2 with the measured one.

C. Digital Predistortion

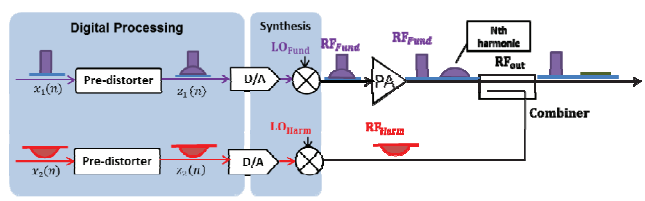

Fig. 3. Predistortion and harmonic cancellation scheme.

The negative version of the modelled $y_{1,p}$ should be sent to the PA output to cancel its p-th harmonic, but in consideration of the second key point mentioned in section II A, this signal has to be pre-distorted in order to compensate for the cancelling-channel's distortion and delay. Thus digital predistortion (DPD) is used to fulfill this purpose. A block called predistorter is added in the digital domain before the DAC to predistort the cancelling signal $y_{1,p}$.

The parameters of the predistorter are calculated by the method of indirect learning [3]. For this method, the predistorter is an inverse model of the channel, as in (3):

$$x_2 = \sum_{m=0}^{M-1} G_{2,1,m}^{(i)} \left[\left| y_{2,1}(n-m) \right|^2 \right] \cdot y_{2,1}(n-m). \qquad (3)$$

$G^{(i)}_{2,1,m}(|y_{2,1}(n\text{-}m)|^2)$ is the gain function of the inverse model or namely the predistorter. This gain functions can be calculated from $y_{2,1}$ obtained from the dual band system identification. Then we predistort the cancelling signal $-y_{1,p}$ by substituting $-y_{1,p}$ for $y_{2,1}$ in (3) while using the gain functions of the predistorter $G^{(i)}_{2,1,m}(|y_{1,p}(n\text{-}m)|^2)$ just extracted:

$$z_2 = \sum_{m=0}^{M-1} G_{2,1,m}^{(i)} \left[\left| y_{1,p}(n-m) \right|^2 \right] \cdot (-y_{1,p}(n-m)). \qquad (4)$$

z_2, as shown in Fig. 3, is the predistorted cancelling signal, which will yield the desired $-y_{1,p}$ signal at the combiner after experiencing all the distortions and delay from the cancelling channel. We use the same predistortion procedure for the desired fundamental signal at the same time to reduce the in-band intermodulation caused by the PA.

III. Measurement Setup

The cancellation of the third harmonic generated by a Mini Circuit ZX60-14012L+ PA is done as a proof of concept. Figure 2 shows the system diagram of the test bed setup. A set of 10 MHz bandwidth LTE signal is used as the fundamental signal transmitted in the lower band through the PA channel, and a set of 30 MHz bandwidth WCDMA signal is transmitted in the upper band through the cancelling channel in the system identification procedure. Digital predistortion of the upper band cancelling signal is done within MATLAB and the predistorted data is then stored in an Arria V FPGA which is used to pass the digital data to two 16-bit DACs at a sampling rate of 307.2MHz, incorporated in a dual-band transmitter Texas Instrument board TSW30SH84. Then the fundamental signal in lower band and the cancelling signal (or identifying signal) in the upper band are transmitted simultaneously by the dual band transmitter. The center frequencies are 888.4 MHz and 2665.2 MHz for lower band and upper band signals, respectively. The output signal of the combiner is received by the TSW1266 receiver board after passing a set of filters and switch used to tuned the *IQ* demodulator to the desired band. Within the receiver, the received data are down-converted, sampled and digitized by the ADC's at a sampling rate of 614.4MHz and stored in the FPGA, before being passed to MATLAB for analysis.

IV. Result and Discussion

In Fig 4b, the right part shows the comparison of the original third harmonic signal and the cancellation result. The third harmonic is suppressed by 31 dB. Since the upper band does not impact the lower band, the lower band signal can still be linearized by digital predistortion method as shown in Fig 4a.

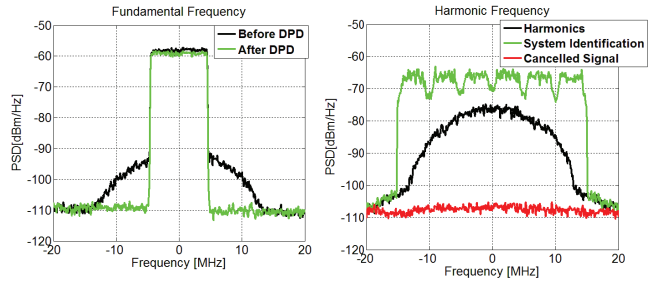

Fig. 4.a) Left: main band and b) Right: harmonic cancellation result.

Table I summarized the measurement results. Harmonic model NMSE is the normalized mean square error of the modelled 3rd harmonic, i.e., $y_{1,3}$ compared to the actual 3rd harmonic. Harmonic before and after cancellation is the harmonic strength relative to the fundamental signal.

TABLE I
SUMMARY OF MEASUREMENT RESULTS

Evaluation Criterion	Measured Value
Harmonic Model NMSE	-49.5 dB
Harmonic before cancelling	-28 dBc
Harmonic after cancelling	-59 dBc
Harmonic cancellation	31 dB
Main Channel NMSE after DPD	-40.1 dB
ACPR after DPD (LSB,USB)	-49.5,-50.3 dB

V. Conclusion

This work presents a digital solution for a fast and accurate channel distortion modelling and compensation of broadband PAs that enables an automatic harmonic cancellation via feed-forward and linearization via predistortion.

VI. Acknowledgement

This work was supported by Rockwell Collins and the National Science Foundation under Grant ECS1129013.

References

[1] M. Rawat, P. Roblin, C. Quindroit, K. Salam, C. Xie, "Digitally supported feed-forward harmonic cancellation for filter-less ultra-wideband transmitters," in *IEEE Intern. Microw. and RF Conf. (IMaRC)*, vol., no., pp.84-87, 15-17 Dec. 2014

[2] N. Naraharisetti, P. Roblin, C. Quindroit, S. Gheitanchi, "Efficient Least-Squares 2-D-Cubic Spline for Concurrent Dual-Band Systems," in *IEEE Trans. Microw. Theory and Techn.*, vol.63, no.7, pp.2199-2210, July 2015

[3] Lei Ding, G.T. Zhou, D.R. Morgan, M. Zhengxiang, J. Kenney, Jaehyeong Kim; C. Giardina, "A robust digital baseband predistorter constructed using memory polynomials," in *IEEE Trans. Commun.*, , vol.52, no.1, pp.159-165, Jan. 2004

Enhanced PHD Model Extraction by Improving Harmonic Response Superposition During Extraction

D.T. Bespalko and S. Boumaiza

Emerging Radio Systems Group, 200 University Ave. W., University of Waterloo, Waterloo, ON, N2L 3G1, Canada

***Abstract*—A Poly-Harmonic Distortion (PHD) model extraction procedure is proposed to improve the model accuracy for unmatched, broadband RF transistors by minimizing multi-harmonic signal reflections within the measurement system. As a result, the fictitious need for higher-order models is avoided by minimizing the order of the nonlinear measurement system used to extract the model. Under strongly nonlinear conditions the accuracy of the PHD model is improved by $5dB$, in terms of Normalized Mean-Squared Error (NMSE), averaging less than 1% time-domain output power error.**

***Keywords*—Poly-Harmonic Distortion, X-Parameter, Behavioural Model, Nonlinear Vector Network Analyzer.**

I. Introduction

AVERAGE efficiency enhancement PA design techniques, such as Doherty and Envelope Tracking (ET), are too complex to design using empirical design techniques, hence they must be implemented inside a Computer-Aided-Design (CAD) tool. CAD tools are essential for achieving multi-objective design trade-offs between power-efficiency, linearity, and RF bandwidth. However, nonlinear circuit simulation is inherently limited by the accuracy of nonlinear transistor models.

Previous circuit models typically focusses on improving characterization accuracy by using measurement de-embedding[1], model component decomposition[2], and dynamic-range maximization. Alternatively, publications in large-signal behavioural modelling focus heavily on model formulation[3][4], increasing the model nonlinear order and memory length to improve model accuracy. While both of these methods improve overall prediction accuracy, little work combines the knowledge of nonlinear characterization and modelling to improve the model extraction procedure. This paper uses the PHD model to predict the device response under a highly nonlinear Large-Signal Operating Condition (LSOP). Rather than implement a high-order behavioural model, greater emphasis is placed on enhancing the existing model extraction conditions, thereby maximizing the utility of a simple model formulation. It is demonstrated that eliminating mismatch reduces system feedback, reducing the complexity of the model formulation that is needed to predict a highly-nonlinear system.

II. Impact of Mismatch on PHD model

The formulation of the PHD model in (1-2)[5] relies heavily on the harmonic superposition principle, the separability of the model kernels ($X^S_{ik,jl}$ and $X^T_{ik,jl}$) with respect to input port and harmonic. This simple model formulation ensures that the hardware requirements are minimized by utilizing a rotating harmonic signal source, as shown in Fig. 1. As the DUT becomes strongly nonlinear, the model inputs (a_{jl}) are no longer separable, hence a high-order model must be used, and dedicated signal sources are required on all ports and harmonics in Fig. 1.

Unfortunately, during model extraction the nonlinear order of the DUT is artificially increased by mismatch in the measurement system. Fig. 2 demonstrates that a nonlinear DUT will emit multi-harmonic, multi-port power-waves, shown in red. When the measurement system is mismatched (at any port/harmonic), the output power-waves are reflected back into the DUT as non-zero input power-waves, shown in blue. Therefore, in a mismatched system, the model formulation 1 implies that the inputs (a_{jl}) cannot be applied individually without simultaneously applying all other model inputs.

X-Parameters is a registered trademark of Keysight Technologies

978-1-4673-9247-1/15/$31.00 ©2015 IEEE

$$
\begin{aligned}
B_{ik} &= X^F_{ik}(LSOP) \\
&+ \sum_{(jl)\neq(11)} X^S_{ik,jl} a_{jl} \\
&+ \sum_{(jl)\neq(11)} X^T_{ik,jl} a^*_{jl} \qquad (1) \\
LSOP &= (V_{10}, V_{20}, |A_{11}|, |A_{21}|) \qquad (2)
\end{aligned}
$$

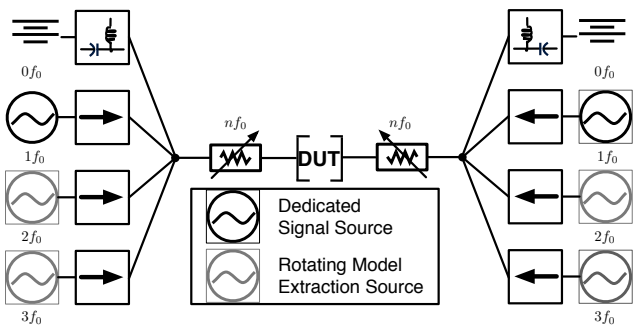

Fig. 1. Hybrid Active/Passive Load-Pull System Overview

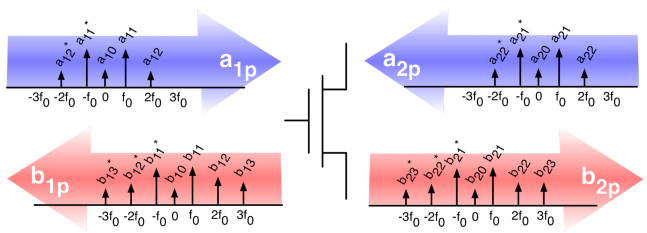

Fig. 2. The Multi-Harmonic MIMO System

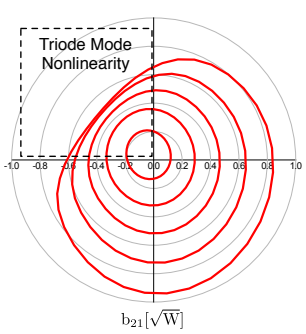

Fig. 3. Nonlinear Sensitivity of the DUT to $|A_{21}|$ at a fixed $|A_{11}|$

III. Pre-Model Characterization

The hybrid load-pull system, shown in Fig. 1, can use passive multi-harmonic impedance tuners to provide good matching, while active signal injection provides multi-harmonic power sweeps to extract the coefficients of the model. Although a nonlinear DUT multi-harmonic input and output impedance will vary during extraction, a well-matched LSOP greatly reduces the average feedback over the measurement space. As a result the following procedure is proposed for extracting the most accurate PHD model by optimizing the test-bench to achieve the best model under the "strongest nonlinear LSOP":

1) Select the DC bias point (class of operation).
2) Conjugate match the DUT at all ports/harmonics using passive multi-harmonic impedance tuners.
3) Perform a large-signal power-sweep of $|A_{11}|$, $|A_{21}|$, and $\angle A_{21}$ to determine the "strongest nonlinear LSOP", shown in Fig. 3
4) Re-tune the multi-harmonic passive impedance tuners to maximize the output power-waves $(b_{ik}, \forall ik \neq 11)$ so that harmonic power dissipation is maximized.

The LSOP *is optimized for model extraction, not a specific design condition*, and the resulting model will cover a portion of the measurement space that is often used to design high-efficiency PAs. If additional load-impedance coverage is desirable, a look-up table (LUT) model can be constructed by sweeping A_{11} and A_{21}, and all other LSOPs are assumed to have a lower nonliner order. All harmonic source/load impedance matching conditions are typically predicted by the model coefficients, however strongly nonlinear conditions can add another A_{jl} condition to the LSOP definition in (2). Extracting the PHD model under the conditions described will ensure that the system inputs better reflect the model inputs, therefore a A_{21}-dependent PHD model will be more accurate than a Load-dependent (Γ_{21}) LUT.

IV. Model Extraction and Validation

A Cree CGH60060D 60W bare-die transistor compact circuit model operating at 2 GHz over 3-harmonics is the chosen nonlinear system for this study. Although this procedure has been performed on a measurement test-bench, the bare-die transistor simulation allows us to synthesize an irrefutable strongly nonlinear operating condition at the intrinsic transistor reference plane. The PHD model is extracted and all Γ_{12} measurements made during model extraction (using a a_{jl} phase sweep) are shown in Fig. 4b. The points in the center demonstrate that the Γ_{12} response does not deviate from the

LSOP when extraction signals are applied at other ports/harmonics($a_{12} = 0$ for all measurements). Furthermore, the shape of the Γ_{12} response when a_{12} is applied represents a low-order elliptical response, well within the assumptions of the PHD model formulation in (1-2). Alternatively, the exact same LSOP was reproduced using a $Z_{1j} = 50\Omega$ (source) termination impedance, as shown in Fig. 4a. In Fig. 4a, the Γ_{12} response changes when extraction signals are applied at other ports/harmonics, and the response to a_{12} appears to be more distorted than the shape in Fig. 4b. Each model has been validated using a phase-sweep (fixed-amplitude) stimulus, sequentially applied at each port/harmonic, and the accuracy improvement of the Enhanced PHD model is shown in in Table I in terms of Normalized Mean Squared Error (NMSE) for each output power-wave.

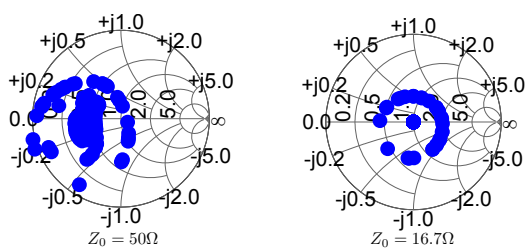

(a) Existing PHD Model) (b) Enhanced PHD Model

Fig. 4. PHD Model Extraction Measurement Coverage of Γ_{12}

TABLE I. MODEL EXTRACTION VALIDATION

	NMSE [dB]	Existing PHD Model	Enhanced PHD Model
I_{DS}	$0f_0$	-20.3	**-25.5**
P_{OUT}	$1f_0$	-23.4	**-28.3**
	$2f_0$	-7.38	**-10.0**
	$3f_0$	-18.0	**-23.0**

TABLE II. INDEPENDENT MODEL VALIDATION

		NMSE [dB]	Enhanced PHD Model
Frequency	I_{DS}	$0f_0$	-24.5
	P_{OUT}	$1f_0$	-21.7
		$2f_0$	-2.25
		$3f_0$	-18.7
Time	P_{OUT}	nf_0, $n > 0$	-20.6

Although the model validation in Table I provides an indication of relative model performance, it does not accurately approximate the final application of the model inside a nonlinear circuit. Therefore, an independent model validation is used to verify the harmonic superposition assumption by sweeping all harmonic input signals *simultaneously*, using dedicated signal-sources in the measurement system shown in Fig. 1. This validation is presented in Table II in terms of the frequency-domain NMSE at each harmonic, and the RF time-domain NMSE. The time-domain error represents a "weighted average" of the multi-harmonic frequency-domain components. Although the prediction error of the second harmonic is quite large, it's power is significantly lower than other harmonics and does not contribute to the time-domain error. Overall, the differences between Table I and Table II demonstrates that another $3-7dB$ could be achieved if harmonic cross-mixing terms were included in the model formulation.

V. CONCLUSION

This paper presented a method for extracting the best PHD model with enhanced accuracy by conjugate matching all harmonics of each port using multi-harmonic passive impedance tuners. By conjugate matching the source impedance, the NMSE of the DC drain current and fundamental output power were each improved by $5dB$. Furthermore, a rigorous independent validation methodology evaluated the PHD model harmonic superposition assumption, suggesting that the output-power prediction degrades by $6dB$ when all harmonic impedances vary simultaneously from the LSOP, as is intended in a PA design application . The Enhanced PHD model achieves less than 1% average time-domain error at a strongly nonlinear LSOP.

REFERENCES

[1] G. Crupi, D. M. M. P. Schreurs, A. Caddemi, A. Raffo, F. Vanaverbeke, G. Avolio, G. Vannini, and W. D. Raedt, "In-deep insight into the extrinsic capacitance impact on GaN HEMT modeling at millimeter-wave band," *International Journal of RF and Microwave Computer-Aided Engineering*, vol. 22, no. 3, pp. 308–318, May 2012.

[2] P. Aaen, J. A. Plá, and J. Wood, *Modeling and Characterization of RF and Microwave Power FETs*. Cambridge: Cambridge University Press, 2009.

[3] P. Roblin, *Nonlinear RF Circuits and Nonlinear Vector Network Analyzers*, ser. Interactive Measurement and Design Techniques. Cambridge: Cambridge University Press, 2011.

[4] S. Woodington, R. Saini, D. Williams, J. Lees, J. Benedikt, and P. J. Tasker, "Behavioral model analysis of active harmonic load-pull measurements," *Microwave Symposium Digest (MTT), 2010 IEEE MTT-S International*, pp. 1688–1691, 2010.

[5] J. Verspecht and D. E. Root, "Polyharmonic distortion modeling," *Microwave Magazine, IEEE*, vol. 7, no. 3, pp. 44–57, 2006.

Towards Faster, Swept, Time-Coherent Transient Network Analyzer Measurements

J. Martens, E. Vayner and J. Tu

Anritsu Company, Morgan Hill, CA US

***Abstract* — Time- and phase-coherent swept network analyzer measurements are increasingly important for everything from harmonic waveform reconstruction needs in power amplifier analysis to transient pulse response problems in radar and phased array applications and generic memory effect analysis in device characterization. Classically, there have been several solutions to these problems but these have often been slow or have required sometimes complicated reference-generation schemes to enable phase recovery. By employing a wide-IF digitizer in a sampling receiver along with a somewhat novel triggering/marking scheme, it is possible to perform synchronous complex measurements during a frequency or power sweep at 10s of μs/point sweep rates. This configuration is demonstrated with a waveform reconstruction experiment and with sensitive swept transient DUT measurements delineating thermal response differences of more than 1.5 dB and 15 degrees on a fast sweep timescale.**

***Index Terms* — nonlinear characterization, vector network analyzer, transient response, millimeter wave.**

I. Introduction

Performance and modeling demands have increased the need for coherent (with that meaning having multiple levels) quasi-linear network analyzer measurements of a variety of devices at both microwave and mm-wave frequency ranges. In one context, this coherence refers to the ability to retain phase information on a given quantity *during the sweep* when simple ratioing may be difficult (e.g., harmonic and intermodulation measurements). The calibration of the phase information has been covered extensively elsewhere (e.g., [1]-[6]) and that is not the subject of this work. Rather, how can one easily maintain repeatable phase information at all on these kinds of quantities during a fast sweep? Existing techniques include the use of a nonlinear generator of some kind in the reference path of a VNA (e.g., [7]-[8]), certain higher-order statistical methods (e.g., [9]), the use of a pilot signal generator (e.g., a waveform generator feeding a reference path or feeding the main detection path at an offset frequency) among others. While these approaches can work well, they often require added hardware, can reduce measurement throughput and can have their own signal-to-noise issues (particularly for higher-order nonlinearities) that may limit measurement capabilities. Internal synchronization approaches (e.g., [10]) can offer a simpler approach to this problem and a similar method will be followed here although with a sampling front-end.

A second problem is that of more global time coherence where a DUT state variable (e.g., bias or a control signal) or the phase of a modulating signal must be aligned both with the sweep and with the acquisition. As modulation bandwidths increase, these timing requirements are sometimes not far from basic phase timing needs. While various triggering solutions exist for this class of concerns, speed and the ability to handle rapid transitions have sometimes been issues. Monitoring transients on sweeps of this kind is of some interest in analyzing thermal and trapping responses and synchronizing the modulation, state variables, and the measurement can be important.

In the present work, the use of a wideband and a deep-memory digitizer to address both problem types is explored. Of particular interest is when the source and/or receiver are sweeping (in terms of frequency and/or power) and somewhat detailed information about the synthesizer behavior is needed in order to establish both phase and time coherence. The use of a time record to keep phase information coherent is, of course, the basis of time domain measurements in general. The description here is more centered on how the time record measurements are marked with synthesizer information and synthesizer synchronization is used to align the phase information in the time record without the use of another reference signal but maintaining timing between all of the relevant variables. Such a structure enables somewhat simpler and faster measurements covering a variety of categories.

The measurement structure will be presented in section II showing the sweep control process, synchronization and data marking aspects. An initial example in section III of harmonic waveform reconstruction will be used to confirm the behavior and motivate the discussion. In section IV, it is shown that sensitive DUT transients can be captured with this approach that can possibly be missed or misinterpreted with a more traditional sweep/synchronization protocol.

II. Measurement Structure

As the measurements of interest here, and the proposed protocol, have much to do with transient swept measurements and details of timing and synchronization, this section will be devoted to a number of aspects of triggering and timing control. A very basic, high-level measurement structure is shown in Fig. 1. A device will be stimulated at some starting time, often with some modulated signal, and the device turned on (or sent to an active state) at some related time, and the measurements recorded relative to those timing events. Nothing is new at this point. The next level of detail is shown in Fig. 2.

978-1-4673-9247-1/15/$31.00 ©2015 IEEE

Some important aspects:

- The ADCs for all channels are recording continuous time records during a sweep (of frequency or power). Having multiple gigabytes of memory allows relatively long sweep processes.

- The 'sweep control' in Fig. 2 moves the sources, LO (and ADC clock) to their appropriate locations over time and knows when they are in position. The sweep control engine places time-coherent marks in the live ADC data streams so that data is now phase-aligned with the source hardware. Phase resets of the signal sources create absolute starting points for the timing.

- The external triggering process (to the DUT, to sweep control, to acquisition control and to modulation control (if needed)) could all have different latencies (marked as τ_1, τ_2, τ_3 and τ_4 in the figure). Characterizing these latencies can be important in maintaining overall time alignment.

- It is the data marking coherence with the sources along with triggering coherence that is somewhat novel.

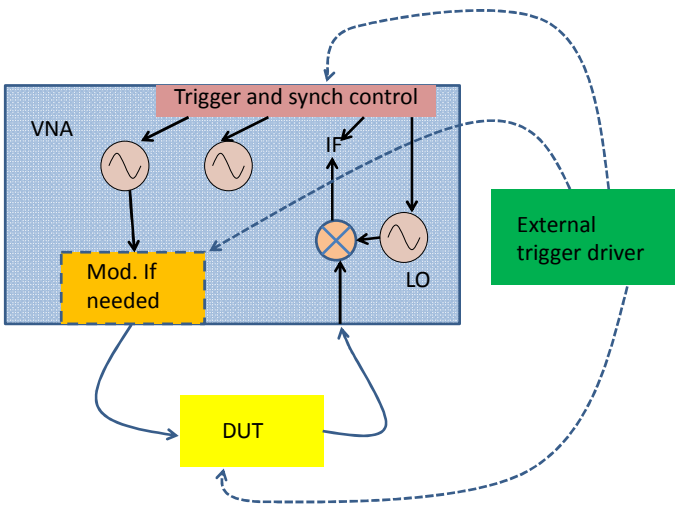

Fig. 1. A very high-level block diagram of the measurement is shown here. For this measurement there is a global measurement trigger and then point-by-point synchronization control.

- The timing related to the modulation process can be important in the transient measurements to be discussed in this paper as that timing (along with that of the trigger to the DUT) often play a large role in thermal evolution of the DUT.

- The time scales for the trigger and synch events vary widely depending on the application. For the present hardware, the fastest time between per point synch events is on the order of 10 µs. The minimum time resolution of the data record and marking is 2.5 ns but the acquisition rate can go as slow as 10 MHz. Depending on the number of frequency/power points in the sweep, the global start trigger rate (for the whole sweep) can be as fast as a few ms although this is typically much slower when the measurement is one of thermal/trap transient analysis. The upper limit on the length of sweep is set only by memory and is typically 100s to 1000s of frequency/power points.

- A sampling front-end allows harmonic sweeps without synchronization and this will be exploited in some measurements. This will be used in concert with non-harmonic acquisition and marking.

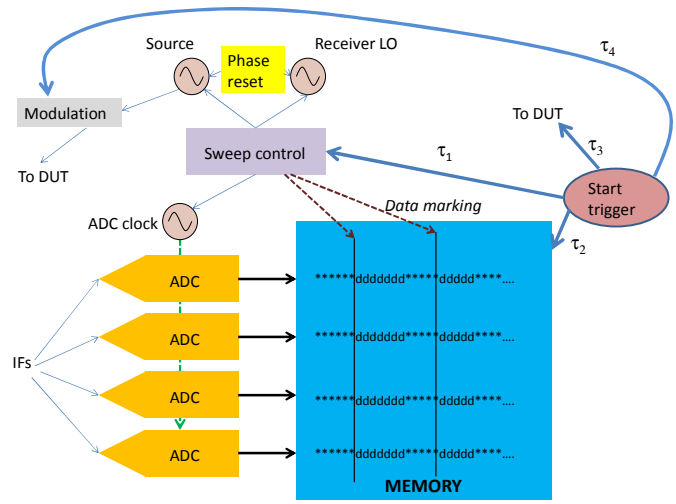

Fig. 2. A lower level block diagram is depicted here. At the point synchronization level, phase resets of the synthesizers along with coherent marking of the data stream are important. The *d* symbols represent data corresponding to a sweep point and the '*'s represent (usually not useful) data occurring between sweep points.

III. Harmonic Reconstruction Example

As a means of validation, the harmonic reconstruction of a DUT waveform is a possible vehicle. The data can be acquired in two well-known ways for comparison:

- In a single (non-swept, sampler-based) measurement where the harmonics (through 5th for this example) downconvert into the receiver into the harmonics of the IF (using harmonics of the LO). The base IF used in this case will be 30 MHz with the DUT output harmonic signatures appearing at 30, 60, 90, 120 and 150 MHz.

- Using a swept LO with the continuous acquisition process discussed and a fixed IF (100 MHz in this case). The harmonic responses in the IF system are not analyzed in this case and the measurement relies on the repeatable phase relationship of the LO and ADC clock during the various receiver positions.

For both measurements, a harmonic phase calibration is required to correct for receiver phase variation as usual but the difference is in the reprogramming of the receiver LO between measurements. Classically, a level of ratioing was normally employed to remove phase scrambling in that process. The intent here is to show that through continuous acquisition and enough internal synchronization, that the same result can be achieved as with a single measurement. Schematically, the two measurements are illustrated in Fig. 3.

The two reconstructed waveforms for a 20 GHz input stimulus (so harmonics to 100 GHz are used) are shown in Fig. 4. Harmonic phase calibration errors are common to both extractions so that does not enter into the comparison. This is more a measure of distortions introduced by the sweep process in the continuous acquisition case. The maximum difference on the time waveform reconstruction is about 5% at the peaks.

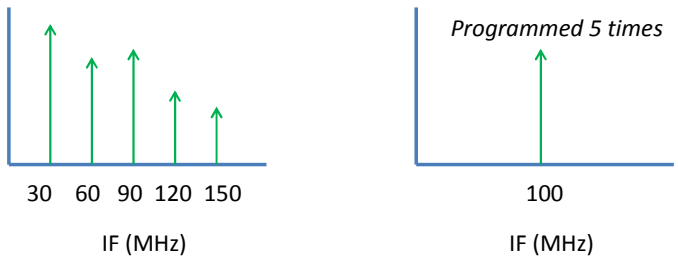

Fig. 3. The two measurement protocols for the experiment of this section (in receiver IF space) are shown here. On the left, harmonics of a single LO are used to convert DUT harmonics to harmonics of the system IF. On the right, in continuous acquisition mode, the receiver is sequentially programmed to the harmonic locations.

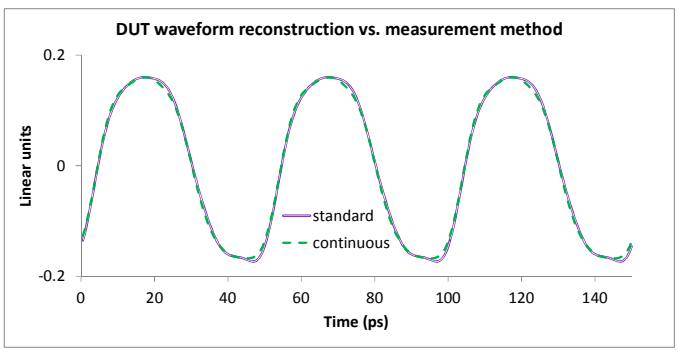

Fig. 4. The reconstructed DUT output waveforms using the continuous acquisition approach and a standard, swept receiver approach are plotted here to show approximate equivalency.

Perhaps more useful are the differences in terms of the complex harmonic amplitudes. These ranged were <0.2 dB/<3.5 degrees through the 3rd harmonic (<0.55 dB/ <10 degrees through the 5th). This provides some level of validation of the swept approach and perhaps allows the methods to be used in concert.

IV. Measurements

A primary measurement of interest for this continuous acquisition method is that of start-up transient interrogation where a sweep (of some variable) accompanies the start process (e.g., [11]-[12]). If that start process also involves the beginning of some modulation envelope and DUT state, the complexities increase even on a scalar level. In this case, however, phase evolution is also important as it may be for any number of modeling, phased array, and radar application.

The first measurement will be a pulsed power sweep at 60 GHz of a moderate power amplifier and the primary parameter of interest is AM/PM of *a modulation sideband* (i.e., phase deviation versus power) starting from a cold state. This particular DUT must be pulsed, in this case with a 1 ms period and a 20 µs width. On every pulse from start, a different power is to be applied ranging from -25 dBm to 0 dBm in a total of 35 steps (i.e., 35 pulses). Because the thermal evolution from start is of interest, it is important that the power change by the determined amount on every pulse and that no pulses be skipped.

A classical approach would be to start the pulse generator and DUT running at initial trigger and start the measurements at the same time but allow the measurement sweep to proceed asynchronously. In this 'standard' method, typically multiple pulses would hit the DUT at each of the given power steps (although in some configurations, it could go the other way where the DUT never would actually see every power step but then acquisition would be incomplete).

The results comparing the continuous approach of this paper with the standard classical approach are plotted in Fig. 5. The x-axis in this plot is listed in time *but equivalently converts to input power* with the maximum value of 0 dBm. The linear value of the phase shift through the DUT at this frequency was about -90 degrees. In the continuous method, one sees less than a few degrees of AM/PM up until the 33rd pulse/step where a sharp increase occurs. With the standard approach, more AM/PM is noted at lower power levels with a softer transition when the higher levels are reached. It is believed that this is due to accumulated thermal load on the DUT from multiple pulses (average 4) at each of the power levels. This thermal history propagates into the AM/PM plot and may misrepresent the DUT behavior under its intended operating conditions. From single-shot measurements at the 30th pulse, it was believed that the AM/PM should be less than 2 degrees which does not agree with the standard method.

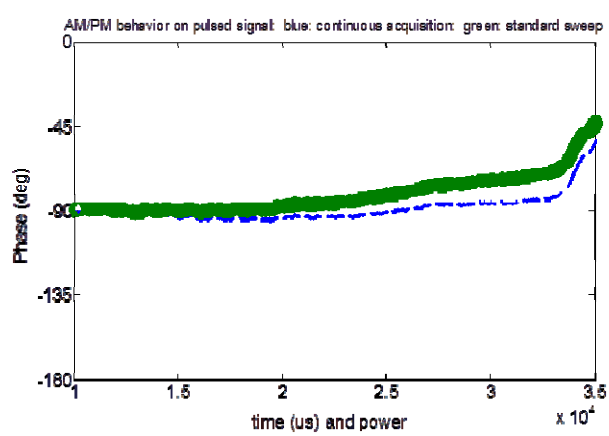

Fig. 5. AM/PM measurements of a sideband from cold start of a 60 GHz DUT are shown here for the proposed continuous acquisition and for the standard classical approach. The X-axis corresponds to time (up to 35 ms) or input power (up to 0 dBm).

A second measurement case is that of a frequency sweep from 6 to 20 GHz (31 points) of a power amplifier where

output power and harmonic phase are of interest. In this case, the envelope is not classically pulsed but only has ~ 15 dB attenuation during quasi-off-states. The frequency is to change between each on-state from the cold start event. The objective again is that each frequency propagates to the DUT during precisely one on-state. The power out response using the continuous acquisition method of this paper and the standard approach is plotted in Fig. 6. At the lower frequencies (immediately after the cold start), there is only ~0.1 dB difference between the two methods but this increases to over 2 dB by the last frequency. In the standard method, the DUT sees each frequency for 3-4 on-states so it is again believed that the thermal load through the measurement accumulates and reduces the gain and output power of the device below what occurs with the intended protocol. The DUT temperature at the end of the measurement was ~2C higher with the standard vs. the continuous method (both starting from the same cold point) which would tend to support the hypothesis. If the DUT was left running for several minutes prior to the measurement, the traces overlaid.

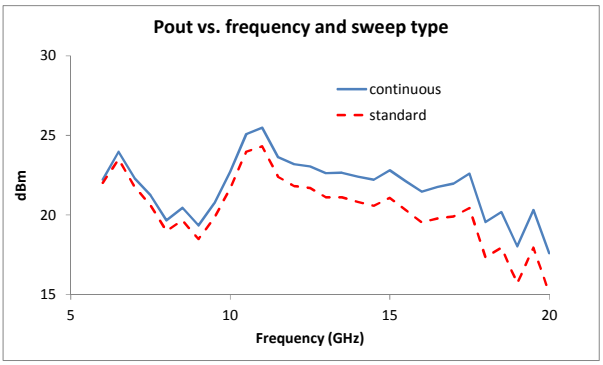

Fig. 6. The power output responses of a thermally sensitive device using the continuous acquisition method of this paper and a standard method (where there is little coordination between the modulation and sweep timing) are shown here. Both measurements were triggered from a cold start.

The 2nd harmonic phase difference (between the two methods) is plotted in Fig. 7 and also shows an evolution from near 0 difference at the earlier points and now over 15 degrees at the highest frequency. The same thermal load mechanism would seem to explain this result. Again, this particularly measurement is exploring both synchronization on a basic harmonic phase level but timing coherence of the sweep and DUT excitation as well.

V. Conclusion

While phase/time-coherent swept VNA measurements have been possible for many years, some hardware and configuration simplification is possible by managing triggering, synchronization and the live data stream from the measuring receiver. This type of measurement, and simplification of it, has been shown to be apparently useful in measurements such as swept transient analysis of timing-sensitive devices and subsystems.

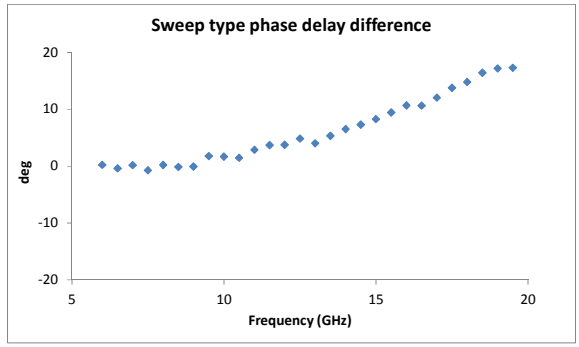

Fig. 7. The difference in phase delays measured using the continuous acquisition and standard methods for the DUT of Fig. 6 is plotted here.

References

[1] T. Van den Broeck and J. Verspecht, "Calibrated vectorial nonlinear network analyzers," *1994 Int. Micr. Symp. Dig.,* June 1994, pp. 1069-1072.

[2] S. Vandenplas, J. Verspecht, F. Verbeyst, E. Vandamme, and M. Vanden Bossche, "Calibration issues for the large signal network analyzer (LSNA)," *60th ARFTG Conf. Dig.*, Dec. 2002, pp. 99-106.

[3] D. Gunyen and Y. P. Teoh, "Characterization of active harmonic phase standard with improved characteristics for nonlinear vector network analyzer calibration," *2008 Int. Micr. Symp. Dig.,* June 2008, pp. 73-79/

[4] M. Mirra, M.. Marchetti, F. Tessitore, M. Spirito, L. C. N. de Vreede, and L. Betts, "A multi-step phase calibration procedure for closely spaced multi-tone signals," *75th ARFTG Conf. Dig.*, June 2010, pp. 1-5.

[5] P. Heymann, R. Doerner, and M. Rudolph, "Multiharmonic generators for relative phase calibration of nonlinear network analyzers," *IEEE Trans. On Instr. And Meas,*, vol. 50, pp. 129-134, Jan. 2001.

[6] K. A. Remley, "Practical applications of nonlinear measurements," *73rd ARFTG Conf. Dig.,* June 2009, pp. 1-15.

[7] V. Teppati, S. Pinarello, A. Ferrero, and J. –E. Mueller, "An unconventional VNA-based time-domain waveform load-pull test bench," *2010 Asia-Pacific Micr. Conf. Proc.,* Nov. 2010, pp. 1893-1896.

[8] J. Martins and N. B. Carvalho, "Spectral filtering setup for uncorrelated multi-tone phase and amplitude measurements," *34th Eur. Micr. Conf. proc.,* Oct. 2004, pp. 201-204.

[9] J. C. Pedro, J. P. Martins, and P. M. Cabral, "New method for phase characterization of nonlinear distortion products," *2005 Int. Micr. Symp. Dig.,* June 2005, pp. 971-974.

[10] A. Aldoumani, P. J. Tasker, R. S. Saini, J. W. Bell, T. Williams, and J. Lees, "Operation and calibration of VNA-based large signal RF I-V waveform measurements system without used a harmonic phase reference standard," *81st ARFTG Conf. Dig.*, June 2013, pp. 1-4.

[11] K. El-Akhdar, G. Neveux, D. Barataud, and J. M. Nebus, "Calibrated oscilloscopic system for RF time-domain characterization of non-linear devices," *2013 Med. Micr. Symp. Dig.*, Sept. 2013, pp. 1-4.

[12] P. Roblin, Y. Ko, H. Jang, and J. P. Teyssier, "Pulsed RF calibration for NVNA measurements," *80th ARFTG Conf, Dig.*, Dec. 2012, pp. 1-6.

Hurdles to On-Wafer Harmonic Measurements

Kathleen Muhonen

Qorvo, Greensboro, NC

***Abstract* — With the ever increasing need for spectrum the mobile phones, specifications are tougher for spurious emissions. Harmonics can fall into bands that are used for other services so prior evaluation of those harmonics is critical in product development. An on-wafer harmonic bench is used for fast evaluation of material and designs without having to build a final product to predict what the harmonic performance will be. Harmonic measurements are not new; but high power (4 watts), on-wafer harmonic measurements present hurdles that have not been solved. Low passive intermodulation (PIM) components, probe selection, connector selection and bench configuration all play into building a measurement system with low enough system noise to be able to evaluate the state-of-the-art technologies for mobile applications.**

***Index Terms* — Harmonics, low PIM, on-wafer measurements, passive intermodulation, probes.**

I. Introduction

With the advent of LTE, mobile phones now have more frequency bands and functionality which has put more capability into user's hands. The added bands have created tougher specs for spurious emission to ensure functionality is not hindered by distortion from various parts of the phone. A good example of this is in the 900MHz cellular band. Both the 2nd harmonic at 1.8GHz and the 3rd harmonic at 2.7GHz fall into other bands that may be used in the same phone. Specifications on these harmonics levels for antenna switches have become more challenging in the last few years.

New specifications tend to drive the need for better measurement capabilities. For the antenna switch in a mobile phone, it is important to have very low harmonics. For IC manufacturers of those chips, it is advantageous to be able to evaluate different material for harmonic generation before a product is designed. This has produced a need for on-wafer harmonic measurements as a part of technology assessment in this type of application.

Measuring harmonics is not new. Measuring harmonics at 4 watts of power on-wafer, however, pose tougher set of problems. In addition, advances in semiconductor material has also posed a need for a measurement system that has incredibly low system noise floors in order to be able to determine the harmonic generation from the material and not the measurement system. This paper outlines the many hurdles to developing a high-power, low noise floor, on-wafer measurement system. The paper is organized as follows. Section II highlights changes made to the bench configuration to lower the system noise floor. Section III discusses what passive intermodulation distortion (PIM) is and why it is important when measuring harmonics. The last section looks at many RF probes available and how they too will affect the system noise floor. Probe and pad wear-out is also discussed.

II. Bench Configuration

When measuring harmonics it is well known that the spectrum analyzer input cannot be over-driven because the internal detector will generate harmonics. Even if proper care is taken to attenuate the signal to proper levels, any attenuation in the spectrum analyzer path will subtract directly off the noise floor. Figure 1 shows critical changes made to a harmonics bench to remove attenuation in the spectrum analyzer path and how these greatly improve the system noise floor. The lower block diagram in figure 1 shows the "old" set-up. Here the fundamental was attenuated with a 20dB coupler and various attenuators after the coupler. Note that the 3dB pads in the fundamental path are there to help present 50 ohms to the device under test (DUT) interface. This configuration degraded the system noise floor by about 32dB (four 3dB pads and one 20dB coupler). The upper block diagram is the "new" set-up which shows how almost all of this attenuation was taken out of the spectrum analyzer path to improve it by 28dB. The new set-up used a diplexer to remove the fundamental signal. Thus allowing for virtually no attenuation at the harmonic frequencies but only at the fundamental frequency. Two 3 dB pads had to remain next to the DUT to maintain a 50 ohm environment.

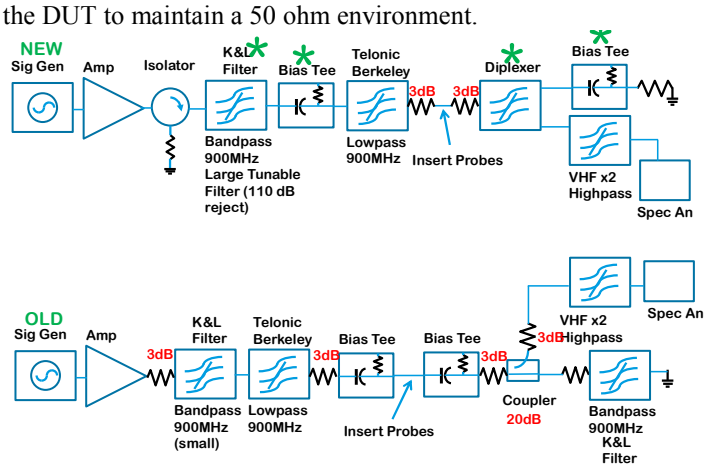

Fig. 1. Harmonics bench block diagram with and without changes to improve PIM.

In addition to the diplexer, the bias tees were found to generate passive harmonics. The bias tee on the input was moved between two rejection filters so that one filter could attenuate harmonics caused by the bias tee. The output bias tee was moved after the diplexer so it was out of the spectrum

978-1-4673-9247-1/15/$31.00 ©2015 IEEE

analyzer path. Several other components were changed as well due to PIM generation. Low PIM components are described in the next section.

III. Low PIM Components

Intermodulation distortion, IMD, is a well understood concept. Passive intermodulation distortion (PIM) also has been a common problem in satellite communication for many years. Just recently PIM has been a concern for mobile applications because of multiple bands, higher power levels and sensitive front ends. PIM is specified with a two-tone test (f1 and f2) in order to measure the level of the mixing products in-band (2f2-f1 and at 2f1-f2) [1]. The topic here is harmonic distortion. There is no theoretical development here between the relationship of harmonics and PIM, but in general low PIM components will have better harmonic performance than those that are not designed for low PIM.

One of the main causes for PIM are material that have hysteresis like nickel and stainless steel. Any material that is ferromagnetic will exhibit hysteresis. Dirty connectors also cause passive harmonics and connectors with poor center conductor contacts [2]. Thus connector and cable construction is very important as well as constantly cleaning connectors. N-type connectors are preferred because they have a larger mating interface and have repeatable connections if the proper torque wrench and mating techniques are used. Copper is preferred over nickel and stainless steel but white bronze is a better choice since it doesn't oxidize and stands up to temperature fluctuations[3]. To mitigate PIM further, almost all connectors were changed to torquable N-type connectors. New bias tees were ordered with N-type connectors. Components were all measured individually on the bench to see if the system noise floor degraded upon comparison.

Figure 2 shows initial improvements on the system noise floor with the above mentioned changes. Spectrum analyzer

Setup Name	Color	RBW	VBW	Noise level 2nds	Noise level 3rds
				dBm	dBm
Old	Cyan	100kHz	20kHz	-85	-82
New - 1	Red	100kHz	20kHz	-108	-105
New - 2	Blue	100Hz	100Hz	-115	-115
New - 3	Magenta	10Hz	1Hz	-128	-125

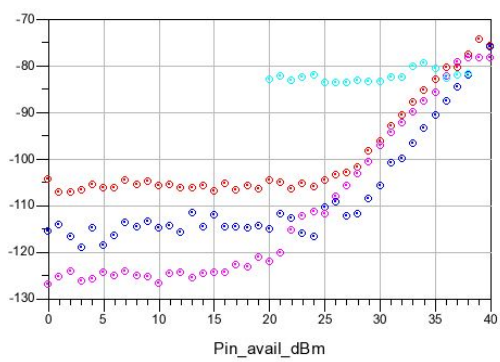

Fig. 2. Improvements made in the system noise floor

settings also affect the noise floor. It is best to use the lowest resolution bandwidth and video bandwidth possible to make the needed measurements. Figure 2 is an example of the second harmonic on a thru structure on SOI material.

Although the circulator in the "new" block diagram is made of magnetic material and causes hysteresis, it is located behind two rejection filters. Each filter offers about -100dB of rejection above 900MHz. The third harmonic was not degraded at all with the insertion of the circulator. The second harmonic did change slightly as shown in Figure 3 but this most likely due to measurement variations from probing.

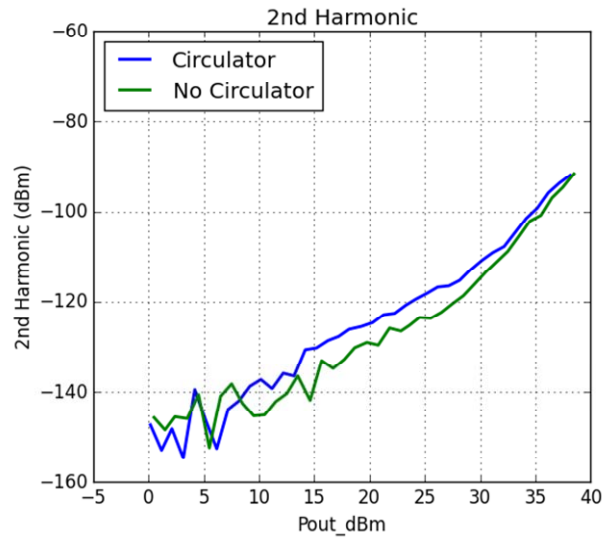

Fig. 3. Circulator harmonics are rejected by two filters on the input side of the DUT.

IV. Probes

Not all connectors could be changed to N-type because of the RF probes needed in the system. 3.5mm cables interface to the RF probes on the bench. Probe composition was investigated especially because many RF probes are made of a nickel alloy, and nickel degrades the harmonic performance. Six types of probes are shown here and each has been measured several times to ensure repeatability. The probes investigated have different metal compositions and different footprints. Composition was probably a leading factor, but footprint also made a difference in the harmonics.

Figure 4 shows the second harmonic measurement over power on aluminum pads of very short SOI thru. It is seen that at high power, Probe 1 performs very close to the bullet in which there are no probes in the measurement. Here the bullet was a simple female-to-female adapter so the two 3.5mm cables could be connected and the probes bypassed. Figure 5 shows the third harmonic where clearly Probe 1 has the best harmonic performance. The trends from Figures 4 and 5 are fairly the same. Care was taken that all the measurements were done at the same temperature and that the thru was not over probed.

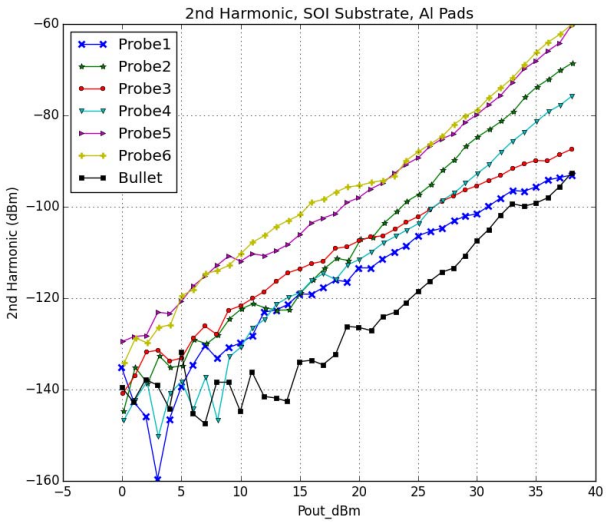

Fig. 4. Measurement of the 2nd harmonic of an SOI thru with various RF probes

All the probes in this study are ground-signal-ground, GSG, probes. The thrus that were used can accommodate either 100um or 150um pitch probes. Only Probes 5 and 6 were 150um pitch and the remainder were 100um pitch. Figure 6 shows a photo of each probe tip and its material construction provided by each vendor.

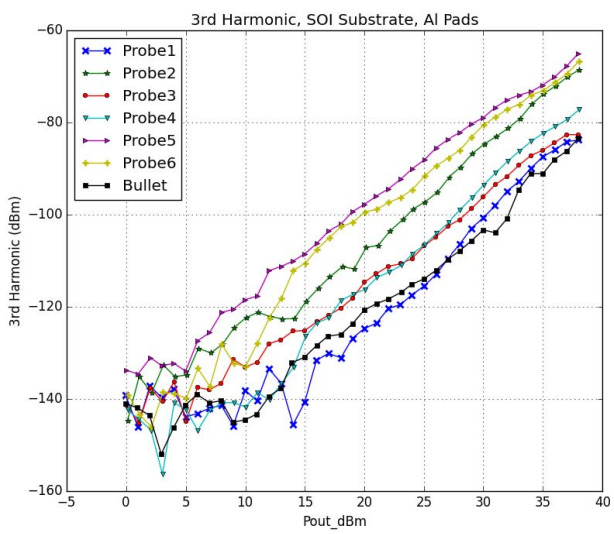

Fig. 5. Measurement of the 3rd harmonic of an SOI thru with various RF probes.

Of the probes used, Probe 1, 2, 5 and 6 have a larger footprint than the other two (3 and 4). The footprint here is the size of the signal or ground contact area with the pad. Probe 1 has the best harmonic performance possibly due to the fact it is made out of Beryllium Copper instead of nickel and that its footprint is larger than that of 3 and 4. Probe 2 has a larger footprint but it is made out of nickel and this could be causing some of the harmonic degradation. Interestingly, Probe 3 does quite well despite being made out of nickel and it has a small footprint. It was noted that this particular probe dug deeper into the aluminum pads than the other probes, possibly breaking through any oxide layer on the pads better than the other probes in the study. Probe 1, although made out of beryllium copper, did not have a heavy footprint like 3. Finally Probes 5 and 6 were designed for 5 and 10 watts respectively. They also have the larger footprint. Despite their larger footprint, they did not dig deep into the pad like probe 3, and they are made of nickel which is the likely reason for the degradation in performance. This information is summarized in Table 1.

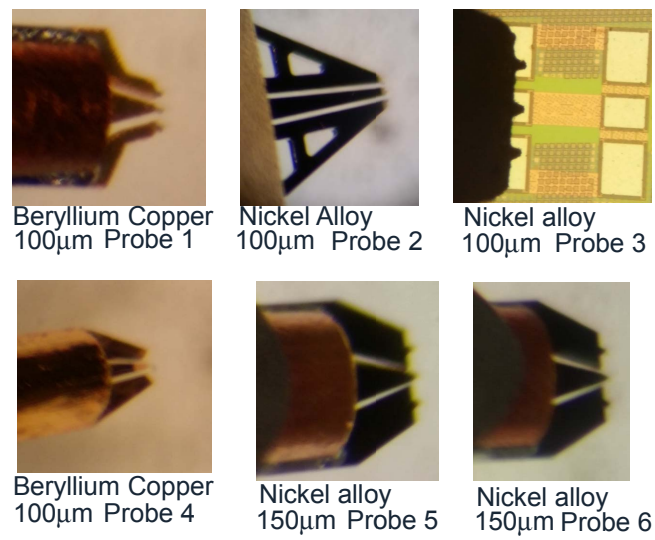

Fig. 6. Probe images showing pitch and material construction.

Table 1: Probe Specifications and Harmonic Performance

Probe	Composition	Footprint	Power	Harmonic Performance
1	Be-Cu	Large	30W	1st
2	Ni	Large	15W	4th
3	Ni	Small	5W	2nd
4	Be-Cu	Small	?	3rd
5	Ni	Large	5W	6th
6	Ni	Large	10W	5th

Another problem with the probes (and the pads that they contact) is wear. The only probe investigated long term is Probe 3. Although the specification say it is good for over 250,000 contacts on Aluminum pads, the harmonics degrade much quicker. It is estimated that these probes are only good for less than 2000 contacts. Even though the harmonics degrade, these probes are still good for S-parameters.

One of the procedures on this bench is to perform a system verification each morning the bench is in use. Originally the verification was done on a gold thru from a ceramic

calibration substrate. Over time, the thrus would start to wear and even with brand new probes, the harmonics were degraded. It is estimated that the thru could not be probed more than 10 to 15 times before its harmonics were permanently degraded. Seeing that the ceramic substrate is very expensive, the system verify is now done on an SOI wafer that has many thru structures available on it. Even an SOI thru can only be probed on average 10 times as well before its harmonics degrade.

Figures 7 and 8 show similar trends on the ceramic substrate. This is shown here for completeness even though the SOI thru is now used for system verification.

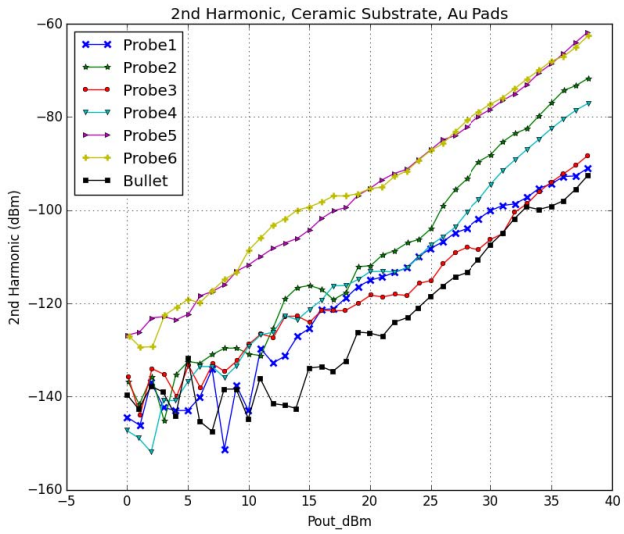

Fig. 7. Measurement of the 2nd harmonic of a thru on a ceramic substrate with various RF probes.

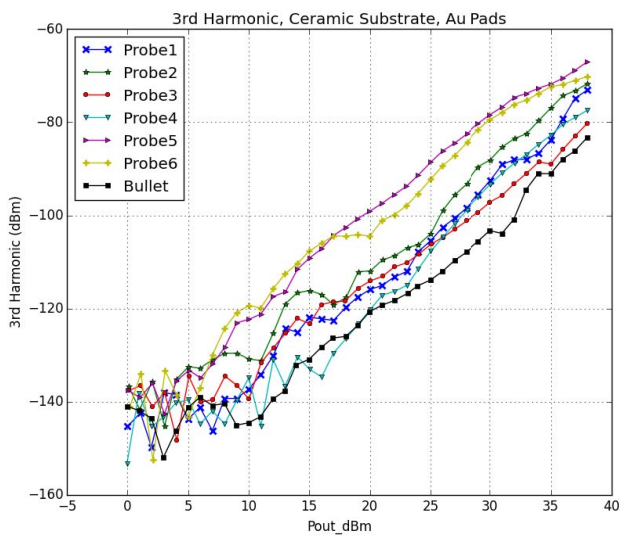

Fig. 8. Measurement of the 2nd harmonic of a thru on a ceramic substrate with various RF probes.

Lastly, probes specifically designed for high power and high current were also evaluated. These probes all had a larger footprint like Probe 1. It is speculated that despite the larger contact area, the material construction is degrading performance. It is important to have both a larger footprint and the absence of nickel in the material construction of the probes.

V. Conclusion

Improving the system harmonics on a high power, on-wafer bench has posed many hurdles. Recommendations to avoid these hurdles include:

- Use of N-type connectors is preferred for the superior center conductor mating surface. This poses a problem when all RF probes connectors are 3.5mm.
- Elimination of all materials that have hysteresis, like nickel, stainless steel or any ferromagnetic materials.
- Diplexers are used instead of couplers for the spectrum analyzer path so attenuation does not degrade the noise floor of the spectrum analyzer.
- Probe material is important, and nickel should be avoided if possible. It can be used if the footprint is heavy enough to cut thru any oxide growth.
- Probe footprint is better if it is has a large area. Contact area is important to minimize PIM. This may not be desirable for compact layouts.
- Probe wear will increase the cost of maintaining the system.
- Pad wear of the thrus for system verification is also a problem. A thru will only be acceptable if it is probed less than 10 times. Use of gold thrus on a ceramic substrate is costly.

Improvement of the harmonic bench is an ongoing process. New components are always being evaluated. Probe development for low PIM, however, hasn't caught much attention as of yet. It is hoped that the probe manufacturers can research other probe solutions for applications such as this one.

Acknowledgement

The author would like to thank David Wernsing and Harry Randall for help in data collection and to Tim Howle for help in modifying drivers for equipment.

References

[1] R. Rice, "Intermodulation Distortion," *RF Precision Products App Note*, RF Connectors, San Diego, CA.

[2] D. Weinstien, "Passive Intermodulation Distortion in Connectors, Cable and Cable Assemblies," *Amphenol App Note,* Danbury, CT.

[3] "White Bronze Plating", *RF Connectors App Note,* San Diego, CA.

A compact measurement set-up for envelope-tracking RF PAs with calibrated sensing of baseband V/I at the supply terminal

Julien Couvidat[1,2], Gian Piero Gibiino[1,3], Guillaume Pailloncy[4], Marc Vanden Bossche[4], Anthony Ghiotto[2], Dominique Schreurs[1]

[1]ESAT-TELEMIC, KU Leuven, Belgium

[2]Bordeaux INP, CNRS, IMS, University of Bordeaux, France

[3]DEI "G. Marconi", University of Bologna, Italy

[4]Network Analysis Centre of Excellence, National Instruments, Belgium

***Abstract* — This paper presents a compact set-up to perform automated measurements of RF PAs under envelope-tracking (ET) operation. In addition to RF signal generation and acquisition, it allows calibrated measurements of the baseband voltage and current at the supply terminal with up to 40 MHz bandwidth, enabling instantaneous efficiency measurements. The presented set-up is used to extract two different shaping tables, and to test ET operation with a 5 MHz WCDMA and a 20 MHz LTE signals at 838 MHz. The used devices are an InGaP/Silicon RF power amplifier (PA) from Skyworks and a high voltage extra fast complementary bipolar (XFCB) power modulator (PM) from Analog Devices.**

***Index Terms* — Envelope-tracking, Power amplifiers, Efficiency measurements, Supply modulation.**

I. Introduction

The last generations of wireless communications are requesting better energy saving, and therefore much effort is dedicated to improve the efficiency of the transmitter. Consequently, new PA architectures such as Doherty [1], out-phasing [2] and various supply-modulated PA architectures [3] have been proposed. Among these, the envelope-tracking (ET) technique consists of modulating the PA supply voltage so that it follows the RF waveform envelope amplitude, with the aim of keeping the PA at its maximum efficiency [4]-[5]. ET requires a supply modulator (SM), also called power modulator (PM), that is fast enough to follow the RF envelope, while efficiently providing the current requested by the PA [6]. In order to correctly adapt the drain voltage to the envelope of the RF PA input, PA gain and efficiency curves should be acquired at different RF power levels and supply voltages [7]. Then, a *shaping table* is implemented to define a relationship between the PM output waveform and the PA input envelope. In particular, through the shaping table, the PA operation can be optimized with respect to linearity, efficiency, or a combination of both, depending on the application. In order to achieve best efficiency, the PA is often driven into compression, generating nonlinear distortion. Moreover, the presence of supply modulation increases the level of nonlinear and memory effects. To maximize the linearity-efficiency trade-off, digital pre-distortion (DPD) techniques should be used to linearize the ET PA [8]. These techniques often consist of system-level approaches that may not account for a complete PA-PM characterization, moreover, their application range may be limited, as they are often based on local optimization. An alternative approach consists of identifying and designing general behavioral models [9]. In this way, the electrical behavior of the components and their mutual interactions can be mathematically described, and eventually used for linearization enhancements [10]. However, such methods usually require extensive large-signal characterization, especially if accounting the voltage and current at the supply node [11]. In this work, we propose a flexible set-up to perform automated ET PA measurements. Despite its extreme

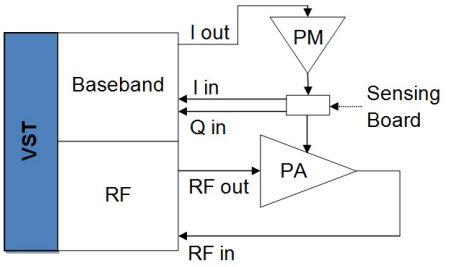

(a)

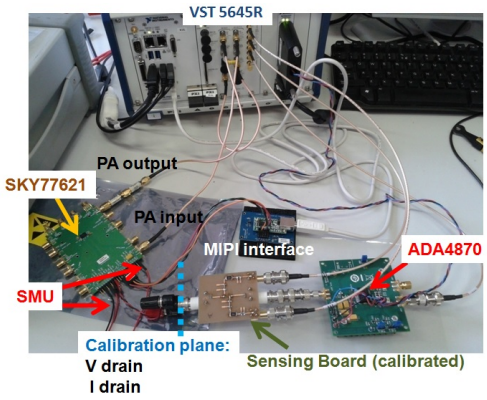

(b)

Fig.1. (a) Measurement set-up. The VST RF channels are connected to the RF PA I/O, while baseband channels are connected to the sensing board and the PM input. (b) Picture of the set-up.

978-1-4673-9247-1/15/$31.00 ©2015 IEEE

compactness with respect to alternative commercial solutions, the proposed set-up features voltage and current calibrated sensing at the supply node between the PA and PM, enabling instantaneous PAE evaluations. Moreover, it allows generating user-defined signals, making possible the implementation of standard DPD algorithms as well as custom behavioral modeling approaches. Section two of this document describes the measurement set-up features while section three addresses the measured results.

II. Measurement Set-Up

The principal instrument of the set-up is the Vector Signal Transceiver (VST) NI PXIe-5645, equipped with 80 MHz of modulation bandwidth RF channels and 40 MHz of modulation bandwidth baseband channels. The NI PXIe-1082 chassis supplies an internally generated 10 MHz clock with an independent buffer on the backplane, used to synchronize all the modules. The VST instrument combines a vector signal generator (VSG) and a vector signal analyzer (VSA) with FPGA-based real-time signal processing, which allows the user to define, via software, the instrument capability. In this work, the baseband FPGA-based hardware control has been customized in order to generate dynamic signals to feed the PM and acquire the voltage and current flowing at the PA drain supply node. To sense the current, a resistive sensing board has been designed, following the approach in [12]. The measurement set-up is shown in Fig. 1.

A. VST Baseband Channels Specifications

The VST baseband output channels can generate AC voltage up to 0.5V peak-peak on a 50 Ohm load in single-ended configuration, and a DC voltage between -1V and +1V. The VST baseband input channels, DC-coupled, can acquire up to 2V peak-peak signals. To optimize the dynamic range, 36 different amplitude ranges from 32mV to 2V peak-peak can be configured (several ranges resolution are reported in Table I). The baseband generation and acquisition sample rates are fixed to the internal VST sample clock (120 MS/sec), with 16 bit resolution.

B. Calibrated Sensing At The Supply Terminal

The schematic of the sensing board inserted between the PA and the PM is reported in Fig. 2. By acquiring the voltages at

TABLE I
BASEBAND Input Ranges Resolution

Range (Vpkpk)	I Channel (µV)	Q Channel (µV)
0.032	27	28
0.1	31	32
0.5	77	79
1	158	161
1.5	238	243
2	293	300

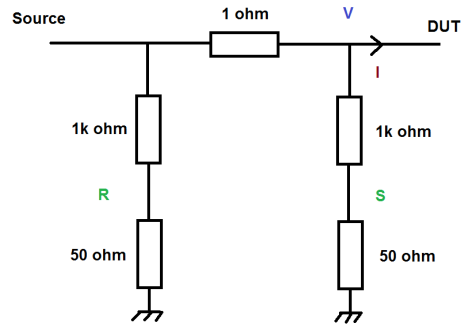

Fig. 2. The sensing board schematic. PM output is wired on the source terminal while PA drain input is wired on the DUT terminal. R and S correspond to the voltages measured by the VST baseband channels while V and I correspond to the voltage and current measured at the calibration plane.

the terminals of a 1 Ohm power resistor, it is possible to retrieve the voltage and the current flowing between the PA and the PM. To limit the current at the channels, a voltage divider composed by 1kOhm resistors is placed. This voltage divider applies a 1/21 ratio on the measured voltages. Since no bias-tee is used, AC and DC components are not separated, possibly leading to lower precision in presence of signals with large dynamics. In this sense, we take advantage of the high-resolution of the baseband VST channels: for example, if setting input channel range to 0.4Vpeak-peak, the maximum measurable voltage at the supply node is 10V peak-peak with a resolution of 3.4mV, which we consider acceptable to characterize PAs for mobile applications. A short-open-load (SOL) relative calibration procedure is implemented using a multi-tone signal designed to cover the bandwidth of interest. The calibration Error Coefficients Matrix (ECM) is expressed as:

$$\begin{pmatrix} V \\ I \end{pmatrix} = \begin{pmatrix} \alpha & \beta \\ \gamma & \delta \end{pmatrix} \times \begin{pmatrix} R \\ S \end{pmatrix} \tag{1}$$

where R and S are the voltages measured by the instrument and V and I are the voltage and the current at the calibration plane (Fig. 2). Since SOL procedure only gives three equations, an additional absolute calibration step is performed to solve the system of equations and obtain the calibration coefficients. Thus, a multi-tone reference signal is measured beforehand on a 50 Ohm terminated scope. Then, measurements are acquired while the same multi-tone is applied at the DUT side of the board, and the source side is terminated with 50 Ohm. It should be mentioned that the VST baseband input channels show an intrinsic DC offset, which is not compensated by the SOL calibration. Such an offset has been characterized for ten DC values and for each input range. Then, it is compensated by referring to voltmeter measurements. The voltage drop on the sensing resistor is taken into account by acquiring two additional DC measurements.

C. Software Applications

A set of software applications has been developed to exploit the hardware capabilities. Specifically, a shaping table extraction software and a characterization bench for the PA-PM system have been developed. Furthermore, an ET-DPD reference application by National Instruments has been updated and tailored to the custom hardware configuration. The shaping table extraction is obtained through nested sweeps of measurements for which a continuous wave (CW) on the RF input and constant voltage on the PA supply terminal are applied. Then, the user can automatically extract and save constant gain (*IsoGain*) or optimized PAE (*OptiPAE*) shaping tables. The characterization bench application allows driving the PA and the PM with continuous wave (CW), modulated, or other user-defined identification signals, as well as voltage, power, and modulation frequency sweeps. The ET DPD reference application allows operating the PA under ET and visualizing RF input/output waveforms, supply voltage/current waveforms, as well as the instantaneous PAE. The AM-AM/AM-PM characteristics, the normalized mean square error (NMSE), and the adjacent channel power ratio (ACPR) can be evaluated. The RF and baseband paths reciprocal delay is estimated and compensated by minimizing the standard deviation of the AM-PM characteristics.

III. Experimental Results

A multi-mode and multi-band PA evaluation board from Skyworks (SKY77621-51) and a PM evaluation board from Analog Devices (ADA4870) have been used in ET configuration with the described set-up. This specific PA evaluation board is not tailored for ET operation, but the drain capacitors have been removed in order to support supply modulation. The PM features high slew rate and bandwidth, making it a good choice to deliver a dynamic voltage and test the PA under ET operation. Two shaping tables have been extracted: a 20-dB IsoGain shaping table (Fig. 3) and an OptiPAE shaping table (Fig. 4). The shaping tables are obtained by sweeping the input power levels, and applying a moving average to remove discontinuities. Then, measurements are linearly interpolated on 200 RF power levels. The 20-dB IsoGain and the OptiPAE shaping tables are shown in Fig. 5. A comparison of the instantaneous gain obtained with the two shaping tables is shown in Fig. 6, while the measured instantaneous PAE is shown in Fig. 7. In Fig. 8, baseband voltage and current measured at the supply node for the LTE standard are also shown. A 5 MHz WCDMA signal and a 20 MHz LTE signal have been measured. The OptiPAE determines a 23dB average gain, higher than the 22dB average gain given by the 20-dB IsoGain shaping table. However, in case of the OptiPAE table, the gain shows larger variations versus input power, thus higher nonlinear distortion will be produced. It can be noted that the curves extracted with the WCDMA signal show less dispersion with respect to the ones extracted with the LTE signal. Since no DPD has been implemented in this case, this is mainly a consequence of the higher modulation bandwidth of the LTE with respect to the WCDMA. The average PAE measured with OptiPAE shaping table shows an increase of 0.9% for the WCDMA and 1.5% for the LTE, as a consequence of the higher instantaneous PAE reached at large RF input signal. These results show that, for this PA, the drain voltage is impacting the PAE not more than 10% at large RF input signal, as illustrated in Fig. 4.

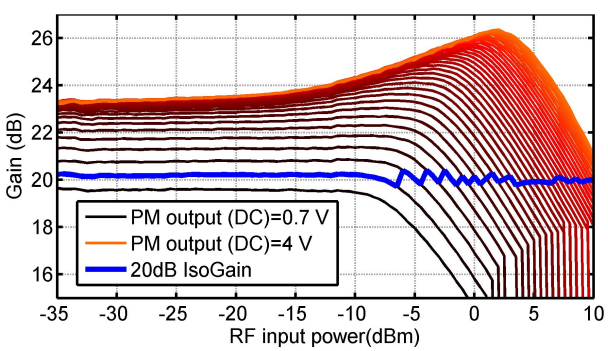

Fig. 3. IsoGain shaping table extraction. The blue curve links the selected points to keep a 20dB power gain over the RF power level. Measured results.

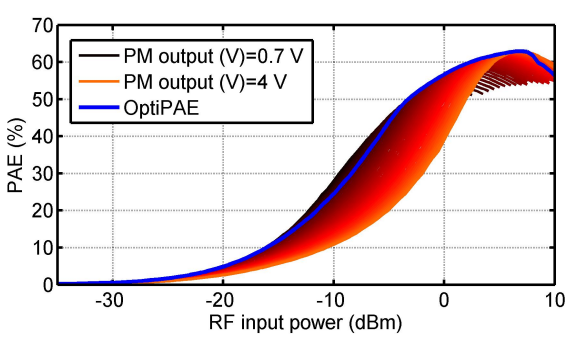

Fig. 4. OptiPAE shaping table extraction. The blue curve links the selected points to keep the maximum PAE over the RF power level. Measured results.

IV. Conclusion

An innovative and compact set-up for the automated characterization of ET PAs has been presented. Apart from the standard features, the set-up can acquire the calibrated dynamic voltage and current at the supply node between the PA and the PM. This is achieved by including a resistive sensing board and customizing the high-resolution baseband

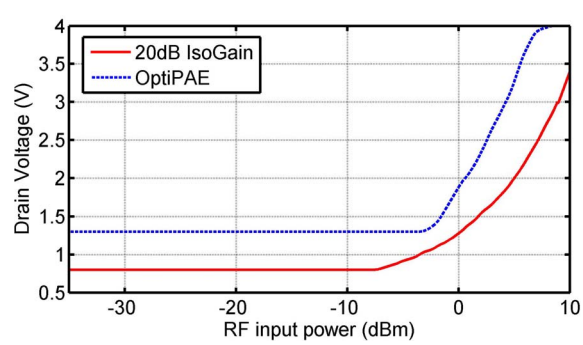

Fig. 5. Comparison between the 20 dB IsoGain (red) and the OptiPAE (blue) extracted shaping tables.

acquisition channels of the VST instrument. The set-up operability has been shown by extracting two shaping tables and performing linearity and efficiency measurements for a given PA-PM system, using both WCDMA and LTE signals.

REFERENCES

[1] B. Kim, K. Jangheon, K. Ildu, and C. Jeonghyeon, "The Doherty Power Amplifier," *IEEE Microw.Mag.*,vol.7, no.5, pp.42-50, Oct. 2006.

[2] F. H. Raab, "Efficiency of outphasing power-amplifier systems," *IEEE Trans. Commun.*, vol. 33, no. pp. 1094-1099, Oct. 1985.

[3] B. Kim, M. Junghwan, and K. Ildu, "Efficiently Amplified," *IEEE Microw.Mag.*, vol. 11, no. 5, pp. 87-100, 2010

[4] M. Hassan, K. Myoungbo, V. W. Leung, H. Chin, and J.J. Yan, "High Efficiency Envelope Tracking Power Amplifier with Very Low Quiescent Power for 20 MHz LTE," *Proc. of the IEEE RFICSymp.*, pp. 1-4, 2011.

[5] J. Staudinger *et al.*, "High efficiency CDMA RF power amplifier using dynamic envelope tracking technique," *IEEE MTT-S Int. Microw.Symp. Dig.*, vol. 2, pp. 873–876, 2000.

[6] Z. Wang, "Demystifying Envelope Tracking," *IEEE Microw.Mag.*, vol. 16, no. 3, pp. 106-129, Apr.2015.

[7] T. Aitto-oja *et al.*, "High Efficiency Envelope Tracking Supply Voltage Modulation for High Power Base Station Amplifier Applications,"*IEEE MTT-S Int.l Microw.Symp.Dig.*, pp. 668-671, May 2010.

[8] P. M. Lavrador, T. R. Cunha, P. M. Cabral, and J. C. Pedro, "The Linearity-Efficiency Compromise," *IEEE Microw.Mag.*, vol. 11, no. 5, pp. 44-58, Aug.2010.

[9] D. Schreurs, M. O'Droma, A. A. Goacher, and M. Gadringer, *RF Power Amplifier Behavioral Modeling*, Cambridge University Press, October 2008.

[10] J. Verspecht, D. Root, and T. Nielsen, "Digital predistortion method based on dynamic X-parameters*", Proc.of the 82nd ARFTG Microwave Measurement Conference*, 2014.

[11] G.P. Gibiino, G. Avolio, D. Schreurs, A. Santarelli, and F. Filicori, "Mixer-like modeling with dynamic baseband characterization for supply-modulated PAs," *Proc. of the European Microwave Integrated Circuit Conference (EuMC)*, pp. 369-372, Oct.2014.

[12] G. Avolio, G. Paillonc y, D. Schreurs, M. Vanden Bossche, and B. Nauwelaers, "On-Wafer LSNA measurements including dynamic-bias", *Proc. of the European Microwave Conference (EuMC)*, pp. 930-933, Oct.2009.

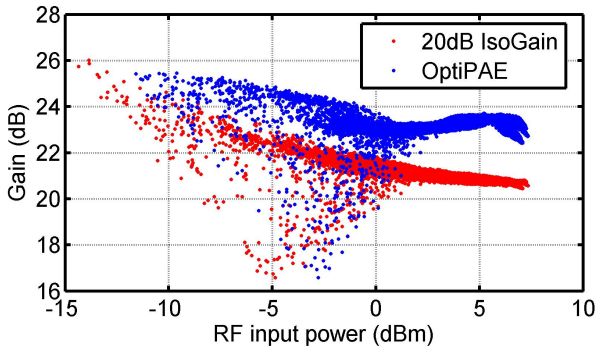

(a)

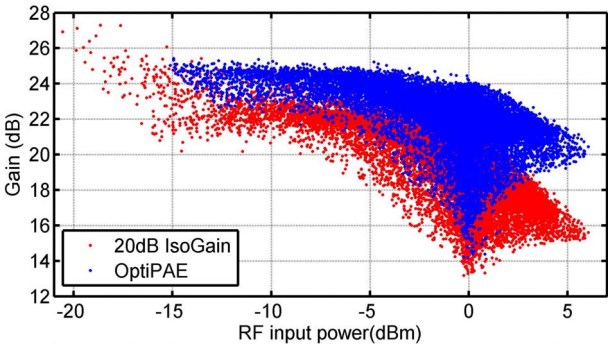

(b)

Fig. 6. Measured instantaneous gain comparison using the 20-dB IsoGain (red) and the OptiPAE (blue) shaping tables. (a) WCDMA, 5 MHz; (b) LTE, 20 MHz.

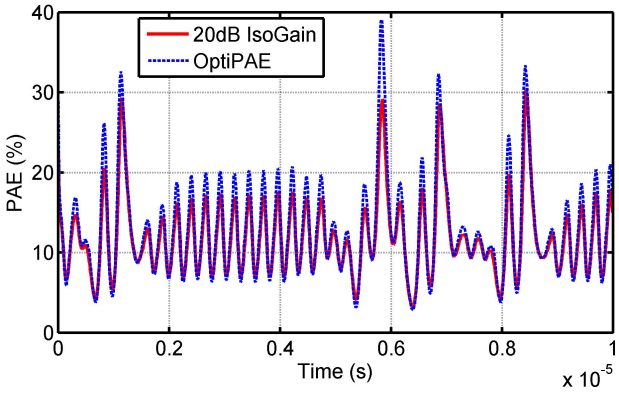

(a)

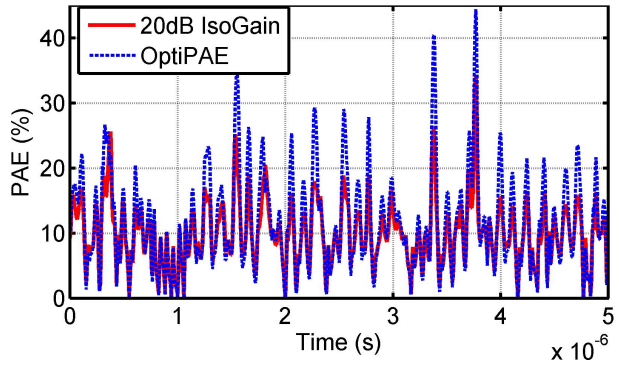

(b)

Fig. 7. Measured instantaneous PAE comparison using the 20-dB IsoGain (red) and the OptiPAE (dashed blue) shaping tables. (a) WCDMA, 5 MHz - IsoGain average PAE: 12%, OptiPAE average PAE: 12.9%; (b) LTE, 20 MHz - IsoGain average PAE: 10%, OptiPAE average PAE: 11.4%.

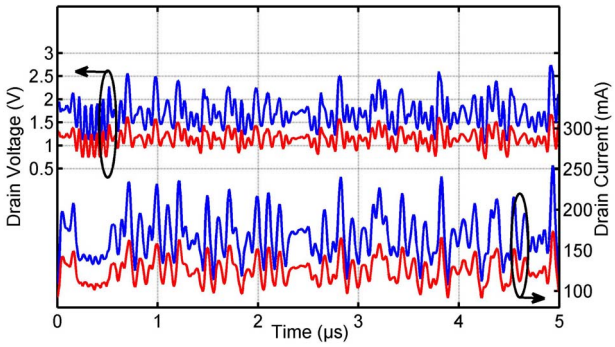

Fig. 8. Voltages (top) and currents (bottom) measured at the PA supply node. Comparison between the 20 dB IsoGain (red) and the OptiPAE (blue) shaping tables using the same LTE 20 MHz test signal.

Continuing Challenge of Improving Measurement Accuracy in Terahertz Vector Network Analyzers (INVITED) - The Taming of "Terahertz Vector Network Analyzers "-

Masahiro Horibe

Research Institute of Physical Measurements, National Metrology Institute of Japan, National Institute of Advanced Industrial Science and Technology

***Abstract* — Metrological traceability is required for testing and spurious emission management. Even if above 110 GHz frequency, metrological traceability is universally important, however the system set-up and calibration method are as important as the metrology standards due to high cost and low stability / reproducibility for the measurement system and standards as compared to those in the microwave frequency range. In recent years, operation frequency of commercial vector network analyzers (VNA) reaches currently up to 1.6 THz.**

Key priorities for improvement of VNA measurement accuracy are waveguide interface performance, operation conditions, hardware set-up, calibration standards and methods. Then, measurement traceability and uncertainty, further verification process, including measurement comparison, are absolutely necessary for quality of measurements.

The presentation introduces all key priority together with latest research achievements, then gives recommendation for accurate VNA measurement in Terahertz.

***Index Terms* — Ceramics, coaxial resonators, delay filters, delay-lines, power amplifiers.**

I. Introduction

In recent years higher frequency signals have been used not only in radio astronomy but also in such industrial applications as telecommunications. There the use of millimeter-wave electronic applications and instruments has accelerated in recent years, and commercial vector network analyzers are now operating up to 1.6 THz [1].

Therefore the national metrology institutes (NMIs) are making effort to develop an S-parameter national measurement system and standards due to establishing the precise measurement at frequencies above 110 GHz. The connection repeatability of waveguide flanges and stability of measurement system, etc. are serious issues in the accurate measurement at the millimeter wave and terahertz frequencies.

Details of priorities for improvement of VNA measurement accuracy are as follows;

1) Waveguide Flange: Connection repeatability,
2) Operation conditions: Connection clump (tool), Connection torque, Air floating connection plat form,
3) Hardware set-up: System noise, Cable effect on phase measurements, linearity evaluation,
4) Calibration standards and methods: Thru-Reflect-Line and offset shorts, Oversized and undersized waveguide aperture,
5) Metrological traceability
6) Uncertainty analysis
7) Verification and Measurement comparison

This paper discusses the issued mentioned above for improving measurement accuracy in vector network analyzer at Terahertz frequency. The issues are basically separated two categories of hardware and software. Regarding above issues, 1) to 3) are relating to hardware, others mention software, i.e. analysis. The paper presents the research achievements in typical case of a waveguide VNA measurements system at Terahertz frequency.

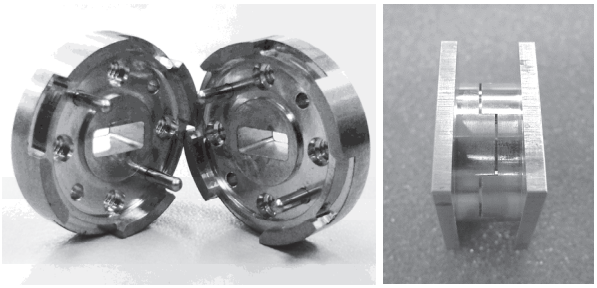

Fig. 1 (a) Claw flanges and (b) mated flanges

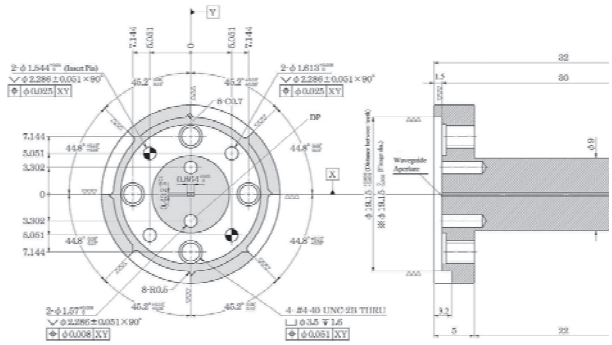

Fig. 2 Schematic view of claw flange

978-1-4673-9247-1/15/$31.00 ©2015 IEEE

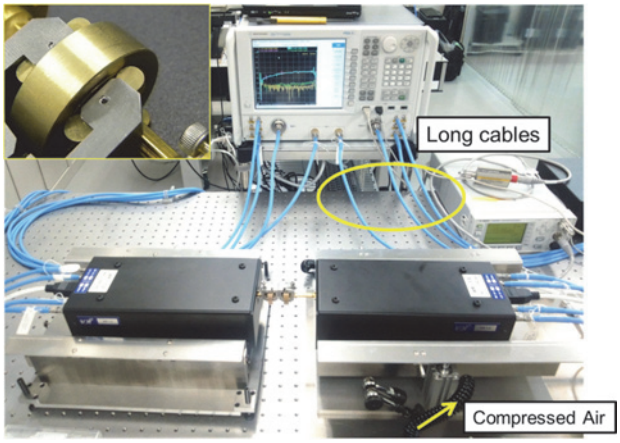

Fig. 3 Measurement system with connection platform

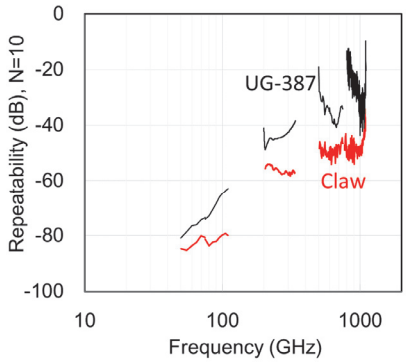

Fig. 4 Complex connection repeatability for S_{11} at interface

II. Waveguide Flange: Connection repeatability

Photographs of WM-250 waveguide with the newly designed claw flanges are shown in Fig. 1. The design of flange [2] has a precise machined flange outer diameter and claws inner diameter is established by claws themselves (Fig. 1). The 1.565 mm diameter pins and 1.570 mm holes, fitted to the precision UG-387 / IEEE P1785 [3] flanges design, are used to make angular alignment. The two holes can provide a precise alignment compared to the precision UG-387 and IEEE P1785 flanges. Precision claws achieve a precise alignment in the direction of height, width and rotational direction of aperture (Fig. 2).

It is available to perform the TRL calibration of VNA with claw waveguide flanges. The precision dowel holes can be used to provide angular alignment of the "Line" standard shim in TRL calibration. Claws are sufficiently centering the standard shim on the waveguide apertures. For the evaluation of the capability of connection repeatability, a set of waveguide sections with the claw waveguide flanges was designed in the

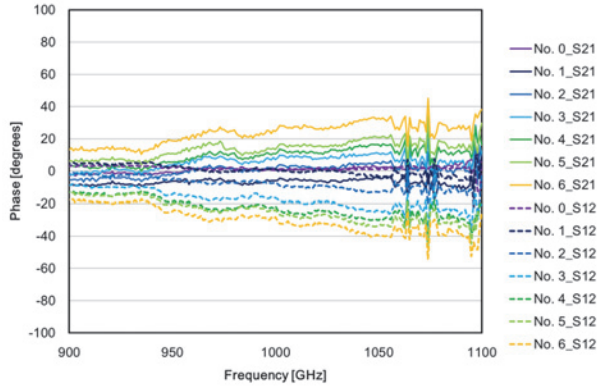

(a)

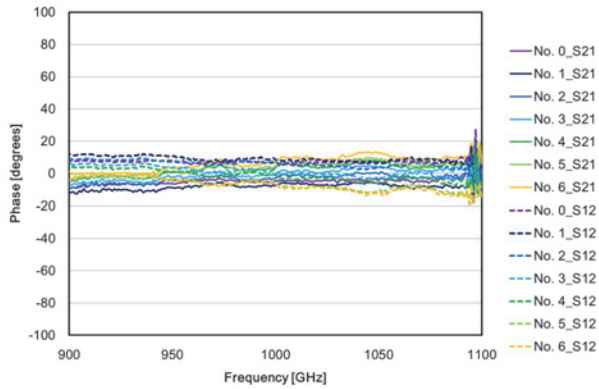

(b)

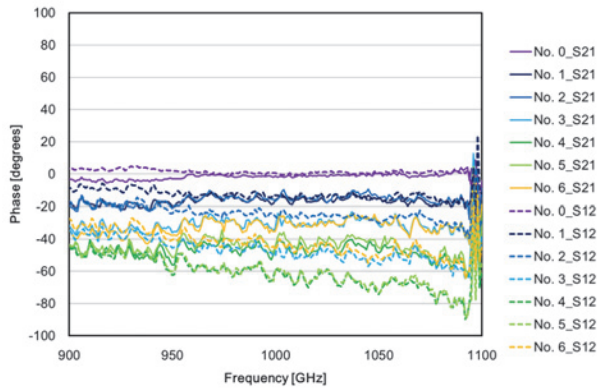

(c)

Fig. 5 Measurement results of phase characteristics of S_{12} and S_{12} for MW-250 waveguide thru connection (after measurement of applox. 25 mm-long line) (N=6). (a) Cable-A, (b) Cable-B and (b) Cable-C.

WM-250 and fabricated on a CNC milling machine for flange interfaces and an electroforming for a waveguide aperture section.

III. Operation Conditions

The S-parameter measurement was made by using a PNA Vector Network Analyzer from Keysight Technologies (former Agilent Technologies) and a WR-1.0 (WM-250) frequency extension modules from Virginia Diode Inc. (VDI), and Oleson Microwave WM-864 frequency extension modules. In this study, the VNA was first calibrated by TRL calibration for two port measurements before which repeated S-parameter measurements were performed. The system repeatability (system noise floor) was evaluated; the noise floor characteristics were much worse at both edges of the WM-250 band due to lower output power and lack of sensor dynamic range at both band edges. The clamps and air floating stage on the connection stage shown in Fig. 3 are used to connect verification devices quickly rather than the usual connection scheme of waveguides using four screws [4, 5]. Using the clamp, tightening one screw produces easily managed mating force on the flange plane. This way reduces measurement time and obtains a repeatable result in VNA measurements.

The complex repeatability of reflection coefficients representing mated interface characteristics of conventional flanges, fitted to UG-387, and claw flange were drawn in Fig. 4. Ten independent reconnection and disconnection cycles were made at position of the interface under test. The obtained complex reflection coefficient traces indicate a capability of the flange connection repeatability. The figure shows that the repeatability of claw flange is less than -45 dB in the WM-250 frequency band. However, the value of connection repeatability reaches -15 dB at 850 GHz for a conventional flange fitted to UG-387.

IV. Hardware Set-up

Due to investigation a cable flexure influences in VNA measurement, MW-250 waveguide straight line (L=25.4 mm) have been measured. 6 independent through/line cycle were made just after VNA calibration. Frequency extension module for port-1 side was fixed and module of port-2 was only moved for the line measurement. Movement distance was at least 50 mm. After measurement of straight line, port-2 module went back to initial position to make a direct through connection. After obtaining full two port scattering parameter, the phase characteristics of S_{21} and S_{12} of each measurement were calculated. Figure 5 shows results of phase difference between S_{21} and S_{12} for through connection measurements, respectively. In the results, deviation of six traces indicates the measurement repeatability from cable flexure influence [6].

Figure 5(a) shows the repeatability of through measurements can be estimated and distribution of phase is up to a maximum of 40 degrees in the six independent measurements. Over 900 GHz, phase value of S_{21} is approximately +20 degrees to +40 degrees, however, S_{12} phase is -20 degrees to -40 degrees. Entire frequency range and movement range, S_{12} phase change is definitely at the opposite end of the scale from S_{21} phase change.

Figure 5(b) shows the repeatability of long straight line measurements can be estimated and distribution of phase is from 10 degrees to 20 degrees in the six independent measurements. In addition, phase difference of S_{21} and S_{12} was 20 degrees variation in the six independent measurements. This means that movement of frequency extension module provides the both phase change and phase offset in the S_{21} and S_{12} measurement. S_{12} phase change is definitely at the opposite end of the scale from S_{21} phase change.

Figure 5(c) shows the repeatability of long straight line measurements can be estimated and distribution of phase is from 45 degrees to 90 degrees in the six independent measurements. In addition, phase difference of S_{21} and S_{12} was 20 degrees variation in the six independent measurements. This means that movement of frequency extension module provides the both phase change and phase offset in the S_{21} and S_{12} measurement. S_{12} phase change is definitely at the same end of the scale from S_{21} phase change.

Cable flexure influence in reflection phase measurement, S_{22}, was also investigated, however no change of phase measurement results of S_{ii} are observed when flush short termination was measured. This means the movement of frequency extension modules are providing cable flexure, and then making an impact on only transmission, S_{ij}, phase measurements.

Table 1 Deviation and its expanded uncertainty of waveguide aperture size of offset shorts from test-port (Unit: μm)

Offset length of offset short terminations	Small aperture				Standard aperture			
	a	*U*(*a*)	*b*	*U*(*b*)	*A*	*U*(*a*)	*b*	*U*(*b*)
365 mm	-12.3	1.7	-11.5	1.8	-3.7	2.3	-2.1	2.2
1000 mm	-12.0	1.8	-11.7	1.7	-4.1	2.3	-1.6	2.1
1291 mm	-11.9	1.8	-11.5	1.8	-3.1	2.4	-1.0	1.8

Frequency expansion in the modules are typically established by frequency multipliers and harmonic mixers and using RF and LO signals from VNA. In the case of WM-250 modules, submillimeter wave signal are generated by multiplying RF and LO signals, then IF signals are obtained by harmonic mixing using multiplied LO signals. At first, characteristics of all component, mixers and LO cables, etc., in the VNA system can be corrected by a calibration. Thus, measured value of phase is zero with no frequency dependence for S_{21} and S_{12} of direct thru connection just after calibration. If the modules are moved, it is experience changes in flexure conditions of LO cable depending on moving module to different position after calibration. This thus produces the change of phase of LO signals in the cables. Then phase change at submillimeter wave frequency is magnified by multiplying signal in the module.

V. Calibration Standards and Methods

A. Thru-Reflect-Line calibration Major Subsections

Waveguide transmission lines known as thru-reflect-line (TRL) 'Line' standards are usually used as S-parameter measurement standards in VNA applications. In the sub-millimeter wave frequency band the connection repeatability of waveguide flanges becomes a serious issue for accurate measurement and calibration. Waveguide "Line" standards were developed to fit the new flange design and as above, the apertures of the "Line" standards were accurately centered by the use of a coupling ring. The "Line" standard fitted in this way made possible accurate TRL calibrations and accurate VNA measurements in the sub-millimeter wave frequency band. The length of the "Line" standard was chosen so that it typically provides a 90 degree phase change with respect to the through connection at the waveguide mid-band frequency (925 GHz in WM-250 band) [7]. However, quarter wave length around 1.0 THz is very thin, i.e. approximately 100 μm. It is user's concern about stability and robustness for electrical properties of TRL lines standards.

In the use of different concept of TRL calibration scheme, two line standards in the "3λ/4" TRL scheme are chosen to give phase changes between 180 degrees and 360 degrees. In particular case, a longer line is used for the lower frequency band of the waveguide band and a shorter line covers at the higher frequency band. Both two line standards can be longer than the quarter-wave length line used with conventional TRL scheme. This means that the lines are more robust mechanically than the λ/4 length line. Thus, Connection repeatability of S_{ij} of line standard is much better for thick lines compared to λ/4 length line. It is recommended that improvements to the mechanical measurement technique and machining process, and then use of thick TRL line standards will make larger contribution to the improving VNA measurements uncertainty at terahertz frequency bands.

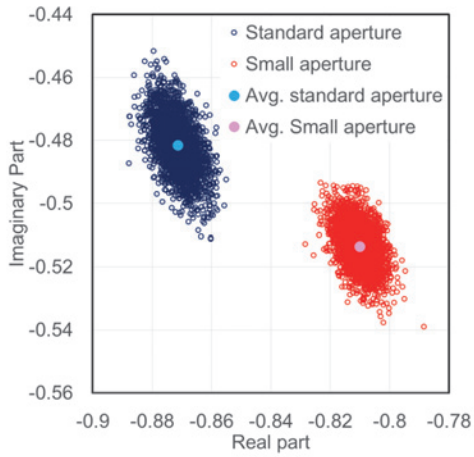

Fig. 6 Monte Carlo calculation results of reflection coefficients at 330 GHz for offset short terminations with 1.291 mm offset length. Blue open square indicates reflection coefficients of offset short with standard aperture waveguide. Red open circular indicates reflection coefficients of offset short with small aperture.

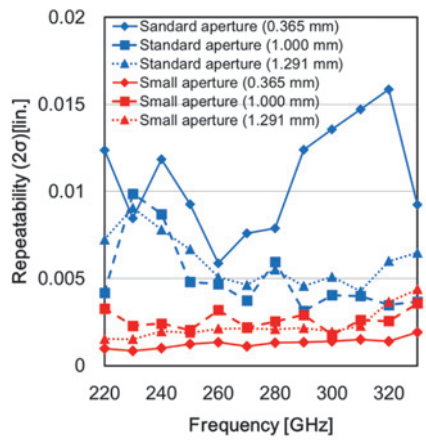

Fig. 7 Results of experimental standard deviation, 2□, (i.e. repeatability) for a series of 10 repeat reconnection/disconnection measurements for offset short terminations with three different length in the WM-864 waveguide frequency band. Blue symbols indicate results of offset short terminations with standard aperture size, and red symbols means results of offset short terminations with small aperture size.

B. Offset Short Calibration Major Subsections

Alternative solution for accurate calibration is use of offset short terminations were formed by combination of waveguide standard line and flush short termination. Three different length lines were used for forming the three different offset short

terminations. Then, standard aperture fitted with WM-864 and oversized/undersized aperture fitted with waveguide for test-port were prepared as the offset lines. Table 1 shows the dimensional difference between the both waveguide apertures of test-port and standard lines. Lines with standard aperture have almost the same aperture size of test-port. However, lines have undersized aperture size of test-port.

The reflection characteristics of offset short were estimated from the dimensional measurements: width, height, corner radii and line length of the WM-864 rectangular waveguide when connected to test-port waveguide which aperture size measured above. The reflection characteristics and their associated uncertainties were estimated from a series expansion of the field in eigenmodes by a Monte Carlo simulation involving 100,000 trials. Figure 6 shows real and imaginary plot of reflection characteristics for offset short with offset length of 1.291 mm and two different aperture size together with their mean values at 330 GHz. In the figure the calculated results of reflection coefficient are different each other due to the different reflection characteristics cause from aperture size difference. The expanded uncertainty of reflection characteristics of all offset short terminations are plotted in Fig. 3.The offset short terminations with standard aperture have larger than those with small aperture. This is because the dimensional measurement uncertainties, U(a) and U(b), of offset short with standard aperture are greater than those with small aperture in the dimensional measurements. The expanded uncertainty of the offset short terminations ranges from 0.005 to 0.017.

The dominant effect of VNA measurement accuracy at the sub-millimeter wave frequency was usually the connection repeatability of reflection characteristics at the connection interface. The repeatability of connections was evaluated using a PNA Vector Network Analyzer from Agilent Technologies and a WR-3 (WM-864) frequency extension module from Oleson Microwave Laboratory Co. (OML). All results in this paper were obtained with an IF bandwidth of 100 Hz and a point averaging factor of 16. For these evaluations the VNA was first calibrated by TRL calibration for two port measurements before which repeated reflection characteristic measurements were performed.

Ten independent disconnect and reconnect cycles were made at the interface of offset short terminations with 0.365 mm, 1.000 mm and 1.291 mm of offset length. For comparison the evaluations were made using flush short and waveguide lines with two different size of apertures. The standard deviation of each set of reflection coefficients, represents the connection repeatability performance at the test port flange interface. Repeatability test results are shown in figure 7. For a series of n repeat disconnect/reconnect measurements of S_{11}, the experimental standard deviation of the mean was given by

$$s(\overline{S_{11}}) = \frac{s(S_{11k})}{\sqrt{n}} \tag{1}$$

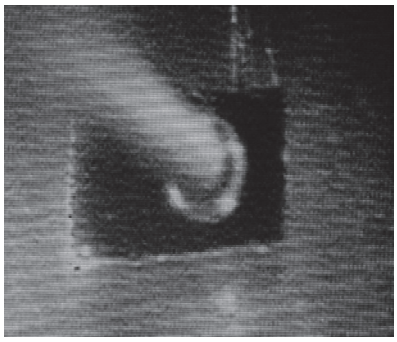

(a)

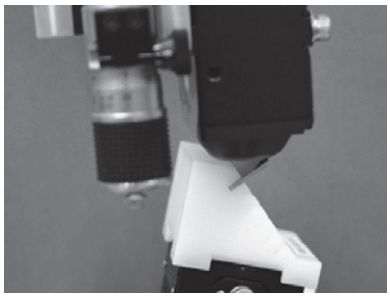

(b)

Fig. 8 Dimensional measurement systems (a) 3-dimensional coordinated measuring machine (3DCMM), (b) Laser displacement meter system (LDMS)

where

$$s(S_{11k}) = \sqrt{\frac{1}{(n-1)}\sum_{k=1}^{n}\left|S_{11k} - \overline{S_{11}}\right|^2} \tag{2}$$

$$\overline{S_{11}} = \overline{S_{11\mathrm{Re}}} + j.\overline{S_{11\mathrm{Im}}} = \frac{1}{n}\left(\sum_{k=1}^{n} S_{11\mathrm{Re}_k} + j\sum_{k=1}^{n} S_{11\mathrm{Im}_k}\right) \tag{3}$$

where S_{11}Re and S_{11}Im are the real and imaginary parts of S_{11}, respectively.

The capability of connection repeatability for the reflection measurement was evaluated by measurements. The repeatability results shown in figure 7 indicate that the new concept design of standard terminations provides the better capability of connection repeatability compared to use of standard size aperture in the offset short terminations. Here, the value of repeatability is less than 0.005 for short terminations with small apertures. As a result of this, the terminations with small size aperture provide better connection repeatability than that with standard size aperture [8].

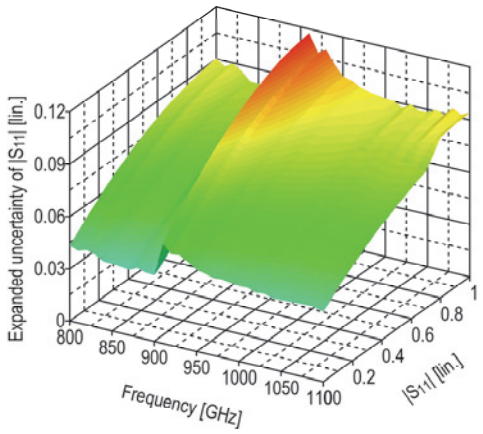

(a)

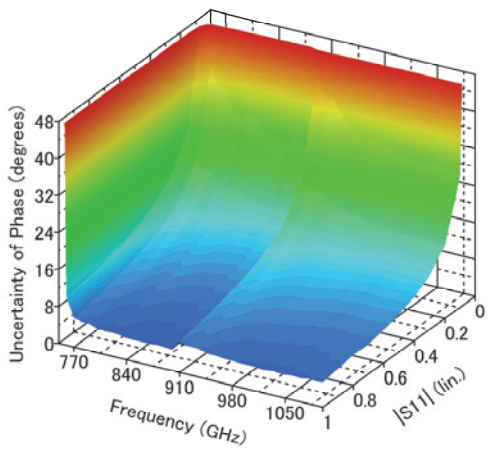

(b)

Fig. 9 example results of VNA measurement uncertainty analysis

VI. Metrological Traceability

Traceability to international standards (SI) was established via mechanical dimensional measurements of a standard quarter wavelength "Line." For aperture dimensional measurements, Keyence LT9010M laser displacement meter (LDMS) was used with a specialized stage to adjust the incident angle of the laser beam (Fig. 8) at standard conditions (23 ºC) of the electrical calibration laboratory. The laser beam entered the "Line" aperture at approximately 45 degrees. The aperture wall surface was scanned by moving the sample stage. Dimensional measurements were traced back to the SI base unit of length via reference gauge blocks with temperature corrections from 20 ºC to 23 ºC using the linear thermal expansion coefficient of steel. The resulting 3-dimensional data array included aperture dimensions, corner radii, center position of aperture and center position as determined by outer circumference of flange.

The systematic uncertainty (k = 2) of our dimensional measurements was approximately 0.75 µm including the uncertainty value of the gauge block. The uncertainty of reproducibility for aperture dimensions was 0.65 µm (k = 2). The resulting expanded uncertainty (k=2) contribution from the measurement system was approximately 2.0 µm for the small aperture waveguide. The dimensional variations of the individual aperture width and height values were added to the overall expanded measurement uncertainty. Measurements of width dimensions were made at varying positions along the height and depth. The expanded uncertainty of aperture measurements of Line is 11.3 µm for width dimension, and 16.5 µm for height dimension.

The differences between the aperture center and flange center were obtained [9]. The aperture displacement of H-plane and E-plane directions were calculated by the differences of the center positions between aperture and flange. In VNA measurements the center offsets of both test ports and "Line" provide H-plane and E-plane displacements at the waveguide interfaces. Such displacements at a mated interface produce reflections that diminish VNA measurement accuracy. H-plane displacement between Port-1 and Port-2 is 4.9 µm. The resulting E-plane displacement is 4.7 µm when direct thru connection.

VII. VNA Measurement Uncertainty

A VNA measurement uncertainty can be estimated from dimensional measurement uncertainties via the S-parameter calculation for the "Line" standard [4, 9, 10]. Connection repeatability and, to some extent, reflection characteristics at the interfaces for the "Through" connection can contribute to increased measurement uncertainty [4, 9, 10].

The uncertainty was determined by reflection characteristics of line standard and interface for both "Line" and "Thru" connections in the TRL calibration scheme. A major source of uncertainty of the S_{11} measurement was the uncertainty (0.068) of S_{11} of Line. Uncertainty of S_{21} was determined by almost S_{21} repeatability of the "Thru" connection. S_{21} values of the "Line" characteristic do not affect measurement uncertainty in the self-calibration scheme.

Other uncertainty contributions were linearity, approximately 0.01dB/dB, and noise floor, approximately 60 dB, in the frequency range from 800 GHz to 1.05 THz.

The 3D plots in Fig. 9 show the dependence of expanded uncertainty of S_{11} on the operating frequency and the characteristics of the device under test for VNA measurement calibrated by TRL calibration scheme with double standard lines.

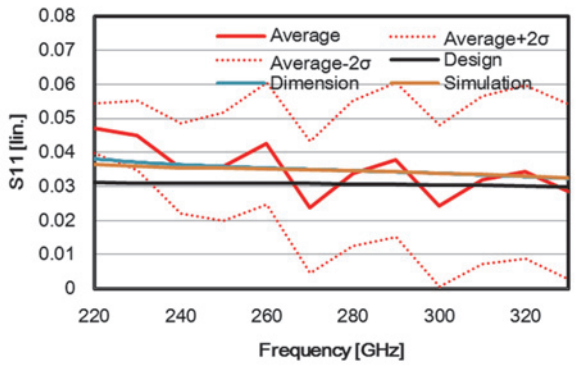

(a)

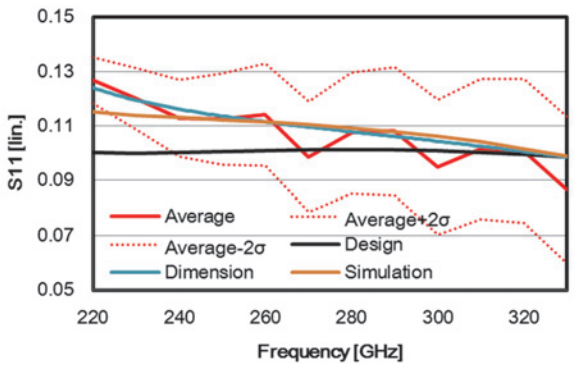

(b)

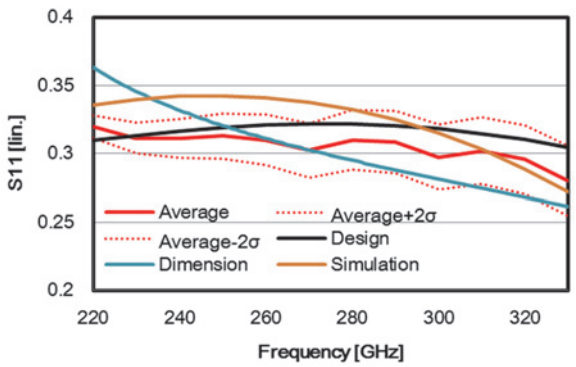

(c)

Fig. 10 Results of VNA measurement and mechanically-derived analysis for return loss of (a) -10dB, (b) -20 dB, and (c) -30 dB in the WM864 waveguide frequency band.

VIII. Verification and Measurement Comparison

Two-port mismatch lines as verification devices was designed to fit the claw waveguide flanges, WM-864, and fabricated on a CNC milling machine for flange interfaces. Before estimations and measurements of device characteristics, aperture dimensions were measured by dimensional measurement system used for TRL line standard [9, 10] and following S-parameters and their associated uncertainties were estimated from a series expansion of the field in eigenmodes [11] by a Monte Carlo simulation involving 100,000 trials.

The 10 disconnection/reconnection was made the measurement of four verification devices. Real and imaginary values of reflection characteristics, derived from measured and calculated S_{11}, for three mismatch lines with their associated uncertainties are shown in Fig. 10 together with designed characteristics.

To verify the both VNA measurement and verification device characteristics, we compared two different values from VNA measurement and dimensionally-derived calculation results of return loss. We estimated the both values, Δ, and equivalency $U(\Delta)$, i.e. uncertainty of difference, Δ, in the comparison of return loss measurement results. The differences Δ between both values of return loss were almost less than equivalency $U(\Delta)$for all verification device, however, Δ is larger than equivalency $U(\Delta)$ at some of measured frequency points. Δ and $U(\Delta)$ are expressed as follows

$$\Delta = |S_{11\_meas} - S_{11\_mech}| \,, \tag{6}$$

$$U(\Delta) = k\sqrt{u^2{}_{(S_{11\_meas})} + u^2{}_{(S_{11\_mech})}} \tag{7}$$

where S_{11_meas} and S_{11_mech} are the values obtained from VNA measurements and dimensional characterization, respectively, and $u_{(}S_{11\_meas)}$ and $u_{(}S_{11\_mech)}$ are the standard uncertainties in these S_{11} values.

In the case of RL measurements at low to medium RL, i.e. -10 dB (0.03) and -20 dB (0.10), dimensional values and measured value obtained from VNA were agree with each other. However, at the high RL, -30 dB (0.33), dimensional characterization was equivalent to VNA measurement results at lower frequency edge. This is because the dimensional characterization process do not take into account aperture offset and misalignment effects. Thus, for a high reflective device having narrow aperture, reflection characteristics at interface might be sensitive to misalignment.

IX. Recommendations

Waveguide VNA with external frequency extension modules can operate up to 1.6 THz frequency. However, researchers and engineers are making effort to ensure a precision S-parameter measurement system including both hardware and measurement techniques above 110 GHz. This paper

recommends to improve measurement accuracy (uncertainty and stability, etc.) in VNA at Terahertz frequency. The use of precision flange providing excellent connection repeatability at interface and user friendly measurement tools, i.e. clamps and connection support platform, producing stability of measurement system for the establishment of accurate measurement hardware system at the millimeter wave and terahertz frequencies. Then, choosing suitable calibration standard and method, and following verification process is also key for accurate VNA measurement. Finally, traceability and uncertainty analysis archives a high quality calibration and measurement system.

X. Conclusion

This paper proposes flange, calibration standards, verification standards, user friendly waveguide connection clump, VNA measurement hardware system with cabling effects, and calibration with metrological traceability. These study archives improvement for accuracy of waveguide VNA measurements above 110 GHz.

Acknowledgement

The work described in this paper was supported by the Industrial Technology Research Grant Program in 2009 from NEDO of Japan. The authors are grateful to Mr. Nick Ridler, NPL, for calculation of waveguide "Line" design, Mr. K. Noda, Oshima Prototype Manufacturing Co., for fabricating flanges, Dr. Atsushi Sanada, Yamaguchi University, for supporting VNA measurements in the terahertz frequency band and Dr. Jeffry Heslaer, Virginia Diode Inc., for valuable discussion for VNA measurements in the terahertz frequency band. The part of work described in this paper was supported by Junkosha Inc. as a provider of coaxial cables, used for RF and LO cables to connect to the frequency extension modules.

References

[1] Jeffery Hesler, et. al., "Development of THz Test & Measurement Instrumentation to 1.6 THz," FTT2015, Hamamatsu, Japan, 2015.

[2] "Flanges for waveguides. Part 2: Relevant specifications for flanges for ordinary rectangular waveguides", IEC 60154-2 ed. 3rd will be published.

[3] "IEEE Standard for Rectangular Metallic Waveguides and Their Interfaces for Frequencies of 110 GHz and Above," IEEE P1785, http://grouper.ieee.org/groups/1785.

[4] M. Horibe, and R. Kishikawa, "Performance of New Design of Waveguide Flange for Measurements at Frequencies from 800 GHz to 1.05 THz," *81th ARFTG Conference Digest*, pp. 1-6, June. 2013.

[5] M. Horibe K. Shimaoka, K. Fujii, A. Widarta, H. Iida, and R. Kishikawa, "Standards Research in Japan: Latest Development of Millimeter-Wave and Submillimeter-Wave Measurements", *IEEE Microwave Magazine,* Vol 14, No 7, pp 59-66, November/December 2013.

[6] M. Horibe, R. Kishikawa, Y. Kato and Y. Tsukahara, "Consideration of Error Model with Cable Flexure Influences on Waveguide Vector Network Analyzers at submillimeter-wave frequency," *85th ARFTG Conference Digest*, pp. 1-8, June. 2015.

[7] N M Ridler, "Choosing line lengths for calibrating waveguide vector network analysers at millimeter and sub-millimetre wavelengths", NPL Report TQE 5, National Physical Laboratory, UK, March 2009.

[8] M. Horibe, and R. Kishikawa, "Measurement Uncertainty in Waveguide VNA calibrated by Offset Short Calibration with Oversized Waveguide Aperture at Sub-millimeter Wave Frequency," *84th ARFTG Conference Digest*, pp. 1-4, Dec. 2014.

[9] M Horibe, R Kishikawa and M Shida, "Complete characterization of rectangular waveguide measurement standards for vector network analyzer in the range of millimeter and sub-millimeter wave frequencies", *76th ARFTG Microwave Measurement Conference digest*s, pp 1-15, , 2-3 December 2010.

[10] M. Horibe and R. Kishikawa, "Metrological Traceability in Waveguide S-parameter Measurements at 1.0 THz Band," IEEE Trans. Instrum. Meas., vol. 62, no. 6, pp. 1814 – 1820, June 2013.

[11] K. C. Gupta, "Microstrip Lines and Slottlines", Dedham: Artech House Inc. 1979.

Performance assessment of VNA calibration schemes for millimeter-wave and submillimeter-wave frequencies, using the 33 GHz – 50 GHz band

Karel Dražil, Adam Pavliš, Martin Hudlička

Czech Metrology Institute, Dept. of Primary Metrology of RF Electrical Quantities, Prague, Czech Republic, E-mail: kdrazil@cmi.cz

***Abstract* — In this article vector network analyzer (VNA) calibration schemes suitable for traceable scattering parameter measurements in rectangular waveguides at millimeter-wave and submillimeter-wave frequencies are compared with well-established techniques being used at lower frequencies. Comparison measurements were performed in the frequency band 33 GHz – 50 GHz.**

***Index Terms* — Vector network analyzer, Calibration method, millimeter wave.**

I. Introduction

The aim of this work is to compare the conventional VNA calibration schemes used at lower frequency bands with ones recently proposed for millimeter-wave and submillimeter-wave frequencies by measurements in the band 33 – 50 GHz. In contrast to conventional calibrations, using of three-quarter-wavelength or longer calibration lines at millimeter-wave and submillimeter-wave bands is preferable because of better mechanical robustness of the lines and better connection repeatability [1, 2, 3]. One of the most serious factors causing degradation of calibration accuracy at high frequencies is flange misalignment. This problem can be minimized by using calibration standards which do not suffer from these errors such as radiating waveguides and flush shorts [1, 4]. Therefore, apart from traditional calibration standards, longer air lines and radiating open-ended waveguides were used as calibration standards. Several one-port and two-port devices were measured using different calibration techniques and the results were compared.

II. MEASUREMENT SETUP

A VNA type Agilent PNA series E8364B with 2.4 mm flexible test port cables and 2.4 mm to waveguide adapters with Maury Microwave Precision WR22 Flange (MPF22) was used with a Maury Microwave calibration kit model J7007H, including a precision 2.4 mm shim. The calibration kit includes further two precision waveguide loads and one flush short. Two precision shims of the nominal length of 2 mm and 4.4 mm were at disposal.

A. Devices under test

For the comparison the following devices were used:

- 8.8 mm offset short
- matched waveguide load
- 6.8 mm airline
- direct connection of waveguide test ports (methods not using Thru as fully known calibration standard)
- 20 dB attenuator
- mismatched load (realized by 2.4 mm attenuator with 2.4 mm to WR22 adapter)

B. Calibration methods

A set of following calibrations were performed:

- **TRL** (this calibration was chosen to serve as a reference)
  - Thru – direct connection of the flanges MPF22, defines the reference plane
  - Reflect – flush short from the calibration kit
  - Line – precision λ/4 shim, length 2.4 mm
- **SSLL**
  - Short – flush short
  - offset Short – 2.4 mm shim + flush short
  - precision waveguide Load
  - offset Load – 2.4 mm shim + the above load

Following calibrations use schemes suitable for mm-wave and sub mm-wave frequencies:

- **TRL2** (calibration using two roughly ¾-λ lines, as only one line cannot cover the whole frequency band)
  - Thru and Reflect – identical to TRL
  - Line – two lines of the length roughly ¾-λ, i.e., 2 mm + 4.4 mm shims and 2 mm + 2.4 mm + 4.4 mm shims, respectively
- **LRL**
  - 1st Line –2 mm + 4.4 mm shims
  - Reflect – see TRL
  - 2nd Line – 2 mm + 2.4 mm + 4.4 mm shims
- **SSM** (optionally **SSMT** for 2 ports)
  - Short and offset Short – see SSLL
  - Matched standard – radiating open, i.e. open flange MPF22 of the adapter 2.4 mm to WR22
  - Thru – see TRL
- **TRM**
  - Thru and Reflect – see TRL
  - Matched standard – see SSM
- **SSMU** (this type of calibration was tested because the Unknown thru method was expected to be able to

978-1-4673-9247-1/15/$31.00 ©2015 IEEE

remove the errors associated with misalignment of the flanges of the Thru standard)

- Short and offset Short – see SSLL
- Matched standard – see SSM
- Unknown thru – direct connection of the flanges MPF22

For VNA calibrations and corrections of measurements we used standard firmware procedures excluding the TRM method and SSMU (Unknown thru) method.

III. Open-ended waveguide reflection standard

Some of the calibration schemes proposed for mm-wave and sub-mm wave frequency bands use an open-ended waveguide as an impedance standard. Sufficient accuracy of the standard characterization is very important. As mentioned above, two 2.4 mm to waveguide WR22 adapters (model J236A3) with Maury Microwave Precision WR22 Flange (MPF22) were used as radiating open standards. At first we considered to use infinite flange model calculated by [5] for characterization of the standard but we found out by measurement that this approximation is not adequate for the real flange. Second way we used is based on more detailed simulation of the open waveguide with the flange and the third way consists in measurement using the VNA. Reflection coefficient magnitude measurement and simulation results for several MPF22 flange configurations can be seen in Fig. 1. Details of the flange model are depicted in Fig. 2. Nominal dimensions presented in [6] were used for the simulation. Characterization of the flange was performed using full-wave electromagnetic field simulator using FDTD method, measurements were performed utilizing the TRL calibration with flanges aimed against 10 cm long foam pyramidal absorbers. As the magnitude representation does not yield full information about the accuracy of characterizing of the open-ended waveguide standards, deviations of measured and simulated (complex valued) reflection coefficient values are plotted in Fig. 3.

Open flanges with two pins, i.e. normal configuration, were chosen to be used as calibration standard for measurements described in this paper. Other configurations were used only for evaluation of the accuracy of the simulation. Difference of measured reflection coefficient of the flange with two pins and data modelled for infinite flange is also shown in Fig. 3. This characterization of the standard was optionally used for one of the tested calibration schemes.

Further, repeatability of the reflection coefficient of the open waveguide standards was investigated. Standard deviation in the order of 0.003 was observed for repeated measurements and calibrations. Changes in order of 0.001 or smaller were observed when the absorber placed in front of the waveguide flange was removed and the waveguide was left to radiate just into the laboratory. Differences in (complex valued) reflection coefficient between two MPF22 flanges were found to be not greater than 0.005.

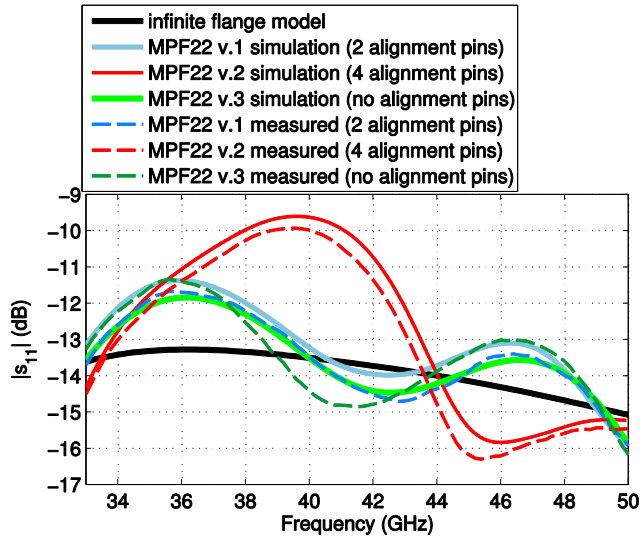

Fig. 1. Comparison of reflection coefficient measurements and simulations of the radiating open waveguide.

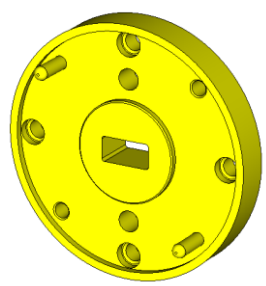

Fig. 2. MPF22 flange model version 1 with two alignment pins, this configuration was used for reported VNA calibrations.

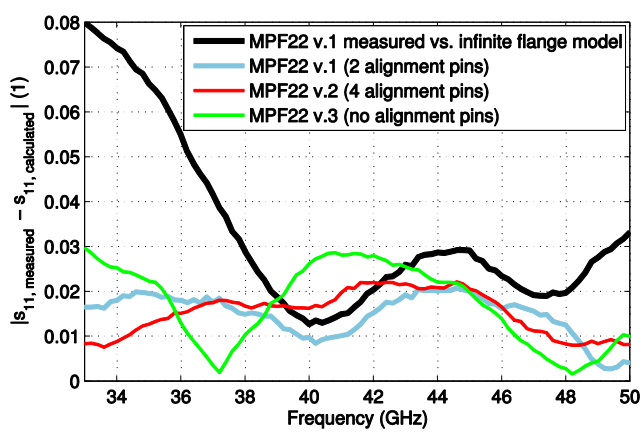

Fig. 3. Deviations of the measured and simulated reflection coefficient values for the radiating Maury Microwave Precision WR22 Flange (MPF22).

Finally, it can be concluded that the agreement between electromagnetic simulation (flange with nominal dimensions)

and measurement can be considered as quite good, yet not sufficient for accurate characterization of the measurement standard. For the above described simulations the mesh of approximately 17 points per (the shortest used) wavelength was used but increasing of number of points did not improve the results. Also the sensitivity for some dimensional changes due to tolerances specified for the flange MPF22 was investigated but the changes in the reflection coefficient were insignificant.

However, the flange used with waveguides operating at millimeter-wave and submillimeter-wave frequencies [7] is usually the same despite the fact that the width and height dimensions of a WM-250 waveguide operating at 1000 GHz are ten times smaller than those of a WM-2540 waveguide operating at 100 GHz. Thus, for higher frequency bands better accuracy of the electromagnetic simulation can be expected because the "troublesome" structures (alignment holes, pins, threaded holes etc.) are electrically further from the waveguide aperture.

IV. Experimental results

Measurement results obtained using calibration schemes being of interest are presented in following graphs. Details of tested devices and calibration methods and standards used are described above. Results are presented in graphs either together with the results obtained by the reference method or as the difference/ratio of the tested and reference data. In the legend of the graphs the abbreviations referring to calibration methods/schemes are amended by indexes specifying definition of the calibration standards (only when it is relevant). The meaning of used indexes is as follows: *no index* – definition of the standard supplied by the manufacturer, *m* – standard characterized by measurement (usually using TRL method), *s* – standard characterized by simulation, *si* – standard (radiating waveguide) approximated by infinite open flange model. For example, meaning of the SS_mM_sU is as follows: two-port calibration using Short – offset Short – Matched load – Unknown thru calibration scheme with Short characterized by manufacturer's definition (as ideal), offset Short characterized by measurement and Matched load realized by open-ended waveguide characterized by electromagnetic simulation.

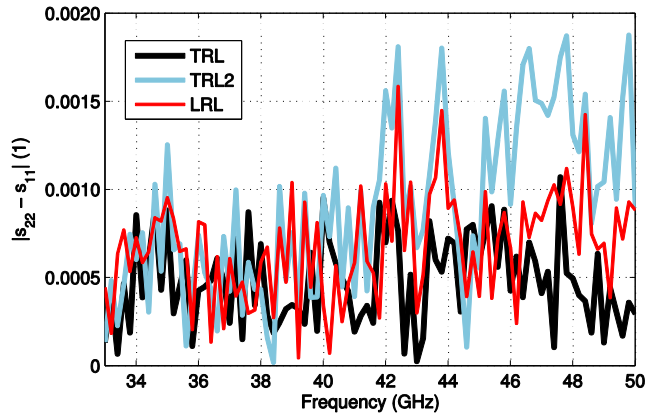

Fig. 4. Differences of reflection coefficient measurements of matched load at port 1 and port 2 for three calibration schemes

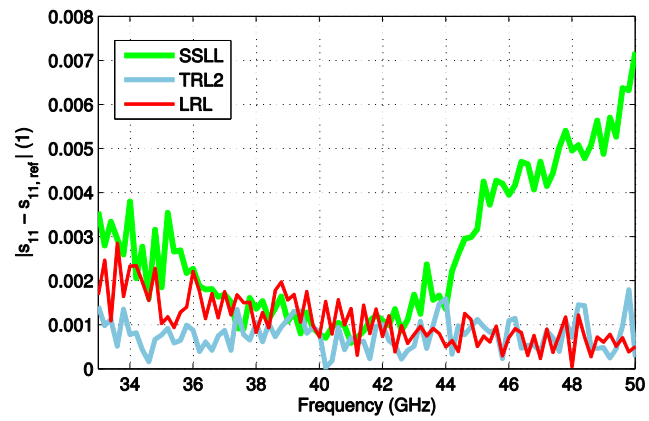

Fig. 5. Results of the measurement of the matched waveguide load reflection coefficient, differences of the measured and reference data (TRL) are plotted

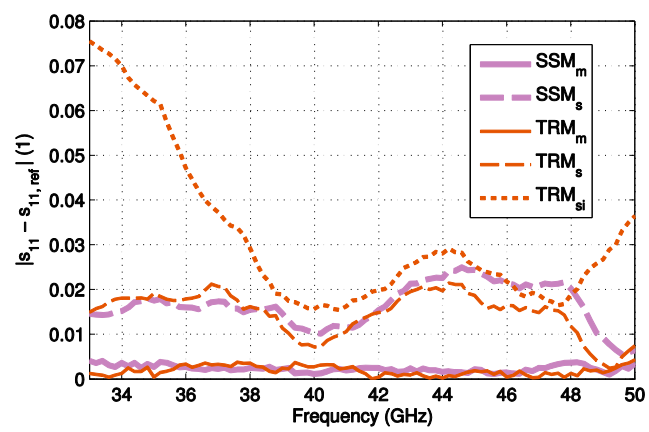

Fig. 6. Results of the measurement of the matched waveguide load reflection coefficient, differences of the measured and reference (TRL) data are plotted

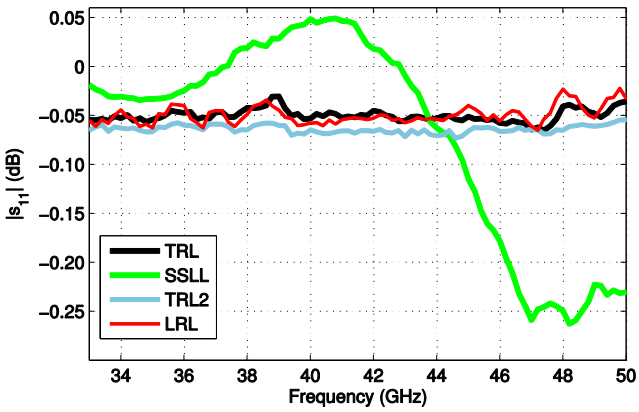

Fig. 7. Results of the measurement of the offset short reflection coefficient magnitude

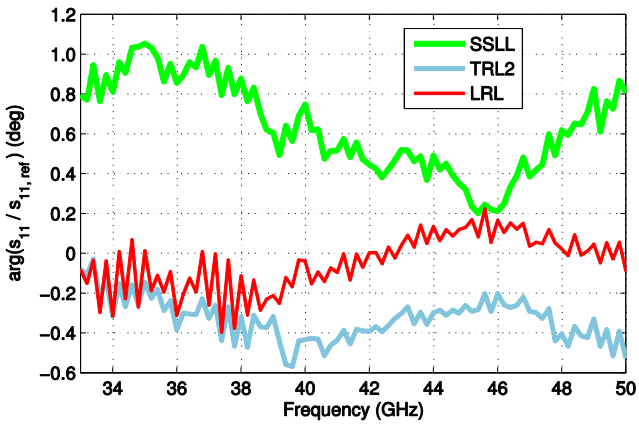

Fig. 8. Results of the measurement of the offset short reflection coefficient phase, differences of the measured and reference (TRL) data are plotted

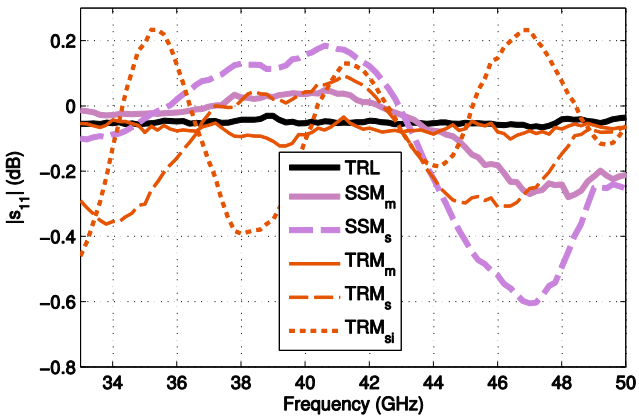

Fig. 9. Results of the measurement of the offset short reflection coefficient magnitude

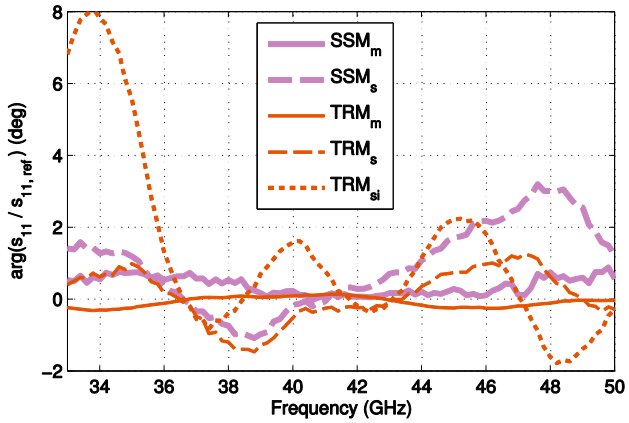

Fig. 10. Results of the measurement of the offset short reflection coefficient phase, differences of the measured and reference (TRL) data are plotted

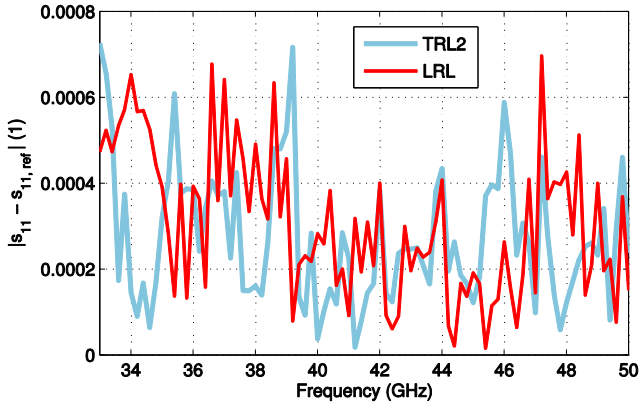

Fig. 11. Results of the measurement of the mismatched load reflection coefficient, differences of the measured and reference (TRL) data are plotted

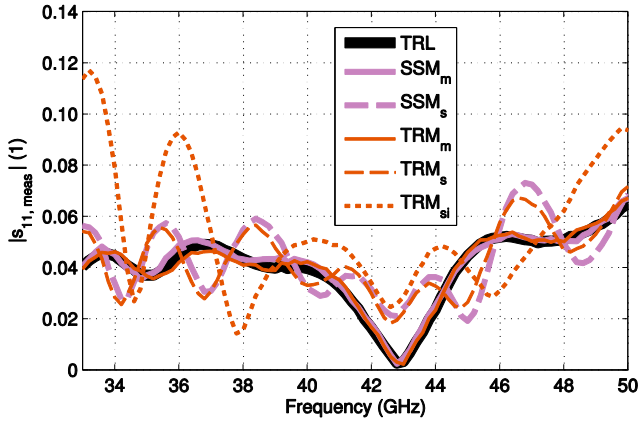

Fig. 12. Results of the measurement of the mismatched load reflection coefficient

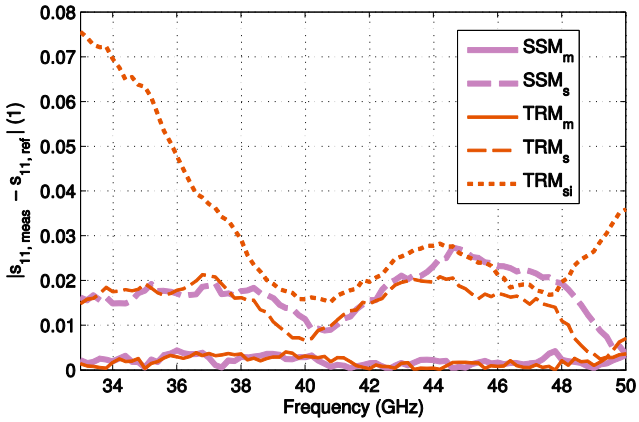

Fig. 13. Results of the measurement of the mismatched load reflection coefficient, differences of the measured and reference (TRL) data are plotted

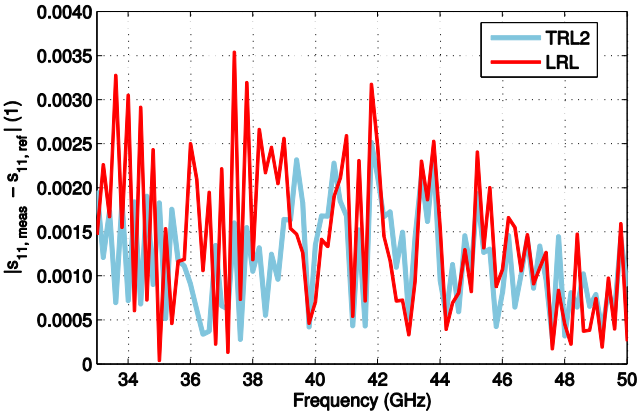

Fig. 14. Results of the measurement of the 6.8 mm air line reflection coefficient, differences of the measured and reference (TRL) data are plotted

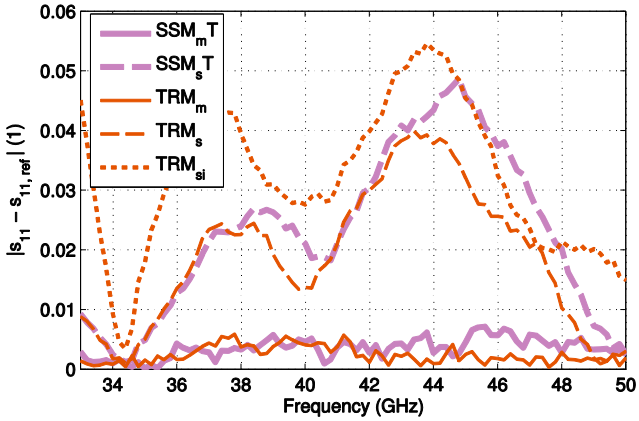

Fig. 15. Results of the measurement of the 6.8 mm airline reflection coefficient, differences of the measured and reference (TRL) data are plotted

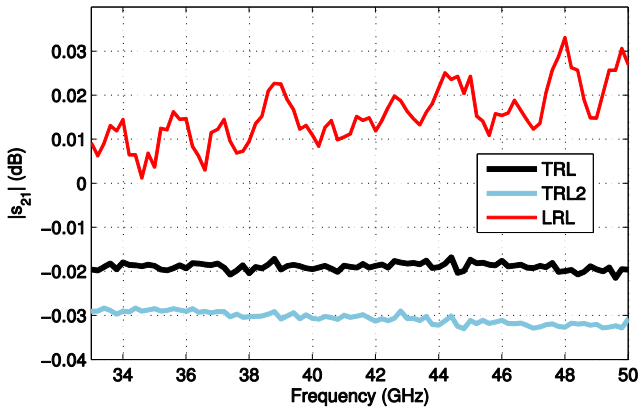

Fig. 16. Results of the measurement of the 6.8 mm airline transmission coefficient magnitude

Note that the results for the TRM calibration scheme are based on one set of measurements and were obtained by computation for individual standard definitions.

As the misalignment of waveguide flanges can influence scattering parameters of the direct connection of measurement ports, a method called „unknown thru“ was chosen for testing. As the simplest way, measurement of an ideal direct connection of test ports was performed. Measurement results presented in Figs. 20 and 21 include results for LRL method as well because it is the second method being tested which does not use an ideal Thru as fully known calibration standard.

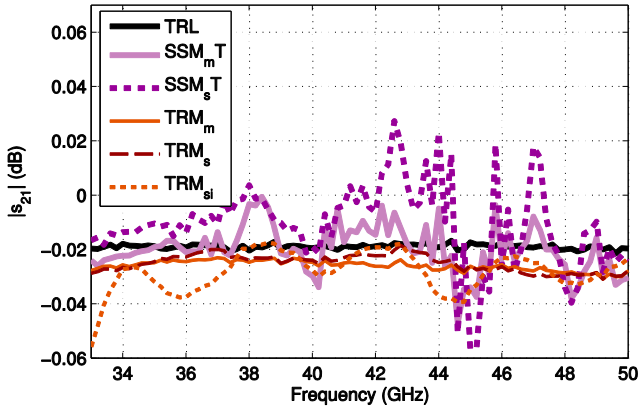

Fig. 17. Results of the measurement of the 6.8 mm air line transmission coefficient magnitude

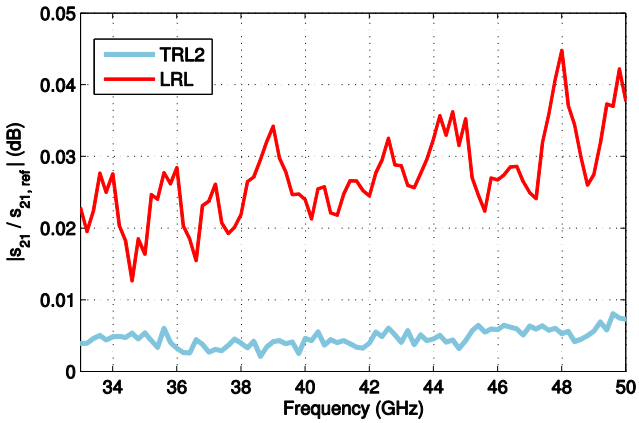

Fig. 18. Results of the measurement of the 20 dB attenuator transmission coefficient magnitude, differences of the measured and reference (TRL) data are plotted

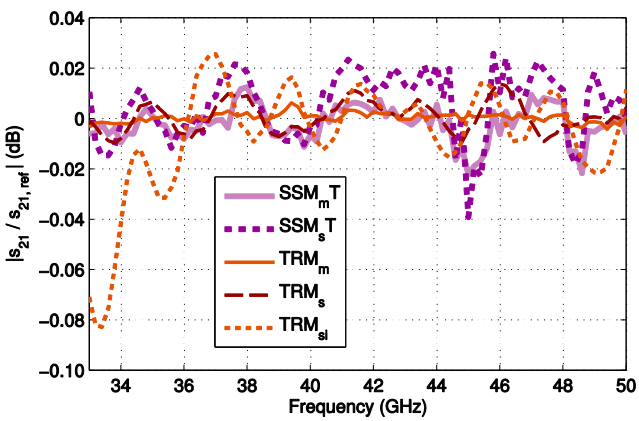

Fig. 19. Results of the measurement of the 20 dB attenuator transmission coefficient magnitude, differences of the measured and reference (TRL) data are plotted

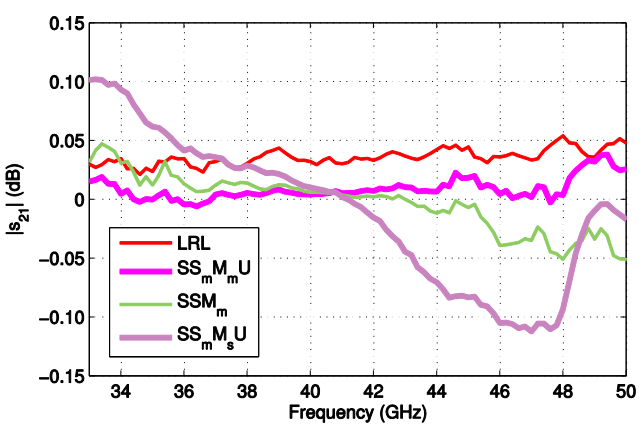

Fig. 20. Results of the measurement of ideal Thru transmission coefficient magnitude

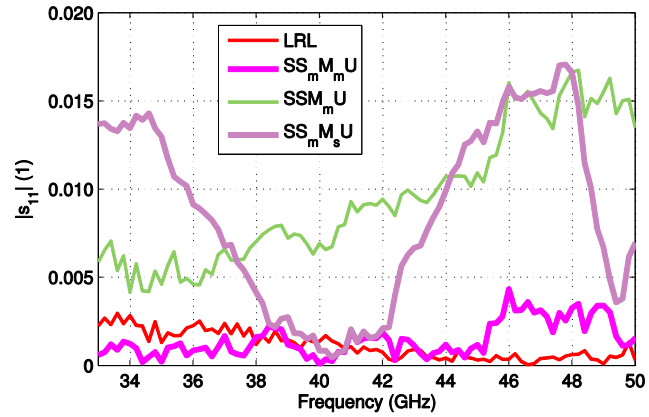

Fig. 21. Results of the measurement of ideal Thru reflection coefficient magnitude

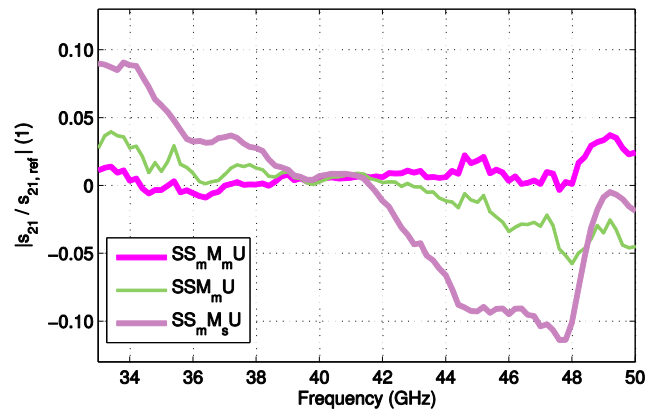

Fig. 22. Results of the measurement of the 20 dB attenuator transmission coefficient, differences of the measured and reference (TRL) data are plotted

Note that the results for the SSMU calibration scheme are based on one set of VNA measurements and were obtained by computation for individual standard definitions.

V. Discussion of the Results

A. TRL calibration scheme

A conventional TRL calibration scheme with a λ/4 line length was expected to give the most accurate results and was chosen to serve as a reference. Acceptable quality of performed TRL calibration can be documented by the quite small differences of low-reflective load measurements at both ports of the VNA (see Fig. 4) and no significant ripple visible on the offset short magnitude trace (see Fig. 9). However, it can be seen that the performance of the measurement system is affected by random errors, likely predominantly originated in cable flexure.

B. SSLL calibration scheme

This calibration was performed using the manufacturer's definition of the calibration standards.

In the plot of the $|S_{11}|$ measurement of the offset short (Fig. 7), significant ripple can be seen. From the ripple, the residual test port match value of 0.018 can be roughly estimated [8], mainly originating in imperfect offset short calibration standard definition. Systematic errors in low-reflection device measurement visible in Fig. 5 were found to be repeatable and perhaps could be caused by the imperfect definition of the offset load.

C. TRL2 calibration scheme

As mentioned above, two roughly ¾λ lines were used as calibration standards for this calibration scheme. The first line of the length of 6.4 mm was used as a standard at frequencies from 39 GHz to 48 GHz (transmission coefficient phase from -221° to -308°). The second line of the length of 8.8 mm was used as standard at frequencies from 33 GHz to 39 GHz (transmission coefficient phase from -210° to -304°) and from 48 GHz to 50 GHz (transmission coefficient phase from -424° to -449°). The Thru standard was used for reference plane setting. As can be seen in Fig. 4, the differences of low-reflective load measurements at both ports of the VNA are notably greater in comparison with conventional TRL calibration scheme. Most likely it is caused by the worse uniformity of the calibration lines put together from several shims. The results of measurement of the matched load and 6.8 mm line can be seen in Figs. 5 and 14, respectively. The deviation from the reference TRL calibration is in both cases better than 0.0025.

D. LRL calibration scheme

The combination of 2 mm and 4.4 mm shims was used as the shorter line, and the combination of 2 mm, 2.4 mm and 4.4 mm shims was used as the longer line, i.e. difference of both lengths is roughly λ/4. A Reflect standard (flush short) was presumed to be more suitable for the reference plane setting and only this option of the calibration was tested. As can be seen in Fig. 4, the differences of low-reflective load measurements at both ports of the VNA are somewhat greater in comparison with conventional TRL calibration scheme. The results of measurement of the matched load and 6.8 mm line can be seen in Figs. 5 and 14, respectively. The deviation from the reference TRL calibration is in both cases notably greater in comparison with the previous calibration scheme TRL2. Notably larger deviations were observed also in transmission measurements (see Figs. 16 and 18). The deviations can be partly explained by the random errors due to cable flexure and probably also by the fact that the measurement of reflection standard was used for reference plane definition.

E. SSM/SSMT calibration scheme

In these calibration schemes, the radiating open ended waveguide serves as the impedance standard, which does not suffer from misalignment of waveguide flanges. For the radiating open, two definitions were used; first one obtained by measurement using TRL method (SSM_m/SSM_mT) and second one obtained by electromagnetic simulation (SSM_s/SSM_sT). At the plot of the reflection coefficient magnitude measurement of the offset short (Fig. 9), significant magnitude ripple can be seen. For SSM_m the trace is very similar to SSLL, which is due to imperfect definition of the offset short supplied by manufacturer of the calibration kit. For SSM_s both residual test port match and residual directivity are increasing due to imperfect definition of the impedance standard.

F. TRM calibration scheme

In this calibration scheme, radiating open ended waveguide serves as the impedance standard as well. For the radiating open, three definitions were used here; first one obtained by measurement using TRL method (TRM_m), second one obtained by electromagnetic simulation of the MPF22 flange (TRM_s) and the third one obtained by modelling, whereas the real flange is approximated by the infinite flange model (TRM_{si}). From the measurement results it can be concluded that the maximum errors due to imperfect definition of the radiating open standard are a bit larger for SSM/SSMT calibration scheme in comparison with TRM calibration scheme for both reflection and transmission measurements.

G. SSMU calibration scheme

The unknown thru method was expected to be able to remove errors due to waveguide flange misalignment by direct connection of test ports. This scheme was tested only for two-port devices. For one-port devices, the characteristics correspond to SSM scheme here. The sensitivity of the transmission measurement accuracy on the definition of the reflection standards is especially noticeable. Results for three definitions of calibration standards can be seen in Fig. 20 to Fig. 22. For example, difference between traces marked SS_mM_mU and SSM_mU is due to the change of the length of the offset short standard definition by approximately 12 μm which corresponds to the change of the offset short reflection coefficient phase of 1.2° at 50 GHz. For example, in [3] it can be found that the standard deviation of the (complex valued) reflection coefficient of the offset short in the frequency band 750 GHz – 1100 GHz is approximately 0.1 which could generate significant errors for this calibration scheme. Considerable improvement can be expected by using of the method described in [4] that utilizes flush short, two offset shorts with unspecified but different phases and open-ended waveguide for one-port calibration.

VI. Conclusion

The purpose of this work was to gain knowledge applicable in the common European research programme aimed at VNA calibration methods for millimeter and submillimeter waves, on basis of experimental measurement in the frequency band 33 GHz to 50 GHz.

A set of measurements designated for the comparison of the conventional calibration schemes and calibration schemes suitable for frequencies above 100 GHz were performed. It is obvious that the accuracy of the used measurement system was negatively affected by random errors, most likely arising from the effect of cable flexure. However, the measurement results enable to compare some specific features of the calibration schemes of interest. The main observations for the frequency band 33 GHz – 50 GHz are as follows.

The ¾-λ TRL calibration results shows best agreement with the reference ¼-λ TRL calibration results, second best is the LRL calibration results. The calibrations using radiating opens (as calculable standards) show worst results caused by insufficiently accurate characterization of the open waveguide with real flange by the electromagnetic field simulator. Provided the same accuracy of characterization of the open waveguide standard the TRM calibration gives slightly more accurate results than SSMT.

The main conclusions regarding expected calibration performance at mm- and submm-wave frequencies can be formulated as follows. The ¾-λ TRL calibrations are expected to perform well and should be suitable as reference calibrations. LRL calibrations can perform quite well but they exhibit a bit worse performance than the previous ones. SSLL calibrations can be used but are less suitable as reference calibrations. Calibrations with radiating opens were found as the worst ones in frequency band 33 GHz to 50 GHz. However, it might be expected that with increasing frequency the accuracy of the simulation of the radiating open waveguide with flange could increase to a certain extent while the accuracy of the TRL calibration will decrease due to flange misalignment. Thus, it seems to be possible that the calibration schemes with radiating open waveguide, especially TRM, could outperform the other ones at higher frequency bands.

ACKNOWLEDGEMENT

This work was funded through the European Metrology Research Programme (EMRP) Project SIB62 “Metrology for New Electrical Measurement Quantities in High-frequency Circuits“. The EMRP is jointly funded by the EMRP participating countries within EURAMET and the European Union. Authors appreciate the contributions of C. Eiø and N. Ridler from NPL and K. Kuhlmann from PTB who offered critical comments concerning the manuscript. C. Eiø from NPL gave a loan of waveguide shims.

REFERENCES

[1] D.F. Williams, “500 GHz–750 GHz Rectangular–Waveguide Vector Network Analyzer Calibrations,” *IEEE Trans. THz Sci. Technol.*, Vol. 1, Issue 2, , pp. 364-377, Nov. 2011

[2] M. Horibe, R. Kishikawa, “Comparing Accuracy of Waveguide VNA Measurement Calibrated by TRL using Different Length of Line Standard in Terahertz Band,” *Proc. 81st. ARFTG Microwave Measurement Conf.*, Seattle, WA, June 2013, pp. 1-7

[3] N. Ridler, R. Clarke, M. Salter, A. Wilson, “The Trace Is on Measurements,” *IEEE Microwave Magazine*, Vol. 14, No. 7, pp. 67-74, November-December 2013

[4] Z. Liu, R. M. Weikle, “A Reflectometer Calibration Method Resistant to Waveguide Flange Misalignment,” *IEEE Trans. Microw. Theory Tech.*, Vol. 54, No. 6, pp. 2447-2452, June 2006

[5] J. H. Kim, B. Enkhbayar, J. H. Bang, B. C. Ahn, E. J. Cha, “New Formulas for the Reflection Coefficient of an Rectangular Waveguide Radiating into Air including the Effect of Wall Thickness or Flange,” *Progress In Electromagnetic Research M*, Vol. 12, pp. 143–153, 2010

[6] *Maury Microwave Corp., Precision WR22 and WR19 Waveguide Flanges*, Engineering data 5E-030, September 1996

[7] *IEEE Std 1785.1-2012*, IEEE Standard for Metallic Waveguides and Their Interfaces for Frequencies of 110 GHz and Above – Part 1: Frequency Bands and Waveguide Dimensions, March 2013

[8] *Guidelines on the evaluation of vector network analysers*, EURAMET/cg-12/v.01 (previously EA-10/12)

An IQ-Steering Technique for Amplitude and Phase Control of mm-Wave Signals

Akshay Visweswaran*†, Carmine de Martino*, Emilio Sirignano*, and Marco Spirito*

* Delft University of Technology, Electronic Research Laboratory (ERL), Delft, The Netherlands
†Imec, Leuven, Belgium

***Abstract* — In this contribution we present a custom test-bench capable of delivering multi-path mm-wave signals with amplitude and phase control to an on-wafer environment. The setup employs direct IQ up-conversion in the 7.5GHz to 10GHz band, with high resolution DACs to modulate both amplitude and phases of *n* coherent LO signals. Signal amplification followed by frequency multiplication generates mm-wave signals in the 30 to 40GHz range. An amplitude pre-distortion technique, to level the IQ mixer output power versus phase angle, and a calibration technique are developed to achieve accurate amplitude and phase control between the signals at the wafer probe-tip level.**

***Index Terms* — IQ modulation, phase coherent, calibration, mm-wave.**

I. Introduction

In present mm-wave applications such as phased arrays and MIMO, there is a growing need (at characterization and testing level) to generate signals having accurate and independent phase/amplitude control relative to a common reference.

The generation of high frequency signals with known and constant relative phases has always been a challenge due to the increased sensitivity to mechanical tolerances as frequency increases, i.e., passive hybrid imbalances are in the order of ±10°, and matched phase cables are difficult to realize and expensive.

In addition, most phase locking loops (type I) used in commercial synthesizers only permit frequency-control, and do not provide phase adjustability of the signal in the loop. As an example, if two analog synthesizers are locked to the same crystal reference, two error mechanisms occur causing the relative phase to diverge:

1) short term and long term drift effects (caused by the mismatch in the phase discriminators of the two synthesizers), resulting in different time constants of the two PLLs, and different leakage currents, respectively.

2) the switching instant of the frac-N is asynchronous with the RF signal, as a result, after frequency division the phases can potentially end up in a different quadrants.

More advanced solutions that require dedicated hardware to track signal phases are only embedded in expensive network analyzers [1].

In this contribution we will present an IQ up-conversion system, similar to the one presented in [2][3], capable of aligning and controlling both phase and amplitudes of mm-wave signals. The paper is structured as follows, first a description of the hardware setup is given, then the calibration procedure is described and benchmarked via circuit level simulations, finally the experimental data are presented and discussed.

II. Hardware Setup

In order to generate the multiple (the proposed setup employs four paths) phase coherent mm-wave signals, the output of a single frequency source is split into four paths using a Wilkinson power divider. These signals provide the necessary LO drive to operate the IQ modulators, which provide independent amplitude modulation and phase steering capabilities in each path. The 20dB isolation provided by the Wilkinson power divider is sufficient to avoid pulling between the modulators. The LO signals are amplitude modulated and phase steered using programmable 12-bit digital to analog converters (DACs) that set the (static) voltages on the in-phase (I) and quadrature (Q) ports of the modulators, as shown in Fig. 1. Interface amplifiers ensure adequate drive to the X4 multipliers that generate the required mm-wave signals in the target 30-40GHz band.

The entire assembly of active and passive components is mounted on a 6mm thick aluminum plate, which provides mechanical stability, and acts like a heat sink for the active components (see Fig.2).

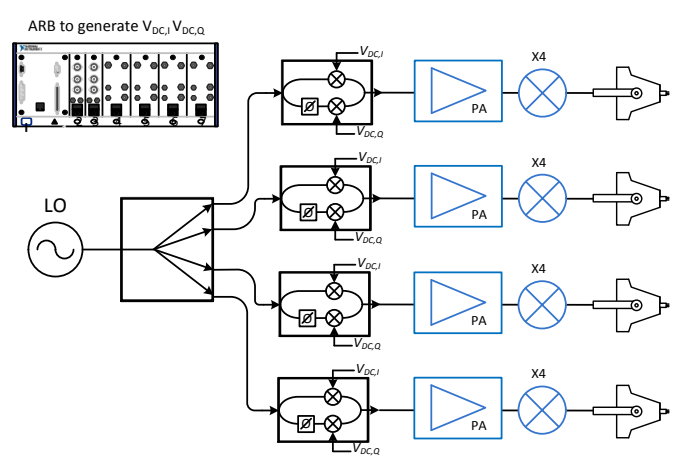

Fig. 1: Simplified block scheme of the proposed setup.

978-1-4673-9247-1/15/$31.00 ©2015 IEEE

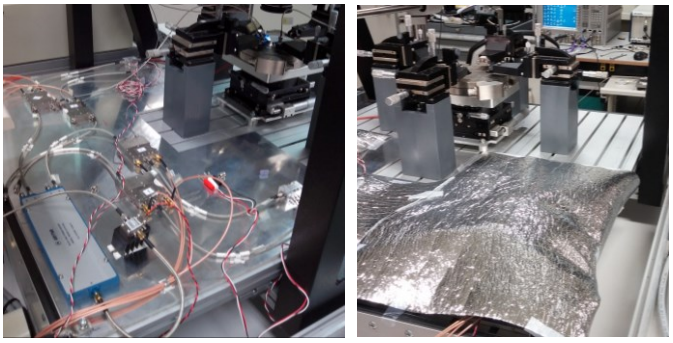

Fig. 2: Hardware implementation of the proposed setup detailing the LO distribution to IQ mixers (left) and the thermal shielding through aluminum foils (right).

The RF coaxial cables are then clamped in place, and covered in isolation foil to minimize temperature fluctuations which would lead to phase variations (Fig. 2 inset).

III. Calibration

The calibration procedure is required to convert the I and Q information into phase values at the defined reference plane, and to absorb the mismatches between the various components of the setup (i.e., mixers, amplifiers and cables).

As a first step the individual modulators have to be characterized and DC compensated for their zero-offset, to minimize LO leakage (see Fig. 3).

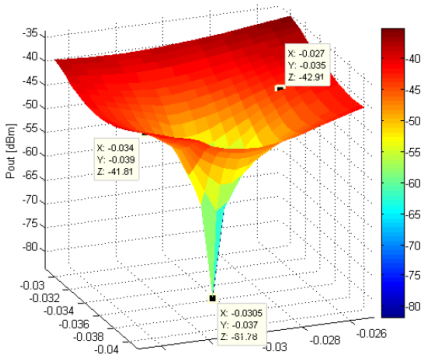

Fig. 3: Reduction of the LO to RF leakage as a results of the IQ minimization procedure.

The minimization I and Q voltages represent the effective center around which the high frequency phasor rotates, in a polar representation.

In order to preserve a constant amplitude versus steering angle (i.e., constant radius of the rotating I/Q phasor), the modulator input is pre-distorted. The I and Q voltage settings are modified *a priori* to achieve independent amplitude and phase control.

The pre-distorted amplitude variation is less than 0.1 dB in the required quadrant (0 to 90°) as seen from Fig. 4. Note, that due to the x4 multiplication, linearization of the modulator in a single quadrant is sufficient to achieve orthogonal phase and amplitude control over 360° in the mm-wave band.

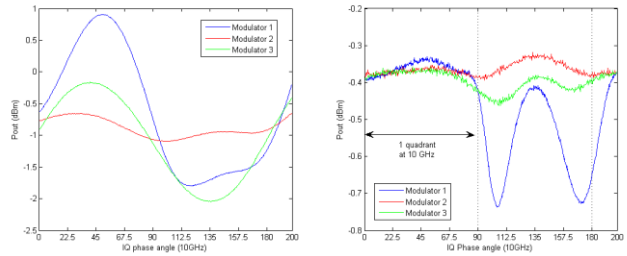

Fig. 4: Amplitude response of the modulators: (left) before pre-distortion, after the multi-setup pre-distortion procedure.

To compensate the mismatches arising from the different lengths and losses present in the various signal paths (probes included), an on-wafer power-combing calibration procedure was developed using a symmetric combiner. The fully symmetric CPW T-junction prototypes were designed and simulated using a 2.5D fullwave EM software (i.e., Keysight MoMentum), and then integrated in a fused silica wafer, see Fig. 5.

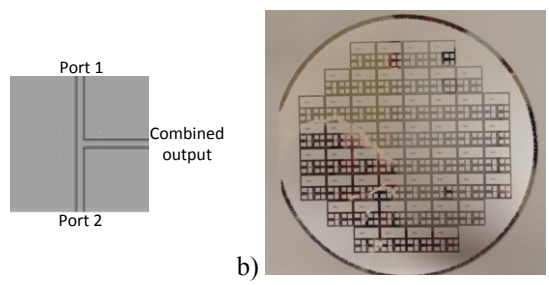

Fig. 5: Fully symmetric CW T-junction: (left) layout view, (right) fabricated fused silica wafer with aluminum metallization layer.

A. Validation of calibration procedure

In order to validate the calibration procedure a simulation environment was created Keysight's Advanced Design System (ADS) software.

The circuit schematic is shown in Fig. 6. A numerical optimizer is used to find the I and Q voltages of mixer 2 to achieve a minimization at the *combined output* while mixer 1 is kept constant. In order to account for a realistic system, imbalances (extracted from classical data-sheet performance) where added on the following parameters: minimization point of the mixers, phase delay on the LO drive, port mismatch at the combiner and divider ports and finite isolation of the combiners.

The combiner used in the simulation environment, as well as the one from experimental setup is a simple T-junction, which provide no path isolation and presents a frequency independent match of close to -9dB. This results in a small change of load impedance seen by the two IQ mixers from the calibration phase to the measurement phase, when the driving paths are separated (i.e., isolated).

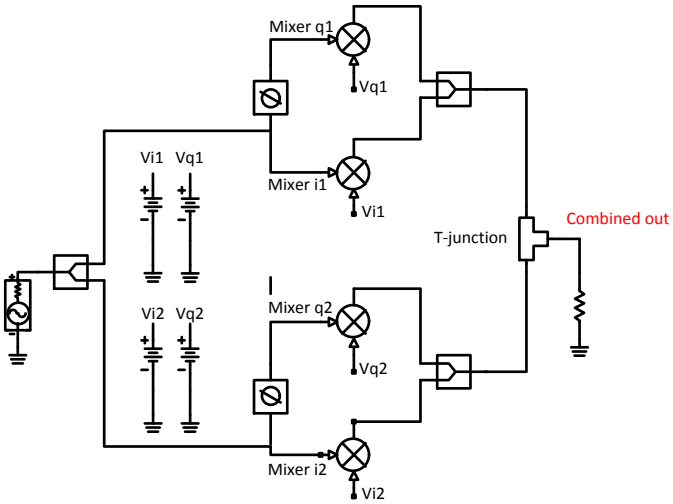

Fig. 6: Block diagram of the experimental setup. Error models accounting for the components (i.e., phase shifter, combiner and T-junction) non idealities are included, in an ADS simulation test-bench.

The results of the simulated calibration procedure, and the effective phase offset achieved when the mixer are used in isolated paths are shown in Fig. 7.

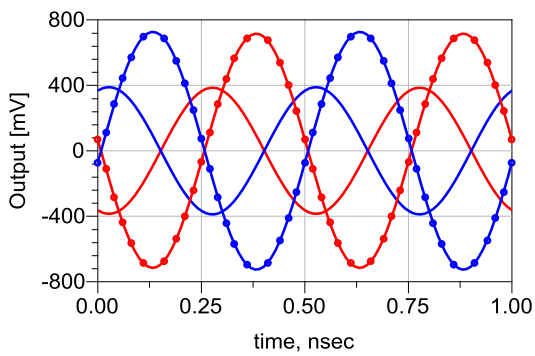

Fig. 7: Simulated output voltages of each IQ modulator, when their outputs are combined with the T-junction in the calibration phase (dashed), and measurement phase (solid with symbols).

As can be seen by the figure the 180° phase offset is preserved when moving from the combined case (dashed) to the isolated one (solid with symbols). The phase imbalance achieved is less than 0.5°.

IV. Experimental Results

In order to achieve multiple equi-amplitude, controllable phase coherent signals a round robin procedure is implemented, where one path is assigned as reference. The amplitude and phase of the other paths are subsequently (one variable path at a time) aligned to it by monitoring their combined output power with the reference. In the T-junction two paths are connected to the modulators (i.e., reference and modulator under test) and the third arm of the junction is connected to the spectrum analyzer. The calibration procedure described in section III monitors the output power for sequentially varied DC values on the IQ ports of the variable path. The 180° difference is found by identifying the output cancellation point and mapping the entire curve to 360° as shown in Fig. 8.

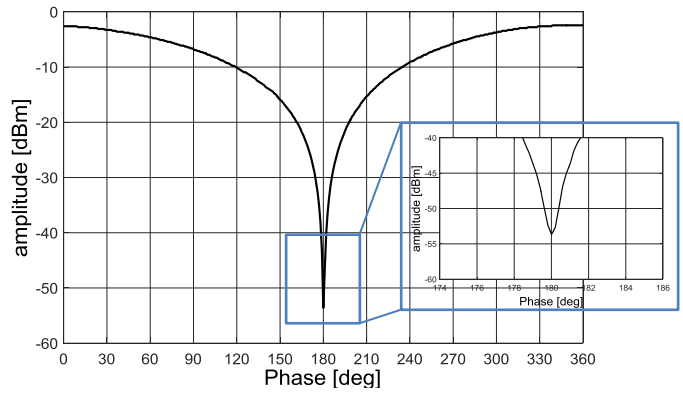

Fig. 8: Power combined output of the T-junction versus phase angle of the variable modulator. The inset is a zoom-in around the cancellation point.

After calibration, the the I and Q bias voltages on the modulators can be programmed to set the desired signal phases with respect to the reference.

The developed measurement system was calibrated, and then two modulators were set at opposite phases to gauge the stability of the set-up over time. Data compiled over a 10-hour measurement are shown in Fig. 9.

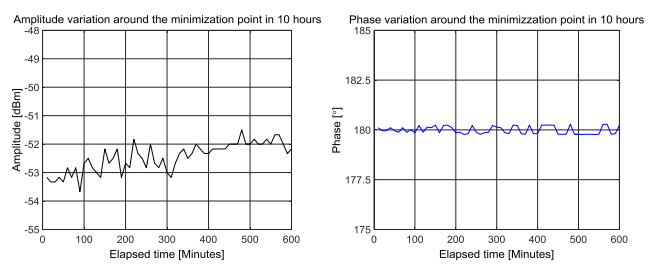

Fig. 9: Measurement setup stability computed for a time interval of 10 hours at the cancellation point, i.e., 180 ^{o} described in terms of: output power (left), and computed phase (right).

The amplitude error observed over 10 hours is 2dB, which translates to a small ±0.3° relative phase drift when referenced against measurement results from Fig. 8.

V. Conclusions

In this paper we presented a simple measurement-setup that provides amplitude and phase controlled mm-wave signals to an on-wafer environment. The hardware of the system is centered around IQ modulators controlled by precision DACs. The leakage minimization procedure, pre-distortion and calibration procedure that achieves equi-amplitude phase controllable outputs have been discussed and validated by means of circuit level simulations. Experimental results show that the implemented system achieves a phase stability better

then ±0.3° in a measurement frame of 10 hours in a ±1 °C temperature controlled lab.

VI. Acknowledgements

This work was funded by the EMRP MORSE project. The EMRP is jointly funded by the EMRP participating countries within EURAMET and the European Union.

References

[1] J. Simon, "True differential stimulus gives additional insight into nonlinear device behavior," in ARFTG Conference, 2007 69th , vol., no., pp.1-9, 8-8 June 2007.

[2] J. Dunsmore, "New methods & non-linear measurements for active differential devices," in Microwave Symposium Digest, 2003 IEEE MTT-S International , vol.3, no., pp.1655-1658 vol.3, 8-13 June 2003.

[3] G. Vlachogiannakis, H.T. Shivamurthy, et. all, “An I/Q-Mixer-Steering Interferometric Technique for High-Sensitivity Measurement of Extreme Impedances”, International Microwave Symposium, May 2015.

The Impact of Knowing the Impedance of the Lines Used in the TRL Calibration on the Load-Pull Characterization of Power Transistors

M.A Pulido-Gaytán[1], J.A. Reynoso-Hernández[1], M.C. Maya-Sánchez[1], J.R. Loo-Yau[2]

[1]Centro de Investigación Científica y de Educación Superior de Ensenada (CICESE). Ensenada, B.C., México.
[2]Centro de Investigación y de Estudios Avanzados del I.P.N (CINVESTAV). Guadalajara, Jalisco, México.

***Abstract* — In this paper, the impact of knowing the impedance of the lines used in the TRL calibration (*Z*) on the load-pull (LP) characterization of power transistors is assessed. Relevant parameters, such as input impedance (Z_{IN}), load impedance (Z_{LD}) and large-signal gain are considered. By using the *ABCD*-parameters matrix formalism in the calibration of the LP measurement setup, closed form expressions for evaluating the impact of knowing *Z* on the calculation of these parameters are presented. It is demonstrated that knowing *Z* is of paramount importance in the calculation of Z_{IN} and Z_{LD}. Regarding the gain, it is demonstrated that while the voltage and current gains do not depend on the knowledge of *Z*, the gain expressed as the ratio of the transmitted to incident waves does.**

***Index Terms*— Load-pull, TRL calibration, power transistors, characteristic impedance, *ABCD*-parameters.**

I. Introduction

The objective of the characterization of power devices using a load-pull (LP) system is the evaluation of its performance under different loading conditions in order to determine the load under which its optimal performance may be obtained [1]. Nevertheless, elements of the measurement setup such as cables, adapters, couplers or test fixtures, introduce errors in the measurement of the impedances and large-signal behavior at the device's plane. Thus, to accurately characterize a device under test (DUT), the measurement setup has to be calibrated.

The calibration of a LP measurement setup, such as the one depicted in Fig.1, is divided into two parts: 1) a relative calibration, in which ratios of parameters of interest (e.g., voltages and currents or incident and scattered waves) may be determined, and 2) a power calibration, in which the power levels at the DUT ports are determined.

The relative calibration may be carried out by using conventional vector network analyzer calibration techniques (Fig. 2) such as the thru-reflect-line (TRL) [2]-[3] or the thru-reflect-match (TRM) [4]. The power calibration, on the other hand, may be carried out by using a power meter (PM) connected at the calibration plane [2], [5]. When the DUT is mounted in a microstrip test fixture or is contacted using coplanar probes, a PM cannot be connected at such a plane. In those cases the power calibration is carried out by connecting a PM at a coaxial plane located far from the calibration plane (Fig. 3) and using a procedure to determine the power at the calibration plane [6].

In order to be characterized, packaged power transistors are accommodated in transmission lines, whose characteristic impedance depends on the transistor's power capabilities; the higher the power capabilities, the lower the line's impedance. In this order, the test fixtures used to mount those devices utilize wideband impedance transformers [7]-[8] to adapt low impedance lines to 50 Ω lines. As a consequence, the impedance value of the lines used as calibration elements in a TRL calibration (*Z*) vary according to the transistor's power capabilities.

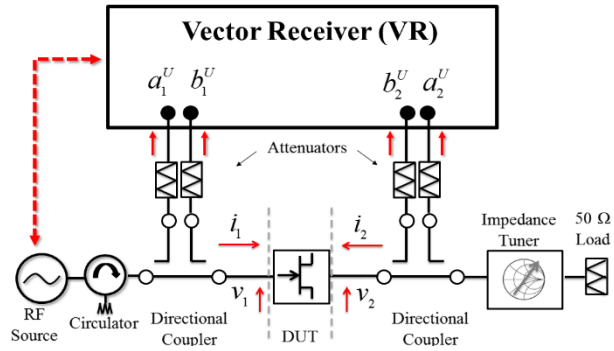

Fig.1. Measurement setup of a real-time load-pull system (neither driver amplifier nor networks for DUT biasing are depicted).

Previously published works [7]-[8] have reported that in order to refer the TRL calibration to the measuring system impedance (Z_0), in both S-parameters and LP measurements, it is necessary to know the value of *Z*. However, to the best of the authors' knowledge, a rigorous analysis explaining the significance of accurately knowing *Z* in the LP characterization of power transistors has not yet been reported. In this paper, by using the *ABCD*-parameters matrix formalism in the calibration of a LP setup, closed form expressions to assess the impact of knowing the value of *Z* on the LP characterization of power transistors are presented for the first time.

II. Load-Pull Setup Calibration

In order to analyze the calibration of the LP setup depicted in Fig. 1, we use the structures shown in Fig. 2 and Fig.3 [5]. The calibration procedure described in this section uses the *ABCD*-parameters formalism for representing the measurements in the vector receiver (VR) and the power meter depicted in Fig. 2 and Fig. 3. Hence, the analysis is developed in terms of voltages and currents.

A. Relative calibration

The voltages and currents at the VR ports, v_k^U and i_k^U; $k=1,2$, which are defined as a function of the waves measured in the VR (Fig.2) as

$$v_k^U=\sqrt{Z_0}\left(1+\frac{b_k^U}{a_k^U}\right)a_k^U=\sqrt{Z_0}\left(\frac{a_k^U}{b_k^U}+1\right)b_k^U, \qquad (1)$$

978-1-4673-9247-1/15/$31.00 ©2015 IEEE

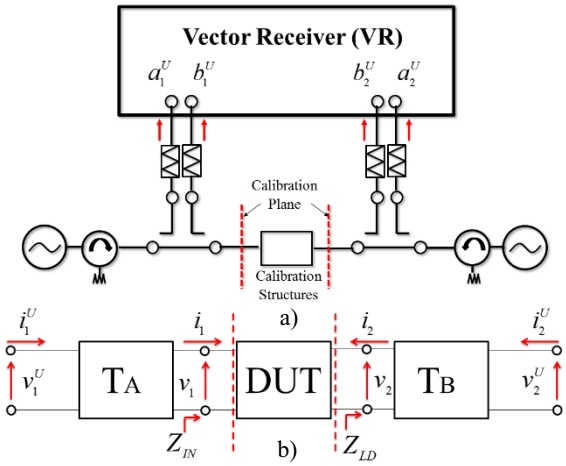

Fig.2. Relative calibration: a) Measurement setup configuration and b) model for the setup (networks for DUT biasing are not depicted).

$$i_k^U = \left(1 - \frac{b_k^U}{a_k^U}\right)\frac{a_k^U}{\sqrt{Z_0}} = \left(\frac{a_k^U}{b_k^U} - 1\right)\frac{b_k^U}{\sqrt{Z_0}}, \tag{2}$$

may be related to the voltages and currents at the DUT ports, v_k and i_k, as follows

$$\begin{bmatrix} v_1 \\ i_1 \end{bmatrix} = \mathbf{T_A^{-1}} \begin{bmatrix} v_1^U \\ i_1^U \end{bmatrix}, \tag{3}$$

$$\begin{bmatrix} v_2 \\ -i_2 \end{bmatrix} = \mathbf{T_B} \begin{bmatrix} v_2^U \\ -i_2^U \end{bmatrix}. \tag{4}$$

In (3)-(4), $\mathbf{T_A}$ and $\mathbf{T_B}$ are matrices representing the networks connecting the DUT ports to the VR ports, as shown in Fig. 2b. According to the theory presented in the appendix, these matrices may be expressed as

$$\mathbf{T_A} = D_X \begin{bmatrix} \overline{A_X} & \overline{B_X} \\ \overline{C_X} & 1 \end{bmatrix} \begin{bmatrix} -Z & Z \\ 1 & 1 \end{bmatrix}^{-1}, \tag{5}$$

$$\mathbf{T_B} = D_Y \begin{bmatrix} -Z & Z \\ 1 & 1 \end{bmatrix} \begin{bmatrix} \overline{A_Y} & \overline{B_Y} \\ \overline{C_Y} & 1 \end{bmatrix}, \tag{6}$$

where the term Z represents the impedance of the lines used as standard in a TRL calibration. As presented in the appendix, the seven terms $\overline{A_X}$, $\overline{B_X}$, $\overline{C_X}$, $\overline{A_Y}$, $\overline{B_Y}$, $\overline{C_Y}$ and $D_X D_Y$ are determined by using only information provided by the measurement of the TRL calibration structures.

Then, by substituting (5) in (3) and (6) in (4), and developing the resultant expressions, one has

$$v_1 = \frac{-Z}{D_X \cdot \Delta_X}\left[\left(1+\overline{C_X}\right)v_1^U - \left(\overline{B_X}+\overline{A_X}\right)i_1^U\right], \tag{7}$$

$$i_1 = \frac{1}{D_X \cdot \Delta_X}\left[\left(1-\overline{C_X}\right)v_1^U - \left(\overline{B_X}-\overline{A_X}\right)i_1^U\right], \tag{8}$$

$$v_2 = Z \cdot D_Y\left[\left(\overline{C_Y}-\overline{A_Y}\right)v_2^U - \left(1-\overline{B_Y}\right)i_2^U\right], \tag{9}$$

$$i_2 = -D_Y\left[\left(\overline{C_Y}+\overline{A_Y}\right)v_2^U - \left(1+\overline{B_Y}\right)i_2^U\right], \tag{10}$$

where $\Delta_X = \overline{A_X} - \overline{B_X}\,\overline{C_X}$. From (7)-(10), the impedance at the input of the DUT and the load impedance at the DUT plane defined as $Z_{IN} = v_1/i_1$ and $Z_{LD} = -v_2/i_2$, may be expressed as

$$Z_{IN} = -Z \cdot \frac{\left(1+\overline{C_X}\right)Z_1^U - \left(\overline{B_X}+\overline{A_X}\right)}{\left(1-\overline{C_X}\right)Z_1^U - \left(\overline{B_X}-\overline{A_X}\right)}, \tag{11}$$

$$Z_{LD} = Z \cdot \frac{\left(\overline{C_Y}-\overline{A_Y}\right)Z_2^U - \left(1-\overline{B_Y}\right)}{\left(\overline{C_Y}+\overline{A_Y}\right)Z_2^U - \left(1+\overline{B_Y}\right)}, \tag{12}$$

where $Z_k^U = v_k^U / i_k^U$; $k = 1,2$. Meanwhile, the DUT's voltage gain and current gain, defined as $G_V = v_2/v_1$ and $G_I = -i_2/i_1$, may be expressed as

$$G_V = -\Delta_X \cdot D_X D_Y \cdot \frac{\left(\overline{C_Y}-\overline{A_Y}\right) - \left(1-\overline{B_Y}\right)Y_2^U}{\left(1+\overline{C_X}\right) - \left(\overline{B_X}+\overline{A_X}\right)Y_1^U} \cdot G_V^U, \tag{13}$$

$$G_I = \Delta_X \cdot D_X D_Y \cdot \frac{\left(\overline{C_Y}+\overline{A_Y}\right)Z_2^U - \left(1+\overline{B_Y}\right)}{\left(1-\overline{C_X}\right)Z_1^U - \left(\overline{B_X}-\overline{A_X}\right)} \cdot G_I^U, \tag{14}$$

where $Y_k^U = 1/Z_k^U$, $G_V^U = V_2^U / V_1^U$ and $G_I^U = I_2^U / I_1^U$. The commonly used definition for gain in terms of transmitted and incident waves $G_D = b_2/a_1$, can be determined as

$$G_D = \frac{v_2 - Z_0 i_2}{v_1 + Z_0 i_1} = \frac{Z_{LD}+Z_0}{Z_{IN}+Z_0} G_I = \frac{1+Z_0/Z_{LD}}{1+Z_0/Z_{IN}} G_V. \tag{15}$$

It may be noted from (11)-(12) that for determining Z_{IN} and Z_{LD} the knowledge of Z is mandatory. Regarding the gain, according to (13)-(14) the voltage and current gains do not depend on the knowledge of Z. On the other hand, the gain in terms of incident and transmitted waves G_D depends on Z through its own dependence on Z_{IN} and Z_{LD}.

It is worth noting that the power gain G_P, defined as

$$G_P = |G_V|^2 \frac{\mathrm{Re}\left(1/Z_{LD}\right)}{\mathrm{Re}\left(1/Z_{IN}\right)} = |G_I|^2 \frac{\mathrm{Re}\left(Z_{LD}\right)}{\mathrm{Re}\left(Z_{IN}\right)}, \tag{16}$$

depends on Z through its dependence on $\mathrm{Re}(Z_{IN})$ and $\mathrm{Re}(Z_{LD})$.

B. *Power calibration: problem statement*

Thus far, expressions to determine the impedance at the input of a DUT, its gain and the load impedance at the DUT plane have been derived. Nonetheless, in LP an important concern is to specify the power levels at the input and output of the DUT. In this order, by analyzing the structure shown in Fig. 2b, the power at the input and output of a DUT may be expressed as

$$P_{IN} = |v_1|^2 \,\mathrm{Re}\left(1/Z_{IN}\right), \tag{17}$$

$$P_{OUT} = |v_2|^2 \,\mathrm{Re}\left(1/Z_{LD}\right), \tag{18}$$

with $|v_1|$ and $|v_2|$ defined as

$$|v_1| = \frac{|Z|}{|D_X|}\left|\left(1+\overline{C_X}\right) - \left(\overline{B_X}+\overline{A_X}\right)Y_1^U\right| \frac{|v_1^U|}{|\Delta_X|}, \tag{19}$$

$$|v_2| = |D_Y||Z|\left|\left(\overline{C_Y} - \overline{A_Y}\right) - \left(1 - \overline{B_Y}\right)Y_2^U\right||v_2^U|. \quad (20)$$

From (17)-(20), it is noted that for determining P_{IN} and P_{OUT} it is mandatory to know $|D_X|$ and $|D_Y|$. These terms may be calculated by using the measurement setup configuration shown in Fig.3, as described next.

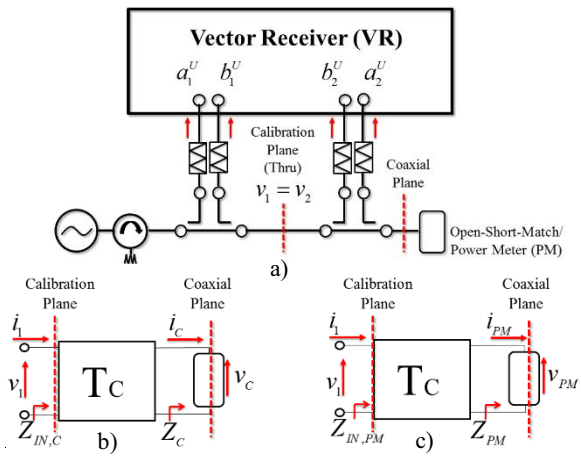

Fig.3. Power calibration: a) Setup configuration, b) measurement of coaxial loads and c) measurement of power meter.

C. Determination of $|D_X|$ and $|D_Y|$

The procedure for determining $|D_X|$ and $|D_Y|$ consists of: 1) to make a thru connection at the calibration plane, 2) to connect three loads of known impedance at a coaxial plane and 3) to connect a PM at that coaxial plane [5], as shown in Fig. 3a.

According to the structure shown in Fig. 3b, the voltages and currents at the calibration plane, v_1 and i_1, may be related to the voltages and currents at the coaxial plane, v_C and i_C, as

$$\begin{bmatrix} v_1 \\ i_1 \end{bmatrix} = \mathbf{T_C} \begin{bmatrix} v_C \\ i_C \end{bmatrix}, \quad (21)$$

with $\mathbf{T_C}$ defined as

$$\mathbf{T_C} = D_C \begin{bmatrix} \overline{A_C} & \overline{B_C} \\ \overline{C_C} & 1 \end{bmatrix}. \quad (22)$$

Then, by substituting (22) in (21) and developing the resultant expression, the following equation may be derived

$$\overline{A_C}\, Z_C + \overline{B_C} - \overline{C_C}\; Z_C Z_{IN,C} = Z_{IN,C}, \quad (23)$$

where $Z_{IN,C}=V_1/I_1$ is the input impedance at the calibration plane when a load of impedance $Z_C=v_C/i_C$ is connected at the coaxial plane; $Z_{IN,C}$ may be calculated from (11). By connecting three loads of known impedance (open, short, match) at the coaxial plane and using (23), a linear system of equations may be formed; the terms $\overline{A_C}$, $\overline{B_C}$ and $\overline{C_C}$ are calculated by solving the resultant system of equations.

Once $\overline{A_C}$, $\overline{B_C}$ and $\overline{C_C}$ are known, let now analyze the connection of a PM at the coaxial plane. First, the impedance of the PM, Z_{PM}, is calculated as

$$Z_{PM} = \left(Z_{IN,PM} - \overline{B_C}\right) \Big/ \left(\overline{A_C} - \overline{C_C}\, Z_{IN,PM}\right). \quad (24)$$

Then, from the analysis of the structure shown in Fig. 3c, using (21)-(22), the following expression may be derived

$$v_1 = D_C\left(\overline{A_C} Z_{PM} + \overline{B_C}\right) v_{PM}, \quad (25)$$

where v_{PM} represents the voltage at the PM. Now, let $P_{PM}=|v_{PM}|^2\,\mathrm{Re}(Y_{PM})$, with $Y_{PM}=1/Z_{PM}$, be the power measured in the PM. From (25) one can derive the following expression

$$|v_1|^2 = |D_C|^2 \left|\overline{A_C} + \overline{B_C}/Z_{PM}\right|^2 P_{PM}/\mathrm{Re}(Y_{PM}). \quad (26)$$

The term $|D_C|^2$ is calculated by assuming that the network represented by the matrix $\mathbf{T_C}$ is reciprocal [6] (the determinant of $\mathbf{T_C}$ equals the unity) as $|D_C|^2 = 1\Big/\left|\overline{A_C} - \overline{B_C}\,\overline{C_C}\right|$.

Since a thru connection at the calibration plane is considered, $v_1=v_2$, by solving (19) and (20) for $|D_X|$ and $|D_Y|$, and substituting (26) in the resultant expressions one has

$$|D_X|^2 = \frac{|Z|^2\left|\left(1+\overline{C_X}\right) - \left(\overline{B_X} + \overline{A_X}\right)Y_1^U\right|^2 \mathrm{Re}(Y_{PM})|v_1^U|^2}{|\Delta_X|^2 |D_C|^2 \left|\overline{A_C} + \overline{B_C}/Z_{PM}\right|^2 P_{PM}}, \quad (27)$$

$$|D_Y|^2 = \frac{|D_C|^2 \left|\overline{A_C} + \overline{B_C}/Z_{PM}\right|^2 P_{PM}}{|Z|^2\left|\left(\overline{C_Y} - \overline{A_Y}\right) - \left(1 - \overline{B_Y}\right)Y_2^U\right|^2 \mathrm{Re}(Y_{PM})|v_2^U|^2}. \quad (28)$$

Note that the dependence of $|D_X|^2$ and $|D_Y|^2$ on Z in (27)-(28) is not only through the factor $|Z|^2$, but also through the dependence of $\overline{A_C}$, $\overline{B_C}$ and $\overline{C_C}$ on $Z_{IN,C}$ for three different coaxial loads and through the dependence of $|D_C|^2$ on $\overline{A_C}$, $\overline{B_C}$ and $\overline{C_C}$. Hence, deriving an expression for calculating P_{IN} and P_{OUT} from (17)-(20) as an explicit function of Z may result in a lengthy mathematical formulation, which is not addressed in this paper.

III. Experimental Results

A real-time LP measurement setup was implemented by using as a vector receiver the Agilent PNA-X N5245A, having this instrument external access to the receivers. As variable load impedance, a MPT-1808 tuner from Focus Microwaves was used. The DUT, a CGH40045 power transistor from Cree, was mounted in a test fixture comprising wideband impedance transformers that adapt 10 Ω transmission lines to 50 Ω transmission lines (Maury Microwave MT964C2-10).

The measurement setup was calibrated at 3 GHz using the procedure presented in section II and the output power LP contours of the DUT (V_{DS}=20V; V_{GS}=-2.5V) were measured. In order to demonstrate in a simple manner the importance of knowing the line's impedance on the LP characterization of the DUT, the actual value of Z was assumed to be real and identical to 10 Ω. Fig. 4 shows the output power LP contours calculated by using the actual value of Z (10 Ω) in the calibration procedure along with the contours calculated using three erroneous values of Z. It may be observed that knowing Z is very important in the calculation of the load impedance; an

error in the knowledge of Z represents a proportional error in the calculation of Z_{LD}. In this order, the optimum impedance (Z_{opt}) is underestimated or overestimated, depending on the error in the value of Z. This parameter is very important in the design of power amplifiers (PAs); calculating erroneously the value of Z_{opt} will result in suboptimum behavior of the transistor in a PA.

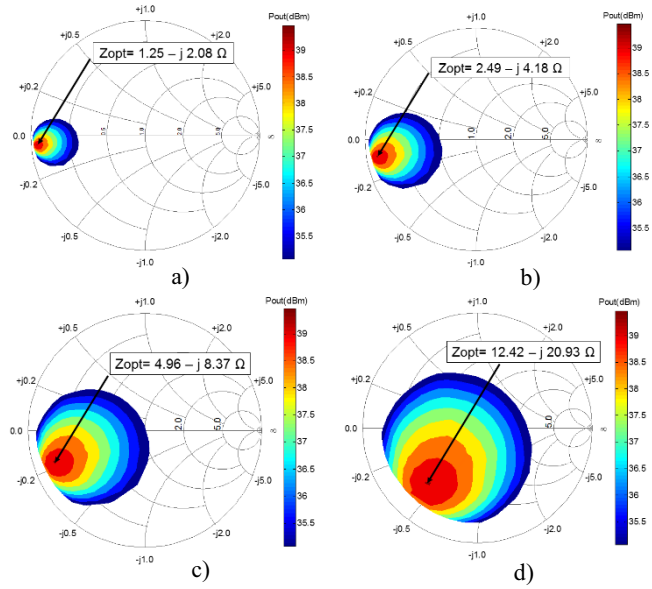

Fig.4. Contours of constant output power of a CGH40045 power transistor (VDS=20 V, VGS=-2.5 V) using a) Z=5 Ω, b) Z=10 Ω, c) Z=20 Ω, d) Z=50 Ω in the calibration procedure.

Then, we fixed the load impedance at Z_{opt}=2.49-j 4.18 Ω and the input impedance was measured. Fig. 5 shows the input impedance calculated by using the actual value of Z in the calibration procedure along with the input impedance calculated using three erroneous values of Z. It can be observed that, as expressed in (11), the calculated value of Z_{IN} varies proportionally with the value used for Z in the calibration procedure. Z_{IN} is of paramount importance in the design of PAs since it provides PA designers with the information necessary to appropriately design the input matching networks of a PA.

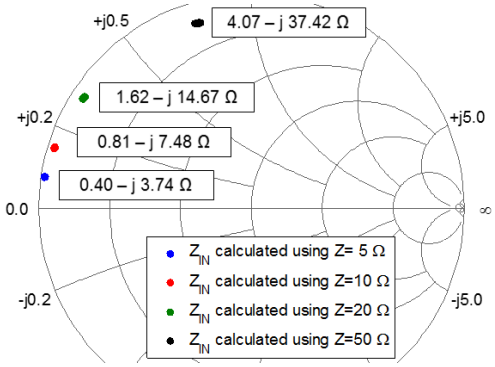

Fig. 5. Input impedance of the DUT calculated using different values of Z in the calibration. The load impedance was fixed at Z_{LD}=Z_{opt}.

Finally, the impact of an error in the knowledge of Z in the calculation of the large-signal gain was investigated. Since the calculation of the voltage gain and the current gain is not dependent on Z, the gain expressed as the ratio of the transmitted to the incident waves G_D was considered.

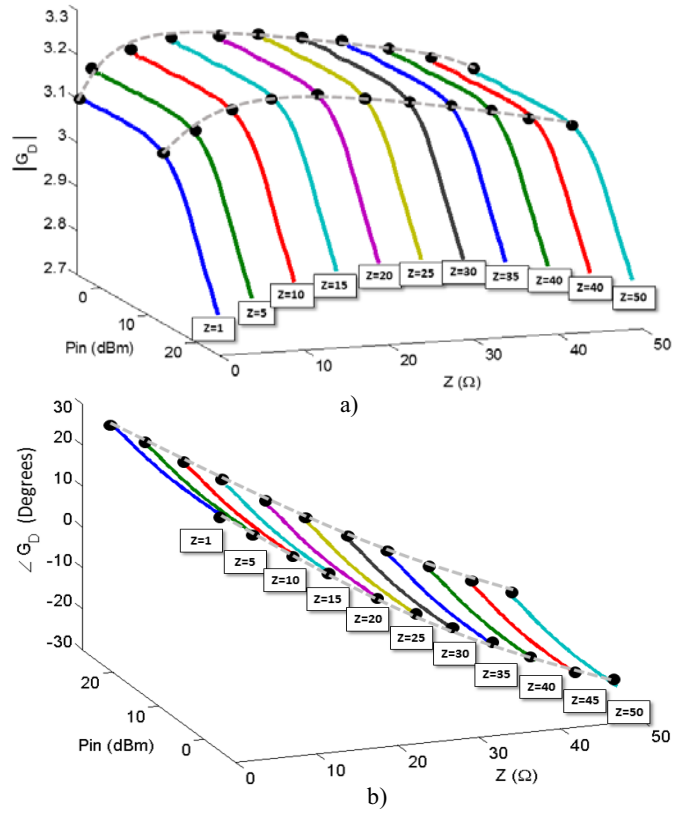

Fig. 6. Gain of the DUT calculated using different values of Z in the calibration: a) magnitude and b) phase. The load impedance was fixed at Z_{LD}=Z_{opt}.

As presented in section II.A, the calculation of G_D depends on Z through its dependence on Z_{IN} and Z_{LD}. Nevertheless, as predicted in (15), G_D does not vary proportionally with Z as in the case of Z_{IN} and Z_{LD}. Fig. 6 shows the magnitude and phase of G_D calculated using different values of Z in the calibration procedure. It may be observed that (for this particular example) the calculation of $|G_D|$ does not vary significantly when the value of Z is varied. Even if the value of Z is considered as 1 Ω or as 50 Ω, the calculation of $|G_D|$ varies less than 10% from the $|G_D|$ calculated using the actual value of Z. The calculation of the phase of G_D, on the other hand, is greatly affected by errors in the knowledge of the Z.

IV. Conclusions

In this paper the impact of knowing the characteristic impedance of the lines used in the TRL calibration on the LP characterization of power transistors was analytically and experimentally shown. It was demonstrated that errors in the knowledge of the line's impedance has a negative impact on the determination of some important parameters of the LP characterization of power transistors.

Acknowledgement

This work was supported in part by the National Council for Science and Technology (CONACYT-Mexico) under Project INFR-2014-228580 and Project CB-2013-01-222949.

REFERENCES

[1] F.M. Ghannouchi; M.S. Hashmi, *Load-Pull Techniques with Applications to Power Amplifier Design*. Springer, 2012.

[2] G.F. Engen and C.A. Hoer, "Thru-Reflect-Line: An Improved Technique for Calibrating the Dual Six-Port Automatic Network Analyzer," *IEEE Trans. Microw. Theory Techn.,* vol.27, no.12, pp. 987- 993, Dec 1979.

[3] J.A. Reynoso-Hernandez, M.A. Pulido-Gaytan, M.C. Maya-Sanchez, and J.R. Loo-Yau, "What can the ABCD parameters tell us about the TRL?" *79th ARFTG Microw. Measurement Confer.*, pp.1-4, Jun. 2012.

[4] M.A. Pulido-Gaytan; J.A. Reynoso-Hernandez; J.R. Loo-Yau; A. Zarate-de Landa; M.C. Maya-Sanchez, "Generalized Theory of the Thru-Reflect-Match Calibration Technique," *IEEE Trans. Microw. Theory Techn.*, vol.63, no.5, pp.1693-1699, May 2015.

[5] U. Pisani; A. Ferrero, "A unified calibration algorithm for scattering and load pull measurement," *IEEE Instrumentation and Measurement Technology Conference.* pp. 1250-1253, Jun 1996.

[6] A. Ferrero; U. Pisani, "An improved calibration technique for on-wafer large-signal transistor characterization," *IEEE Trans. Instrum. Meas.,* vol.42, no.2, pp.360,364, Apr 1993

[7] Peter Aaen, J.A. Plá, D. Bridges, and E. Shumate, "A wideband method for the rigorous low-impedance load-pull measurement of high-power transistors suitable for large-signal model validation," *56th ARFTG Microw. Measurement Confer.*, pp.163-169, Dec. 2000.

[8] J.A. Reynoso-Hernandez, M.A. Pulido-Gaytan, A. Zarate-de Landa, J.E. Zuniga-Juarez, J.R. Monjardín-Lopez, A. Garcia-Osorio, D. Orozco-Navarro, J.R. Loo-Yau, and M.C. Maya-Sanchez, "Using lines of arbitrary impedance as standards on the TRL calibration technique," *81st ARFTG Microwave Measurement Conference*, pp.1-4, Jun. 2013.

APPENDIX

The seven terms necessary for the relative calibration of a LP measurement setup may be determined by using this TRL procedure. The *ABCD*-parameters are used to represent the VR measurements and the structures shown in Fig.10. Unlike the previously published TRL procedure using *ABCD*-parameters [3], this TRL allows determining the seven calibration terms without knowledge of line's impedance (*Z*). This feature allows expressing some parameters of the LP characterization of a DUT as explicit functions of *Z* in section II of this paper.

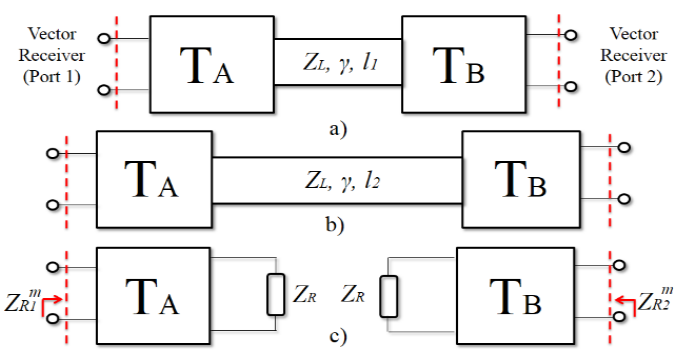

Fig.10. TRL structures a) thru, b) line and c) symmetrical reflecting load. The measurements of the structures are carried out by using the VR ports.

In this TRL, the *ABCD*-parameters matrix of a transmission line of length *li*, propagation constant γ, and characteristic impedance *Z* is expressed as in [4] as

$$\mathbf{T_{Li}} = \mathbf{T_Z}\mathbf{T_{\lambda i}}\mathbf{T_Z^{-1}}, \tag{A1}$$

where

$$\mathbf{T_Z} = \begin{bmatrix} -Z & Z \\ 1 & 1 \end{bmatrix}, \tag{A2}$$

$$\mathbf{T_{\lambda i}} = \begin{bmatrix} \lambda_i & 0 \\ 0 & \lambda_i^{-1} \end{bmatrix}; \tag{A3}$$

$\lambda_i = e^{-\gamma l_i}$, *i=1,2*. Thus, the equivalent *ABCD*-parameters matrix of the structures shown in Fig.10a-b may be expressed as

$$\mathbf{M_i} = \mathbf{T_A}\,\mathbf{T_{Li}}\,\mathbf{T_B} = \mathbf{T_X}\,\mathbf{T_{\lambda i}}\,\mathbf{T_Y}\ , \tag{A4}$$

with $\mathbf{T_X}$ and $\mathbf{T_Y}$ defined as follows

$$\mathbf{T_X} = \mathbf{T_A}\,\mathbf{T_Z} = D_X \begin{bmatrix} \overline{A_X} & \overline{B_X} \\ \overline{C_X} & 1 \end{bmatrix}, \tag{A5}$$

$$\mathbf{T_Y} = \mathbf{T_Z^{-1}}\,\mathbf{T_B} = D_Y \begin{bmatrix} \overline{A_Y} & \overline{B_Y} \\ \overline{C_Y} & 1 \end{bmatrix}. \tag{A6}$$

The seven terms to be determined are: $\overline{A_X}$, $\overline{B_X}$, $\overline{C_X}$, $\overline{A_Y}$, $\overline{B_Y}$, $\overline{C_Y}$ and $D_X D_Y$. According to the procedure reported in [3], expressions for four of these terms ($\overline{A_Y}$, $\overline{B_Y}$, $\overline{C_Y}$ and $D_X D_Y$) are derived by using the measurement of a transmission line provided that $\overline{A_X}/\overline{C_X}$, $\overline{B_X}$, $\overline{C_X}$ and γ are known.

The terms $\overline{A_X}/\overline{C_X}$ and $\overline{B_X}$ and γ are determined by combining the measurements of the two structures shown in Fig.10a-b. Let calculate $\mathbf{M_{21}} = \mathbf{M_2}\mathbf{M_1^{-1}}$ using (A4)-(A6) as

$$\mathbf{M_{21}} = \mathbf{T_X}\mathbf{T_\lambda}\mathbf{T_X^{-1}} \triangleq \begin{bmatrix} m_{11} & m_{12} \\ m_{21} & m_{22} \end{bmatrix}, \tag{A7}$$

with $\mathbf{T_\lambda} = \mathbf{T_{\lambda 2}}\mathbf{T_{\lambda 1}^{-1}}$. Then, by developing (A7) and equating term by term the resulting expression, using (A3) and (A5), the following expressions are obtained

$$\overline{A_X}/\overline{C_X}, \overline{B_X} = \frac{(m_{11}-m_{22}) \pm \sqrt{(m_{11}-m_{22})^2 - 4m_{21}m_{12}}}{2m_{21}} \tag{A8}$$

$$\gamma = \ln\left(\frac{\overline{A_X}/\overline{C_X}\,m_{11} + m_{12} - \overline{A_X}/\overline{C_X}\cdot\overline{B_X}m_{21} - \overline{B_X}m_{22}}{\overline{A_X}/\overline{C_X} - \overline{B_X}}\right)\cdot\frac{1}{l_2 - l_1}. \tag{A9}$$

The appropriate root in (A8) may be determined by using the criterion $\mathrm{Re}(\overline{B_X}) > \mathrm{Re}(\overline{A_X}/\overline{C_X})$.

Finally, $\overline{C_X}$ may be calculated by using a pair of reflecting loads (Fig.10c) as [4]

$$\overline{C_X} = \pm\sqrt{(\eta_1/\eta_2)\overline{A_Y}\cdot\overline{C_X}}\ , \tag{A11}$$

where

$$\eta_1 = \left(Z_{R1}^m - \overline{B_X}\right)\Big/\left(Z_{R1}^m - \overline{A_X}/\overline{C_X}\right), \tag{A12}$$

$$\eta_2 = \left(1 - \overline{C_Y}Z_{R2}^m\right)\Big/\left(Z_{R2}^m - \overline{B_Y}/\overline{A_Y}\right). \tag{A13}$$

In (A12)-(A13), Z_{R1}^m and Z_{R2}^m represent the impedances at the input of ports one and two of the VR (Fig.2a) when a pair of loads of impedance Z_R are connected at the calibration reference plane. $\overline{A_Y}\cdot\overline{C_X}$ and $\overline{B_Y}/\overline{A_Y}$ may be determined by using the measurement of a transmission line, as presented in [3]-[4].

Improved RSOL Planar Calibration via EM Modelling and Reduced Spread Resistive Layers

M. Spirito[1], L. Galatro[1], G. Lorito[2], T. Zoumpoulidis[2], F. Mubarak[1,3]

[1]Delft University of Technology, Electronic Research Laboratory (ERL), Delft, The Netherlands
[2]Iszgro Diodes BV, Delft, The Netherlands
[3]Van Swinden Laboratorium (VSL), Delft, The Netherlands

***Abstract* — In this contribution we analyze the accuracy improvements of Reciprocal SOL planar calibrations when employing full-wave EM simulation to extract the standard's models. The calibration accuracy is benchmarked with the conventional (polynomial fit) standard definitions as well as with calibration techniques employing standards with partially-unknown parameters, as the LRM.**

Moreover, an outlook at a technology based on integrated circuit fabrication, employing fused silica substrates is described in terms of the achievable spread of its conductive and resistive layers. Such technology, in combination with the proposed EM modelling of the standards would allow to reduce the residual errors of planar calibrations.

***Index Terms* — VNA, calibration, on-wafer, EM simulation, fused silica.**

I. Introduction

The accuracy of a vector network analyzer (VNA) calibration is directly related to the knowledge of the standards employed in the procedure. Traditionally, calibration techniques requiring little standards knowledge (e.g., TRL, LRL, LRM) have been considered the most accurate, with TRL reaching metrology institute precision, by only requiring the information of the characteristic impedance of the line [1].

Nevertheless, when moving to broad-band calibration in an on-wafer environment, reduces the practical usability of TRL. This is due to the large number of lines required by multi-line TRL [2], which occupy a large chip/substrate area and impose large probe movements, due to the different lines lengths.

More space efficient calibration procedures, such as the LRM [3], suffer from a non-reactive load in its original definition. Imposing partial or full knowledge of some standards allows to extract or incorporate a reactive behavior in the match load, as done in the LRRM [4] and LRM+ [5].

Nevertheless, as the TRL also the LRM technique sets the calibration reference plane in the middle of the (non-zero) coplanar thru line, thus requiring an accurate model of the thru to shift the reference plane back to the probe tips.

When coupled with accurate standard models, the reciprocal SOL (RSOL) using an unknown thru [6] can provide accuracy levels comparable to those of the TRL technique [7][8] directly setting the reference plane at the probe tips. Moreover, the lumped nature of the employed standards, when compared to TRL/LRM techniques, makes some of the standards employed in the RSOL less sensitive to probe is placement. Up to date only simple, purely reactive models are provided with commercially available calibration kits, due to the required compatibility with old firmware analyzers.

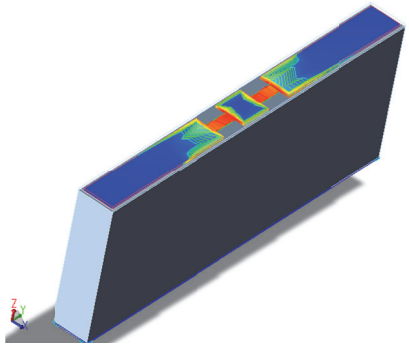

Fig. 1: 3D model of match load after Momentum simulation, indicating field intensity over the conductor and resistive layer surfaces.

In [7] accurate frequency dependent models were acquired employing a measurement procedure, thus requiring a first-tier accurate calibration to be performed.

In this contribution we propose the use of full wave EM simulations to extract the standard's behavior, thus increasing the accuracy of the calibration without increasing the complexity or number of measurements.

The paper is structured as follows, first the EM model generation is described and benchmarked against the conventional standard definitions using an experimental one-port calibration. After, we analyze the error propagation due to probe misplacement for the RSOL and LRM calibration, using a measurement based simulation environment coupled with electro-magnetic models for the planar standards. Finally, a technology outlook on next generation calibration standards implemented using integrated circuit manufacturing techniques on fused silica is given. The accurate control (vertical) of the conductive and resistive layers is presented by means of their resistivity uniformity over a 4 inch wafer. Moreover the height control of thin wafers and the suppression of possible roughness arising from the carrier substrate is presented using TEM images.

978-1-4673-9247-1/15/$31.00 ©2015 IEEE

II. EM Modelling of The Standards

In order to accurately extract the frequency response of the standards, a precise measurement of the dimension was performed using a Dektak 8 profilometer with a few nanometer of vertical resolution together with an optical analysis with a reference scale.

The standards composing a Cascade Microtech ISS model 101-190C were then drown and simulated in a 2.5D fullwave EM environment (i.e., Keysight Momentum), as shown in Fig. 1. As was mentioned in [8], the short and open standard are fundamentally determined by their inductive and capacitive behavior, respectively, as also included in the simple polynomial fitting approach provided by the manufacturer of commercial kits. Nevertheless, the absence of the (small) conductive losses makes the models inaccurate and often leading to non-physical s-parameters, i.e., reflective standard providing $|\Gamma|>1$.

The largest difference between the model provided by the manufacturer and the EM simulated one is observed on the load standard, see Fig. 2. Here is clearly seen that the pure inductive model of the load is inaccurate, since the large capacitive loading provided by the contacting metal stripes is neglected, or under estimated when included as a negative inductance [4].

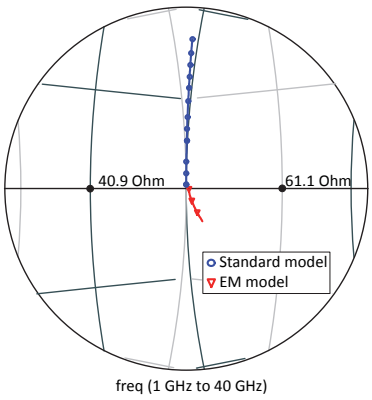

Fig. 2: Zoom-in of Smith chart presenting the standard model from the kit manufacturer and the EM extracted model for the load resistor.

A. Experimental benchmarking of commercial standards

In order to evaluate the impact of the new standard definitions (derived from the EM simulations) various one-port measurements were performed.

When analyzing data from the open termination, while no information of the accuracy can be derived, being the SOL a fully known calibration, it is evident from Fig. 3 that only a definition of the standard including losses (right), avoids the generation of non-physical s-parameter data (left).

The improved accuracy achieved when using EM simulations for the standards definition can be better quantified using a worst case bound metric. Here, two calibration were performed on the same set of measurements using the classical models (std.) and the proposed ones (EM).

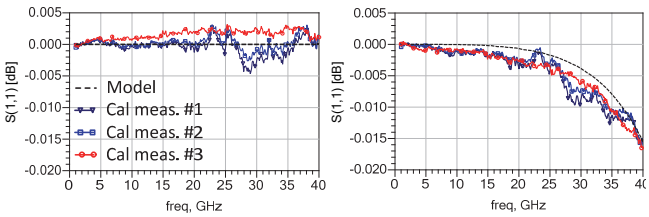

Fig. 3: Measurement versus model of the open standard: (left) employing standard model definitions, (right) employing EM extracted model definition for the calibration.

After, three raw measurements where performed on different samples of a 220um 50 Ohm line, with port two left open and the two calibration terms where applied to the same data. All the data acquisition, generation of the calibration terms, and data correction was performed using Cascade Microetch Wincal XE ver. 4.5 [9].

In order to compare the different calibrations, the method of [10] has been adapted to a one port-calibration , defining an error metric (for the standard and the EM calibration) as:

$$WCB = \max\left|S'_{11,n} - S_{11}\right| \qquad (1)$$

Where S_{11} is the s-parameter associated to the reference data (i.e., simulation of the open-ended thru line), and $S'_{11,n}$ is the nth s-parameter measured with $n \in [1,2,3]$.

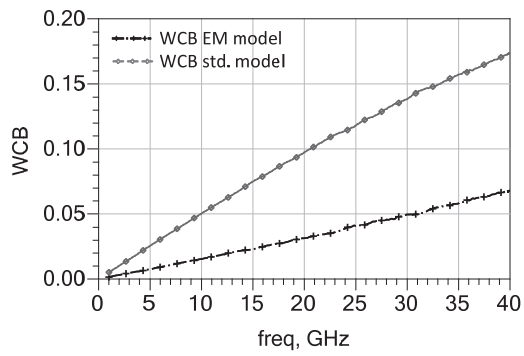

Fig. 4: Worst case error bound (WCB) as computed from equation 1, among three calibrated measurement employing the standard models (○) and the EM derived models (+).

Fig. 4 indicates how the WCB for the calibration using EM simulated standards is well below the value achieved by the conventional standard definitions.

III. Measurement Based Simulation Environment

When considering two-port s-parameter measurements we can opt for different calibration algorithms, which impose diverse requirements on the standard's knowledge. In order to evaluate the differences in uncertainty and accuracy, with the constraints of on-wafer calibration, we need to propagate the errors caused by probe misplacement through the various

calibration algorithms. For this purpose a simulation environment was created in the Keysight ADS environment as described in [11], see Fig. 5.

To correlate the simulation environment to the experimental setup, a calibration was first performed on the VNA in the frequency band of interest, including probes and cables as will be used in the final experimental analysis. The input and output error-terms (e_d, e_s and e_t) were extracted from the VNA and converted in a two port data item imposing $S21=e_t$ and $S12=1$.

Using this approach, when performing a calibration in the simulation environment, the computed error-terms will be exactly the one of the considered measurement setup.

At this point the calibration standards created in the Momentum EM environment (see section II) are converted in a parametric model, where the variable is the offset of the EM port to the nominal position, see Fig. 6.

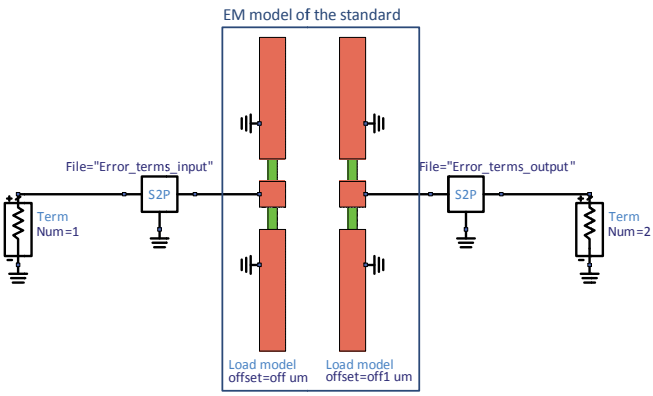

Fig. 5: Block diagram of measurement system, using experimental setup error model, implemented in Keysight's Advanced Design System (ADS) software.

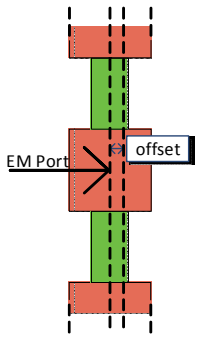

Fig. 6: Offset variable in parametric EM models used to propagate probe misplacement through different calibration algorithms.

The calibration techniques compared by the proposed simulation approach were the RSOL and LRM technique. The first technique requires full knowledge of the one-port standards (SOL) while only requiring passivity from the two-port connection. The LRM technique, in its original form, requires full knowledge of the two-port standard (i.e. thru), a known resistive behavior from the match termination, and only the phase quadrant information of the reflect (i.e., knowledge if it has an open or short behavior). Moreover the LRM technique employs one standard less than the RSOL. A Montecarlo simulation (employing 101 iterations) is then performed on two independent uniformly distributed variables representing the EM port position (i.e., mapping the probe misplacement at port one and two) of ±7.5µm.

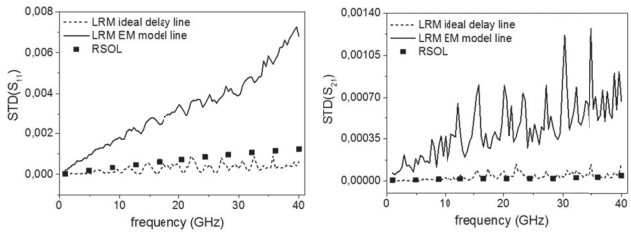

Fig. 7: Standard deviation computed from the Montecarlo simulation, for the magnitude of the reflection (left) and transmission (right) parameter for: the RSOL calibration (symbols) and the LRM one employing an ideal delay line (dashed) or the realistic EM simulated line (solid).

After the simulation the standard deviation versus frequency is computed for the RSOL and LRM calibration. When employing a realistic thru line (with small mismatch and fluctuation in the group delay) it can be seen that the LRM technique results in a large standard deviation (i.e., propagated uncertainty from the probe misplacement) for both reflection and transmission terms, Fig. 7 left and right, respectively. Only when the thru line is replaced with an ideal delay line (i.e., no mismatch and delay fluctuation) does the LRM present an uncertainty comparable to the RSOL. Note, that this indicates that an accurate model of the thru line is required to properly apply the LRM calibration, which is in contrast to the simple data available from the calibration substrate definitions.

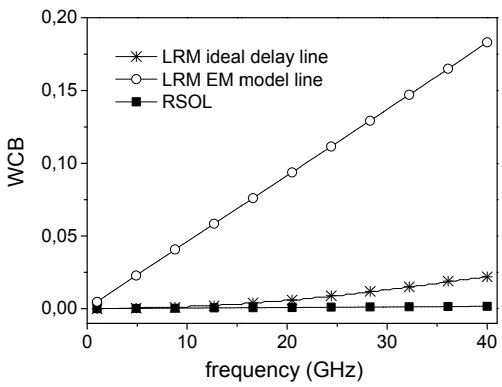

Fig. 8: Worst case error bound computed as in [10] from simulated data using as a 450µm verification device line and employing the EM simulation of the line as the reference for the metric computation.

When computing the WCB (computed using the mean value of the S parameters, as obtained from the Montecarlo simulation) as described in [10] we see a similar trend as seen for the uncertainty, with the LRM using the EM simulated data presenting the largest error. Note, that even when we

employ an ideal delay line, the non-zero WCB is due to the reactive component of the load, which is not properly accounted by the standard LRM. As mentioned in section I, by providing more knowledge on the standards (i.e., model of the reflect or non-ideal load behavior) the error bound of the LRM can be reduced, when doing so, the reduced standard requirements of the technique are traded away. It is important also to mention that the error bound of the RSOL only represents a best case scenario, since within the simulation environment there is no discrepancy between the knowledge of the standards and the standards itself, this is obviously not the case for real devices.

IV. Two-Port Experimental data

In order to validate the simulation findings of section III, two-ports measurements were conducted on a Cascade Microtech ISS model 101-190C. A unique set of raw data of the standards was employed to derive the error-terms for the RSOL, employing manufacturer and EM definitions, and the LRM calibration. All the data acquisition, generation of the calibration terms, and data correction was performed using Cascade Microetch Wincal XE ver. 4.5 [9].

A raw measurement of a 450µm line present on the same calibration substrate was used to compare the data obtained applying the three set of error terms mentioned above and compute a WCB. As done for the error computed in Fig. 8 also here the EM simulation of the 450µm line was used as reference data. The WCB is shown in Fig. 9, indicating a similar behavior for the LRM as expected from simulation. The RSOL employing standards definition through EM simulations provides an improvement in the error bound, compared to the conventional definition, confirming the findings of section II.

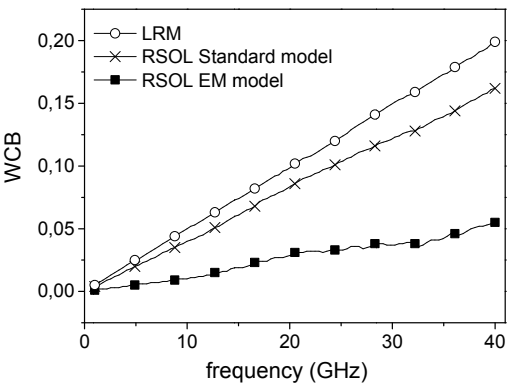

Fig. 9: Worst case error bound computed as in [10] from experimental data, using 450µm line as a verification device and employing the EM simulation of the line as the reference for the metric computation.

In general it can be stated that the WCB presented in Fig. 9 will depend strongly on the position placement accuracy for the LRM, and on the consistency of the model with the artifact for the RSOL. For this reason, the RSOL trades off complexity in the probing environment (i.e., motorized manipulators) for higher quality standards.

V. Fabrication Technology

As it has been discusses in the previous sections in order to achieve accurate on-wafer calibration the manufacturing quality of the standards needs to be improved.

In [8] it was shown that the variation of the load resistance is one of the biggest sources of uncertainty in planar SOL type calibrations. When accurate models of the standards are employed it becomes crucial to fabricate these standards and especially the load with as little variation as possible. In this section we present some preliminary results of the performance achieved by employing integrated circuits processing techniques to manufacture the calibration standards. The aimed process is based on a fused silica substrate with a simple layer stack of a resistive nitride layer and a conductive aluminum layer as sketched in Fig. 10.

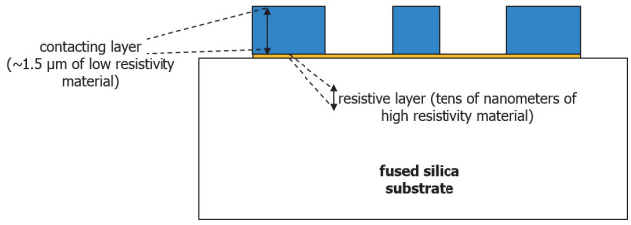

Fig. 10: Schematic cross-section of the 50 Ohm resistors fabricated on fused silica substrate.

First analysis of the uniformity of the conductive layer, measured using a 4-probe resistance measurement over the entire 4 inch wafer, show a σ variation close to 1.2%. This leads to a variation within the 2x2 cm^2 calibration die around 1% (see Fig. 11).

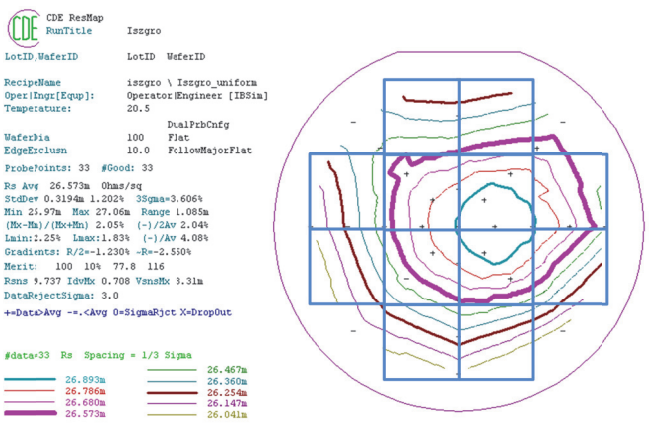

Fig. 11: Resistivity contour map over the 4 inch wafer, superimposed by the grid of 2x2 cm^2 dies. Measured standard deviation over 33 points over the entire wafer is 1.202%.

Similar measurement performed on the resistive layer show within the die a standard deviation just above 1%. The target

for the process optimization is a variation below 0.5% within the die, which would allow to remove the process of laser trimming of the resistors.

Preliminary tests on the conductive layer show a smooth surface already after 200 nm thickness, in spite of the presence of a rough substrate (see Fig. 12). The targeted substrate (i.e., fused silica), however, will provide extremely flat polished surfaces. Based on this, it is reasonable to assume that the layer roughness in the final devices will be negligible.

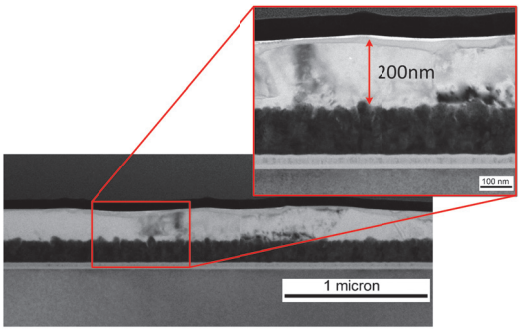

Fig. 12: TEM image of 200nm aluminum layer sputtered over a rough surface. As it can be seen by the inset the roughness is already absorbed after 200nm.

Moreover, the tests conducted on the resistive layer have shown a very good control of the targeted layer thickness (around 80 nm) and a defect-free aluminum-to-nitride interface (see Fig. 13).

As last technology remark, it has to be mentioned that all the lithography steps of the fabrication process will be performed with an ASML PAS 5500 wafer-stepper. This allows for an accuracy of few hundreds of nanometers in the planar dimensions of the final devices.

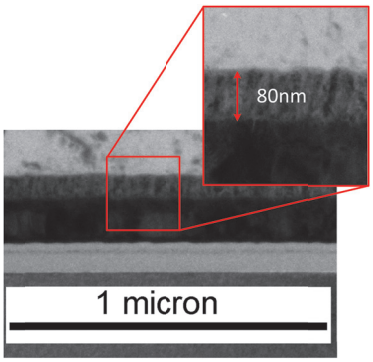

Fig. 13: TEM image of the targeted 80 nm resistive layer.

VI. Conclusions

In this paper we presented the accuracy improvement which can be obtained employing full wave EM simulations to generate the planar calibration standard definitions. In both one-port and two-port experimental verification the usage of the improved standard definitions allowed to avoid non-physical s-parameter behavior and a reduced worst case error bound. Moreover, the error propagation due to probe misplacement was analyzed in a simulation environment to compare RSOL and standard LRM calibrations. The insensitivity of the RSOL to the probe misplacement of the thru device led, in conjunction with the improved standard definitions, to a reduced worst case error bound. Experimental data was presented confirming the simulation analysis. Finally, and outlook of a technology to potentially improve the manufacturing quality of the standards was briefly discussed.

References

[1] G. F. Engen and C. A. Hoer, “Thru-Reflect-Line: An Improved Technique for Calibrating the Dual Six-Port Automatic Network Analyzer,” *Microwave Theory and Techniques, IEEE Transactions on,* vol. 27, no. 12, pp. 987-993, Dec. 1979.

[2] D.C. De Groot, J.A. Jargon, and R.B. Marks, "Multiline TRL revealed," 60th ARFTG Conf. Dig., Washington, D.C, Fall 2002, pp. 131-155.

[3] H. J. Eul and B. Schiek, “Thru-Match-Reflect: One result of a rigorous theory for deembedding and network analyzer calibration,” in hoc. 18th Euro. Microwave Conf, Sept. 1988, pp. 909-914.

[4] A. Davidson, E. Strid, and K. Jones, “LRM and LRRM calibrations with automatic determination of load inductance,” 36th ARFTG Conf Dig., pp. 57-62, Nov. 1990.

[5] R. Scholz, F. Komdoerfer, B. Senapati, A. Rumiantsev. "Advanced Technique for Broadband On-Wafer RF Device Characterization", 63rd ARFTG Conf. Digest, pp. 83-90, June 2004.

[6] A. Ferrero, U. Pisani, "Two-port network analyzer calibration using an unknown 'thru'," in Microwave and Guided Wave Letters, IEEE , vol.2, no.12, pp.505-507, Dec. 1992

[7] M. Imparato, T. Weller, L. Dunleavy, “On-Wafer Calibration Using Space-Conservative (SOLT) Standards”, 1999 MTT-S Int. Microwave Sym. Digest, pp. 1643-1646.

[8] S. Padmanabhan, L. Dunleavy, J. E. Daniel, A. Rodriguez, and P. L. Kirby, “Broadband space conservative on-wafer network analyzer calibrations with more complex load and thru models,” IEEE Trans. Microw. Theory Tech., vol. 54, no. 9, pp. 3583–3593, Sep. 2006.

[9] WinCal 2006, Cascade Microtech Inc., Beaverton, OR. Note: eLRRM is in release SP1 (version 4.0.1) available Feb. 2006.

[10] D. Williams and R. B. Marks, “Calibrating On-Wafer Probes to the Probe Tips,” *ARFTG Conference Digest-Fall, 40th,* vol. 22, pp. 136-143, Dec. 1992.

[11] F. Mubarak, R. Romano and M. Spirito, “Evaluation and Modeling of Measurement Resolution of A Vector Network Analyzer for Extreme Impedance Measurements”, to be presented at the *86th ARFTG Conference Fall,* Dec. 2015, Atlanta, Georgia, USA.

Calibration/Verification Standards for Measurement of Extremely High Impedances

Martin Haase, Karel Hoffmann

Czech Technical University in Prague, Prague, Czech Republic

***Abstract* — The paper concerns the design of calibration/verification standards suitable for a system developed to be capable of measuring extreme impedances. Values of standard impedances cover the range from 5 kΩ to approx. 200 kΩ. The paper focuses on selecting a structure compatible with an APC-7 connector and its optimization taking into account also the presence of higher order modes and technology demands. CST Microwave Studio (CST) is used for simulations. S-parameters of the final structure are verified by means of an independent 3D simulator ANSYS HFSS (HFSS).**

***Index Terms* — CST, High impedances, HFSS, Higher order modes, Measurement standards, Microwave connectors, Resistors, Scanning microwave microscopy, Thin film devices.**

I. Introduction

Extreme impedances are often discussed in relation to nanoscale devices [1] – carbon nanotubes and nanowires. As their DC resistance is of the order of kΩ, broadband RF characterization, with common 50 Ω vector network analyzers (VNAs), remains a great challenge due to significant impedance mismatch [2]-[3]. This reality results in worse VNA stability and poor accuracy (high measurement uncertainty). The measurements are practically insensitive to variations of the measured impedance since the reflection coefficient varies in the area of extreme impedances at the order of 10^{-2} and less which is comparable or even smaller value in comparison to VNA measurement uncertainty, see for instance [4]. Another area related to the measurement of extreme impedances is scanning near-field microwave microscopy [5]. This technique, used for local characterization of materials, employs a microwave microscope consisted of a near-field probe associated to common microwave measurement instruments. Near-field probes exhibit impedances in the range of tens or hundreds of kΩ.

A method which substantially improves the measurement uncertainty of the VNA and enables measuring the extreme impedances by VNA has been developed and published in [6] and [7]. A calibration process requiring at least three fully known calibration standards was also proposed. It was recommended to use standards located in the area of extreme impedances to fully utilize the ability of the developed method.

The first verification measurements of the recommended concept based on SMD resistors [8] were not satisfactory due to low mounting repeatability and absence of well-defined standards. Therefore, a preliminary design of calibration standards combining the microwave coaxial connector APC-7 and a fused silica coaxial line, serving as a carrier for resistive strips, was proposed in [9]. APC-7 connectors were chosen with respect to their well-defined reference plane and high mounting repeatability. The authors analyzed different configurations of calibration standards with extremely high impedances in a frequency band up to 18 GHz to determine basic problems connected with the design. Subsequently, two extremely high impedance structures, see Fig. 1, and their potential applications have been proposed.

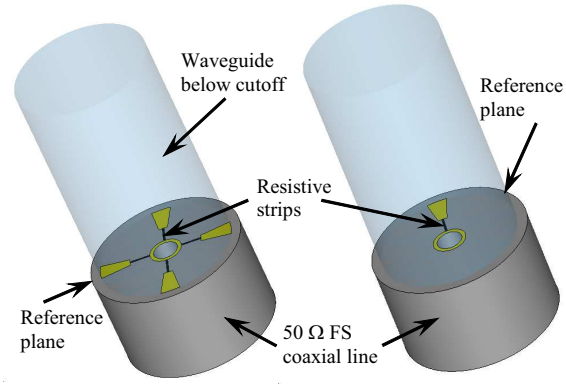

Fig. 1. Final structure from [9]

In this paper, in contrast to [9], the concept of calibration/verification standards was changed in terms of the reference plane position due to the complexity of the resistive strip behaviour and the presence of higher order modes. More detailed explanation is given in the following chapter.

The main objective of this paper is to introduce a final, optimized concept of well-defined calibration/verification standards based on APC-7 connector components. The S-parameters of the final structure achieved by CST simulations are compared with results obtained by the independent electromagnetic simulator HFSS in order to verify the correctness of the computed results.

II. Structure Optimization

The design of the standards was optimized to satisfy the following requirements: First, the structure of the standards has to be suitable for the calibration and subsequent verification and measurement at the reference plane of the APC-7 connector (7 mm coaxial line); Second, standards with extremely high impedances in the range from 5 kΩ to approx. 200 kΩ and Open are required; Third, to minimize the technological demands on fabrication, the structure of the

978-1-4673-9247-1/15/$31.00 ©2015 IEEE

standards should utilize individual parts of the APC-7 connector extremely effectively.

A. Mechanical optimization

The structure of the standards was designed so that the inner conductor and inner contact of the APC-7 connector could be used. The part of the inner conductor including the thread behind the bead is being removed, as shown in Fig. 2. The support bead of the standards was designed to be similar to the

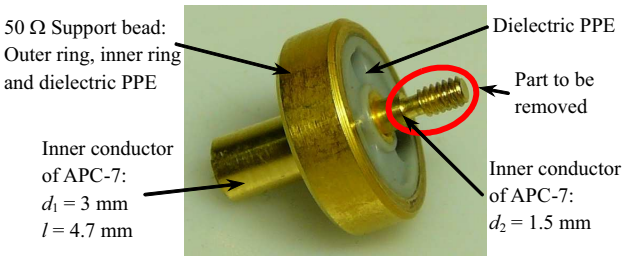

Fig. 2. Support bead and inner conductor of APC-7 connector.

support bead of the APC-7 connector but with a different dielectric fused silica (FS) with $\varepsilon_r = 3.8$ and without an inner ring. FS was chosen due to mechanical, electrical and technological reasons [9]. The diameter of the inner conductor of the FS coaxial line d_{in} in the new bead was adjusted to 1.5 mm whereas the outer diameter d_{out} was adjusted in the beginning to 7 mm, see Fig. 3. The FS line should be fixed in a new, gold-plated brass ring by a sufficiently conductive glue, and as well as the inner conductor should be fixed in the FS line. The length of the air coaxial line ($l_a = 4.7$ mm, see Fig. 3) is equal to the length of the inner conductor in the APC-7 connector with the diameter $d_1 = 3$ mm, see Fig. 2. Taking into account these mechanical constraints, the only parts to be optimized are the length of the FS coaxial line l_g, the resistive strips, the metal parts and the length of the air waveguide below the cut-off formed by the cylindrical part of the APC-7 connector with an inner diameter $d_w = 7$ mm, see Fig. 3.

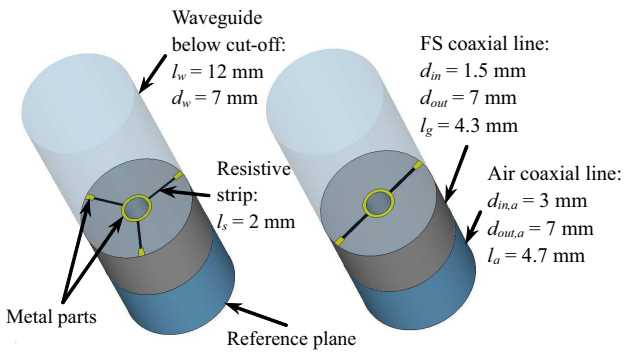

Fig. 3. Examples of simulated structures: two-strip and three-strip configurations.

B. CST simulations

In [9] the standards were comprised of resistive strips themselves and their pure resistive behaviour was expected due to their dimensions and presupposed TEM field distribution at the reference plane. But detailed simulations revealed frequency-dependent properties of the strips and presence of higher order modes. Therefore, the original assumption of pure resistive behaviour of resistive strips had to be abandoned and the reference plane was moved to the plane of APC-7 connector (7 mm air coaxial line), see Fig. 3. The current concept of standards comprising resistive strips, FS coaxial line, and air coaxial line is correct since they are described by computed S-parameters and not by values of an ideal resistor. The condition of TEM mode presence at the reference plane must be naturally fulfilled.

The simulated standards featured one to four resistive strips. Fig. 3 shows two such configurations. The available Cr-Ni resistive material, provided by a thin film technology, enables the maximum resistance approx. 1 kΩ/□. The technology limits the minimum width of the resistive strips to 5 µm and the Cr-Ni material limits the number of resistive strips as they are connected in parallel. Other aspects to be optimized, in terms of fringing capacitnace, are the length of the resistive strips and the shape and dimensions of the metal parts connecting the resistive strips to the inner and the outer conductor of the FS coaxial line. The necessary length l_w of the air waveguide below the cut-off was also properly determined so as not to influence the computed S-parameters. Corresponding length l_w must be at least 12 mm.

The two-strip symmetrical structure was chosen as a compromise between the available technology and acceptable symmetry. Some symmetrical configuration was required due to the presence of higher order modes in unsymmetrical structures, see [9]. Further, a different shape of the metal part, which connects the resistive strips to the outer conductor of the FS coaxial line, was chosen to ensure a satisfactory electric connection, see Fig. 4.

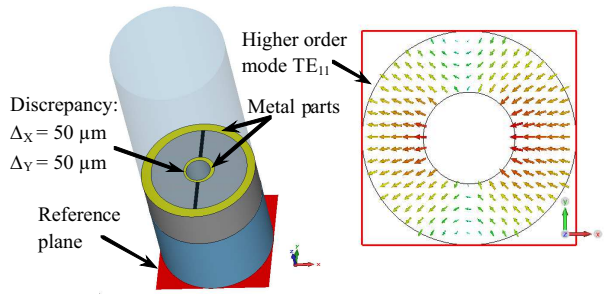

Fig. 4. Analyzed 5 kΩ standard and its electric field distribution at the reference plane at 15.66 GHz.

Symmetrical arrangements of resistive strips do not excite higher order modes in the analyzed structure, see [9]. However, some discrepancies in symmetry must be considered with respect to fabrication dimension uncertainties, see Fig. 4.

Discrepancies were analyzed for symmetrical standards with two, three and four resistive strips. The simulations showed that even a symmetrical structure with a small discrepancy in symmetry can excite higher order modes in the FS coaxial line. The two-strip structure excites a higher order mode TE_{11} in the FS coaxial line making a resonance of the analyzed structure at 15.66 GHz, see Fig. 5. This TE_{11} mode starts to

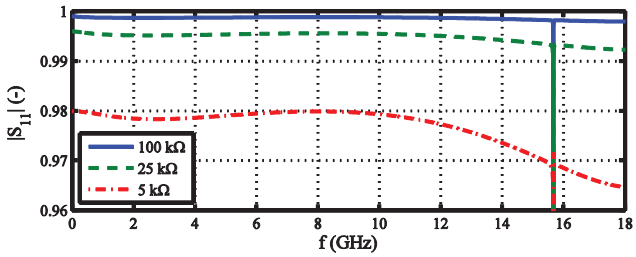

Fig. 5. $|S_{11}|$ of standards with different values (5 kΩ, 25 kΩ and 100 kΩ) but with the same discrepancy in the symmetry $\Delta x = \Delta y = 50$ µm.

propagate in the FS coaxial line from a frequency of 11.5 GHz due to its higher permittivity. The resonant frequency relates to the length of the FS coaxial line. The shorter the length, the higher the resonant frequency. Therefore, the length l_g was adjusted to 2.8 mm as a reasonable trade-off between resonant frequency, strong capacitive coupling, which was observed in [9] for very short FS coaxial lines, and robustness.

Fig. 4 shows the electric field distribution at the reference plane of the standard at the resonant frequency of 15.66 GHz where the TEM mode is strongly affected by the presence of the TE_{11} mode despite the fact that the air coaxial line forms a waveguide below the cut-off for this mode.

Nevertheless, it is possible to determine the maximum applicable frequency for the standard when l_a = 4.7 mm. At frequencies below 15 GHz the amplitude of TE_{11} mode is only 10^{-5} with respect to TEM mode amplitude. To ensure TEM mode only in the reference plane, the upper applicable frequency was limited to 14 GHz.

C. Final structure

Taking into account all of the aforementioned demands, the two-strip standards with 2 mm-long resistive strips were chosen for the final realization, see Fig. 6. The strips make it

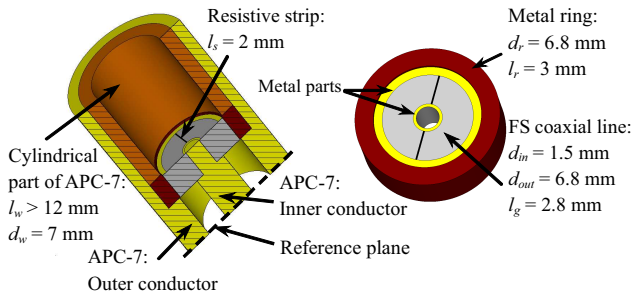

Fig. 6. Final structure of the standard with two 2 mm-long resistive strips and its new support bead.

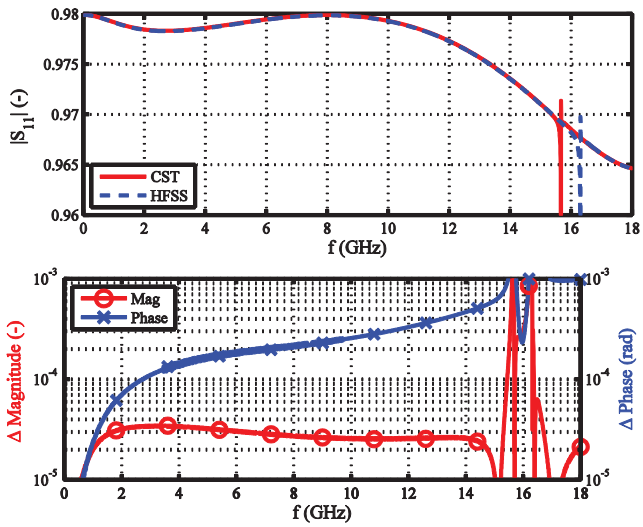

Fig. 7. A comparison of simulated S-parameter $|S_{11}|$ of the final 5 kΩ standard with discrepancy in symmetry ($\Delta_X = \Delta_Y = 50$ µm) using both simulators CST and HFSS.

possible to create standards with a range of resistance from 5 kΩ to 200 kΩ in the dependence on the width of the strip. Since the resistive strips are 2 mm long, the contact metal parts are far enough apart to minimize the fringing capacitance. The inner diameter d_r of the metal ring of the new support bead was adjusted to 6.8 mm, and the length l_r was set to 3 mm due to technological reasons, see Fig. 6. The structure without resistive strips forms the standard Open.

In order to verify the results achieved in CST, the standards were analyzed in the independent, electromagnetic simulator HFSS. It can be clearly seen that both computed S-parameters are in good correspondence below 14 GHz, see Fig. 7, as an example of the 5 kΩ standard. The difference in magnitude is to the order of 10^{-5}. The difference in phase increases with the frequency and is to the order of 10^{-4} radians. Nevertheless, at frequencies where higher order modes exist at the reference plane, the results are significantly different. It seems that each simulator works differently with higher order modes.

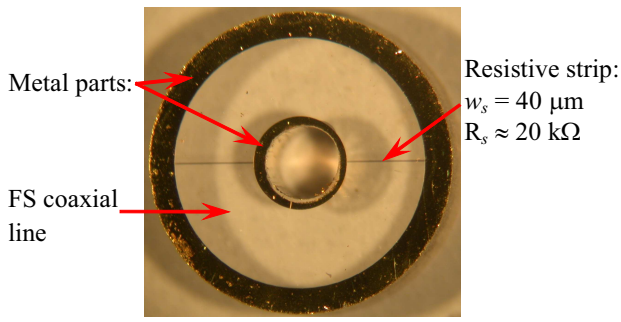

Fig. 8. An example of manufactured FS coaxial line with two deposited resistive strips each of the value approx. 20 kΩ and metallic parts.

A fabricated sample of the FS coaxial line with deposited resistive strips and metal parts is shown in Fig. 8 and some samples of new support beads with fixed inner conductor of APC-7 connector are depicted in Fig. 9. Ablebond 84-1LMINB1 die attach adhesive was used as the conductive glue.

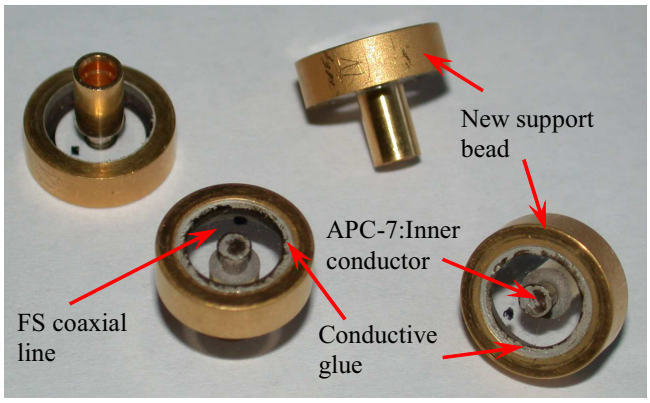

Fig. 9. An example of manufactured support beads with inner conductor of APC-7 connector.

Fig. 10 shows a disassembled sexless APC-7 adaptor (Rosenberger 02KR107-P0AS3) which enable to utilize two manufactured support beads and thus create two calibration standards each at the end of the adaptor.

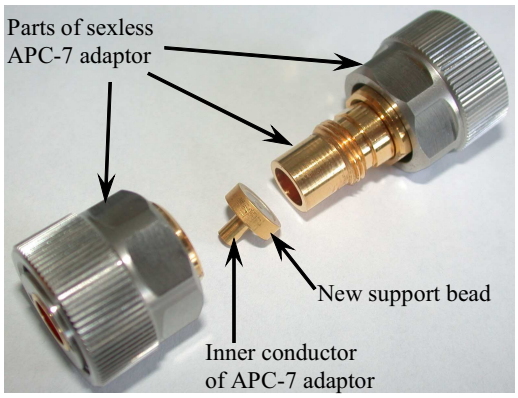

Fig. 10. An example of disassembled sexless APC-7 adaptor.

III. Conclusion

Well-defined calibration/verification standards, applicable up to 14 GHz, were developed. A comparison of results obtained by CST and HFSS showed a good correspondence between both simulators in a working frequency range limited by the TE_{11} mode. At least three different standards must be used for calibration, another as reference impedance, see [6] and [8], and the remaining enable verification measurements.

Standards are suitable for verification of the concept of high impedance calibration/verification standards for extreme impedance measurement. Experimental verification of standards and the whole concept is expected in the near future.

Authors realize that the current position of the reference plane does not enable to measure high impedance DUT. Nevertheless, the test fixture, compatible with manufactured standards, which enables to measure such DUT is being manufactured and will be used for experimental verification.

Acknowledgement

This work was funded through the European Metrology Research Programme (EMRP) Project SIB62 'Metrology for New Electrical Measurement Quantities in High-frequency Circuits'. The EMRP is jointly funded by the EMRP participating countries within EURAMET and the European Union.

References

[1] P. J. Burke, Z. YU, and C. Rutherglen, “Carbon nanotubes for RF and microwaves,” *Gallium Arsenide and Other Semiconductor Application Symp.*, Paris, pp. 1-4, Oct. 2005.

[2] A. Lewandowski, D. LeGolvan, R. A. Ginley, T. M. Wallis, A. Imtiaz, and P. Kabos, “Wideband measurement of extreme impedances with a multistate reflectometer,” *72nd ARFTG Microw. Meas. Symp.*, Portland, OR, pp. 45-49, Dec. 2008.

[3] H. Happy, K. Haddadi, D. Théron, T. Lasri, and G. Dambrine, “Measurement Techniques for RF Nanoelectronic Devices: New Equipment to Overcome the Problems of Impedance and Scale Mismatch,” *IEEE Microw. Mag.*, vol. 15, no. 1, p. 30–39, Jan. 2014.

[4] *R&S®ZVA Vector Network Analyzer Specifications*, Version 13.00, Rohde & Schwarz GmbH & Co. KG, Munich, Germany, 2015, pp. 10-18.

[5] H. Bakli, K. Haddadi, and T. Lasri, “Interferometric Technique for Scanning Near-Field Microwave Microscopy Applications,” *IEEE Trans. Instrum. Meas.*, vol. 63, no. 5, pp. 1281-1286, May 2014.

[6] M. Randus and K. Hoffman, “A method for direct impedance measurement in microwave and millimeter-wave bands,” *IEEE Trans. Microw. Theory Techn.*, vol. 59, no. 8, pp. 2123-2130, May 2011.

[7] M. Randus and K. Hoffman, “Microwave Impedance Measurement for Nanoelectronics,” *Radioengineering*, vol. 20, no. 1, pp. 276-283, Apr. 2011

[8] M. Randus and K. Hoffman, “A simple method for extreme impedances measurement – Experimental testing,” *72nd ARFTG Microw. Meas.Symp.*, Portland, OR, pp. 40-44, Dec. 2008.

[9] M. Haase and K. Hoffmann, “Study of calibration standards for extreme impedances measurement,“ *83rd ARFTG Microw. Meas. Conf.*, Tampa, FL, pp. 1-6, Jan. 2014.

Evaluation and Modeling of Measurement Resolution of A Vector Network Analyzer for Extreme Impedance Measurements

Faisal Mubarak[*†], Raffaele Romano[†] and Marco Spirito[†]

[*]Van Swinden Laboratorium (VSL), Thijsseweg 11, 2629 JA Delft, The Netherlands; fmubarak@vsl.nl

[†] Delft University of Technology, Electronic Research Laboratory (ERL), Delft, The Netherlands

***Abstract* — A broadband S-parameter measurement system for extreme impedance measurements is proposed and analyzed in terms of its accuracy. Measurement speed and system resolution at extreme impedance values is comparable to that of a conventional Vector Network Analyzer performance achieved for 50 Ω device measurements. A dedicated one-port calibration method is modeled in a circuit simulator environment and implemented for the proposed system. Compared to the 0.05 % measurement resolution in extreme impedance measurements using a state-of-art 50 Ω VNA, an almost fifty times lower 0.001 % resolution is achieved with the proposed VNA system utilizing an interferometric principle, with active compensation of reflected waves.**

***Index Terms* — Extreme impedance, S-parameter, VNA, interferometric principle, active compensation, SMM.**

I. Introduction

The number of applications and devices demanding a broadband instrument for extreme impedance measurements is rapidly growing, with the diversity of such devices ranging from nanoscale devices to high power amplifiers. They all share a similar metrological need, namely the availability of a broadband instrument with high measurement resolution at extreme impedance values. Conventional vector network analyzers (VNAs) lack the measurement resolution required for accurate characterization and modeling of devices with large mismatch in impedance with respect to the system reference impedance, i.e., 50 Ω. A major problem of such extreme impedance measurements is the large signal reflected back into the system, which causes significant degradation of measurement resolution and accuracy compared to the 50Ω cases.

This problem can be solved by applying interferometric techniques traditionally used in optical metrology in designing new microwave VNA systems. Such systems exploit an interferometric principle to cancel the large reflected signal and achieve system-level noise reduction. In [1], one of the first VNA systems relying on interferometric principles for extreme impedance measurements is proposed. The system realizes interferometry-based signal cancellation employing a 4-port hybrid coupler. However, the accuracy achieved with a hybrid coupler is limited by the non-perfect quadrature of the output signals, also resulting in bandwidth limitations. In [2], a mechanical impedance tuner with a power divider is employed to realize interferometric signal cancellation. However, this approach is limited in speed and repeatability when frequency sweeps are required.

The first attempt to realize signal cancellation employing *active* signal injection was proposed in [3]. In figure 1 a simplified block diagram of the measurement system is shown. The interferometric principle relies on injecting a continuous waveform (CW) signal in the direction of the reflected signal from the device under test (DUT). The objective of the injection signal is to cancel the reflected wave as if a matched device is measured. This results in significant instrument noise reduction at extreme impedance values. The superiority of the measurement system lies in its truly broadband and high speed measurement capability combined with the highest measurement resolution over the complete range of impedance values of interest, ranging from mΩ up to MΩ values.

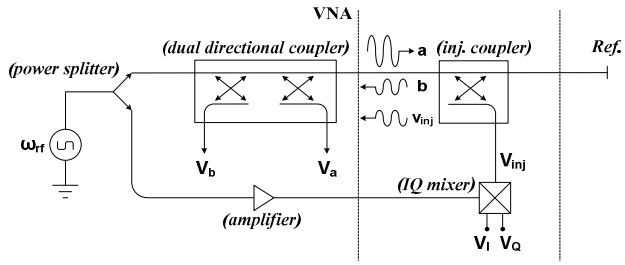

Figure 1. A system-level simplified block diagram of the measurement system based on the active signal injection principle.

In this contribution we present a simulation method to evaluate the measurement resolution over the entire impedance range of the proposed system with active compensation of reflected waves. A system-level model is designed to simulate the instrument performance. Furthermore, noise evaluation techniques are proposed and compared to the classically known methods. Measurement resolution of the proposed system is compared to the state-of-art S-parameter measurement system designed for matched device measurements.

978-1-4673-9247-1/15/$31.00 ©2015 IEEE

II. Measurement System

The proposed measurement system incorporates a conventional VNA together with external signal injection hardware to realize interferometry-based signal cancellation. In figure 1, the VNA is modeled with a dual bi-directional coupler to allow measurement of the forward 'a' and reverse 'b' waves. Phase coherence between the a-wave and the injected wave V_{inj} is necessary for metrology grade measurements. This phase coherence is realized by splitting of the a-wave into two separate signals using a power divider. The first the signal is fed back into the VNA and serves as the measurement signal. The second signal is amplified and used as the oscillator (LO) signal to drive the quadrature (IQ) mixer. The in-phase and quadrature-phase ports are sourced with DC signals generated with high precision 16 bit DACs and are used to steer the phase and vary the amplitude of the LO signal. The generated signal is injected into the VNA with a high-directivity coupler. The measurement reference plane is set at the output port of the coupler.

A. Calibration method

The one-port calibration of the measurement system is partly based on the widely used SOL (Short-Open-Load) method. The proposed system is modelled with three error-terms consisting of systems directivity, source match and reflection tracking terms.

The injection signal V_{inj} is switched off during the first three calibration measurements. The SOL method relies on three calibration devices with known electrical properties Γ_i, resulting in three independent measurements $\Gamma_{meas(i)}$ with three unknown error-terms, which are determined using the following system:

$$\begin{bmatrix} 1 & \Gamma_1 \cdot \Gamma_{meas(1)} & -\Gamma_1 \\ 1 & \Gamma_2 \cdot \Gamma_{meas(2)} & -\Gamma_2 \\ 1 & \Gamma_3 \cdot \Gamma_{meas(3)} & -\Gamma_3 \end{bmatrix} \cdot \begin{bmatrix} e_{00} \\ e_{11} \\ \Delta \end{bmatrix} = \begin{bmatrix} \Gamma_{meas(1)} \\ \Gamma_{meas(2)} \\ \Gamma_{meas(3)} \end{bmatrix} \tag{1}$$

$$\Delta = e_{00}e_{11} - e_{10}e_{01}$$

Here, the error-terms e_{00}, e_{11}, and $e_{10}e_{01}$ present directivity, source match, and reflection tracking of the calibrated VNA. The reflection coefficient Γ at calibration reference plane (ref. in fig. 1) can then be calculated using equation (2):

$$\Gamma = \frac{\Gamma_{meas} - e_{00}}{e_{10}e_{01} + e_{11} \cdot (\Gamma_{meas} - e_{00})} \tag{2}$$

Then, a highly mismatched device Γ_{HI} with accurate knowledge of its electrical properties serves as the fourth calibration device. The fourth calibration measurement is completed with the injection hardware turned 'on' and facilitates transfer of instruments' high sensitivity (achieved for matched devices) to mismatched devices with extreme impedance values. The injected signal is controlled such as if the matched 50-Ω calibration device used for initial SOL calibration is measured. The amplitude and phase of V_{inj} is set such as to match the calibrated Γ of high impedance device to the Γ of a matched 50-Ω device. The following criterion is set in the optimization algorithm:

$$0.0005 \leq |\Gamma_{50\Omega} - \Gamma_{HI}| \tag{3}$$

with:

$\Gamma_{50\Omega}$ *50Ω device calibrated Γ using E-terms from initial SOL calibration.*

Γ_{HI} *High impedance device calibrated Γ using E-terms from initial SOL calibration and injection signal turned-on.*

With optimized amplitude and phase values of V_{inj}, a highly mismatched measurement with superior sensitivity is possible. The calibrated Γ is furthermore used to calculate the device impedance using equation (4).

$$Z = Z_{HI} \left(\frac{1-|\Gamma|}{1+|\Gamma|}\right) \tag{4}$$

with Z_{HI} the impedance value of the high impedance device used during VNA calibration.

III. Measurement System Modeling

The system-level model designed in Keysight's Advanced Design System (ADS) software is shown in figure 2. The model is designed for evaluation of measurement resolution of the system at extreme impedance values. An ideal reflectometer is added in the system-level model. The reflectometer is built using an ideal bi-directional coupler and allows measurements of individual forward and reflected waves. It can be seen as an ideal one-port VNA. To replicate linear operation of a one-port VNA in the model, the three calibrated error-terms are used. A two-port network comprising of calibrated error-terms is included into the system-level model. The method allows for exact mapping of VNA operation in the model. The ideal reflectometer is positioned before the two-port network having one-port VNA error-terms. This method results in exact linear functional behavior between a- and b-waves of the model, as present in the VNA. To realize interferometry-based signal cancellation, a high-directivity coupler is used to inject a signal to optimize the reflected wave.

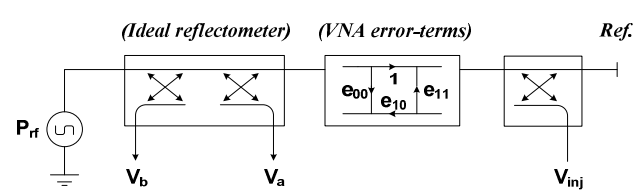

Figure 2. Block diagram of measurement system model designed in Keysight's Advanced Design System (ADS) software.

B. Modelling of system-level noise

VNA noise is classified into two groups: thermal noise and trace noise. The dominant source of noise considerably depends on the electrical properties of the devices. The origin of each noise source is assessed by calculating the sensitivity coefficients of the reflection coefficient and each error-term of the VNA. For a typical one-port calibration of a VNA, the following approximations hold: e_{00}, $e_{11} \approx 0$ and $e_{10}e_{01} \approx 1$. The sensitivity coefficient values can then be derived via:

$$\frac{\partial \Gamma}{\partial e_{00}} \approx -1\,, \quad \frac{\partial \Gamma}{\partial e_{11}} \approx -\Gamma_{\text{meas}}^2\,, \quad \frac{\partial \Gamma}{\partial e_{10}e_{01}} \approx -\Gamma_{\text{meas}} \qquad (5)$$

The measurement noise for matched devices with reflection coefficient linear magnitude value smaller than 0.05 is set by the noise floor of the VNA. From equation (5) it is clear that in this case the noise floor originates from the directivity e_{00} term, and that the influence of the reflection tracking e_{11} and source-match $e_{10}e_{01}$ terms is negligible. The noise floor uncertainty u_{nf} is calculated as standard deviation from a series of measurements with a matched 50-Ω device [4]. For highly mismatched devices with reflection coefficient linear magnitude value greater than 0.1, instrument trace noise uncertainty u_{tn} adds significantly to the total measurement noise. Instrument trace noise for high reflection devices is calculated as the standard deviation from a series of measurements with a high-reflection short device termination [4]. The trace noise result is strongly correlated with reflection tracking and source match terms. For simplicity, the evaluated trace noise uncertainty is assigned only to reflection tracking $e_{10}e_{01}$ term.

$$e_{00} = e'_{00} + u_{\text{nf}}$$
$$e_{10}e_{01} = e'_{10}e'_{01} + u_{\text{tn}} \qquad (6)$$

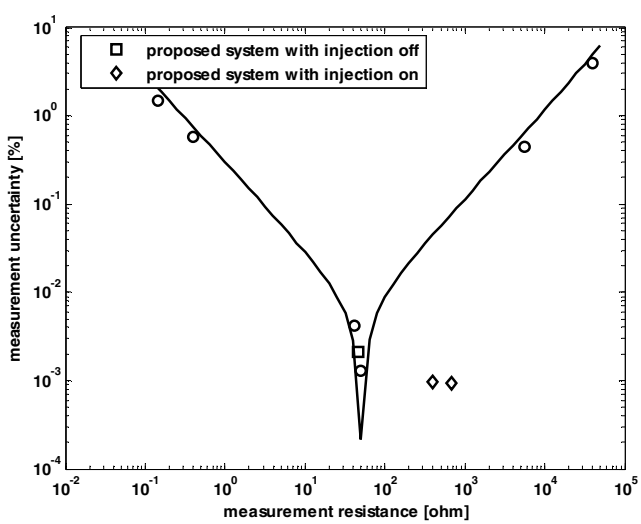

Figure 3. Measurement resolution assessment results of conventional VNA optimized for 50-Ω devices (PNA5225A) at 8 GHz determined with Monte Carlo simulations with the proposed model (line) and with actual measurements (circles). Measurement resolution assessment results of the proposed VNA (PNA5242A) for extreme impedance measurements determined at 8 GHz with experimental measurements (◊).

IV. Experimental Approach & Results

A series of experiments are conducted to study the stability and measurement resolution of a conventional and the proposed VNA for extreme impedance measurements.

In the first experiment the stability of the conventional VNA without injection hardware is evaluated at 50-Ω impedance and highly mismatched impedance values. An Agilent PNA of type 5225A is used during experimental measurements. The two noise sources used in equation (6) are calculated through long-term stability measurement with 2.4 mm mechanical 50-Ω and flush-short standards. The two measurement results are then used in the proposed model and measurement resolution is simulated over the entire impedance dynamic range. A second series of measurements is conducted with 2.4 mm standards to experimentally determine the measurement resolution at a range of different impedance values. The results are shown in figure 3.

In the second experiment measurement resolution of the proposed measurement system for extreme impedance measurements is determined for three different impedance values. An Agilent PNAX of type 5343N is used for experimental measurements.

V. Discussion And Conclusions

Simulation results based on Monte Carlo simulations with the proposed model show strong agreement with experimentally determined values, see figure 3. The model is validated for a VNA system without injection hardware. The proposed model shows much smaller resolution uncertainty for 50-Ω measurement resistance. This is caused by the almost zero reflection occurring with 50-Ω resistance measurement and leading to much smaller uncertainty contribution. Measurement results with the proposed VNA system are compared with that of a conventional VNA system. Both systems show similar measurement sensitivity for 50-Ω resistance measurements. The proposed system is also evaluated for high resistance measurements and almost fifty times better sensitivity is achieved.

Acknowledgements

The authors wish to acknowledge the assistance and support of NXP in providing the funds needed to perform the research and experiments described in this paper.

References

[1] M. Randus and K. Hoffman, "Microwave impedance measurement for nanoelectronics", Radio engineering, April 2011.

[2] K. Haddadi and T. Lasri, "Interferometric Technique for Microwave Measurement of High Impedances", IEEE IMS, June 2012.

[3] G. Vlachogiannakis, H.T. Shivamurthy, et. all, "An I/Q-Mixer-Steering Interferometric Technique for High-Sensitivity Measurement of Extreme Impedances", International Microwave Symposium, May 2015.

[4] F. Mubarak, G.Rietveld and M.Spirito "A Method for De-Embedding Cable Flexure Effects in S-parameter Measurements", in Proc. of the 83nd ARFTG, 2014, Florida, USA.

Uncertainty Analysis in Coplanar Waveguide with Unscented Transformation

Aleksandr A. Savin[1], Vladimir G. Guba[2], Olesia N. Bykova[2]

[1]Tomsk State University of Control Systems and Radioelectronics, Tomsk, Russia,
[2]NPK TAIR, a subsidiary of Copper Mountain Technologies, Tomsk, Russia

***Abstract* — In this paper results of uncertainty analysis of coplanar waveguides (CPWs) parameters are shown in the presence of ambiguities in line geometry and material properties. Calculations are performed with unscented transformation (UT). Error bounds calculated with UT are compared with the results of Monte-Carlo simulation.**

***Index Terms* — Coplanar waveguide, uncertainty, standard deviation, unscented transformation, Monte-Carlo simulation.**

I. Introduction

Uncertainties in coplanar waveguide in presence of ambiguities in dimensions of cross sectional elements and material of CPW were analyzed in paper [1]. CPW parameters calculation was performed based on a model introduced in [2]. Statistical investigation was carried out with Monte-Carlo method.

In the paper UT-calculated statistical characteristics of equivalent-circuit parameters CPW (R, L, C and G) were compared with ones calculated by Monte-Carlo simulation that is more precise. The characteristics could be used for determination of VNA residual parameters accuracies that were defined by adaptive verification algorithm from [3].

In this article for the analysis of CPW parameters uncertainties it is shown that in Gaussian approximation the UT algorithm allows to achieve results similar to ones those were received in multiple statistical tests. Comparison of required computing costs was also made.

II. Unscented Transformation

UT algorithm was received by the authors of [4].

The whole point is that to receive statistical characteristics of a random variable **y** related to random variable **x** through nonlinear function

$$\mathbf{y} = f(\mathbf{x}), \qquad (1)$$

special (limited) sigma-points set is used. It is assumed that **x** is described with mean $\mathbf{m_x}$ and covariance matrix $\mathbf{V_x}$. The mean and covariance matrix of **y** are found with a weighted average algorithm and sigma points set:

$$\mathbf{m_y} = UT_m(\mathbf{m_x};\mathbf{V_x});\ \mathbf{V_y} = UT_V(\mathbf{m_x};\mathbf{V_x}), \qquad (2)$$

where $UT_\bullet$ – transformation operator. Note, Monte-Carlo simulation uses a set of **x** that can have an arbitrary statistic. UT algorithm description in details and its advantages against linearization method are shown in paper [5]. In the study the **x** vector consists of the w_g; w; s; t; k; ε_r; tanδ, to be shown in next chapter. The **y** vector consists of R, L, C, G, Z_0 and γ. Calculation formulas were taken from [2]. Z_0 and γ values are determined by known relations thru R, L, C and G [6].

III. CPWs Parameters

CPW cross section with designations of required dimensions is shown in Fig. 1.

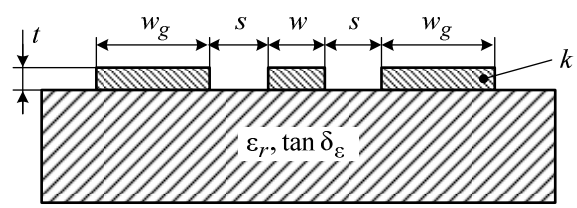

Fig. 1. CPW cross section.

Distributed equivalent-circuit model of CPW is given in Fig. 2 [2]. All elements are defined per length unit (m).

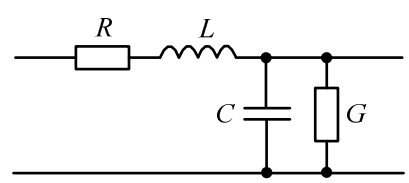

Fig. 2. The equivalent-circuit model of the CPW.

Parameters calculation is performed with quasi-TEM model approach [2]. Data from Table I are used for calculation.

TABLE I
CPWs Parameters and Uncertainties

Parameter	CPW № 1	CPW № 2	half-width of pdf interval	RMSE
w_g	260 µm	200 µm	2 µm	1.15 µm
w	61 µm	40 µm	2 µm	1.15 µm
s	45 µm	5 µm	2 µm	1.15 µm
t	5 µm	1.5 µm	0.2 µm	0.115µm
k	34.5 MS/m	30 MS/m	1 MS/m	0.6MS/m
ε_r	12.9	12.9	0.2	0.115
tanδ	0.0001	0.0001	$5\cdot10^{-5}$	$2.9\cdot10^{-5}$

978-1-4673-9247-1/15/$31.00 ©2015 IEEE

Initial data for Table I were accepted from [1] (CPW № 1) and from [2] (CPW № 2). Root-mean-square error (RMSE) is equal half-width of probability distribution function interval divided by square root of 3. Uncertainties of dimensions and parameters of materials are caused by errors of manufacturing or measurements.

Data of line from [2] are used to check the algorithm from [2] for calculating electrical parameters of the line.

The aim of the modeling is to propagate uncertainties of fabricating the line into uncertainties of R, L, C and G parameters. In Monte-Carlo simulation, uniform distribution is used for every initial data (see 4-th column, Table I). In UT algorithm, Gaussian distribution with zero mean (see 5-th column, Table I) is utilized. It is supposed that components of initial vector are uncorrelated.

IV. Modeling Results

The modeling was carried out over frequency range from 10 MHz up to 100 GHz (37 points). Figs 3-8 show obtained results. Mean values achieved by different methods coincide with high fidelity. To compare dispersion maximum uncertainty is analyzed (tube error). For Monte-Carlo simulation this is a sample with maximum deviation from mean, and while for UT method the 3σ value (99 % probability level) is applied, where σ is a root-mean-square deviation calculated as (2).

Statistical tests number in Monte-Carlo simulation is labeled as M. When modeling M = 10, 100 and 1000. Fig. 3 shows mean and maximum error of total linear resistance for CPW № 2.

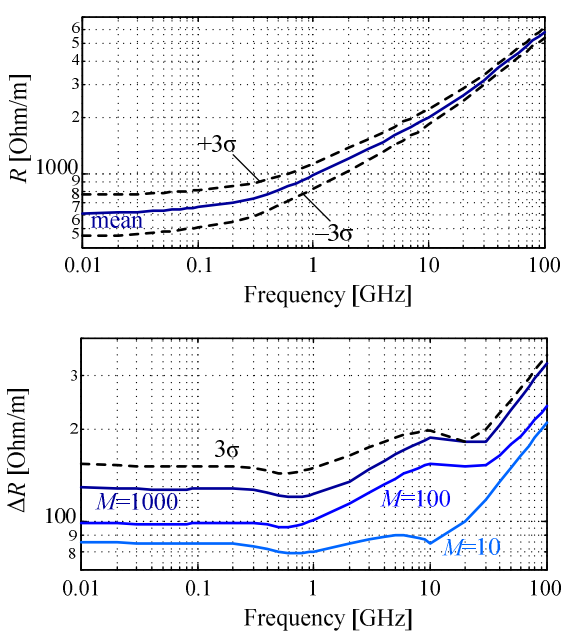

Fig. 3. CPW № 2 total line resistance R as a function of frequency with error tube (up figure), and maximum errors of the resistance ΔR for unscented transformation (value of 3σ) and Monte-Carlo simulation with M = 10, 100, 1000 (bottom figure).

Mean resistance values shown at top of Fig. 3 coincide with calculated data from [2] (see Fig. 4 in [2]). When Monte-Carlo simulation is used and statistical tests number is increased the maximum deviation of resistance (the estimate of maximum error) comes to 3σ value.

Fig. 4 shows mean and maximum error of total line inductance for CPW № 2.

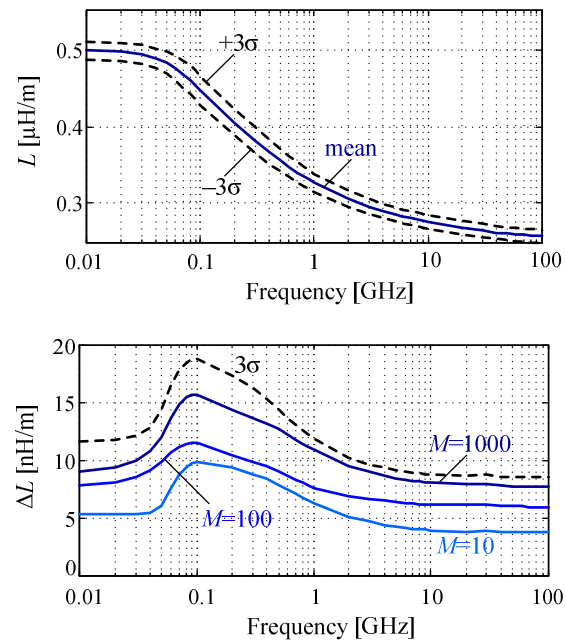

Fig. 4. CPW № 2 total line inductance L as a function of frequency with error tube (up figure), and maximum errors of the inductance ΔL for unscented transformation (value of 3σ) and Monte-Carlo simulation with M = 10, 100, 1000 (bottom figure).

Mean inductance values shown at top of Fig. 4 coincide with calculated data from [2] (see Fig. 5 in [2]). With increasing M the ΔL values tend to 3σ from UT method.

Next, consider in detail the parameters of the CPW line № 1. Fig. 5 shows mean and maximum error of total linear resistance for CPW № 1.

At low frequency range resistance is about 100 Ohm/m. In this case maximum uncertainty is equal to 10 Ohm/m (10 %). When frequency is increased the resistance grows up to 1000 Ohm/m and maximum uncertainty becomes 60 Ohm/m (6 %).

Fig. 6 shows mean and maximum error of total line inductance for CPW № 1.

Inductance and its maximum uncertainty have minor changes up to high frequencies. Ratio of maximum uncertainty to mean of inductance is equal to 10-15 %. Value of linear capacitance is not changed with frequency and is equal to 170.8 pF/m. Maximum uncertainty values are not changed over frequency also. The computed value of 3σ is equal to 5.1 pF/m (3 %). For Monte-Carlo simulation we have the following values: 3.1 pF/m (if M = 10); 3.5 pF/m (if M = 100); 4.1 pF/m (if M = 1000). It is evidence that dispersion of maximum uncertainty estimate at M = 10 is so much more than at M = 1000. In this paper in all of the figures

(for all of the values) we took into account only one of realizations (sample value). Conductance G linearly increases from 10^{-6} S/m to 10^{-2} S/m with increasing frequency from 10 MHz up to 100 GHz. Maximum relative uncertainty is not changed with frequency and equal to 50 %.

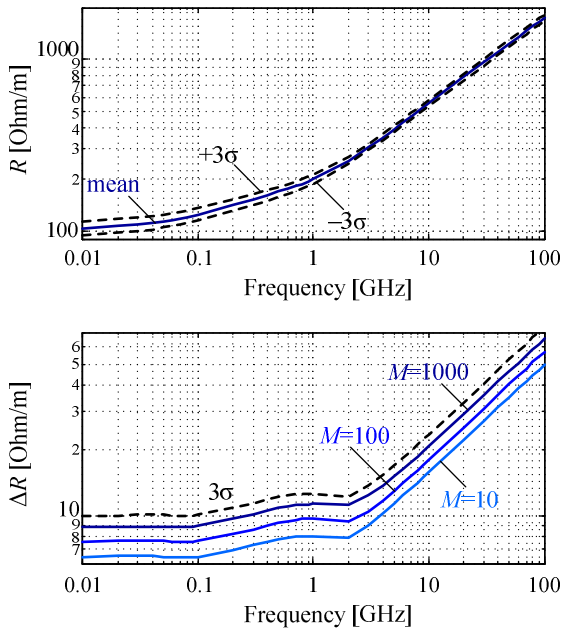

Fig. 5. CPW № 1 total line resistance R as a function of frequency with error tube (up figure), and maximum errors of the resistance ΔR for unscented transformation (value of 3σ) and Monte-Carlo simulation with M = 10, 100, 1000 (bottom figure).

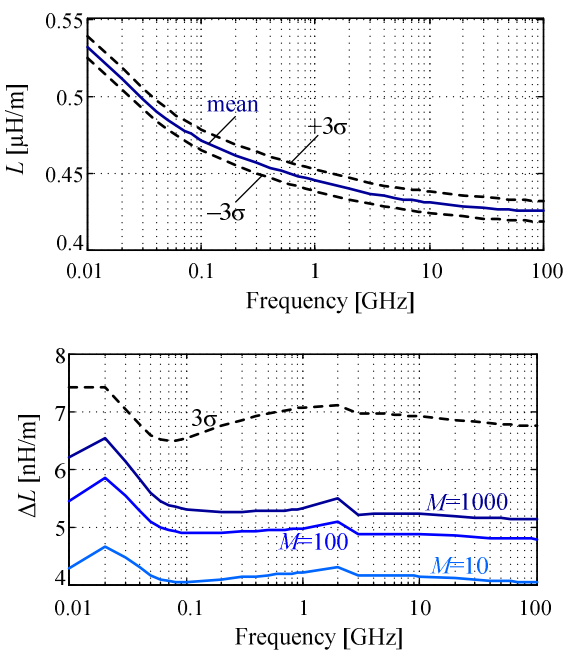

Fig. 6. CPW № 1 total line inductance L as a function of frequency with error tube (up figure), and maximum errors of the inductance ΔL for unscented transformation (value of 3σ) and Monte-Carlo simulation with M = 10, 100, 1000 (bottom figure).

Developed software allows to calculate uncertainties Z_0 and γ. Fig. 7 demonstrates real and imaginary parts of mean value and maximum error of the characteristic impedance Z_0 for CPW № 1.

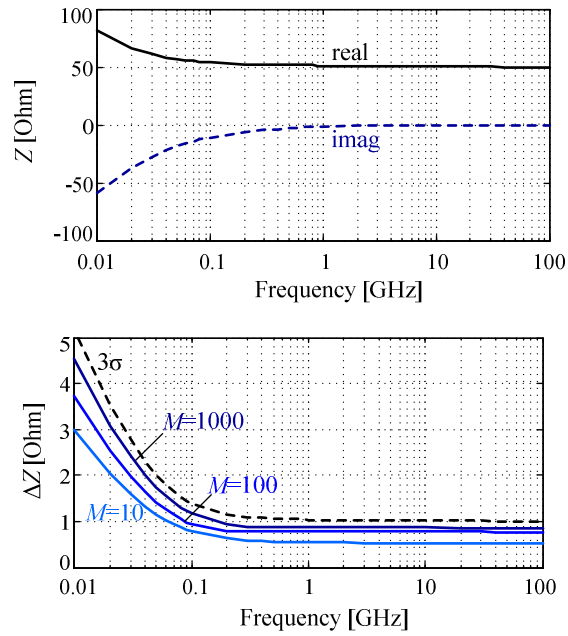

Fig. 7. The properties of the CPW № 1 characteristic impedance calculated with model from [2].

Fig. 8 demonstrates real and imaginary parts of mean value (up figure) and maximum error (bottom figure) of the propagation constant γ for CPW № 1.

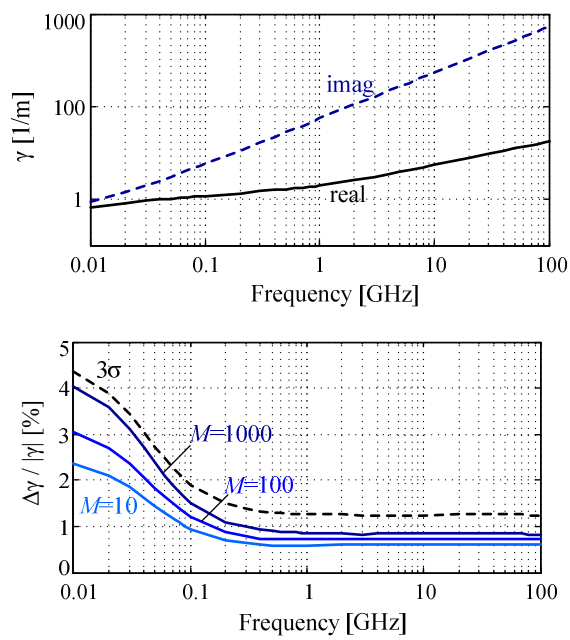

Fig. 8. The properties of the CPW № 1 propogation constant calculated with model from [2].

Impedance uncertainty ΔZ is about 1 Ohm (2 %) in the frequency range above 100 MHz and increases up to 5 Ohm (5 %) at frequencies which are lower than 100 MHz. Relative uncertainty of determination the propagation constant $\Delta\gamma/|\gamma|$ is lower than 1.5 % in the frequency range above 100 MHz and increases to 4.5 % when frequency is reduced to 10 MHz. Thus, we get total uncertainties that were mentioned above if the actual line parameters are selected from Table I.

V. Conclusion

In the paper the results of uncertainty calculation of CPW electrical parameters in presence of deviations from nominal structure's parameters were considered. The calculations were performed with UT method and Monte-Carlo simulation.

When the number statistical tests M in Monte-Carlo simulation is increased, the maximum error approximates to 3σ value achieved with UT method.

To find accuracy estimates of VNA residual parameters, which were achieved by adaptive verification algorithm [3], it will be better to use the largest of all values that is 3σ. The computations show significant uncertainties, therefore it is recommended to take measurements the line parameters more precisely than the data from Table I.

Quantity of sigma points which are needed to perform UT algorithm is defined by the $2n+1$ value, where n is a dimension of initial vector. In the study $n = 7$ and quantity of sigma points is 15.

The calculation time was 0.73 s when UT algorithm was implemented; 0.48 s at $M = 10$, 4.8 s at $M = 100$ and 48 s at $M = 1000$ when Monte-Carlo simulation was used.

Note that increasing M leads to rising of probability to achieve the maximum error at simulation as evidenced by the results.

However even at $M = 1000$ the maximum error that achieved by UT method is more than maximum error by Monte-Carlo simulation. Meanwhile the calculation time for UT method is drastically lower.

Acknowledgement

The authors thank Sergey Zaostrovnykh and Alex Goloschokin from Copper Mountain Technologies, Indiana, USA for support of this work and for their helpful discussions.

The work was supported by Russian President Grant No. MK-3107.2015.8.

References

[1] U. Arz, and K. Kuhlmann, "Uncertainties in Coplanar Waveguide and Microstrip Line Standard for On-Wafer Thru-Reflect Line Calibration," *75th ARFTG Microwave Measurement Conference*, 28 May 2010, pp. 1-5.

[2] W. Heinrich, "Quasi-TEM descriprion of MMIC coplanar lines including conductor-loss effects," *IEEE Trans. Microwave Theory Tech.*, vol. 41, no. 1, pp. 45-52, Jan. 1993.

[3] A. A. Savin, V. G. Guba, A. Rumiantsev, B. D. Maxon, D. Schubert, and U. Arz, "Adaptive Estimation of Complex Calibration Residual Errors of Wafer-Level S-Parameters Measurement System," *84th ARFTG Microwave Measurement Conference*, Boulder, USA, 2014, pp. 1-4.

[4] S. J. Julier, and J. K. Uhlmann, "A General Method for Approximating Nonlinear Transformations of Probability Distributions," *Technical report, RRG, Dept. of Engineering Science*, University of Oxford, Nov. 1996.

[5] A. A. Savin, V. G. Guba, and B. D. Maxson, "Covariance Based Uncertainty Analysis with Unscented Transformation," *82nd ARFTG Microwave Measurement Conference*, 18-22 Nov 2013, Columbus, Ohio, USA, pp. 27-30.

[6] R. B. Marks, and D. F. Williams, "A General Waveguide Circuit Theory," *Journal of Research of the National Institute of Standards and Technology*, vol. 97, no. 5, pp. 533-562, Sep.-Oct. 1992.

Comparison Analysis of VNA Residual Errors Estimation Algorithms with Time Domain Separation

Aleksandr A. Savin[1], Vladimir G. Guba[2], Olesia N. Bykova[2]

[1]Tomsk State University of Control Systems and Radioelectronics, Tomsk, Russia,
[2]NPK TAIR, a subsidiary of Copper Mountain Technologies, Tomsk, Russia

***Abstract* — In the paper results of algorithms' comparison which are utilized for determination of vector network analyzer (VNA) residual parameters are described. Separation of parameters in time domain is the basis for the algorithms. The algorithms based on unscented Kalman filter, least mean square technique and conventional time domain filtering are reviewed. Experimental results are achieved in coplanar waveguide environment in frequency range up to 70 GHz using two precision lines with different lengths.**

***Index Terms* — Vector network analyzer, residual errors, time domain gating, unscented Kalman filter, least mean squares algorithm.**

I. Introduction

Calibration comparison method revealed in [1] is considered as the general method for evaluation of VNA residual errors. Meanwhile few approaches exist based on time-domain technique for residual parameters separating [2]. For the first time in paper [3], a method of joint assessment for the parameters determination of a calibrated one-port instrument with unscented Kalman filter (UKF) was unveiled. Then, UKF method application for two-port VNA verification procedure was discussed in paper [4]. In those investigations a precision line was used as verification standard. During verification test, the line is connected between VNA measurement ports as well as consistently to each of them with a short (or open) termination. For on-wafer verification special adaptive algorithm was developed [5]. Adaptation was caused the lack of a priori verification standards information. Verification with UKF algorithm has employed cubic splines for interpolation of residual parameters. In paper [6] a linear algorithm with a sampling function (sinc function) interpolation was considered. It allowed to implement least mean square technique for residual parameters evaluation. Besides sampling function interpolation, an algorithm that used segments of parabolas was developed.

In this paper comparative analysis of different techniques based on method of joint assessment for residual parameters determination is demonstrated. Furthermore the parameters values are compared with the ones those were obtained with conventional time-domain filtering using a gating. The comparison of residual parameters' estimates at low level (by the example directivity) and at high level (by the example reflection tracking) was done. Calculation times with different algorithms are shown. As a comparison base the UKF algorithm was used.

II. System Model and Windowing Functions

Fig. 1 shows the model of measurement system when verification line is connected between VNA ports.

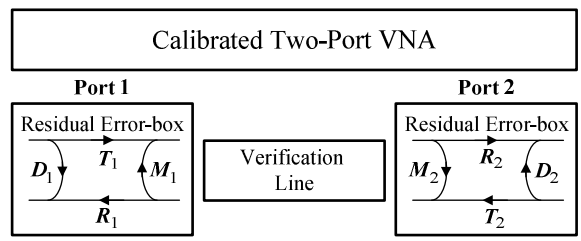

Fig. 1. The model of a two-port calibrated measurement system.

VNA residual parameters: D – directivity, M – match, T – transmission tracking, R – reflection tracking. Measured reflection coefficient in Fig. 1 is defined by two components: D and M. Partial parameters D and M are separated in time-domain at the expense of signal propagation in the line. When line terminated with short or open is used, measured reflection coefficient is defined by three separated parameters: D, $T{\cdot}R$ and M. Comparative analysis was carried out by the example of directivity D and tracking $T{\cdot}R$ in forward direction.

Experimental studies were performed in coplanar waveguide environment. Frequency range was up to 70 GHz (286 points). Wafer material was gallium arsenide [7]. Calibration technique was multiline TRL [8]. For verification procedure two lines with 19.7 mm (L19) length and 6.562 mm (L6) length were applied. Fig. 2 shows time domain diagram and windowing functions for parameters separation to be discussed when line L19 was used.

The windowing functions are defined as:

$$W_{RECT}(r) = [sign(r-c+w) - sign(r-c-w)]/2\,; \quad (1)$$

$$W_{GAUSS}(r) = \exp\left[-\frac{1}{2}\cdot\frac{(r-c)^2}{(2\cdot w)^2}\right]; \quad (2)$$

$$W_{PULSE}(r) = \frac{1}{1+\left(\frac{r-c}{w}\right)^{2m}}\,, \quad (3)$$

where r – distance, c – window center on distance axis, w – window width parameter. Depending on filtered residual

978-1-4673-9247-1/15/$31.00 ©2015 IEEE

parameter the corresponding values for center and width must be inserted into (1)-(3) formulas. Position of center is defined as a residual parameter position on time axis that depends on line length. For example $c = 0$ when directivity filtering is made, and $c = 2L$ (Fig. 2) if match filtering is needed, where L – the line length. Width parameter w is equal to L, $L/6$ and $L/2$ for rectangular, Gaussian and pulse windows respectively. In formula (3) the m defines a pulse form and is equal to 5.

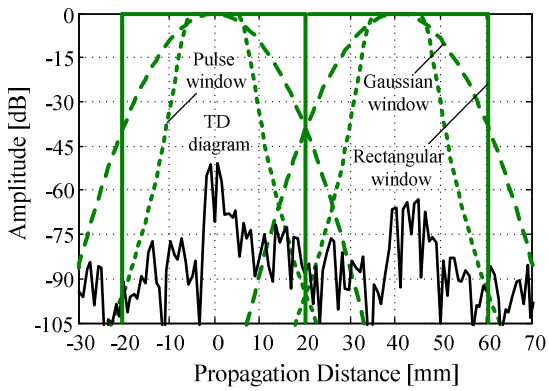

Fig. 2. The time domain diagram (L19).

Fig. 3 displays the time-domain diagram when line L6 was used.

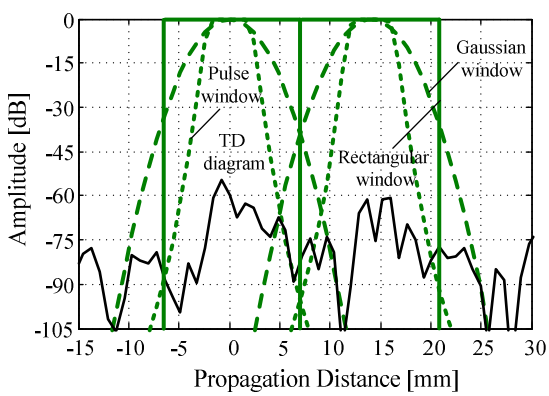

Fig. 3. The time domain diagram (L6).

Time domain diagrams (Fig. 2 and Fig. 3) are received by computing the inverse Fourier transform of the reflection coefficient measurements while verification line was connected to both ports of VNA. At the diagrams the residual directivity (distance about 0) and residual match (distance about $2L$) responses are observed. It is evident that time domain separation by using line L19 is well defined, the residual parameters are localized and do not overlap. It is more difficult to separate (or remove) one of two responses without significant distortions by using line L6. To minimize the distortions one should optimize windows parameters or change a form of windowing function. In the article three windowing functions (formulas from (1) to (3)) used for residual parameters separation are considered.

III. Experimental Results

Results of comparing for residual parameters which were obtained using different algorithms are presented in Figs. 4-7. Fig. 4 shows comparison of residual directivity estimates for port 1 in case line L19 is connected to both ports of VNA. There are estimates received by UKF algorithm, least mean square method with sampling function interpolation (termed as sinc) and also with segments of parabolas (termed as LMS) as well as estimates derived by conventional time domain filtering using different windowing functions. At the bottom in Fig. 4 differences of the estimates are shown, and there estimates by UKF algorithm are used as reference.

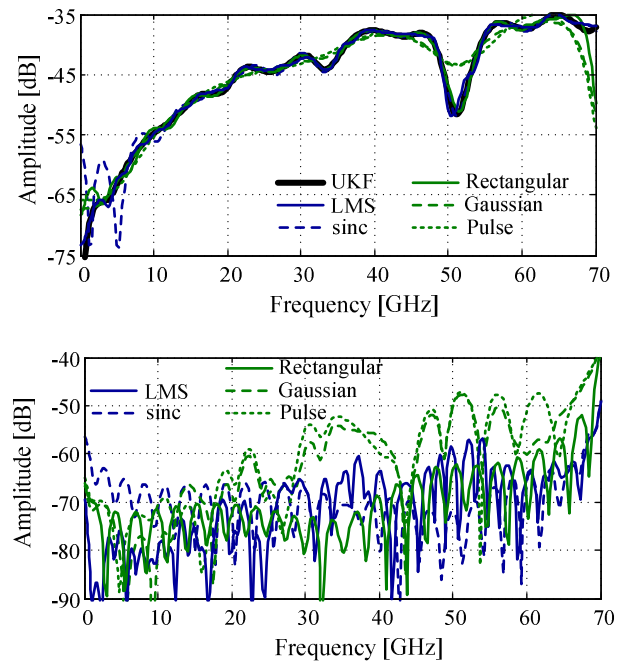

Fig. 4. Comparison of residual directivity estimates D_1 (top figure) and differences with respect to estimate by UKF (bottom figure). L19 was used as verification line.

Residual directivity amplitude does not exceed minus 35 dB. Estimates derived by different methods coincide between themselves with high precision. Graphs at the bottom of Fig. 4 show that difference of estimates does not exceed minus 50 dB over frequency range.

Fig. 5 demonstrates comparison of residual reflection tracking estimates for port 1 when open-circuit line L19 is connected to port 1 of VNA. Influence of inaccurate definition of the line with open stub is not excluded to facilitate visualization.

Residual reflection tracking estimates that were achieved using UKF and LMS algorithms coincide between themselves with high precision. Difference of estimates from other algorithms is significant larger and essentially increases to the edges of frequency range. It is caused by interpolation (for sinc) and Gibbs phenomenon (for conventional time domain filtering).

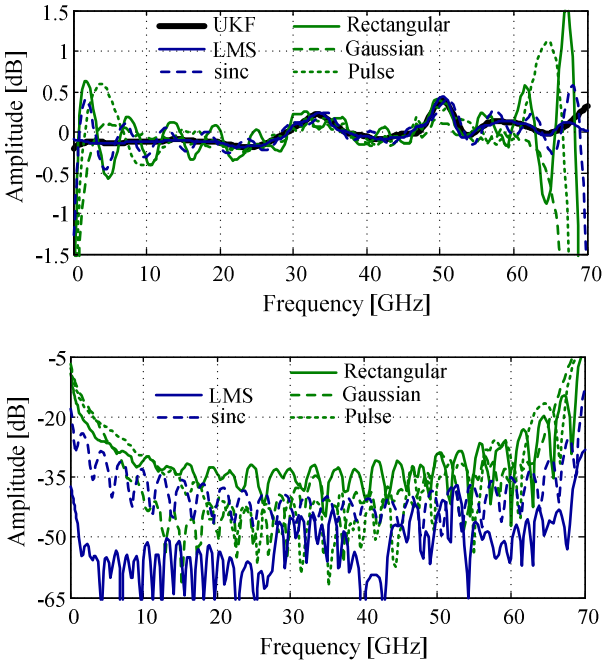

Fig. 5. Comparison of residual reflection tracking estimates $T_1 \cdot R_1$ (top figure) and differences with respect to estimate by UKF (bottom figure). L19 was used as verification line.

Fig. 6 shows comparison of residual directivity estimates for port 1 in case line L6 is connected between VNA ports.

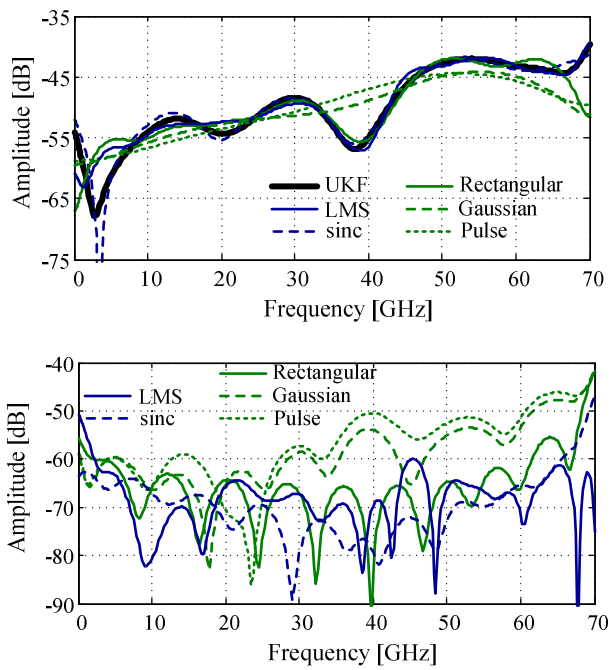

Fig. 6. Comparison of residual directivity estimates D_1 (top figure) and differences with respect to estimate by UKF (bottom figure). L6 was used as verification line.

Residual directivity magnitude increases from about minus 60 dB to minus 40 dB with frequency increasing. Features of residual directivity one could find in detail using UKF and LMS algorithms and conventional time domain filtering with rectangular window.

Fig. 7 displays comparison of residual reflection tracking estimates for port 1 when open-circuit line L6 is used.

Residual reflection tracking estimates shown at Fig. 7 are fully similar to the estimates that are derived with using the L19 line (see Fig. 5 and comments).

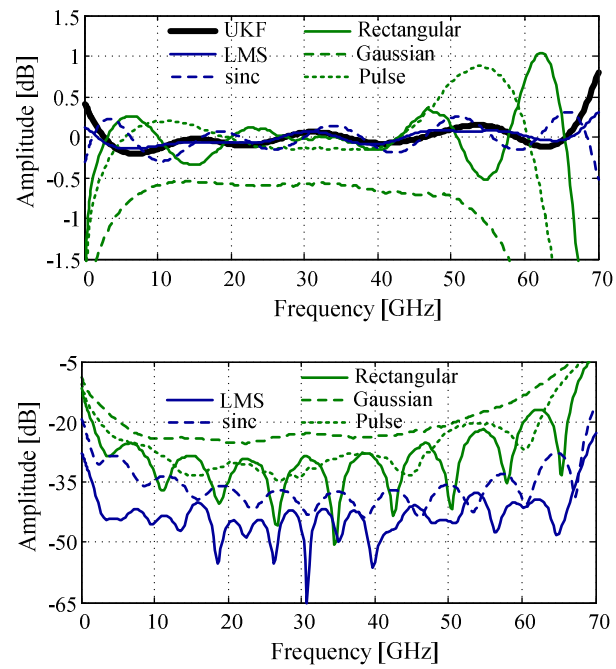

Fig. 7. Comparison of residual reflection tracking estimates $T_1 \cdot R_1$ (top figure) and differences with respect to estimate by UKF (bottom figure). L6 was used as verification line.

Previously performed experimental studies and modeling showed that UKF algorithm is more precise, so UKF results were accepted as a reference. However UKF algorithm requires essential computational resources. Calculation (or simulation) time for different algorithms is 132 s for UKF; approximately 0.37 s and 0.28 s for the least mean square algorithms (sinc functions and segments of parabolas respectively); and about 0.22 s for time-domain filtering (calculation of window and Fourier transform). It should be noted that calculation time of the algorithms base on least mean square technique could be reduced at the expense of use the previously defined interpolating matrix.

As one may have noticed, residual directivity estimates D_1 obtained with two lines are a bit different. Fig. 8 demonstrates the differences ($D_{1,L19} - D_{1,L6}$) for three calibration techniques of VNA: 1) all of lines from calibration wafer are used in calibration procedure; 2) L6 is not used in calibration; 3) L19 is not used in calibration.

Shown in Fig. 8 results could be explained in the following manner. Multiline TRL calibration technique defines an averaged reference (characteristic) impedance of all the lines arranged at the wafer. Impedance of certain line may negligibly deviate from the reference. As a result, the residual

directivity value is derived together with reflection from line $D_{1,L19}=D_1+\Gamma_{L19}$ and $D_{1,L6}=D_1+\Gamma_{L6}$. Difference of directivity estimates is equal to difference of line's reflection coefficients and practically is not depend on calibration technique. Thereby verification with different lines allows to explore the quality of verification standards. The challenge is an object for further detailed study.

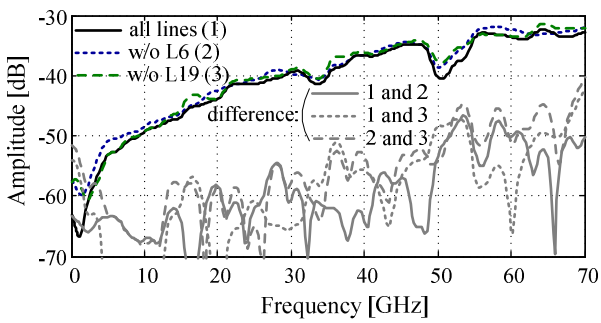

Fig. 8. Differences of residual directivity estimates D_1 for two verification lines L19 and L6 with different length.

IV. Conclusion

A brief description of developed algorithms of joint assessment for residual parameters determination of a calibrated VNA is described. According to experiment's results a number of conclusions could be done. Estimates from conventional algorithm have essential distortions that are increased towards the edges of frequency range. Estimates of low level residual parameters with using conventional time domain filtering are an acceptable accurate. Rectangular windowing function could be used. Accuracy for high level estimates is low for any of windowing functions when conventional time domain filtering is used. In terms of calculation time and fidelity of output data the least mean square algorithm with segments of parabolas interpolation is an optimal. Accuracy of the algorithm is commensurable to the method based on UKF for both low and high level estimates. Meanwhile computation time of least mean square algorithm is significantly lower than for UKF.

Acknowledgement

The authors thank Sergey Zaostrovnykh and Alex Goloschokin from Copper Mountain Technologies, Indiana, USA for support of this work and for their helpful discussions. Uwe Arz from Physikalisch-Technische Bundesanstalt (PTB), Braunschweig, Germany is acknowledged for his great help with the on-wafer measurements.

The work was supported by Russian Foundation for Basic Research RFBR Grant No. 14-07-31312.

References

[1] D. F. Williams, R. B. Marks, and A. Devidson, "Comparison of on-wafer calibration," *38th ARFTG Conf. Dig.*, pp. 68-81, Dec. 1991.

[2] G. Wübbeler, C. Elster, T. Reichel, and R. Judaschke, "Determination of the Complex Residual Error Parameters of a Calibrated One-Port Vector Network Analyzer," *IEEE Transactions on Instrumentation and Measurement*, vol. 58, no. 9. September 2009, pp. 3238-3244.

[3] A. A. Savin, "A Novel Factor Verification Technique for One-Port Vector Network Analyzer," *Proceedings of the 43rd European Microwave Conference*, 7-10 Oct 2013, Nuremberg, Germany, pp. 60-63.

[4] A. A. Savin, V. G. Guba, A. Rumiantsev, and B. D. Maxson, "Estimation of Complex Residual Errors of Calibrated Two-Port Vector Network Analyzer," *83rd ARFTG Microwave Measurement Conference*, 2014, Tampa, Florida, USA, pp. 1-4.

[5] A. A. Savin, V. G. Guba, A. Rumiantsev, B. D. Maxon, D. Schubert, and U. Arz, "Adaptive Estimation of Complex Calibration Residual Errors of Wafer-Level S-Parameters Measurement System," *84th ARFTG Microwave Measurement Conference*, Boulder, USA, 2014, pp. 1-4.

[6] A. A. Savin, "Linear processing of verification data of vector network analyzer for wafer-level application," *Reports of TUSUR*, 2014, no. 3 (33), pp. 53-57. (Russian).

[7] "Reference Material 8130. Coplanar waveguide calibration set," NIST, Gaithersburg, MD 20899, USA, 1998.

[8] R. B. Marks, "A multi-line method of network analyzer calibration," *IEEE Trans. Microwave Theory Tech.*, vol. 39, no. 7, pp. 1205-1215, Jan. 1991.

Impedance Standard Substrate Fabricated by Screen Printing Technology

Masahiro Horibe and Ryo Sakamaki
National Institute of Advanced Industrial Science and Technology,
Research Institute for Physical Measurements

***Abstract*— The paper proposes new fabrication process for an Impedance Standard Substrate (ISS) for on-wafer measurements at microwave and millimeter-wave frequencies. Screen printing technology has provided coplanar waveguides (CPW) lines with low transmission loss and high precision contact repeatability at millimeter-wave frequency up to 110 GHz. The paper demonstrate capability of the screen printed CPW as an ISS for on-wafer measurements. Standard lines with seven different lengths were designed and fabricated by screen printing technology. In the paper, Multiline ThruReflect-Line (TRL) calibration was performed by using ISSs fabricated by both screen printing and conventional pleated technologies. Regarding calibration capability validation, contact repeatability performance was first tested, then, verification devices were measured. According to comparison results, results obtained by calibration of screen printing ISS are almost the same as results measured based on conventional ISS tech**.

***Index terms*— Screen printing; On-wafer measurements; Impedance standard substrate; Scattering parameters; Verification Substrate**

I. Introduction

In recent years, the device electronics at millimeter-wave frequency is demanded in the telecommunication area. For telecommunication device technology, applications require not only performance but also light weight with ultra-slim. In addition, cost efficiency is important factor to familiarize the product to the public. Currently set of conductor plating, photolithography patterning and etching processes are commonly used in the traditional passive device fabrication and packaging. The fabrication is, thus, basically complex and expensive process. In addition, the process have to spend much time and produces waste fluid by the end of fabrication process. Recent interest in the electronic applications is driven by not only the low cost and environmental friendly, furthermore substrate material flexibility is demanded [1]-[5] from the mobile telecommunication and healthcare areas.

The paper proposes new fabrication process, screen printing technology, for an Impedance Standard Substrate (ISS) for on-wafer measurements at microwave and millimeter-wave frequencies. Our screen printing technology has provided coplanar waveguides (CPW) lines with low transmission loss and high precision contact repeatability at millimeter-wave frequency up to 110 GHz [6]. CPW as a standard transmission line producing the characteristic impedance of 50 ohms is fabricated on a thin Almina substrate by a screen printing technology. Screen printed transmission lines provides good insertion losses of 0.17 dB/mm at 60 GHz and 0.30 dB/mm at 110 GHz [6]. For contact reproducibility as important performance in the calibration and measurement process for on-wafer devices, printed conductors achieved excellent reproducibility (N=10), i.e. less than 0.1 degrees for phase in short circuits[6].

The paper also demonstrate capability of the screen printed CPW as an ISS for on-wafer measurements. Standard lines with seven different lengths were designed and fabricated by screen printing technology. In the paper, Multiline Thru-Reflect-Line (TRL) calibration was performed by using ISSs fabricated by both screen printing and conventional pleated technologies. Regarding calibration capability validation, contact repeatability performance was first tested, then, verification devices, i.e. “Keysight Verification Substrate (KVS)” were measured. In the paper, eight types of verification device were measured in order to comparison between both ISSs for certifying a calibration and measurement capability using screen printed ISS.

II. Comparison Devices

The above comparison used eight types of planar devices as follows;

978-1-4673-9247-1/15/$31.00 ©2015 IEEE

i) Thru Line;
ii) High reflects, i.e. Open and Short;
iii) Low reflect, i.e. Matched load;
iv) 30dB Attenuator;
v) Mismatch line;
vi) Two series resistors;

Each verification standards were measured by two different calibration conditions, i.e. commercial ISS and screen printed ISS.

III. Measurements and Uncertainty

A Keysight Technologies (formerly Agilent Technologies) N5250A based on E8361A vector network analyzer and 1.0 mm frequency extension modules with mm-Wave controller were used to measure the Scattering parameter of CPW lines in the range from 10 MHz to 110 GHz. 1.0 mm coaxial probes, Cascade MicroTech Infinity SP-I110-A-GSG-06 with 150 µm pitch of Ground to Signal to Ground, were used.

In this study, multiline TRL calibration was done on Cascade Microtech 101-190C ISS and screen printed ISS at the probe tips. In the case of calibration at probe tip using ISS, "thru" line, L=220 µm, is used as "flush thru". Then, verification standards were measured under the each calibration by 6 times.

On the uncertainty evaluation, dimensions of CPW on the ISSs were measured and characterize the line impedances. The difference between system impedance, i.e. 50 ohms, and ISS's impedance over several GHz provides to the calibration uncertainty. In addition, contact repeatability, presented by Ref. [6], was also taken into account to the calibration and measurement uncertainty.

Finally, the two types of measurement results for the verification devices were compared.

IV. Comparison

In graphs of following results, red and blue lines indicate results obtained by printed ISS and commercial ISS.

A. Thru line

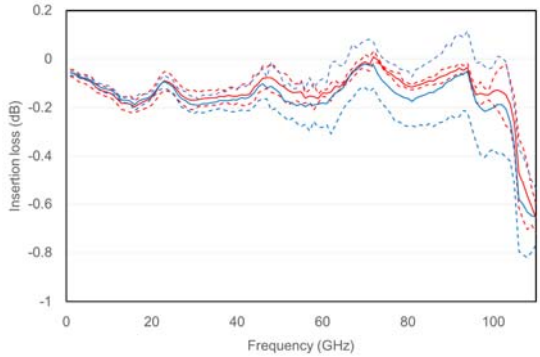

Fig. 1 Amplitude of S_{21} of Thru line

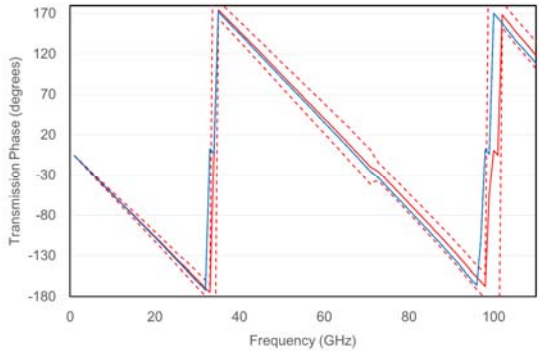

Fig. 2 Phase of S_{21} of Thru line

Regarding transmission line, the both amplitude and phase characteristics are almost agree with each other within uncertainty. However, phase characteristics at high frequency region are different due to difference of electrical measured lengths of thru line standard between commercial and printed ISSs.

B. High reflects (Short)

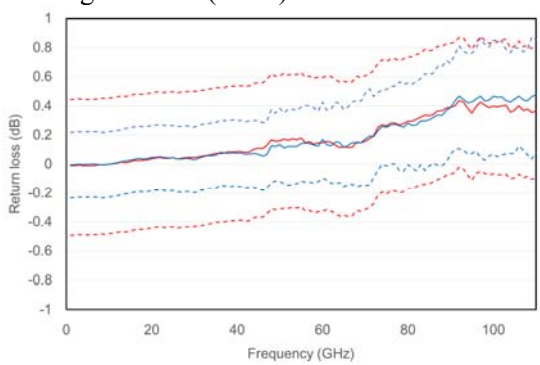

Fig. 3 Amplitude of S_{11} of short device

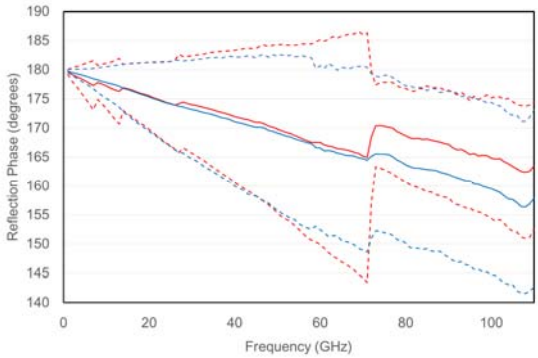

Fig. 4 Phase of S_{11} of short device

Regarding high reflective, the both amplitude and phase characteristics are agree with each other within uncertainty. Below 67 GHz, large uncertainty was provided from dimensional un-uniformity of "Line" standards in calibration and system noise characteristics of VNA.

C. Low reflect (Matched load)

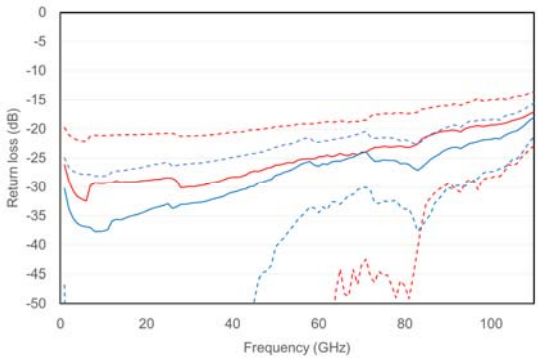

Fig. 5 Amplitude of S_{11} of Matched load device

Regarding low reflective, the amplitude characteristic is agree with each other within uncertainty. At low frequency, the difference is coming from dimensional un-uniformity of "Thru" and "Line" standards providing mismatch error in VNA measurements.

D. 30dB Attenuator

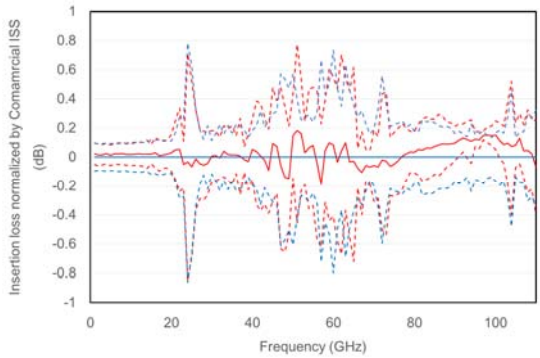

Fig. 6 Normalized Amplitude of S_{21} of 30dB attenuator, normalized by S_{21} of commercial ISS

Regarding low reflective, the amplitude characteristic is agree with each other within uncertainty. Below 67 GHz, large uncertainty was provided from system noise characteristics of VNA.

E. Mismatch line

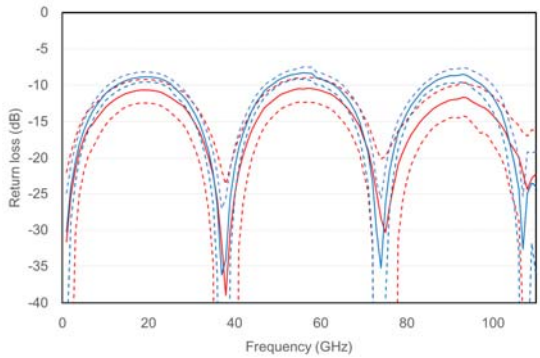

Fig. 7 Amplitude of S_{21} of Mismatch line

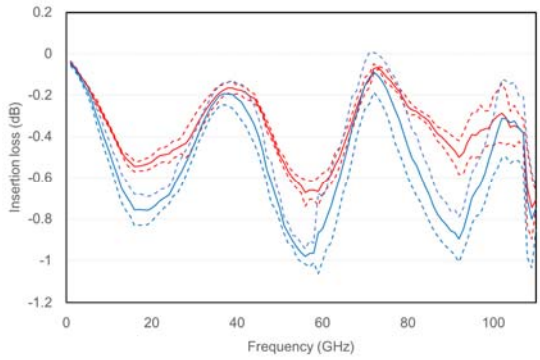

Fig. 8 Phase of S_{21} of Mismatch line

Regarding mismatched transmission line, the both amplitude and phase characteristics are not agree with each other within uncertainty. This was because from dimensional un-uniformity of "Thru" and "Line"

standards, on printed ISS, providing mismatch error in VNA measurements. And "Thru" line's offset loss is different between commercial and printed ISSs.

F. 25 ohms series resistors

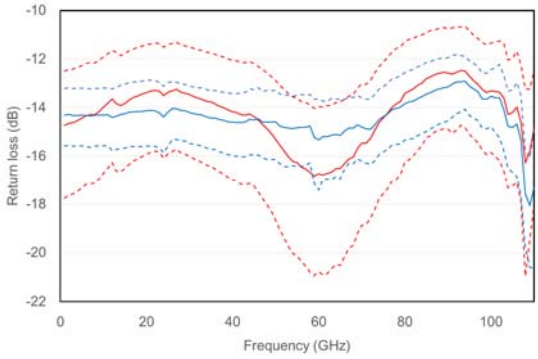

Fig. 9 Amplitude of S_{11} of 25 ohms series resistor

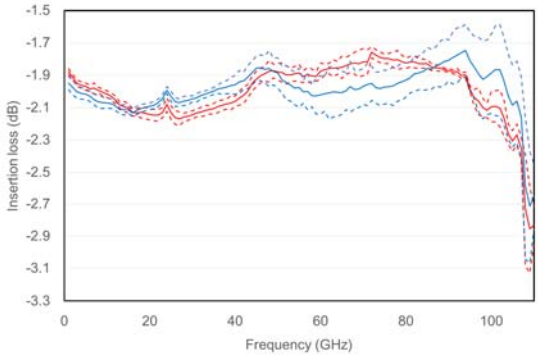

Fig. 10 Amplitude of S_{21} of 25 ohms series resistor

Regarding series resistor, amplitude of S_{11} is agree with each other within uncertainty. However, S_{21} characteristics is not equivalent with each other. This is similar result obtained from mismatch transmission line.

VII. Summary

This paper has demonstrated a capability of transmission lines fabricated by printed electronics to use for calibration standards. According to comparison between commercial ISS and printed ISS, almost characteristics of verification devices is agreed within uncertainty. However, for transmission device having mismatch element, transmission characteristics obtained by printed ISS are not equivalent to those obtained by commercial ISS. This might be "Thru" and "Line" standard imperfection from dimensional un-uniformity and error of dimension of the lines.

However, improvement of fabrication precision by using different screen printing technology, i.e. offset screen printing etc., will be provide accurate ISS.

Acknowledgement

The authors thank Mr. Y. Yanagimoto, Keysight Technologies, for preparation of the KVS verification devices and useful discussions.

References

[1] G. Shaker, M. Tentzeris, and S. Safavi-Naeini " Low-Cost Antennas for mm-Wave Sensing Applications using Inkjet Printing of Silver Nano-particles on Liquid Crystal Polymers", IEEE *Antennas and Propagation Society International Symposium* 2010.

[2] O. Azucena, J. Kubby, D, Sarbrough and C. Goldsmith, "Inkjet Printing of Passive Microwave Circuitry," IEEE MTT-S Int. Microwave Symp 2008.

[3] B. S. Cook, A. Shamim "Inkjet Printing of Novel Wideband and High Gain Antennas on Low-Cost Paper Substrate," IEEE Transaction on Antenna and Propagation, vol. 60, no. 9, 2012.

[4] F.Cai, Y.H. Chang, K. Wang, C. Zhang, J. Papapolymerou, "2.45 GHz Low Cost Low Noise Amplifier on Flexible Organic Substrate," IEEE APMC, 2013.

[5] W. Khan, A. Ulusoy, J. Papapolymerou, "D-Band Characterization of Co-Planar Wave Guide and Microstrip Transmission Lines on Liquid Crystal Polymer," IEEE ECTC, 2012.

[6] M. Horibe, M. Yoshida, "Reliability of Transmission Lines Fabricated by Screen Printing for On-wafer Measurements at Millimeter-wave," EuMW2015 Proceedings, 7-10 Sept 2015, Paris, France, 2015.

Joint Self-Heating and RF Large Signal Characterization

Francisco J. Martinez-Rodriguez[1,2], Patrick Roblin[1], Jose I. Martinez-Lopez[2]

[1]Computer and Electrical, The Ohio State University, Columbus, OH 43210, USA

[2]Facultad de Ingeniería, Universidad Nacional Autónoma de México, Mexico City 04510, Mexico.

***Abstract* — Self-heating affects the RF performance of power transistors and must therefore be characterized for accurate device modeling. This paper presents an active loadpull (ALP) testbed which performs continuous wave measurements with the LSNA for arbitrary loads and substrate temperatures while jointly measuring the device die temperatures with an infrared sensor. Measurements are performed for a 15 W GaN HEMTs for 15, 25, 35 and 45 C substrate temperatures. The thermal resistance is extracted from the dissipated power and temperature data for fundamental loads spanning the entire Smith Chart. The quasi linear relation between the dissipated power and the device temperature increase measured for all loads verifies that a physical temperature is measured. The expected correlation between the dissipated power, output power and device temperature is also evidenced. This ALP testbed provides thus a wealth of joint loadpull, thermal and loadline data which should facilitate the extraction of an electrothermal device model directly from large-signal RF measurements.**

***Index Terms* — HEMT, LSNA, self-heating.**

I. Introduction

AlGaN/GaN HEMTs are known for their ability to handle high power density while exhibiting high efficiency and high reliability [1]. This makes them highly attractive for the design of power amplifiers [2]. However the modeling of HEMTs remains challenging due to memory effects such as self-heating and trapping which affects the IV characteristics (IV knee walk-out) and induce temporary degradations in the RF performance [5]. The activity of these memory effects are determined not only by the dc-bias conditions, but also the output RF load conditions, and the output power levels associated with the RF signals [3]. One of the major memory effects affecting the GaN HEMT is self-heating [4] in which the power dissipated (P_{diss}) increases the temperature device (T_{dev}) via the thermal resistance (R_{th}). Self-heating is a relatively slow memory effect [5] such that under wideband modulated RF excitations such as LTE, the transistor operation remains mostly isothermal. Thus characterizing HEMTs for isothermal operation at different die temperatures is required for accurate non-linear device modelling.

This paper presents an active loadpull (ALP) testbed which performs continuous wave measurements with the LSNA for arbitrary output RF loads while simultaneously measuring the device die temperature. Measurements for various substrate temperatures can then be performed. This allows in turns to extract from the data base, the isothermal response for different load conditions. Isothermal large-signal response could alternately be acquired using pulsed RF operation. However traps do not have time to charge during pulsed-RF operation and their contribution to the CW RF operation is unrealistically preempted. On the other hand having access to the device and substrate temperatures permits ones to extract isothermal data which fully account for the trap activity under CW RF operation. Further the thermal resistance can be extracted since the dissipated power is provided by the RF large signal measurements.

In this paper active loadpull measurements are performed for a 15 W GaN HEMTs for 15, 25, 35 and 45 °C substrate temperatures. The thermal resistance is extracted from the dissipated power and temperature data for fundamental loads spanning the entire Smith Chart. Since thermal equilibrium takes time to establish, the time between measurements must be carefully selected. In this work a delay of 1 min is found to yield an acceptable dispersion in the thermal data but longer time could be used. The accuracy of the thermal resistance extracted can then be verified for all output loads selected in the Smith Chart. The expected correlation between the dissipated power, output power and device temperature during the loadpull is also investigated to evaluate the consistency of the thermal data acquired.

II. Motivation: Self-heating in device modelling

It has been demonstrated for low power devices that the IV and charge characteristics in a nonlinear device model can be directly extracted from large-signal measurements [6,7]. One approach to extract the nonlinear model with memory effects from Artificial Neural Networks (ANN) was reported in [6] for the case of the parasitic bipolar transistor in SOS-MOSFETs. However for power GaN HEMTs the intrinsic drain current (I_D) is not only a function of the gate-source voltage (V_{GS}), the drain-source voltage (V_{DS}) but also the device temperature (T_{dev}). The motivation for this experimental work is to now use an ANN to extract a nonlinear model from large-signal measurements while accounting for self-heating.

III. Experimental testbed

The experimental setup is shown in Fig. 1. The GaN power device used to do the measurement is the CGH27015F of the CREE Inc. The active loadpull measurements are performed using two RF sources placed at the input and output

978-1-4673-9247-1/15/$31.00 ©2015 IEEE

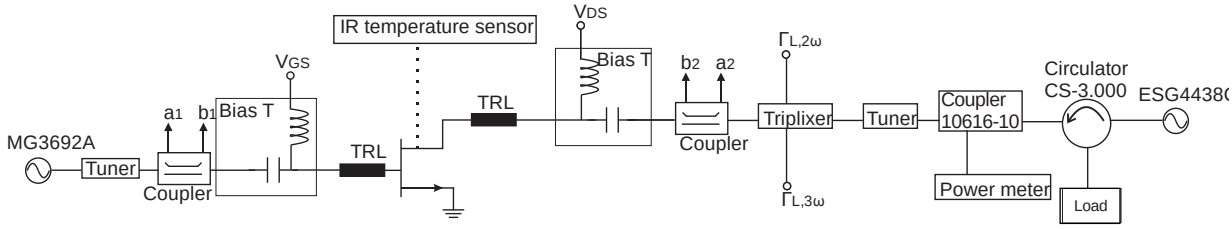

Fig. 1. ALP setup used for the RF and thermal measurements.

respectively. The fundamental frequency of the input RF source (MG3692A) and the output RF source (ESG4438C) used for the active load pull is set to 2 GHz. The second and third harmonic impedances at the triplexer output are selected from embedding simulations to approximate an intrinsic short that approaches the operating condition of class B at the device current source reference planes. The substrate temperature is partially controlled with the chuck plate temperature. The substrate and device temperature T_{sub} and T_{dev} were measured on the transistor heat sink and the transistor die surface respectively. The incident and reflected waves are acquired with an LSNA using two directional couplers (RT0812H).

IV. Experimental Results

When the RF power is applied to the device, the dissipated power P_{diss} and the temperature difference ($\Delta T = T_{dev} - T_{sub}$) increase accordingly [5]. The variation of the device temperature T_{dev} with the substrate temperature T_{sub} for different chuck temperatures is shown in Fig. 2.

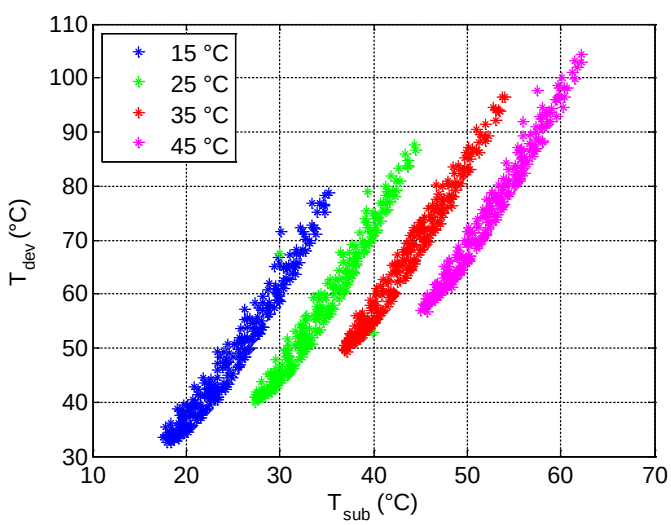

Fig. 2. T_sub and T_dev Measurements.

From the P_{diss} and ΔT data, the device thermal resistance R_{th} is extracted for different chuck plate temperatures and the results obtained are summarized in Table I. The comparison between the measurement and the model is shown in Fig. 3 when the chuck plate temperatures is 35 °C. The correlation between the P_{diss} and ΔT is quasi linear as shown in Fig. 3. This linear relationship is thus well represented by:

$$\Delta T = T_{dev} - T_{sub} = R_{th} P_{diss} \qquad (1)$$

However for P_{diss} below 10 W a departure from the linear relation is observed which requires further investigations.

TABLE I
R_{th} EXTRACTED

Chuck Temperature (°C)	R_{th} (°C/W)
15	1.5596
25	1.5209
35	1.5305

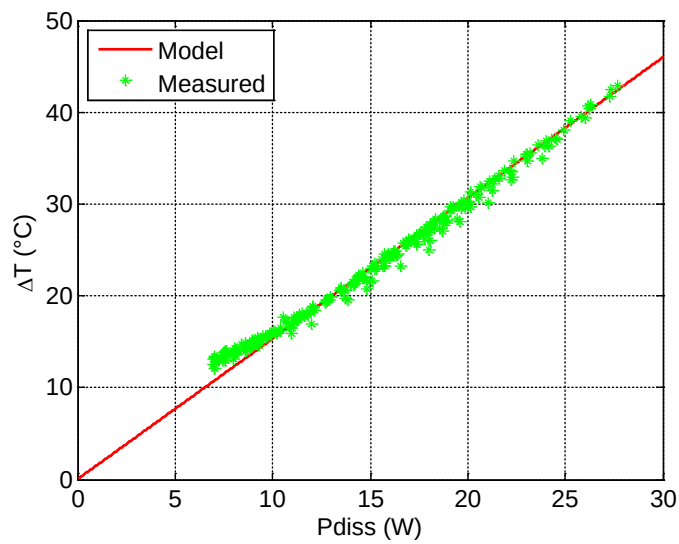

Fig. 3. Comparison of measured and calculated ΔT.

The dissipated power P_{diss} and the device temperature increase ΔT varies with the load output impedances. The device temperature increase ΔT predicted by the model from $R_{th}\, P_{diss}$ is compared to the measured ΔT in Fig. 4 as a function of the loadpull impedances.

The correlation between the dissipated power $P_{diss} \sim \Delta T / R_{th}$ and the output power in the loadpull provides additional valuable insights to evaluate the consistency of the thermal data acquired. Fig. 5 shows the output power (P_{out}) contours in green and the dissipated power P_{diss} contours in purple. Along a given constant output power (P_{out}) level the

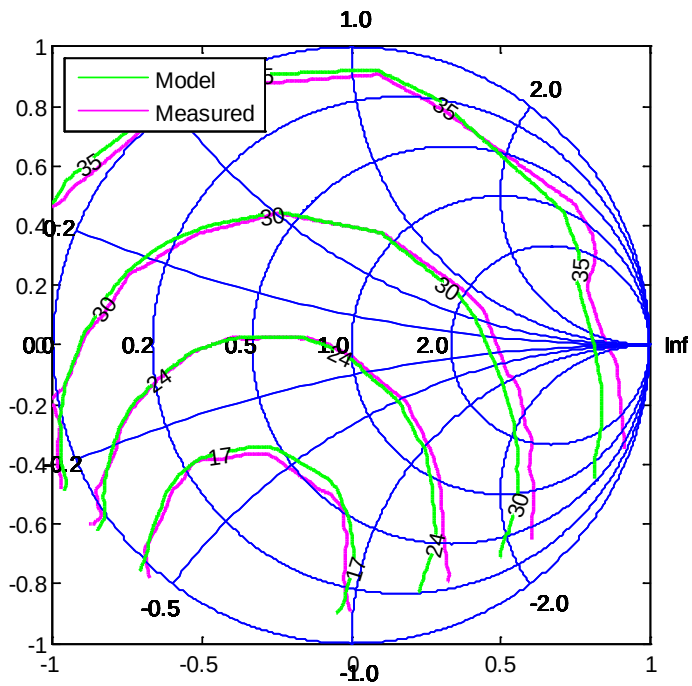

Fig. 4. Loadpull comparison of measured and calculated ΔT.

dissipated power P_{diss} will vary according to purple contour shown in Fig. 5. The blue trajectory gives the output load where P_{diss} and ΔT are minimal and the red trajectory where P_{diss} and ΔT are maximal.

V. Conclusion

The quasi linear relation between the dissipated power and the device temperature increase measured for all loads verifies that a physical temperature is measured. The expected correlation between the dissipated power, output power and device temperature is also evidenced. This ALP testbed provides thus a wealth of joint loadpull, thermal and loadline data which should facilitate the extraction of an electrothermal device model directly from large-signal RF measurements.

Acknowledgement

This work was supported in parts by the National Council of Science and Technology of Mexico (CONACYT), the National Science Foundation (NSF) under Collaborative Grant ECS-1129013 and by Rockwell Collins under a project grant.

References

[1] Xiucheng Huang, Zhengyang Liu, Qiang Li,and Fred C. Lee, "Evaluation and Application of 600 V GaN HEMT in Cascode Structure," *IEEE Transactions On Power Eelectronics*, Vol. 29, No. 5, May 2014

[2] Alaaeddine Ramadan, Tibault Reveyrand, Audrey Martin, Jean-Michel Nebus, Philippe Bouysse, Luc Lapierre, Jean-François Villemazet, and Stéphane Forestier, "Two-Stage GaN HEMT Amplifier With Gate–Source Voltage Shaping for Efficiency Versus Bandwidth Enhancements" *IEEE Transactions On Microwave Theory and Techniques, Vol. 59, NO. 3, March 2011.*

[3] Patrick Roblin, David E. Root, Jan Verspecht, Youngseo Ko,and Jean Pierre Teyssier, "New Trends for the Nonlinear Measurement and Modeling of High-Power RF Transistors and Amplifiers With Memory Effects" *IEEE Transactions On Microwave Theory and Techniques, Vol. 60, NO. 6, June 2012.*

[4] Kelvin S. Yuk, George R. Branner, and David J. McQuate, "A Wideband Multiharmonic Empirical Large-Signal Model for High-Power GaN HEMTs with Self-Heating and Charge-Trapping Effects" *IEEE Transactions On Microwave Theory and Techniques, Vol. 57, No. 12, December 2009.*

[5] P. Roblin, .Nonlinear RF Circuits and Nonlinear Vector Network Analyzers, *Cambridge University Press*, 2011.

[6] Youngseo Ko, Patrick Roblin, Member, IEEE, Andrés Zárate-de Landa, J. Apolinar Reynoso-Hernández, Member, IEEE, Dan Nobbe, Chris Olson, and Francisco Javier Martinez, "Artificial Neural Network Model of SOS-MOSFETs Based on Dynamic Large-Signal Measurements". *IEEE T Transactions On Microwave Theory and Techniques, VOL. 62, NO. 3, March 2014.*

[7] M. Curras-Francos, P. Tasker, M. Fernandez-Barciela, Y. Campos-Roca, and E. Sanchez, "Direct extraction of nonlinear FET QV functions from time domain large signal measurements," *IEEE Microwave and Guided Wave Letters*, vol. 10, no. 12, pp. 531–533, 2000.

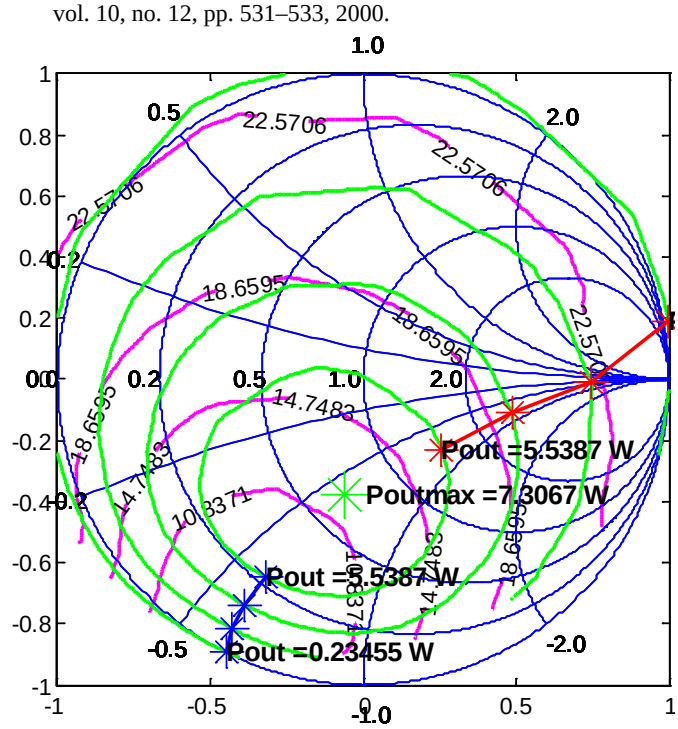

Fig. 5. Pout loadpull contour (green), Pdiss loadpull contour (purple) and trajectory of Pout for the maximum and minimum dissipated power Pdiss.